

https://dspace.org/

Efficiency Enhancement in Photovoltaic Devices Using Light Management and Morphology

Kumalo, Sandile

2024-04
University of the Witwatersrand, Johannesburg
https://hdl.handle.net/10539/46787
Kumalo, Sandile. (2024). Efficiency Enhancement in Photovoltaic Devices Using Light Management and Morphology. [PhD thesis, University of the Witwatersrand, Johannesburg]. WIReDSpace. https://hdl.handle.net/10539/46787

Downloaded from a DSpace repository. https://dspace.org/

Efficiency Enhancement in Photovoltaic Devices Using Light Management and Morphology

Supervisor: Prof. D Wamwangi
Co-Supervisor: Prof. A Quandt

Sandile Kumalo



UNIVERSITY OF THE
WITWATERSRAND,
JOHANNESBURG

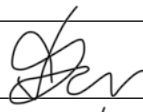
A Thesis submitted to the Faculty of Science,University of the Witwatersrand, Johannesburg, in fulfilment of the requirements for the degree of Doctor of Philosophy in Physics.

April 2024

Declaration

I, Sandile Kumalo (545710), declare that this thesis titled, "Efficiency Enhancement in Photovoltaic Devices Using Light Management and Morphology," and the work presented in it are my own. The research was conducted primarily during my candidature for a PhD degree at the University of the Witwatersrand. I confirm that this thesis has not been submitted, either in whole or in part, for any other degree or qualification at the University of the Witwatersrand or any other institution. I have consulted the work of others, which is duly quoted and acknowledged with complete references.

Name: Sandile Kumalo

Signed: 

Date: 29/07/2024

Place: University of the Witwatersrand

Acknowledgement

The author wishes to express profound gratitude to those who have provided invaluable assistance throughout the research and writing of this dissertation.

First and foremost, appreciation is extended to Prof. Alexander Quandt and Prof. Daniel Wamwangi for their unwavering guidance and support. Their vast wisdom and wealth of experience have been a source of inspiration throughout the studies. It is acknowledged that their mentorship laid the foundation for a strong scientific enthusiasm, with hopes for continued fruitful cooperation in the scientific field. Special thanks are directed to Prof. Wamwangi for his kindness, firmness, and patience, which have contributed significantly to personal and professional growth. His teachings and training in various laboratories have been particularly impactful. The author is deeply grateful to Prof. Quandt for the opportunities provided and for the insightful discussions that have greatly benefited the project.

Gratitude is also extended to the Center of Excellence for Strong Materials (CoE-SM), Eskom TESP grant (Professor Rudolph Erasmus) and the National Research Foundation (NRF) for their generous financial support, which was crucial in enabling the research and covering necessary fees. A heartfelt thank you goes to iThemba LABS and Anthony Miller for offering essential infrastructure that facilitated the work in implantation. Appreciation is further extended to the School of Physics, the Microscopy and Microanalysis Unit (MMU), and Wits University for providing access to exceptional research facilities and resources.

Special thanks are given to the Advanced Functional Materials and Devices (AFMD) Group, led by Professor Moritz Riede at the University of Oxford, for their warm welcome and support. Pascal and Nicky are particularly acknowledged for their invaluable help and advice. The experience of conducting experiments and the time spent at the University have been profoundly rewarding. Sincere thanks are also extended to the Africa Oxford Initiative (AfOx) for facilitating an extended stay by an additional two months, further enriching the research journey.

The author also wishes to thank Prof. Rudolph Erasmus, Dr. Adam Shnier, Mr. Gerard Peters, and Dr. Francis Otieno for their assistance in the lab, introducing various lab equipment and analysis techniques. Dr. Emily Aradi from the University of Manchester is acknowledged for her help with TEM analysis for magnetic nanoparticles. Finally, gratitude is extended to Jonathan Cook, and the Wilkins family-Niall, Ilana, Max, and Ivy-for their support.

Dedication

This thesis is dedicated to my late grandmother, Thembi Eva Kumalo and my mother, Constance Jabulisile Kumalo.

List of Publications

1. Kumalo, S, Wamwangi, D, Quandt, A, Mayimele, N, Otieno, F, "Stained glass revisited - photovoltaics meets glass photonics" book chapter contribution on Jenny Stanford Publishing.

2. Sandile Kumalo, Daniel Wamwangi, Alexander Quandt and Emily Aradi, "Frequency conversion to augment power conversion efficiency in photovoltaic devices" third Workshop on Progress in Nonlinear Photonics and Applications (PNPA2024), IEEE (Accepted).

Publications in Preparation

1. Quandt, A, Wamwangi, D, Kumalo, S, "The use of core-shell nanoparticles in photovoltaics" Review article MDPI Nonlinear Photonics.

2. Sandile Kumalo, Daniel Wamwangi, Alexander Quandt, "Eco-Efficient Fabrication of $PTB7 : PC_{70}BM$ Organic Solar Cells: Leveraging Hansen Solubility Parameters for Optimal Green and Industrial Co-Solvent Selection"

3. Sandile Kumalo, Daniel Wamwangi, Alexander Quandt, "A Comparative Study of Chlorinated and Green Co-Solvents in the Fabrication of Non-Fullerene Acceptor OSCs Based on Hansen Solubility Parameters"

List of Conferences/Workshop Presentation

1. Attended the 8th edition of the International School of Physics for Materials for Energy and Sustainability (ISMES) from 21st -27th of July 2019, hosted by California Institute of Technology (Caltech). Contribution: Poster titled **"Enhancement of a-Si:H Solar Cells By Down Conversion in Combination with Plasmonic Nanoparticles"**

2. Attended the Emerging Concepts in Solar Energy Conversion-from Computation to Implementation Conference from 10th-12th February 2020, hosted by King Abdullah University of Science and Technology, Jeddah, Saudi Arabia. Contribution: Poster titled **"Enhancement of a-Si:H Solar Cells By Down Conversion in Combination with Plasmonic Nanoparticles"**

3. Attended the 3rd Generation PV in the Developing World from 6th-8th January, 2021, hosted virtually by Durham University, United Kingdom. Contribution: Oral Presentation titled **"Plasmonic and magnetoplasmonics as approaches to enhance photo-conversion efficiency of PV devices"**

4. Attended the 2021 Wits PhD Seminar from 30th-31st August, 2021, hosted virtually by University of the Witwatersrand, Johannesburg. Contribution: Oral Presentation titled **"The Road to Resilience with Solar Energy by Enhancing the Power Conversion Efficiency of Solar Cells"**

5. 1 of 10 experts selected to participate in the "Expert Perspective Series on Achieving a Just Transition in South Africa" commissioned by the Presidential Climate Commission, in collaboration with The New Climate Economy (affiliated with World Resource Institute), October-December 2021.

6. Attended the 2024 International Conference on Transport Optical Network from 14th-18th July, 2021, hosted by Polytechnic University of Bari, Italy. Contribution: Oral Presentation titled **"Frequency conversion to augment power conversion efficiency in photovoltaic devices"**

Abstract

Meeting the ever-increasing global demand for energy is society's principal challenge for attaining economic growth and dynamic technological progress. Novel materials and technologies to extend photoabsorption and harness the solar emission spectrum are critical for producing solar-based electricity on a large scale. Current techniques and nanostructure-based approaches can revolutionise the production of solar electricity.

In this work, experimental light management strategies through plasmonic nanostructures in silicon-based thin film solar cells were explored to augment power conversion efficiency (PCE). These devices incorporated plasmonic, magnetoplasmonic, and core-shell nanostructures coated with SiO_2. It was demonstrated that magnetoplasmonic nanoparticles enhance interactions with both the charge of electrons and the unpaired spin with the B-field component of the electromagnetic spectrum. Furthermore, core-shell structures passivate the surface of the nanoparticles, significantly enhancing PCE. The highest PCE (10.7%) was observed for $Au@SiO_2$ nanoparticles, attributed to a bonding plasmon mode at the interface between the nanoparticles and the surrounding bulk material. Additionally, $Fe_3O_4@SiO_2$ nanoparticles primarily enhanced the short-circuit current (J_{sc}), due to magnetic interactions with superparamagnetic nanoparticles.

A detailed investigation into the Curie temperature (T_c) of various magnetic nanoparticles revealed that 4 nm Fe_3O_4 nanoparticles possess the highest T_c of 906.1 K, indicating strong magnetic stability under operational conditions. For Ni@Fe core-shell nanoparticles, a decrease in T_c with increasing Ni content was observed, highlighting the critical role of composition in tuning magnetic properties.

Morphological analysis through TEM imaging revealed uniform dispersion and spherical morphology for Au nanoparticles, crucial for consistent plasmonic properties. The addition of SiO_2 shells to both Au and Ag nanoparticles significantly improved their optical absorption characteristics due to the modification of the local dielectric environment.

Furthermore, a study on the bulk heterojunction of organic solar cells demonstrated that processing solvents play a pivotal role in optimising active layer performance. It was found that solvent mixtures, particularly 2-MEA and toluene in a 7:3 ratio, significantly enhance device efficiency by promoting better phase separation and charge transport, achieving a PCE of 5.77%.

These findings showcase the significant potential of nanostructures and solvent processing in improving the efficiency of photovoltaic devices. The enhanced PCE and stability of devices incorporating plasmonic and magnetoplasmonic nanoparticles, along with optimised solvent processing techniques, provide valuable insights for future research and development in solar energy technologies.

Contents

1 Introduction: Innovative Approaches to Enhance Solar Cell Performance **1**

1.1 The Energy Challenge . . . 1
1.1.1 Photon Flux Dispersion with Energy . . . 4
1.1.2 Hot Carrier and Low-Energy Photon Losses . . . 4
1.1.3 Materials Energy Band Gaps vs. Solar Emission Spectrum . . . 5
1.1.4 Organic Solar Cells Road Map: Binary to Ternary Photoactive Layers (PALs) . . . 6
1.2 Long-Term Viability of Solar Energy . . . 7
1.3 Status of Photovoltaic Materials and Light Management Schemes . . . 9
1.4 Innovative Solutions for Advancing Solar Cell Performance . . . 11
1.4.1 Efficiency Limitations of Thin Film Solar Cell Technology . . . 14
1.5 Aims and Objectives . . . 14
1.6 Thesis Structure . . . 15

2 Literature Review **17**

2.1 Solar Cell Technologies . . . 17
2.1.1 Inorganic Solar Cells . . . 18
2.1.1.1 Silicon-Based Solar Cells . . . 18
2.1.1.2 Thin-Film Solar Cells . . . 20
2.1.2 Organic Solar Cells . . . 22
2.1.3 Hybrid Solar Cells . . . 23
2.1.3.1 Dye-Sensitized Solar Cells . . . 23
2.1.3.2 Perovskite Solar Cells . . . 24
2.1.4 Significance of Solar Cell Efficiency . . . 27
2.2 Efficiency Enhancement in Organic Solar Cells . . . 28
2.2.1 The Role of Morphology in Organic Solar Cell Performance . . . 28
2.2.1.1 Binary OPVs . . . 29
2.2.1.2 Ternary OPVs . . . 30
2.2.2 Morphology Control with Solvent Additives . . . 32
2.2.2.1 Binary OPVs . . . 33
2.2.2.2 Ternary OPVs . . . 33
2.3 Plasmonic and Magnetoplasmonic Nanostructures for Photovoltaic Applications . . . 34
2.3.1 Light-Matter Interaction . . . 34
2.3.1.1 Surface Plasmonic Resonance . . . 34
2.3.1.2 Mechanism of Light Trapping Using Core-Shell Structures 37
2.3.2 Application of Magnetoplasmonic and Plasmonic Nanoparticles in Solar Cells . . . 38
2.4 Nanoparticles Simulation Techniques . . . 39
2.4.1 Simulations of Magnetoplasmonic NPs . . . 39
2.4.2 Simulations of Plasmonic NPs . . . 39
2.5 Morphology Tuning and Nanoparticle Integration . . . 41
2.5.1 Morphology Control with Solvent Additives and Nanoparticle Integration . . . 41

2.5.2 Limitations and Challenges in Fabricating Organic Solar Cells with Fine-tuned Morphology . . . 43
2.5.3 Potential Improvements and Advancements in Magnoplasmonic and Plasmonic Nanoparticle Integration . . . 44

3 Theoretical Foundation of Surface Plasmonic and Magnetoplasmonic Resonance Effects 45
3.1 Surface Plasmon Resonances . . . 45
3.2 Magnetoplasmonics . . . 52
3.2.1 Magneto-Optical Effects . . . 52
3.2.2 The Oscillatory Electron According to the Lorentz Model . . . 55
3.3 Simulation Technique for Magnetoplasmonic NPs . . . 58
3.4 Simulations Results for Magnetoplasmonic NPs . . . 62
3.4.1 Ni, Fe and Fe_3O_4 Bare NPs . . . 62
3.4.2 Pure Magnetic Core-Shell NPs . . . 64
3.4.2.1 Ni@Fe Core-Shell NPs . . . 65
3.4.2.2 Fe@Ni Core-Shell NPs . . . 67

4 Plasmonics and Magnetoplasmonics Effects for Photovoltaic Applications: Silicon Solar Cell 71
4.1 Methodology . . . 71
4.1.1 Materials and Chemicals . . . 71
4.1.2 Synthesis of Nanoparticles . . . 72
4.1.2.1 Synthesis of Au and $Au@SiO_2$ Nanoparticles . . . 72
4.1.2.2 Synthesis of Ag and $Ag@SiO_2$ Nanoparticles . . . 72
4.1.2.3 Synthesis of Fe_3O_4 and $Fe_3O_4@SiO_2$ Nanoparticles . . . 72
4.1.2.4 Synthesis of Ni and $Ni@SiO_2$ Nanoparticles . . . 73
4.2 Characterisation of Nanoparticles . . . 73
4.2.1 Transmission Electron Microscopy (TEM) . . . 73
4.2.2 Ultraviolet-Visible Spectroscopy (UV-Vis) . . . 73
4.2.3 X-ray Diffraction (XRD) . . . 73
4.2.4 Raman Spectroscopy . . . 74
4.2.5 Vibrating Sample Magnetometry (VSM) . . . 74
4.3 Results and Discussion . . . 74
4.3.1 Morphology of Plasmonic and Magnetoplasmonic Nanostructures for Shape and Size Dependence (TEM) . . . 74
4.3.1.1 Plasmonic NPs . . . 75
4.3.1.2 Magnetoplasmonic NPs . . . 77
4.3.2 Optical Spectroscopy . . . 86
4.3.2.1 Plasmonic NPs . . . 86
4.3.2.2 Magnetoplasmonic NPs . . . 86
4.3.3 X-Ray Diffraction Measurements . . . 89
4.3.4 Structural Properties by Raman Spectroscopy . . . 91
4.3.5 Magnetic Measurements . . . 93
4.3.6 J-V Characterisation of Magnetoplasmonic and Plasmonic Incorporated Si PV Devices . . . 96
4.4 Conclusion . . . 102

5 Morphology Tuning of OSCs with Co-Solvent Additives **104**
5.1 Introduction . . . 104
5.2 Hansen Solubility Parameters . . . 105
5.3 Tuning of Morphology of OSCs by Co-Additives . . . 107
5.3.1 Fabrication Techniques for OSCs . . . 108
5.3.2 Methodology . . . 108
5.3.3 Morphology and Optical Properties of the Active Layers . . . 118
5.3.4 Formulation Effect on Morphology . . . 122
5.3.5 Electrical Properties by J-V Measurements . . . 129
5.3.6 External Quantum Efficiency Measurements . . . 164
5.4 Conclusion . . . 165

6 Conclusions and Recommendations **167**
6.1 Conclusion . . . 167
6.2 Future Work . . . 168
6.2.1 Magetoplasmonic and Plasmonic Nanoparticles on Silicon Based Devices . . . 168
6.2.2 Co-Solvents on OSCs . . . 169
6.2.2.1 Future Research Directions . . . 171

List of Figures

1.1 An image showing the number of people without access to electricity by region [5]. . . . 1
1.2 An image illustrating the consequences of global warming [7]. . . . 2
1.3 An image showing projections of global energy demand by region and regional shares from 1990-2025 [16]. . . . 3
1.4 Images showing (a) the superpositioning of the band edge of materials with the Shockley-Queisser Limit (b) spectral-splitting of the solar spectrum [40, 41]. . . . 5
1.5 An image visually representing the evolution from (a) conventional binary, (b) tandem to (c) ternary photoactive layers of OSCs, highlighting the advancements in morphology to improve efficiency in solar cell technology. [64]. . . . 7
1.6 An image showing projected global capacity by 2030 [73]. . . . 8
1.7 An image showing the National Renewable Energy Laboratory (NREL) chart for best research-cell efficiencies [104]. . . . 11
1.8 A schematic diagram of a PV device featuring a top-layer of Au-Si core-shell NPs [114]. . . . 12
2.1 An image showing the fundamental categories of PV cells [161]. . . . 18
2.2 Basic structure of a Si PV cell. . . . 19
2.3 Schematic representation of the crystal structure of an organic-inorganic metal halide perovskite [235]. . . . 24
2.4 Device architecture of (a) mesoscopic perovskite solar cell and (b) planar perovskite solar cell [250]. . . . 26
2.5 Visualising an effective strategy for optimising the active layer through sequential morphology evolution and enhancing vertical distribution [296]. 29

2.6 (a) Structure of three-component bulk heterojunction OSCs, and (b) Four distinct morphologies for the active layer, showcasing the integration of a third component: embedded within either the donor or acceptor phase, positioned at the interfaces, creating a structure parallel to the main donor or acceptor, and forming an amalgam with either the donor or acceptor material [310]. 31
2.7 (a) Schematic diagram of (a) spherical shaped NPs illustrating a single resonance mode and (b) elliptically shaped NPs demonstrating multiple oscillatory modes [382]. 36
2.8 Capturing the film formation process of the P3HT/PCBM blend from CB solution: (a,d) without additives, (b,e) with 2% ODT, and (c,f) with 2% CN. Panels (a-c) illustrate the changes in the extinction coefficient (k) from 605 nm to 462 nm, while (d-f) detail the evolution of film thickness. Panel (g) showcases the GIWAXS diffraction patterns for various solid films [489, 490]. 42
3.1 Schematic diagrams depicting localised (a) and travelling (b) surface plasmons arising from various noble metal NPs [541]. 47
3.2 Layout of the dispersion relation diagram for non-radiative plasmons. The dispersion relation is plotted against the real component and the imaginary component of the wave vector [544]. 52
3.3 A traditional representation of the process by which a magnetic field induces rotation in the polarisation and, consequently, alters the electric field within a material [551]. 54
3.4 Simulation of the mean temperature-dependent magnetisation for Ni NPs in a size range of 4 nm to 10 nm. 62
3.5 Simulation of the mean temperature-dependent magnetisation for Fe NPs in a size range of 4 nm to 10 nm. 63
3.6 Simulation of the mean temperature-dependent magnetisation for Fe_3O_4 NPs in a size range of 4 nm to 10 nm. 63
3.7 Simulation of the mean temperature-dependent magnetisation for complex shapes of bare Ni NPs in a size range of 10 nm to 16 nm. 64
3.8 Simulation of the mean temperature-dependent magnetisation for complex shapes of bare Fe NPs in a size range of 10 nm to 16 nm. 65
3.9 Simulation of the mean temperature-dependent magnetisation for 4 nm Ni@Fe core-shell NPs with varying core-shell ratios. 66
3.10 Simulation of the mean temperature-dependent magnetisation for 8 nm Ni@Fe core-shell NPs with varying core-shell ratios. 66
3.11 Simulation of the mean temperature-dependent magnetisation for octahedron 12 nm Ni@Fe core-shell NPs with varying core-shell ratios. 67
3.12 Simulation of the mean temperature-dependent magnetisation for cubic 16 nm x 16 nm Ni@Fe core-shell NPs with varying core-shell ratios. 68
3.13 Simulation of the mean temperature-dependent magnetisation for 4 nm Fe@Ni core-shell NPs with varying core-shell ratios. 68
3.14 Simulation of the mean temperature-dependent magnetisation for 8 nm Fe@Ni core-shell NPs with varying core-shell ratios. 69
3.15 Simulation of the mean temperature-dependent magnetisation for octahedron 12 nm Fe@Ni core-shell NPs with varying core-shell ratios. 69

3.16 Simulation of the mean temperature-dependent magnetisation for cubic 16 nm x 16 nm Fe@Ni core-shell NPs with varying core-shell ratios. 70
4.1 Image (a) shows image of Au NPs with 20 nm diameter, (b) shows how the Au NPs are distributed on the surface, (c) shows the image of $Au@SiO_2$ spheres having an average diameter of 69.8 nm and (d) shows the size distribution of the core-shell $Au@SiO_2$ NPs. 75
4.2 Image (a) shows image of Ag NPs with 20 nm diameter, (b) shows how the Ag NPs are distributed on the surface, (c) shows the image of $Ag@SiO_2$ spheres having a diameter of $\approx$ 24 nm and (d) shows the size distribution of the core-shell $Ag@SiO_2$ NPs. 76
4.3 (a) Bright Field TEM (BFTEM) showing the distribution of Fe_3O_4 NPs on a carbon film, (b) the Selected Area Electron Diffraction Pattern (SAEDP), (c) Dark Field TEM (DFTEM) showing the distribution of Fe_3O_4 NPs on a carbon film, (d) BFTEM showing the distribution of $Fe_3O_4@SiO_2$ core-shell NPs on a carbon film, (e) SAEDP of $Fe_3O_4@SiO_2$ core-shell NPs and (f) DFTEM showing the distribution of $Fe_3O_4@SiO_2$ core-shell NPs on a carbon film. 77
4.4 High-resolution BFTEM images showing the distribution of the SiO_2 NPs on the surface of the magnetite NPs. These NPs have an average particle size of about 20 nm in diameter. 78
4.5 (a) High Angle Annular Dark Field (HAADF) image and the corresponding energy dispersive x-ray spectroscopy (EDXS) maps for Fe_3O_4 NPs and (b) High Angle Annular Dark Field image and the corresponding EDXS maps for $Fe_3O_4@SiO_2$ core-shell NPs. 79
4.6 BFTEM showing the distribution of aggregated Ni NPs on a carbon film, (b) HAADF image of Ni NPs, (c) BFTEM showing the distribution of $Ni@SiO_2$ core-shell NPs on a carbon film (d) HAADF image of $Ni@SiO_2$ core-shell NPs. 80
4.7 (a) HAADF imaging alongside EDXS mappings, (b) for Ni, (c) Si, (d) O, (e) C, and (f) the aggregate weight percentages within Ni NPs. 81
4.8 (a) HAADF imaging alongside EDXS mappings, (b) for Ni, (c) Si, (d) O, (e) C, and (f) the aggregate weight percentages within $Ni@SiO_2$ core-shell NPs. 82
4.9 The images labeled (a) illustrate the STEM-EDS mapping of samples containing Ni and Si elements, as well as the associated line scan denoted by a white line. Image (b) depicts the plot of the atomic weight percentages of these elements. 84
4.10 In image (c), we observe the electron beam targeted at the red mark seen in the HAADF image. Lastly, image (d) presents the EDS spectrum that reveals the elemental makeup of the$Ni@SiO_2$ core-shell NPs. 85
4.11 Optical absorption spectra of (a) SiO_2 , Au and $Au@SiO_2$ NPs, and (b) Ag and $Ag@SiO_2$ NPs. 86
4.12 Optical absorption spectra of (a) Fe_3O_4 and $Fe_3O_4@SiO_2$, (b) Ni and $Ni@SiO_2$ NPs of various sizes. 87
4.13 XRD pattern of (a) Fe_3O_4 and (b) $Fe_3O_4@SiO_2$ NPs. The diffraction patterns were compared to the known spectra of Fe_3O_4 [589–592]. 89
4.14 XRD patterns of Ni NPs. The pattern was compared with the known spectra of Ni [593–596], confirming the composition of the resulting NPs. 90

4.15 XRD pattern of (a) Fe_3O_4 and (b) $Fe_3O_4@SiO_2$ NPs. The diffraction patterns were compared to the known spectra of Fe_3O_4 [589–592]. 92
4.16 Magnetic hysteresis loop of (a) Fe_3O_4 NPs and (b) $Fe_3O_4@SiO_2$ core-shell NPs. The fit uses a modified Langevin function at 300 K. 93
4.17 Temperature dependence of the zero-field-cooled (ZFC) and field-cooled (FC) magnetisation in a 0 and 100 Oe measuring field of (a) Fe_3O_4 NPs and (b) $Fe_3O_4@SiO_2$ core-shell NPs. 95
4.18 (a) shows the J-V characteristics for the pristine device and when it is incorporated with Fe_3O_4 NPs at different concentrations illuminated with light (1 sun through 1.5 AM filter). (b) shows the J-V dark conditions for all the samples. 97
4.19 (a) shows the J-V characteristics for the pristine device and when it is incorporated with plasmonic, magnetoplasmonic and core-shell NPs illuminated with light (1 sun through 1.5 AM filter). (b) shows the J-V dark conditions for all the samples. 101
5.1 Visualising Compatibility: The Hansen solubility sphere maps the universe of solvents in a 3D space defined by dispersion, polar, and hydrogen bonding forces. 106
5.2 HSP Analysis for Active Layer Materials in OSC Fabrication: Green values indicate solubility of the material in the solvent, while red values signify insolubility. 107
5.3 The structure of the standard inverted device architecture constituting MoO_3 and ZnO as the hole and electron transport layers, respectively. . 109
5.4 (a)Device architecture with the active layer of $PTB7 : PC_{70}BM$ and (b) the energy level diagram of the devices layers comprising of the work-function for the electrodes, the valence and conduction band of the oxides layers, the HOMO and LUMO of the photoactive layers. 111
5.5 (a)Device architecture with the active layer of $PTQ10 : Y6$ and (b) the energy level diagram of the devices layers comprising of the work-function for the electrodes, the Valence and Conduction band of the oxides layers, the HOMO and LUMO of the photoactive layers. 112
5.6 (a)Device architecture with the active layer of $PM : Y6 : PC_{70}BM$ and (b) the energy level diagram of the devices layers comprising of the work-function for the electrodes, the valence and conduction band of the oxides layers, the HOMO and LUMO of the photoactive layers. 113
5.7 Optical absorbance spectra for the $PTB7 : PC_{70}BM$ active layer thin film on glass, showcasing results using chlorinated solvents, industrial-grade solvents, eco-friendly solvents, and their respective blends. 119
5.8 Optical absorbance spectra for the PTQ10:Y6 and $PM6 : Y6 : PTB7 : PC_{70}BM$ active layers. 120
5.9 (a) shows the ex-situ pattern of the morphology of the $PTB7 : PC_{70}BM$(1:1.5) formed from a chlorinated solvent (CB) and (b) the corresponding intensity profiles along Q_{xy} (in-plane) and Q_z (out-of-plane) directions. The thin fims were annealed at 120° C for 10 minutes. 123
5.10 (a) shows the ex-situ pattern of the morphology of the $PTB7 : PC_{70}BM$(1:1.5) formed from a chlorinated solvent (o-DCB) and (b) the corresponding intensity profiles along Q_{xy} (in-plane) and Q_z (out-of-plane) directions. The thin fims were annealed at 120° C for 10 minutes. 123

5.11 (a) shows the ex-situ pattern of the morphology of the $PTB7 : PC_{70}BM$(1:1.5) formed from chlorinated co-solvents (CB:o-DCB) and (b) the corresponding intensity profiles along Q_{xy} (in-plane) and Q_z (out-of-plane) directions. The thin fims were annealed at 120° C for 10 minutes. 124
5.12 (a) shows the ex-situ pattern of the morphology of the $PTB7 : PC_{70}BM$(1:1.5) formed from chlorinated co-solvents (CB:DIO) and (b) the corresponding intensity profiles along Q_{xy} (in-plane) and Q_z (out-of-plane) directions. The thin fims were annealed at 120° C for 10 minutes. 125
5.13 (a) shows the ex-situ pattern of the morphology of the $PTB7 : PC_{70}BM$(1:1.5) formed from a green solvent (Eu) and (b) the corresponding intensity profiles along Q_{xy} (in-plane) and Q_z (out-of-plane) directions. The thin fims were annealed at 120° C for 10 minutes. 126
5.14 (a) shows the ex-situ pattern of the morphology of the $PTB7 : PC_{70}BM$(1:1.5) formed from a green solvent (Lim) and (b) the corresponding intensity profiles along Q_{xy} (in-plane) and Q_z (out-of-plane) directions. The thin fims were annealed at 120° C for 10 minutes. 126
5.15 (a) shows the ex-situ pattern of the morphology of the $PTB7 : PC_{70}BM$(1:1.5) formed from green co-solvents (Eu:Lim) and (b) the corresponding intensity profiles along Q_{xy} (in-plane) and Q_z (out-of-plane) directions. The thin fims were annealed at 120° C for 10 minutes. 127
5.16 (a) shows the ex-situ pattern of the morphology of the $PTB7 : PC_{70}BM$(1:1.5) formed from an industrial solvent an green solvent (2-MEA:Toulene) and (b) the corresponding intensity profiles along Q_{xy} (in-plane) and Q_z (out-of-plane) directions. The thin fims were annealed at 120° C for 10 minutes. 128
5.17 (a) shows the ex-situ pattern of the morphology of the $PTB7 : PC_{70}BM$(1:1.5) formed from an industrial solvent an green solvent (Eu:Toulene) and (b) the corresponding intensity profiles along Q_{xy} (in-plane) and Q_z (out-of-plane) directions. The thin fims were annealed at 120° C for 10 minutes. 128
5.18 (a) J-V curves of devices with the $PTB7 : PC_{70}BM$ (1:1.5) mass ratio with a green solvent (2-MEA) and with various concentration of an industrial solvent (Toulene) being added to the blend. (b) shows the J-V dark conditions for the devices. 132
5.19 Fittings performed by Equation (5.3) over the dark J-V measurements (range of 0.55-0.8 V) for devices with the active of $PTB7 : PC_{70}BM$ in (2-MEA:Toulene) co-solvents at different concentrations. 133
5.20 Statistical device parameters of the active layer in $PTB7 : PC_{70}BM$(1:1.5) using a green solvent (2-MEA). 133
5.21 Statistical device parameters of the active layer in $PTB7 : PC_{70}BM$ (1:1.5) using co-solvents (2-MEA:Toluene) in a 9:1 ratio (900 μL of 2-MEA and 100 μL of Toulene). The total concentration is 20 mg/mL. 134
5.22 Statistical device parameters of the active layer in $PTB7 : PC_{70}BM$ using co-solvents (2-MEA:Toluene) in a ratio of 4:1 (800 μL of 2-MEA and 200 μL of Toulene). The total concentration is 20 mg/mL. 135
5.23 Statistical device parameters of the active layer in $PTB7 : PC_{70}BM$ using co-solvents (2-MEA:Toluene) in a ratio of 7:3. 136
5.24 (a) J-V curves of non-encapsulated devices with the $PTB7 : PC_{70}BM$ with optimal co-solvents (2-MEA:Toulene) concentration and (b) shows the J-V dark conditions for the devices. 139

5.25 Fittings performed by Equation (5.3) over the dark J-V measurements (range of 0.55-0.8 V) for non-encapsulated devices with the active of $PTB7 : PC_{70}BM$ in (2-MEA:Toulene) as the optimal concentration. 140
5.26 Statistical non-encapsulated device parameters of the active layer in $PTB7 : PC_{70}BM$ (1:1.5) using the optimal co-solvents (2-MEA:Toluene) ratio. . 140
5.27 Statistical non-encapsulated device parameters of the active layer in $PTB7 : PC_{70}BM$ (1:1.5) using the optimal co-solvents (2-MEA:Toluene) after 7 days. 141
5.28 Statistical non-encapsulated device parameters of the active layer in $PTB7 : PC_{70}BM$ (1:1.5) using the optimal co-solvents (2-MEA:Toluene) after 8 days. 142
5.29 Evolution of PCE over 8 days for the non-encapsulaled $PTB7 : PC_{70}BM$ devices. 143
5.30 (a) J-V curves of encapsulted devices with the $PTB7 : PC_{70}BM$ (1:1.5) mass ratio with a green solvent (2-MEA) and with various concentration of an industrial solvent (Toulene) being added to the blend. (b) shows the J-V dark conditions for the devices. 144
5.31 Fittings performed by Equation (5.3) over the dark J-V measurements (range of 0.55-0.8 V) for encapsulated devices with the active layer of $PTB7 : PC_{70}BM$ (1:1.5) in (2-MEA:Toulene) as the optimal concentration with a thickness of 136 nm measured over 697 hours. 145
5.32 Statistical encapsulated device parameters of the active layer in $PTB7 : PC_{70}BM$ (1:1.5) using the optimal co-solvents (2-MEA:Toluene) ratio. . 145
5.33 Statistical encapsulated device parameters of the active layer in $PTB7 : PC_{70}BM$ (1:1.5) using the optimal co-solvents (2-MEA:Toluene) ratio after 24 hours. 146
5.34 Statistical encapsulated device parameters of the active layer in $PTB7 : PC_{70}BM$ (1:1.5) using the optimal co-solvents (2-MEA:Toluene) ratio after 96 hours. 147
5.35 Statistical encapsulated device parameters of the active layer in $PTB7 : PC_{70}BM$ (1:1.5) using the optimal co-solvents (2-MEA:Toluene) ratio after light ageing at 85° C for 22 hours in air, 96 hours post fabrication. . . 148
5.36 Statistical encapsulated device parameters of the active layer in $PTB7 : PC_{70}BM$ (1:1.5) using the optimal co-solvents (2-MEA:Toluene) ratio after being stored for 47 hours for the devices to recover, then light ageing at 85° C for 25 hours in air, 165 hours post fabrication. 149
5.37 Statistical encapsulated device parameters of the active layer in $PTB7 : PC_{70}BM$ (1:1.5) using the optimal co-solvents (2-MEA:Toluene) ratio after being stored for 94 hours for the devices to recover, then light ageing at 85° C for 72 hours in air, 284 hours post fabrication. 150
5.38 Statistical encapsulated device parameters of the active layer in $PTB7 : PC_{70}BM$ (1:1.5) using the optimal co-solvents (2-MEA:Toluene) ratio after light ageing at 85° C for 72 hours in air, 365 hours post fabrication. . 151
5.39 Statistical encapsulated device parameters of the active layer in $PTB7 : PC_{70}BM$ (1:1.5) using the optimal co-solvents (2-MEA:Toluene) ratio after light ageing at 85° C for 172 hours in air, 525 hours post fabrication. 152
5.40 Evolution of PCE over 697 hours for the encapsulaled $PTB7 : PC_{70}BM$ devices. 156

5.41 J-V curves of devices formed from Donor: NFA heterojunction with the photoactive layer being formed from the spin casting after dissolving in chlorinated and green co-solvents. 157
5.42 Fittings performed by Equation (5.3) over the dark J-V measurements (range of 0.55-0.8 V) for NFA based devices using various co-solvent systems. 158
5.43 Statistical device parameters of the active layer of $PTQ10 : Y6$ (1:1.2) using Chloroform:1-Chloronapthalene(0.5%) as chlorinated co-solvents. . 159
5.44 Statistical device parameters of the ternary active layer of $PM6 : Y6 : PC_{70}BM$ (1:1:0.2) using co-additives Chloroform:DIO(2.5%):1-CN(0.5%) as chlorinated co-solvents. 160
5.45 Statistical device parameters of the active layer of $PTQ10 : Y6$ (1:1.2) using 2-MeTHF:Eucalyptol as green co-solvents. 161
5.46 Statistical device parameters of the active layer of $PTQ10 : Y6$ (1:1.2) using 2-MeTHF:Eucalyptol as green co-solvents. The blend solution was stirred at temperature of 70° C. 162
5.47 EQE spectra of the $PTB7 : PC_{70}BM$, PTQ10:Y6 and $PM6 : Y6 : PC_{70}BM$ OSCs. The devices had different thicknesses. 164
6.1 HSP calculations on industrial and green solvents. 169
6.2 HSP calculations on various chlorinated solvents. 170

List of Tables

2.1 Overview of common halide perovskite materials: bandgap energies, absorption coefficients, and peak power conversion efficiencies. 25
3.1 Table of constants used in the material file 60
4.1 Summary of the performance of a-Si solar cells incorporated with optimised magnetoplasmonic NPs at different concentrations. 98
4.2 Summary of the performance of commercial a-Si solar cells incorporated with plasmonic/magnetoplasmonic NPs and their core-shell nanostructures with SiO_2. 99
5.1 Comparative Properties of Selected Organic Solvents [654–658]. 114
5.2 Parameters for Active Layer Fabrication. 117
5.3 Charge carrier mobilities of the device with the active layer $PTB7 : PC_{70}BM$ using green and industrial co-solvents at different concentrations. 137
5.4 Photovoltaic parameters of the $PTB7 : PC_{70}BM$ devices with various concentrations of Toulene. 138
5.5 Photovoltaic parameters of the $PTB7 : PC_{70}BM$ (1:1.5) non-encapsulated devices with optimal co-solvent concentration of 2-MEA:Toulene (7:3) measured for a period of 8 days. 142
5.6 Photovoltaic parameters of the $PTB7 : PC_{70}BM$ encapsulated devices with optimal co-solvent concentration of 2-MEA:Toulene (7:3) measured for a period of 697 hours. 153
5.7 Charge carrier mobilities for encapsulated devices with the active layer of $PTB7 : PC_{70}BM$ (1:1.5) in (2-MEA:Toulene) as the optimal concentration with a thickness of 136 nm measured over 697 hours. 154
5.8 Photovoltaic parameters of the NFA active layer devices with chlorinated and green co-solvents. 163

Chapter 1

1 Introduction: Innovative Approaches to Enhance Solar Cell Performance

1.1 The Energy Challenge

The world is changing, new regions are developing and they require enormous amounts of energy. Traditional energy sources cannot attain this substantial demand for energy. Fossil fuels are limited and they leave a large carbon footprint. The world needs solar energy to replace the conventional, fossil-fuel generated electricity in the future years to mitigate and thus reduce climate change related adverse effects. Additionally, the energy supply recipe must continue to meet energy demands by the ever increasing energy dependent society [1]. This transition is already ongoing and it can be ameliorated by enhancing the efficiency of the solar cells with cost effective techniques [2]. It is appalling to know that in a technological dependent society about 1.45 billion people have minimal access to electricity as depicted in Figure 1.1, while 82% of them reside in rural areas. As a consequence of this, the number of people living in rural communities depending on traditional energy sources such as biomass is predicted to rise from 2.85 billion today to 2.93 billion in 2030 [3, 4]. All these needs exist in conflict with their harmful effects to the environment and climate.

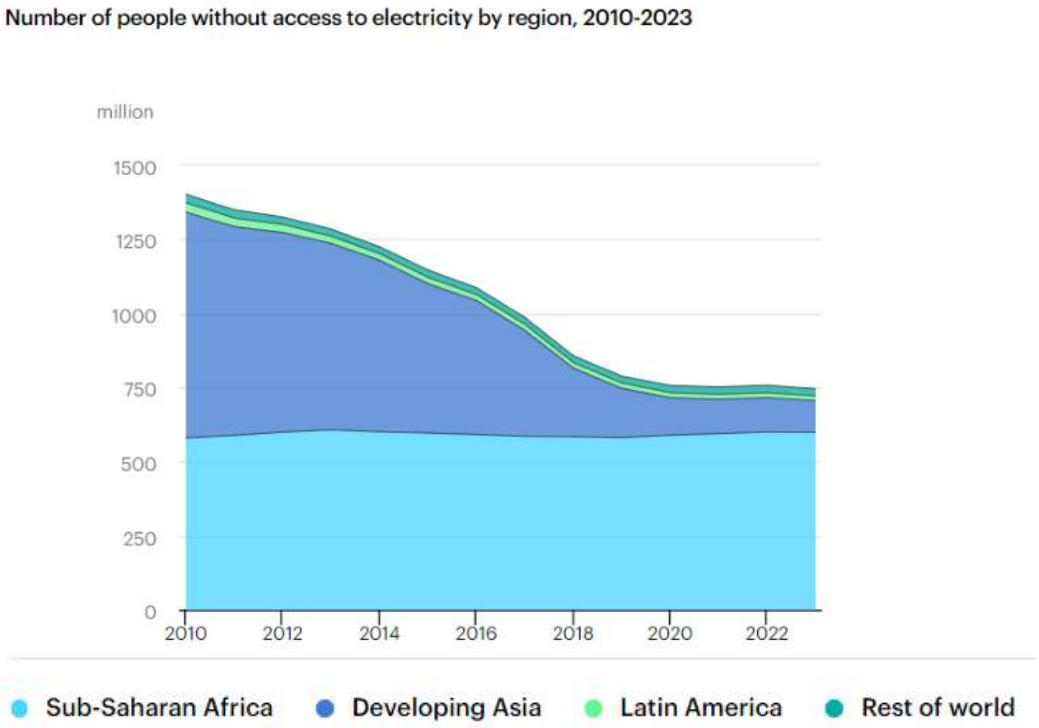


Figure 1.1: An image showing the number of people without access to electricity by region [5].

The impact of climate change is considerable, and its potential outcomes may include

a rise in sea levels due to both ocean expansion and the melting of onshore ice barriers. Additionally, global warming may lead to widespread desertification, unpredictable weather patterns, and a rise in ocean levels. The scarcity of water and the modification of ocean currents are increasingly evident as we are already experiencing some of the adverse effects, and these may result in the collapse of entire ecosystems that are critical for sustaining life on Earth as illustrated in Figure 1.2. In recent years, both science and politics have concurred that the increase in temperature is caused by human activity, and that it is linked to the escalating levels of CO_2 emissions in the atmosphere, which have surged dramatically since pre-industrial times [6].

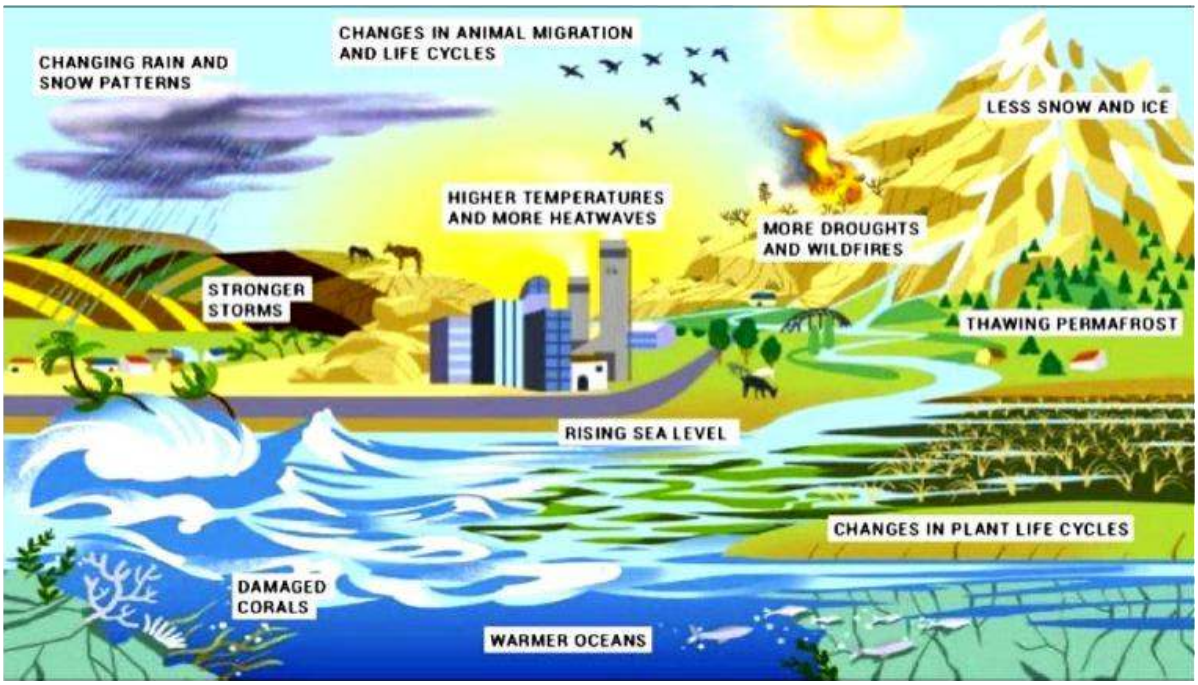


Figure 1.2: An image illustrating the consequences of global warming [7].

To address the issue of climate change, potential energy sources must fulfill a dual requirement: they should generate energy without emitting additional greenhouse gases. It is projected that to stabilise atmospheric CO_2 levels at twice their pre-human levels, a significant amount of carbon-neutral energy will be required by the mid-21st century. The necessary amount exceeds 10 terawatts (TW) and will continue to rise beyond 2050 to sustain economic progress for a growing population.

At present, the worldwide energy consumption is 6.1×10^{20} J per year, which corresponds to an average consumption rate of 14.1×10^{12} W per year [8, 9]. According to the projection shown in Figure 1.3, the global energy consumption rate will more than double by the mid-21st century and expected to triple by 2100 due to the anticipated growth in population and economy, even with strong efforts towards energy conservation. Therefore, for a potential energy source to make a substantial contribution to the global primary energy supply, it must be able to produce a sustained power output of at least 1-10 TW [10].

Utilising renewable energy sources, particularly solar energy, is the leading solution to fulfill the need for carbon-neutral energy usage. It is widely considered as the most

significant alternative. This is bound to change with climate change since the wind directions/speed are on the decline. The available geothermal energy on all continents is 12 TW, with only a small portion being practically extractable [11–13]. The potential wind power that can be harnessed worldwide is estimated to be between 2-4 terawatts of electrical power (TW_e), as per the Intergovernmental Panel on Climate Change (IPCC) and other experts [14]. To put this in perspective, the solar constant at the top of the Earth's atmosphere is 1.7×10^5 TW, with about 1.2×10^5 TW reaching the planet's surface after being scattered by the atmosphere and clouds [15]. It is evident that solar energy can be utilised at the necessary scale to meet global energy demands without significantly impacting the solar resource and in a carbon-neutral manner.

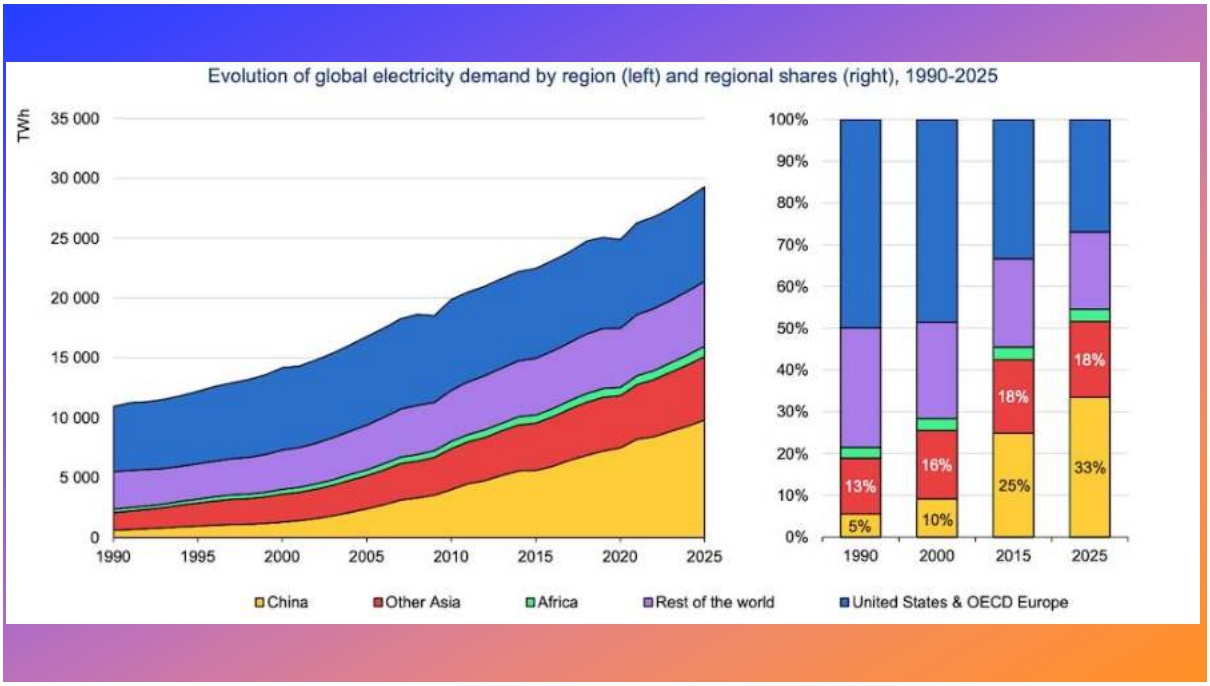


Figure 1.3: An image showing projections of global energy demand by region and regional shares from 1990-2025 [16].

The process of converting solar energy into electricity, known as photovoltaics, provides a promising solution for generating clean electricity without the environmental pollution caused by gas or coal power plants or the safety issues associated with nuclear energy. The high cost of traditional solar cells made of inorganic semiconductors has prevented this technology from making a significant impact on global energy production [17]. Although some types of solar cells, such as crystalline silicon and multi-junction GaAs, have demonstrated high efficiencies of up to 25% and 32% respectively [18], commercially available silicon solar cells only have efficiencies ranging from 12% to 15% [19–21]. The manufacturing process for these devices is expensive, and it can take up to a decade to recover the initial investment [22]. Therefore, there is a need for research to develop new materials for solar cells that are less expensive to manufacture and require less energy to produce than silicon solar cells. Significant research is being conducted to lower the production expenses of solar cells by introducing novel materials or technologies for photovoltaics. This led to the emergence of a new class of solar cells that use organic materials. Although organic solar cells typically have lower power conversion efficiency, their lower cost and simplified processing make them a promising option to replace the

prevailing inorganic semiconductor industry, which primarily relies on crystalline silicon.

1.1.1 Photon Flux Dispersion with Energy

Photon flux dispersion, which denotes the distribution of wavelength dependent photons in the electromagnetic spectrum, is a critical factor that impacts the efficiency and overall performance of solar cells. The complexities of photon behaviour and their energy-level distribution have a significant influence on the effectiveness of capturing solar energy for electricity generation in photovoltaic devices [23, 24].

The absorption spectrum of a solar cell is inherently connected to the dispersion of photon energy. Solar cells are engineered to absorb photons within specific energy ranges, primarily in the visible light spectrum. However, the photon flux from the sun encompasses a broad range of energies, spanning from the ultraviolet to the infrared [25]. By managing the dispersion of photon energy, it becomes feasible to direct a wider spectrum of photons into the absorption range of the solar cell [26].

The incorporation of plasmonic nanoparticles into solar cell designs presents a novel approach to manipulate photon flux dispersion. These nanoparticles exhibit unique optical properties, capable of scattering and absorbing light at specific wavelengths. By tuning the size, shape, and material of these nanoparticles, it's possible to engineer their plasmonic resonance. This resonance can be aligned with the solar spectrum to enhance the absorption of photons in the photovoltaic material, thereby increasing the efficiency of the solar cell [27, 28].

1.1.2 Hot Carrier and Low-Energy Photon Losses

The integration of plasmonic nanoparticles into solar cell designs offers a new approach to address the inefficiency caused by the rapid thermalisation of hot carriers. When photons with energy greater than the band gap of the solar cell material are absorbed, hot carriers, which are high-energy charge carriers, are generated. Typically, these excess energies are rapidly lost as heat through a process known as thermalisation, leading to a major inefficiency in conventional solar cells. However, the use of plasmonic nanoparticles provides a novel way to tackle this issue. By creating strong localised electromagnetic fields, these nanoparticles can increase the probability of extracting hot carriers before they lose their energy, thereby enhancing the energy conversion efficiency [29–31]. Conversely, low-energy photon losses occur when photons with energies below the material's band gap are not absorbed, thereby passing through the solar cell without contributing to electricity generation. This is a fundamental limitation in the solar spectrum utilisation [32, 33].

Plasmonic nanoparticles are a promising solution for addressing both hot carrier and low-energy photon losses in thin-film solar cells. These nanoparticles have the unique ability to manipulate light at the nanoscale, enabling the enhancement of light absorption across a broader spectrum. Additionally, they provide pathways for the extraction of hot carriers, thus serving a dual function that can significantly improve the overall efficiency of solar cells [34, 35]. The integration of plasmonic nanoparticles, particularly core-shell nanoparticles, in the design of thin-film solar cells has shown potential in addressing the

weak absorption of silicon solar cells in the near-infrared region [36]. This integration can lead to a substantial reduction in wafer thickness, representing a significant material saving with only a relative efficiency loss. Furthermore, plasmonic nanoparticles, such as silver and gold, are being explored for their ability to interact more strongly with the peak solar intensity, thereby enhancing light absorption [37]. Additionally, the use of plasmonic structures has been reported as a desirable method for improving localised light absorption and the performance of thin solar cells. These advancements demonstrate the potential of plasmonic nanoparticles in significantly enhancing the efficiency and absorbance of solar cells across a broader spectrum [38].

1.1.3 Materials Energy Band Gaps vs. Solar Emission Spectrum

Understanding the relationship between the energy band gaps of materials used in solar cells and the solar emission spectrum is fundamental to enhancing solar cell efficiency. The energy band gap of a material is a critical factor in determining its ability to absorb photons and convert them into electricity. A solar cell's efficiency is largely dependent on how well the energy band gap of its photoactive layer aligns with the solar emission spectrum. Materials with a band gap that matches the maximum of the solar emission spectrum can absorb photons more effectively, leading to higher photocurrent and subsequently enhancing the power conversion efficiency. For instance, the power conversion efficiency at a band gap of 1.1 eV is two times higher than at 1.8 eV, emphasising the impact of band gap on efficiency as depicted in Figure 1.4 (a) [39].

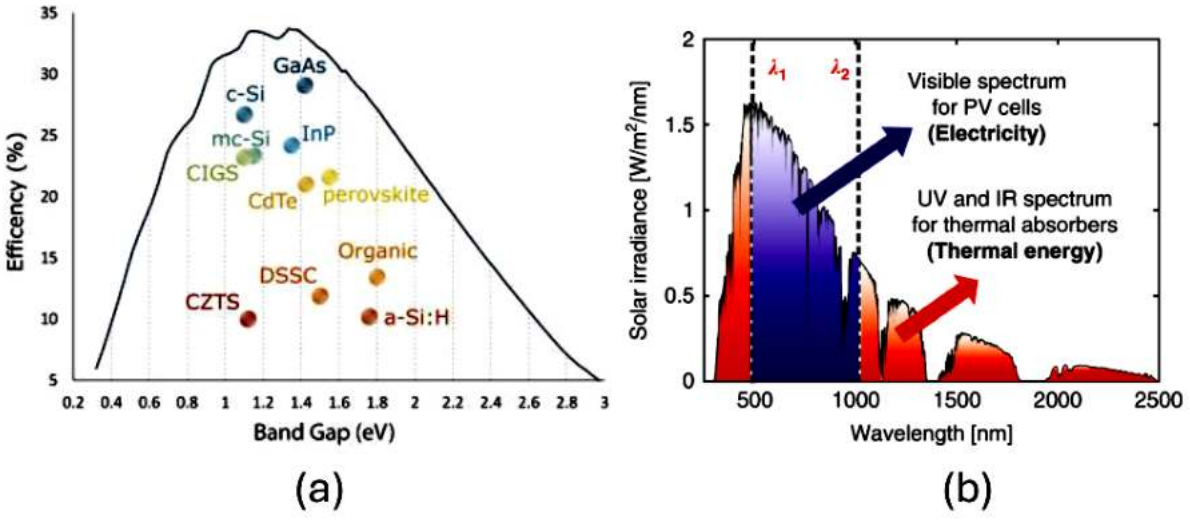


Figure 1.4: Images showing (a) the superpositioning of the band edge of materials with the Shockley-Queisser Limit (b) spectral-splitting of the solar spectrum [40, 41].

The solar emission spectrum encompasses a range of photon energies, from ultraviolet (UV) to visible light, and into the infrared (IR). Most traditional photovoltaic materials are optimised to absorb photons in the visible range, but this leaves a significant portion of the solar spectrum unutilised, particularly in the UV and IR regions. This mismatch,

demonstrated in Figure 1.4 (b), is a key factor in the inherent inefficiency of many solar cells [42, 43].

The integration of plasmonic NPs in solar cells presents an innovative solution to this challenge. These nanoparticles can be engineered to absorb and scatter light across a wider range of the solar emission spectrum incident on the earth's surface, including the UV and IR regions. By doing so, they can effectively bridge the mismatch between the material's band gap and the broader solar spectrum, facilitating the absorption of photons that would otherwise be lost [44, 45]. Achieving an optimal match between a material's energy band gap and the solar emission spectrum is crucial for maximising the efficiency of solar cells. By strategically using plasmonic NPs, it is possible to customise the absorption characteristics of solar cells, allowing them to capture a larger portion of the solar spectrum [46, 47]. This approach not only enhances the efficiency of solar cells but also contributes to the advancement of solar energy technologies as sustainable and potent energy sources.

1.1.4 Organic Solar Cells Road Map: Binary to Ternary Photoactive Layers (PALs)

The evolution of organic solar cells (OSCs) from binary to ternary photoactive layers represents a significant advancement in the field of photovoltaics. Traditional OSCs are commonly based on binary systems, consisting of an electron-donor and-acceptor material. The electron donor is characterised by higher ionization energy while the electron acceptor has a higher electron affinity. As such these materials are electronically dissimilar. While these systems have been fundamental in the development of organic photovoltaics due to their simple design and fabrication, they possess inherent limitations in light absorption and energy conversion efficiency. This is primarily due to their restricted spectral response and short exciton diffusion lengths [48–50]. The increased PCE exceeding 19% and device stability have made them suitable not only for consumer electronics but also for real power applications [51–53]. Despite these notable achievements in enhancing efficiency, the commercialisation of large-scale OSC, their lifetime needs further improvement [54–59].

The transition to ternary photoactive layers in OSCs represents a significant change. Ternary systems integrate a third component, which can be another donor or acceptor, into the binary blend. This addition broadens the absorption spectrum of the solar cell, enabling more efficient harvesting of solar energy across a wider range of wavelengths as illustrated in Figure1.5. Ternary layers also facilitate improved charge transfer and separation, leading to enhanced photocurrent and overall cell efficiency. Additionally, compatible dual-acceptor strategies have been employed to enhance the efficiency and stability of ternary OSCs. These advancements underscore the promising role of ternary systems in advancing the performance of OSCs [59–63].

The optimisation of the morphology of the BHJ in binary and ternary OPVs, is deemed to improve the performance of the OPV devices [65, 66]. One approach to tune morphology is by vacuum deposition of organic molecules to form layered devices or a bulk heterojunction that exhibits lateral combinatorial effects in mass ratios due to thickness gradients. Alternatively, co-deposition of organic molecules to form BHJ has been

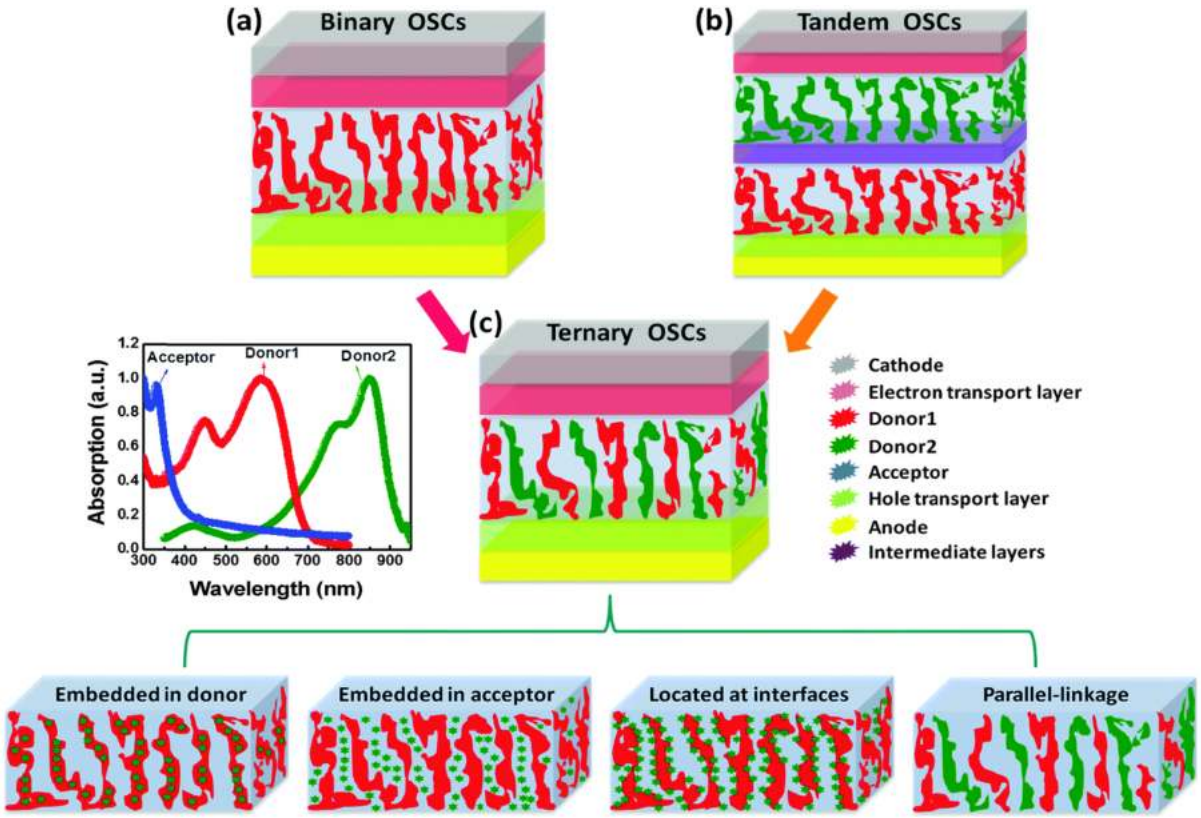


Figure 1.5: An image visually representing the evolution from (a) conventional binary, (b) tandem to (c) ternary photoactive layers of OSCs, highlighting the advancements in morphology to improve efficiency in solar cell technology. [64].

explored as an alternative route for morphology optimisation at the nanoscale [67, 68]. Additionally, the selective combination of solvents with suitable solubility, miscibility and boiling points presents a potential approach to optimising morphology for new OPV materials. The achievement of high PCEs in organic solar cells is heavily reliant on the morphology of the BHJ. Thus, by tuning the nature of the interconnected network can enhance exciton diffusion and dissociation processes. This may entail thermal annealing, solvent vapour annealing, or the use of co-solvents [69, 70].

Co-solvents in OSCs play a crucial role in optimising the morphology and phase separation of the photoactive blend. The right choice of co-solvents can lead to a more uniform and efficient distribution of the three components, thereby maximising the interface for exciton generation and dissociation. This results in improved quantum efficiency and a reduction in energy losses.

1.2 Long-Term Viability of Solar Energy

Solar energy is a long-term alternative to traditional fossil fuel-based energy sources for several reasons. Solar energy is a renewable energy source that is constantly replenished by the sun, making it a reliable source of energy for the foreseeable future. According to a study by the International Energy Agency (IEA), solar energy is expected to become the largest source of electricity by 2030, surpassing both coal and natural gas. This trend is

depicted in Figure 1.6 and predicts that solar PV global capacity is expected to exceed 2500 *GW* up from the current 800 *GW* by 2030, also solar energy has the potential to provide a significant portion of the world's energy needs in the future [71–73].

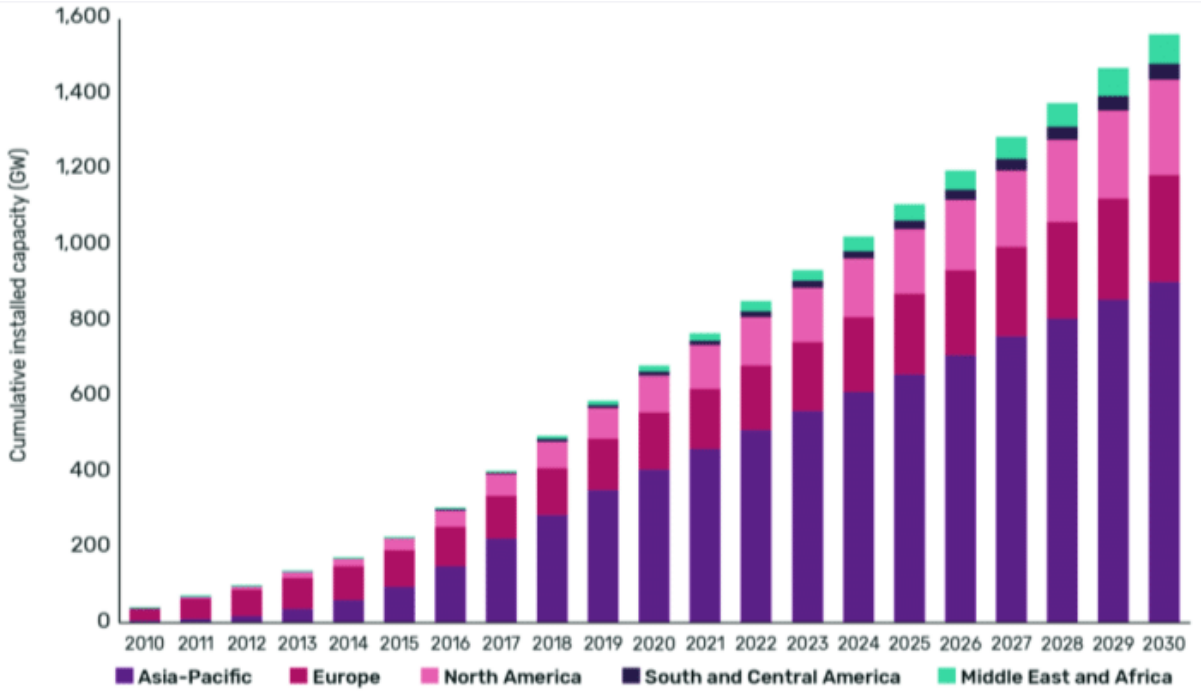


Figure 1.6: An image showing projected global capacity by 2030 [73].

Advances in technology have made solar energy more efficient and cost-effective over time. The National Renewable Energy Laboratory (NREL) reported that the cost of solar PV systems has decreased by over 80% since 2010 [74]. This cost reduction has made solar energy increasingly competitive with traditional fossil fuel-based energy sources in terms of cost, further supporting its long-term viability, which shows that solar energy can be an economically viable option for electricity generation [75].

Solar energy is commonly measured in watts peak (Wp), which serves as the primary unit for determining its cost. The size of a solar module is a determining factor in its price, with larger panels costing more. The installation process accounts for 60% of the higher cost of silicon solar cells, while the remaining 40% is attributed to the cost of materials and manufacturing. The global weighted average cost of solar PV modules was around \$0.16 per Wp in 2020, representing a significant decline in cost from previous years. The price varies with increase or decrease in market growth [76, 77].

In addition to its cost competitiveness, solar energy has minimal environmental impact, making it a sustainable alternative to traditional energy sources. Solar energy systems can help reduce global carbon emissions by up to 6.3 billion tonnes per year by 2050 [78].

1.3 Status of Photovoltaic Materials and Light Management Schemes

In the realm of photovoltaic technology, significant milestones mark the evolution of solar energy utilization. In 1839, Edmund Becquerel's experimentation with metal electrodes and an electrolytic material unveiled the photovoltaic effect, demonstrating the generation of voltage and electric current in materials exposed to light [79, 80]. This pivotal discovery laid the foundation for solar energy harnessing [81]. Following this, in 1877, Willoughby Smith crafted the first selenium-based solar cells [82, 83]. Albert Einstein's 1905 paper on the photoelectric effect, introducing the concept of photons, further advanced understanding. The observation of the photovoltaic effect in cadmium-selenide in 1932 underscored the expanding knowledge in this field [84, 85]. A significant leap occurred in 1954 when Pearson, Chapin, and Fuller at Bell Laboratories introduced the first practical solar cell made of silicon, boasting a power conversion efficiency of 6% [86, 87]. This achievement marked a crucial step towards the practical application of solar energy and the continued development of photovoltaic technology.

The efficiency and cost-effectiveness of a PV cell are intricately linked to the materials from which it is fabricated. Extensive research in the field has focused on identifying materials that strike the best balance between efficiency and cost-effectiveness for PV cell production. The ideal specifications for materials used in PV solar cells include [88–92]:

1. **Band Gap Between 1.1 eV and 1.7 eV:** This range is optimal for efficiently absorbing a broad spectrum of sunlight. Materials within this band gap can effectively convert solar energy without significant thermal losses.

2. **Direct Band Gap Structure:** A direct band gap structure is preferred for PV materials as it allows for more efficient absorption and conversion of photons into electrical energy. Direct band gap materials are characterised by high absorption coefficient as the electronic transition does not require a phonon.

3. **Accessibility and Non-toxicity:** The material should be abundant, environmentally friendly, and safe to handle, making it sustainable for widespread use in solar cell production.

4. **High PV Conversion Efficiency:** The ultimate goal is to achieve high efficiency in converting sunlight into electricity.

Research has shown that PV materials become more efficient as the light becomes more concentrated, with the highest overall efficiencies obtained with concentrated PV cells and modules. Additionally, layering multiple semiconductors to create multi-junction solar cells has been a successful strategy for improving PV cell efficiency. These cells are essentially stacks of different semiconductor materials, with each layer having a different band-gap, allowing for greater use of sunlight than single-junction cells [93].

A significant challenge is to maximise efficiency while minimising production costs. This involves addressing three primary types of internal cell losses: optical, quantum, and electrical, each stemming from distinct origins. Mitigating these losses requires diverse and often sophisticated manufacturing techniques for both cells and photovoltaic modules. The maximal efficiency potential for currently available photoactive materials

is governed by the well-established Shockley-Queisser (SQ) limit, which considers the equilibrium between photo-generation and radiative recombination [94, 95].

Optimising solar cell efficiency is largely dependent on reducing quantum losses, which are directly influenced by the material properties and the internal structure of the cell. Central to this discussion is the concept of the band gap, which determines the minimum photon energy necessary for participation in the photovoltaic conversion process. The efficiency of a solar cell correlates with its band gap value, which is intrinsically dependent on the material composition of the cell. Silicon is the standard material used in solar cells, possessing an indirect band gap of approximately 1.12 eV. However, alterations in its crystal structure can influence its physical attributes, particularly the width of the band gap [96, 97].

Third-generation solar cells are designed to achieve high power-conversion efficiency while being low-cost to produce, with the potential to surpass the SQ limit. They utilise various technologies and materials, such as dye-sensitized solar cells, up-conversion devices, down-conversion and down-shifting devices, hot carrier solar cells, intermediate band photovoltaics, multiple exciton generation, and flexible thin-film solar cells, to enhance efficiency and address specific loss mechanisms [98, 99]

Currently, there are various research approaches being investigated to incorporate intermediate bands into semiconductors. One notable technique among these is ion implantation, which is characterised by two distinct strategies. The first strategy involves doping the semiconductor substrate with extremely high concentrations of impurities, while the second strategy entails embedding a layer of silicon with a high dose of metal ions [100].

In the quest to improve solar cell efficiency, the current state of photovoltaic materials and light management strategies plays a crucial role. The field of photovoltaic materials has undergone significant evolution, transitioning from traditional silicon-based cells to newer thin-film and organic photovoltaics, each offering unique advantages and challenges. There is a recent emphasis on developing materials with higher absorption coefficients, broader spectral sensitivity, and improved charge carrier mobility. Organic photovoltaics, in particular, have attracted attention due to their potential for low-cost, flexible, and lightweight solar cells, despite facing challenges such as lower efficiency and stability compared to inorganic counterparts [101–103].

Various materials have been explored to enhance power conversion efficiency. These materials have been fabricated as thin films and they include hydrogenated amorphous silicon (a-Si:H), cadmium telluride (CdTe), copper indium gallium selenide (CIGS), and halide or hybrid perovskite. Perovskite solar cells, for instance, are being developed as a low-cost, high-efficiency, thin, lightweight, and are poised to be the potential alternative to traditional silicon cells. Recent advancements in design have led to a near-record efficiency of 26.1% and 19.2% for halide perovskite and organic solar cells, respectively as indicated in Figure 1.7, rivalling many existing solar panels, although they still lag in longevity compared to silicon cells [105–109].

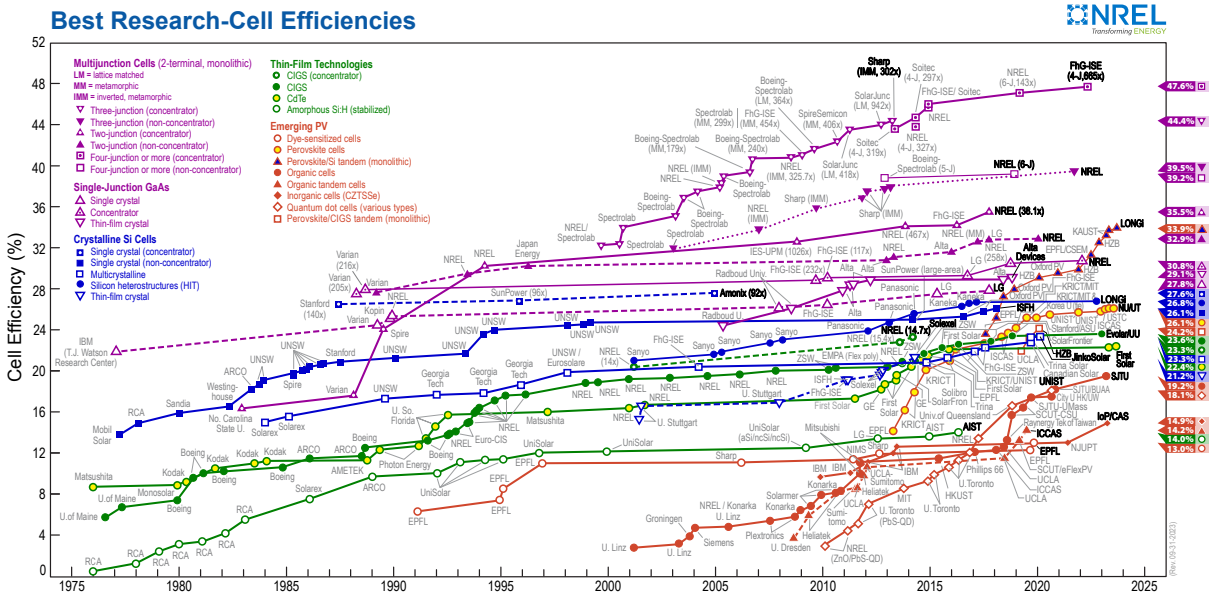


Figure 1.7: An image showing the National Renewable Energy Laboratory (NREL) chart for best research-cell efficiencies [104].

1.4 Innovative Solutions for Advancing Solar Cell Performance

In the rapidly evolving field of photovoltaic, innovative solutions are key to advancing solar cell performance. These solutions not only aim to increase the efficiency of solar cells but also strive to make them more cost-effective, durable, and environmentally friendly. There are cutting-edge technologies and strategies that are shaping the future of device performance.

In the realm of thin-film solar cells, where the physical thickness of the active material poses a challenge for light absorption, plasmonic nanoparticles play a crucial role. These cells, due to their reduced material thickness, often struggle with sufficient light absorption, impacting their overall efficiency. However, by integrating plasmonic nanoparticles into the thin-film solar cells, it becomes possible to compensate for this reduced absorption capacity [34, 110]. The nanoparticles enhance the interaction of light with the solar cell material, enabling a more efficient utilisation of the incident solar spectrum. This enhancement is particularly significant in thin-film technologies, where even a small increase in light absorption can lead to a substantial improvement in device performance [111].

The integration of plasmonic core-shell nanoparticles in the front of thin film solar cells has been shown to enhance the weak absorption of Si solar cells in the near-infrared region, with the maximum optical path length enhancement reaching high levels as demonstrated in Figure 1.8. The choice of plasmonic metal NPs, particularly Ag and Au, is crucial for achieving maximum light absorption in the front surface located nanoparticles, as they interact more strongly with the peak solar intensity. These advancements have paved the way for the development of plasmonic-enhanced solar cells, also known as plasmonic solar cells, which are designed to convert light into electricity using plasmons as the photovoltaic material [36, 112, 113].

Recent research has focused on the use of plasmonic nanoparticles to enhance the

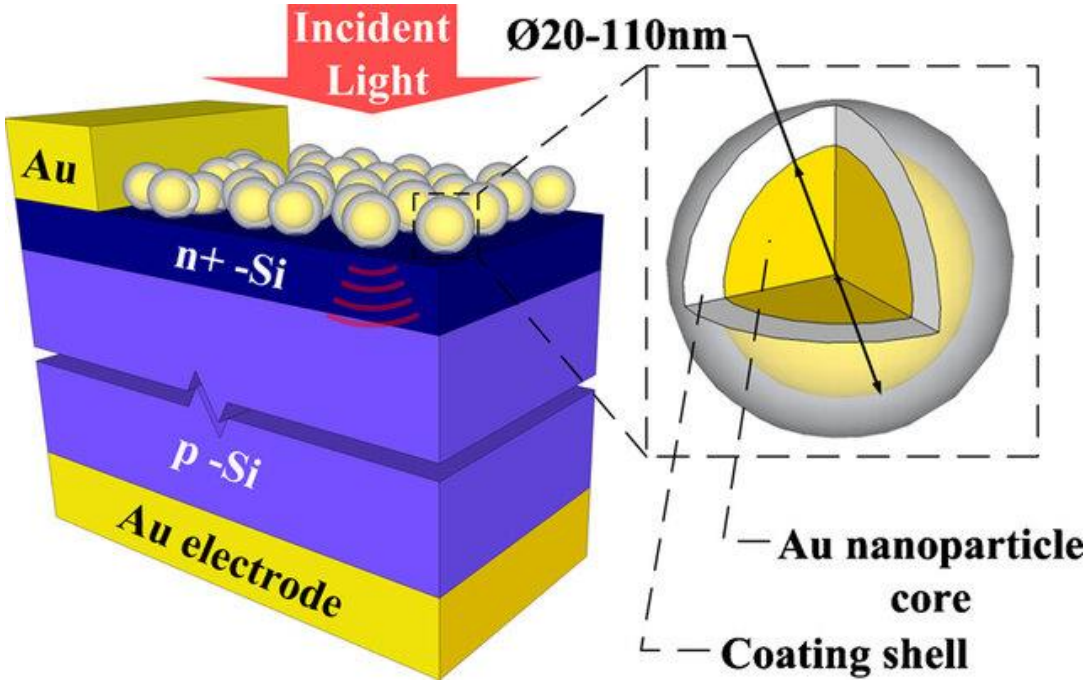


Figure 1.8: A schematic diagram of a PV device featuring a top-layer of Au-Si core-shell NPs [114].

efficiency of solar cells, particularly in the context of carbon-based perovskite solar cells [115–117]. The incorporation of plasmonic nanoparticles has been shown to significantly improve the absorption cross-section and the plasmon resonance of the nanoparticles, leading to enhanced device efficiency in the 5 - 10% range [118–120].

Tandem solar cells offer a multitude of advantages, with their standout feature being significantly higher efficiency that surpass the values imposed by the SQ limit. This translates to a remarkable increase in electricity production from the same amount of sunlight. One of the primary advantages of tandem solar cells is their ability to utilise a broader spectrum of solar radiation. In conventional solar cells, a significant portion of the solar spectrum is redudant because the photovoltaic material can only absorb photons with energies at least equal to its band gap [41, 121]. Tandem cells address this limitation by sequentially combining materials with different band gaps. This allows them to capture photons across a wider range of energies, from the high-energy end of the spectrum to the low-energy end. As a result, more of the solar spectrum is converted into electrical energy, leading to higher overall efficiency [122, 123].

Tandem solar cells have demonstrated the potential to exceed the efficiency limits of traditional single-junction cells [124, 125]. Unlike single-junction solar cells, which are constrained by the SQ limit, tandem cells can achieve higher efficiencies by effectively splitting the solar spectrum and using multiple junctions to absorb different parts of it [126, 127]. This enables them to capture a broader range of solar energies, from the high-energy end to the low-energy end, resulting in a higher conversion efficiency than their single-junction counterparts. This capability to generate a higher conversion efficiency than single-junction cells, given the same solar spectrum, positions tandem solar cells as a promising technology for significantly enhancing solar energy to electricity con-

version [128, 129].

Tandem solar cells, while offering significant advantages, also present unique challenges. The complexity of their design and the requirement for materials with different band gaps that are compatible with each other in a single device contribute to the manufacturing complexity [130, 131]. Additionally, ensuring that each layer optimally contributes to the overall efficiency of the cell is a critical aspect of their design. Ongoing research is focused on addressing these challenges, exploring new material combinations, and improving the integration of layers to realise the full potential of tandem solar cells [132–134].

There is a growing emphasis on sustainability in the field of photovoltaics, reflecting a broader societal shift towards environmentally compatible or friendly practices. This focus is driving significant research and development efforts aimed at creating eco-friendly materials for solar cells and implementing green manufacturing processes [91, 135, 136]. The objective is not only to produce energy in a sustainable manner but also to ensure that the entire lifecycle of solar cells, from production to disposal, aligns with environmental conservation principles.

Solar technology is often considered to be a sustainable technology, as it generates zero emissions and zero toxic waste during operation. However, the sustainability of solar panels is not black and white. Several factors need to be considered, including the raw material sourcing, manufacturing, energy use during mining, transportation, hazardous chemicals used in production, and the amount of e-waste generated [137–139]. While solar panels offer numerous benefits, such as reducing greenhouse gas emissions and contributing to environmental conservation, there are also challenges related to the environmental impact of their production and disposal.

The transition to green manufacturing in solar cell production involves a multifaceted approach. One key facet is the use of non-toxic materials. Traditional solar cells, particularly those based on thin-film technologies, often incorporate heavy metals such as cadmium, lead, as a critical material component of the photoactive layer. These elements pose environmental and health risks on exposure [140, 141]. Research efforts are increasingly directed towards finding safer alternatives that do not compromise the efficiency of the solar cells [142–144]. The environmental impact of solar manufacturing due to the fabrication and manufacture of photovoltaic devices is proposed to be offset through the use of renewable energy through solution processing methods. Solar energy capacity has increased sixfold in the past five years, and as the world seeks cleaner power, efforts are being made to ensure that the manufacturing process aligns with sustainability goals [145].

The move towards green manufacturing in solar cell production encompasses various elements. One critical aspect involves enhancing energy efficiency in the manufacturing process itself. Solar cell production can be energy-intensive, and as a result, there is a growing emphasis on reducing the energy footprint of these processes. Techniques such as low-temperature processing, the use of renewable energy sources in manufacturing, and minimising waste contribute significantly to making solar cell production more sustainable [146, 147].

1.4.1 Efficiency Limitations of Thin Film Solar Cell Technology

Thin film solar cells offer several advantages, such as flexibility and potential cost-effectiveness; however, they also present efficiency limitations that are important to address in the pursuit of enhanced solar cell performance. Some of the key factors contributing to these limitations include [148–151]:

a **Photoabsorption Limitations:** The optical absorption is heavily dependent on the absorption coefficient and the thickness of the photactive layer (PAL). The absorption coefficient is a material property and hence wavelength or band structure dependent. Materials with indirect band gap are characterised by low absorption coefficient which imposes a required for thick film thickness to enhance optional absorption.

b **Intrinsic Material Limits:** The materials used in thin-film solar cells, such as polymers, may have intrinsic limits, such as a small value of the high frequency dielectric constant which leads to the formation of the Frenkel exciton. These electron-hole pairs large binding energy values in the range of 0.1 eV. Large binding energies of excitons favour recombination over charge generation if their lifetime is large. Hence the process of exciton generation, diffusion and dissociation can impact the overall device efficiency for these classes of solar cell devices.

c **Operational Lifetimes and Deployment:** While thin-film technologies have made significant advancements, they have been found to have shorter operational lifetimes which has contributed to their somewhat limited deployment.

Efforts to address these limitations are crucial for the development of innovative solutions to enhance the performance of thin film solar cells. This includes the exploration of new materials, such as plasmonic nanoparticles and novel methods to tune the metastable morphology of the bulk heterojunction using co-solvent additives.

1.5 Aims and Objectives

The overarching aim of this thesis is to explore and develop innovative strategies to enhance the efficiency of solar cells through the incorporation of light management techniques involving plasmonic NPs and using various combinations of co-solvents on the morphology of blend mixture using the solubility criterion (Hansen solubility parameters) essential for device performance. The use of a solvent and co-solvent mixture system, to selectively dissolve one component is based on the calculations for solvents which can be varied depending on their interaction with donor and acceptor materials [152]. The variability of solubility and boiling points of solvents presents an effective route for tuning the morphology of the BHJ [153].

To achieve these aims, the thesis will focus on several key objectives:

1. **Examine the Role of Plasmonic NPs in Enhancing Light Absorption:**
    - Assess the impact of plasmonic NPs on local electromagnetic fields and light trapping in silicon (Si) solar cells.

- Evaluate different materials, sizes, and shapes of plasmonic NPs for their effectiveness in boosting power conversion efficiency in Si solar cells.

2. **Investigate the Effects of Magnetic NPs on Si Solar Cells:**
   - Explore how magnetic NPs influence light absorption and charge separation in Si solar cells.
   - Determine the optimal size, concentration, and placement of magnetic NPs to maximise efficiency.
3. **Develop and Test Core-Shell Structures of Magnetic and Plasmonic NPs:**
   - Design and fabricate core-shell nanoparticles combining magnetic and plasmonic properties.
   - Test the performance of Si solar cells integrated with core-shell nanoparticles, and compare with cells using either magnetic or plasmonic NPs alone.
4. **Explore the Influence of Co-Solvents on Organic Photovoltaic Materials:**
   - Optimise the morphology of bulk heterojunction (BHJ) using Hansen solubility parameters.
   - Fine-tune domain size formation in binary and ternary BHJ.
   - Assess the impact of co-solvents on the efficiency, stability, and lifespan of organic solar cells.
5. **Address Sustainability in the Fabrication of Organic Solar Cells:**
   - Consider the environmental impact and economic viability of using eco-friendly co-solvents in solar cell production.

1.6 Thesis Structure

This thesis is structured to provide a comprehensive exploration of advanced techniques for improving solar cell performance. The thesis is divided into six chapters, each focusing on a specific aspect of this research project. The structure is as follows:

Chapter 1: Introduction: Innovative Approaches to Enhance Solar Cell Performance

The opening chapter of this thesis lays the groundwork for the exploration of innovative solutions to enhance solar cell performance. It outlines the current challenges in solar cell technology and emphasises the potential of innovative approaches to overcome these challenges. Furthermore, it provides a comprehensive background on the importance of enhancing solar cell efficiency and introduces the concepts of plasmonic nanoparticles. These introductions are essential for contextualising the subsequent research and experimental work conducted in the thesis.

Chapter 2: Literature Review

Chapter 2 provides a comprehensive overview of the research relevant to the thesis topic. It encompasses previous studies on plasmonic nanoparticles, their application in solar cells, and the use of eco-friendly co-solvents in OSCs. The primary objective of this chapter is to establish a theoretical and contextual foundation for the research, laying the groundwork for the exploration of strategies to enhance solar cell performance. The review delves into the potential of plasmonic thin film solar cells, the methods for light trapping, and the effects of plasmonic metal core-dielectric shell nanoparticles on light absorption enhancement in thin film solar cells. Additionally, it sheds light on recent advances that employ plasmonics and nano-sized structures and thin-film technologies intended to increase solar cell efficiency.

Chapter 3: Theoretical Foundation of Surface Plasmonic and Magneto-plasmonic Resonance Effects:

This chapter provides an in-depth exploration of the theoretical aspects of surface plasmonics and magnetoplasmonics, elucidating the principles behind these phenomena and their relevance to enhancing solar cell performance. Additionally, it delves into the potential applications of these effects in improving light absorption and efficiency in solar cells. Furthermore, it discusses the effects of plasmonic metal core-dielectric shell nanoparticles on the broadband light absorption enhancement in thin film solar cells, offering valuable insights into the design and optimisation of plasmonic solar cells.

Chapter 4: Plasmonics and Magnetoplasmonics Effects for Photovoltaic Applications: Silicon Solar Cell

Chapter 4 is dedicated to the experimental research conducted as part of this thesis. It details the methodologies used to study the impact of plasmonic and magnetoplasmonic nanoparticles on silicon solar cell performance. This chapter presents the experimental results, data analysis, and findings, providing insights into how these nanoparticles can be effectively utilised in solar cells.

Chapter 5: Morphology Tuning of OSCs with Co-Solvent Additives

In this chapter, the focus shifts to the use of eco-friendly co-solvents in organic solar cells. It discusses the role of solvent additives in tuning the morphology of OSCs, their impact on the efficiency and stability of the cells, and the potential environmental benefits of using eco-friendly solvents.

Chapter 6: Conclusion and Future Work

The final chapter of the thesis encapsulates the key findings and contributions of the research, providing a comprehensive summary of the study. Additionally, it delves into the broader implications of the research for the field of solar energy, considering the evolving landscape of solar cell technology. Furthermore, the chapter proposes areas for future research, aiming to address the current limitations and leverage the potential opportunities identified in the study.

Chapter 2

2 Literature Review

As the world gravitates towards renewable energy sources, the efficiency of solar cells has become a focal point of scientific research. The increasing demand for energy, fluctuating fossil fuel prices, and growing concerns over global warming and environmental impact have led to substantial research and efforts directed towards harnessing solar energy through PV devices and systems [154]. Solar cells, among various renewable energy sources, offer distinct advantages such as silent operation, high power-to-weight ratio, and portability. Photovoltaic arrays are also notable for their quick design, installation, and commissioning timelines, coupled with an extended lifespan and minimal maintenance requirements [155]. A notable attribute of PV cells is their modularity, which allows for economic viability independent of the plant's size, making them adaptable across a broad spectrum of power capacities. Additionally, solar cells are sustainable, environmentally friendly, and offer the potential to eliminate monthly electric bills, making them an economical and easy solution for clean energy production [156, 157]. However, ongoing research and development efforts are focused on addressing these limitations and improving the efficiency and sustainability of solar cell technologies [158–160].

2.1 Solar Cell Technologies

The classification of PV cell technologies can be broadly categorised into organic and inorganic types, each with distinct characteristics and materials as exhibited in Figure 2.1. This classification is significant in understanding the different approaches to photovoltaic technology and their respective applications and efficiencies. The review of this classification encompasses the unique properties, applications, and current research trends within each category.

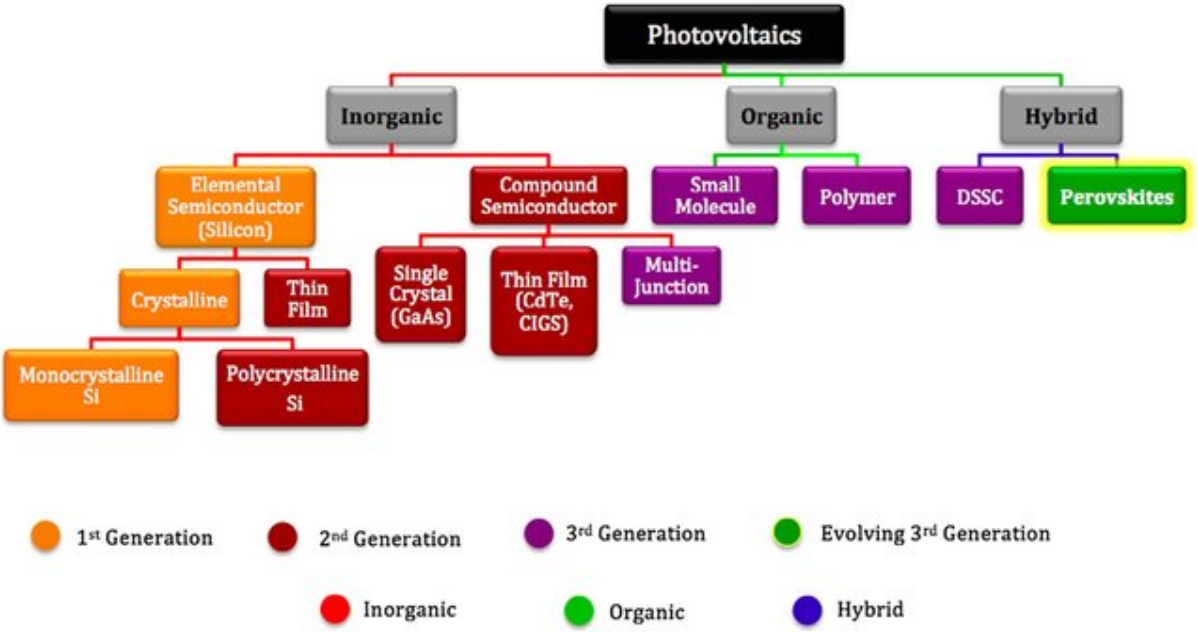


Figure 2.1: An image showing the fundamental categories of PV cells [161].

2.1.1 Inorganic Solar Cells

Inorganic solar cells, primarily composed of inorganic materials, are fundamental for photovoltaic applications. These cells are typically fabricated using semiconductor materials such as silicon, or compounds like cadmium telluride (CdTe) and copper indium gallium selenide (CIGS). The defining characteristic of these materials is their robust and stable crystalline structure, which contributes to the remarkable durability and high efficiency of inorganic solar cells [162]. Overview of the photoactive layers that have been used in solar cells:

2.1.1.1 Silicon-Based Solar Cells

The crystal structure of PV materials, particularly silicon-based solar cells, plays a crucial role in determining their electronic and optical properties. In the context of crystalline silicon solar cells, the crystal lattice formed by silicon atoms is essential for efficient conversion of light into electricity. This organised structure enhances the absorption and conversion of light energy, making crystalline silicon cells highly efficient, cost-effective, and long-lasting [163].

In silicon-based solar cells, the crystal structure consists of front contacts, an anti-reflection coating, an emitter layer (n-type), an absorber layer (p-type), and a back electrode as shown in Figure 2.2. This structure allows for the absorption of light energy and there is also current due to holes, which is then transferred to negatively charged particles called electrons, generating an electrical current. The bandgap of the semiconductor material determines the wavelengths of light that can be efficiently absorbed and converted into electricity. When the bandgap matches the light wavelengths, the cell can effectively utilise the available energy [164].

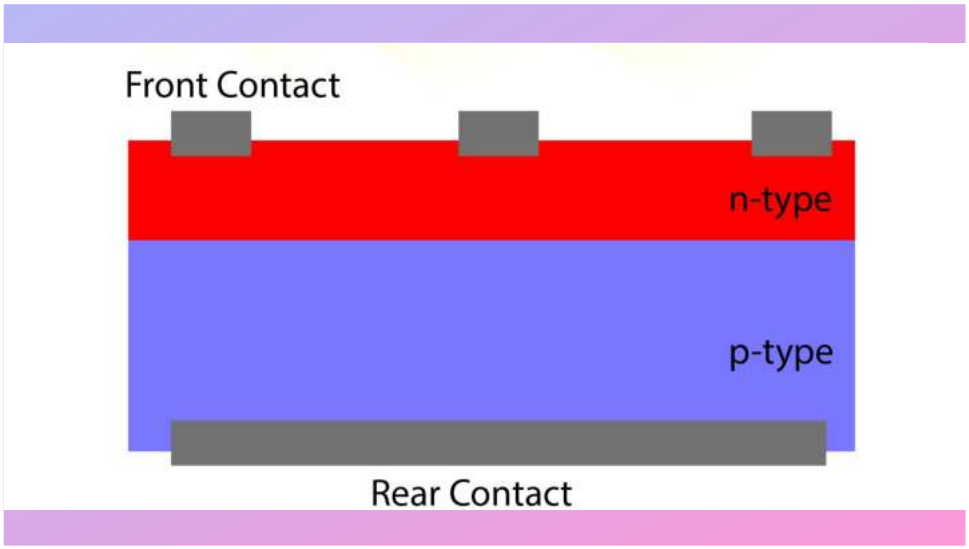


Figure 2.2: Basic structure of a Si PV cell.

Silicon-based solar cells are the foundation of the photovoltaic industry, owing to their established efficiency and reliability. These solar cells are typically classified into two main types: monocrystalline and polycrystalline silicon PV cells, each with distinct characteristics and manufacturing processes. Silicon solar panels, often referred to as first generation panels, have been a dominant technology since the 1950s, with over 90% of the current solar cell market being based on silicon [165, 166]. The use of pure crystalline silicon, while initially expensive, has become more affordable over time, especially with the support of government subsidies [167–170].

1. **Monocrystalline Silicon Solar Cells**

   Monocrystalline PV cells are manufactured from single-crystal silicon using the Czochralski method, where a single crystal silicon is grown from molten silicon and then sliced into thin wafers. This process results in a characteristic uniform dark appearance and high purity level of the silicon, which contributes to the cell's efficiency. Monocrystalline solar cells have a band gap of 1.1 eV and an absorption coefficient ranging from 1.694 to 6.863 cm^{-1}. The high electron and hole mobilities contribute to their high power conversion efficiency of approximately 26.7% in commercial products [124, 171, 172]. Their single-crystal structure allows for optimal electron-hole movement, reducing the likelihood of electron-hole recombination and thus enhancing efficiency. They also perform better in low-light conditions compared to other types of solar cells. The high-purity silicon and intricate manufacturing process make monocrystalline solar cells more expensive [173]. However, their higher efficiency can offset the initial cost in the long term. They are commonly used in applications where space is limited but a high power output is required [174, 175]. Monocrystalline solar cells have the highest confirmed conversion efficiency out of all commercial PV technologies, ahead of polycrystalline and established thin-film technologies [129]. Despite being more expensive than polycrystalline cells, monocrystalline PV cells are widely used due to their high efficiency and space-efficient nature [176].

2. **Polycrystalline Silicon Solar Cells**

   Polycrystalline silicon PV cells are manufactured by melting multiple silicon fragments together, which are then cooled and cut into wafers. This method is less wasteful and more cost-effective than the Czochralski process [177]. The cells are identifiable by their blue, speckled appearance, which is a result of the multiple crystals within each cell. Although less efficient than monocrystalline cells, typically around 15-18%, polycrystalline cells offer a more affordable alternative [178, 179]. The presence of many crystals or grain boundaries in these cells can impede electron transport, slightly reducing their efficiency. They are relatively more efficient in higher temperatures compared to monocrystalline cells [180]. The lower production costs make polycrystalline solar cells a popular choice for large-scale installations and residential applications where space is not a critical constraint [181].

2.1.1.2 Thin-Film Solar Cells

Silicon wafer technology, which primarily utilises highly pure crystalline silicon, is renowned for its high costs, attributed to the complexity and expense involved in procuring pure silicon. However, a promising avenue for reducing the cost of solar cells lies in the deployment of thin films, approximately 1 μm thick [182]. This technique significantly reduces the amount of silicon used compared to traditional wafer-based technology. The inception of amorphous silicon thin films was pioneered by R. Chittick, followed by comprehensive studies by his colleagues on the plasma enhanced chemical vapour deposition technique [183]. Thin-film solar cells are distinguished within the realm of photovoltaic technologies by their distinctive manufacturing process. This process involves the deposition of one or more thin film, ranging from a few nm to a few (μm) layers of photovoltaic material onto a supporting substrate, such as glass, plastic, or metal [184]. The use of thin silicon films presents a promising opportunity to enhance the cost-effectiveness of solar cells, thereby contributing to the wider adoption of solar energy technologies.

1. **Amorphous Silicon Solar Cells**

   Hydrogenated amorphous silicon (a-Si:H) is reliant on the doping to modify its electrical properties. In a standard pn junction solar cell, the minority carriers generated by photoabsorption diffuse across the p and n regions along the entire length of the junction where optical absorption occurs, owing to their significantly large diffusion lengths (approximately 200 μm). However, in the case of amorphous silicon solar cells, the diffusion lengths for minority charge carriers are markedly short, about 0.1 μm [184,185]. This distance is limited by the device architecture and the physics of the materials used. When this diffusion length is too short, relying solely on diffusion for collecting these minority charge carriers becomes impractical. This limitation is due to the fact that the carriers may recombine before reaching the collection electrode, reducing the efficiency of the solar cell. Therefore, alternative strategies such as optimising the device structure or incorporating additional charge collection mechanisms are necessary to improve the overall performance of the solar cell. The extremely low effective doping efficiency of trivalent boron in amorphous tetravalent silicon further complicates the light harvesting of these cells [186].

   The limitations mentioned have led to the predominant use of p-i-n device architecture for the a-Si:H solar cells. Additionally, thin-film technology enables the

fabrication of various types of solar cells, including homojunction, hetero-junction, and multi-junction solar cells. The advantages of thin film solar cell technology are numerous, such as [182, 187–191]:

- Reduced Material Usage
- Shorter Energy Payback Time
- Monolithic Integration
- Production of Large-Area Modules
- Adjustable Material Properties
- Low-Temperature Manufacturing Processes
- Creation of Transparent Modules

The mechanism of light absorption in a-Si:H solar cells leads to the generation of electron-hole pairs, forming bound excitons due to Coulomb attraction. These excitons are dissociated through the differences in the chemical potential of the p and n-doped Si layers to facilitate charge separation and collection [192, 193]. The band edge for a-Si:H, is approximately 1.7 eV. This value is crucial in understanding the optical and electronic properties of a-Si:H, particularly in the context of its applications in solar cells and other electronic devices. This technology has found applications in a range of products from pocket calculators to residential homes, commercial buildings, and remote facilities. With over 15 years in the market, thin film solar cell technology is well-established and continues to evolve [194].

2. **Cadmium Telluride Solar Cells**

   Cadmium Telluride ($CdTe$) thin film solar cells are widely regarded as one of the most promising technologies in the photovoltaic sector. The material's band gap of 1.45 eV aligns well with the solar emission spectrum, making it exceptionally efficient in solar energy absorption [195]. This suitability is further enhanced by its direct band gap properties and high absorption coefficient ($10^4 - 10^5\ cm^{-1}$), allowing for a remarkably thin layer to effectively absorb incident photons [196].

   In terms of efficiency, CdTe solar cells have demonstrated considerable potential. Theoretical efficiency levels are estimated to be around 29% [197], while practical laboratory efficiencies reported by NREL scientists have reached 16.5% [95]. Moreover, advancements by companies like First Solar have pushed the efficiency of CdTe solar cell technology exceeding 22% [198], showcasing its practical viability.

   However, the use of cadmium, a toxic heavy metal, in these solar cells has raised environmental concerns [199–202]. Current research efforts are heavily focused on enhancing the material's safety and developing effective recycling processes to mitigate the environmental impact [203–205].

3. **Copper Zinc Tin Sulfide Solar Cells**

   Copper Zinc Tin Sulfide ($Cu_2ZnSnSe_4$) solar cells are an alternative to CdTe solar cells, in an effort to mitigate the concerns related to toxicity and material scarcity. CZTS cells rely on abundant and environmentally friendly materials, featuring an

optimal direct band gap (1.4 to 1.5 eV) and high optical absorption ($10^4\ cm^{-1}$) [206–208]. However, their efficiency is currently lower than that of CdTe solar cells, with laboratory efficiency for CZTS solar cells recorded at 12.6% [209]. This indicates the potential for further development and improvement in this technology.

4. **Copper Indium Gallium Selenide Solar Cells**

   Copper Indium Gallium Selenide ($CuInSe_2$) is a type of thin film solar cell based on the chalcopyrite family ($CuInSe_2$). The $CuIn_{1-x}Ga_xSe_2$ thin layer typically of thickness 1-2 μm is deposited on a glass substrate with molybdenum (Mo) and cadmium sulfide (CdS) as the front and back electrodes respectively [182,210]. The semiconductor compound utilised in CIGS cells possesses a high absorption coefficient of $10^5\ cm^{-1}$ which is higher than that of Si. This gives it a reasonable tradeoff between high photoabsorption in thin film format [211].

   Research advancements have revealed that incorporating heavy alkali elements such as rubidium and cesium, as substitutes for sodium and potassium, can significantly enhance the efficiency of CIGS solar films. This alteration in the composition has led to remarkable improvements in experimental efficiency [212–216].

   CIGS solar cell technology, based on the ternary chalcopyrite structure of $Cu(In, Ga)Se_2$, has achieved noteworthy efficiency milestones. On flexible substrates, these cells have demonstrated an efficiency of 20.8% [217], while rigid substrates have seen efficiencies reaching 23.4% [218]. These figures underscore the potential of CIGS technology in both flexibility and performance, marking it as a significant player in the field of thin film photovoltaics.

2.1.2 Organic Solar Cells

Organic solar cells (OSCs) are distinguished by several key properties that make them a promising option for future solar technologies. It is notably cost-effective to produce organic polymers and relatively simple to fabricate the OSC devices. Additionally, their reliance on earth-abundant materials adds to their appeal as a sustainable energy solution. They are based on two dissimilar electronic materials that are blended to form an interconnected network of electron donor and electron acceptor materials. These materials can be either polymers or small organic molecules [219, 220].

The principle operation mechanisms are categorised into 4 components, namely [221–226]:

i. Photoabsorption of the electron in the Highest Occupied Molecular Orbital (HOMO) and its excitation to the Lowest Occupied Molecular Orbital (LUMO) of the donor material. This leads to the formation of the electron-hole pair. This quasi particle is known as the exciton. Since these polymers have a low value of the high frequency dielectric constant (~ 4.3) the exciton binding energy is very high typically in the range of 0.1 eV (RT $\sim$ 25 meV) and are referred to as the Frenkel exciton.

ii. Exciton diffusion to the donor and acceptor interface. This process seeks to prohibit the recombination of the exciton and the short exciton diffusion length prescribes on the proximity of the donor and acceptor interfaces to dissociate it.

iii. Exciton dissociation to the formation of unbound charge carriers.

iv. Charge transport to the cathode and anode of the device.

Increased research interest in organic solar cells has been driven by their high efficiency (>19%) and enhanced device stability following the use of non-fullerene acceptor materials [227]. This demonstrates their potential as an effective alternative in the solar cell market, particularly as research continues to advance their efficiency and stability. The combination of environmental sustainability, ease of manufacturing, and improving efficiency rates positions OSCs as a viable and attractive option for renewable energy in the coming years. However these values are still low for the OPV to compete or even replace commercial Si photovoltaic technologies. We shall provide a review of the recent progress on the binary and ternary organic solar cells that have been generated research interest later on this chapter.

2.1.3 Hybrid Solar Cells

Hybrid solar cells are formed from the components of both organic and inorganic solar cells. This blend aims to capitalise on the strengths of each type while mitigating their respective weaknesses, resulting in improved efficiency, stability, and potential for cost reduction [228]. As research progresses, these cells are expected to play a significant role in the future of photovoltaics, potentially bridging the gap between current silicon-based technologies and the next generation of solar energy devices. In the foregoing, a discussion of the promising candidates of these type of PV devices will be presented in detail.

2.1.3.1 Dye-Sensitized Solar Cells

Dye-sensitized solar cells (DSSCs) are well-known for their ability to operate effectively in low-light conditions, such as during dawn, dusk, or cloudy weather. This technology is notable for its use of more affordable materials, including natural dyes, and a simpler fabrication process compared to the more expensive silicon-based solar cells. The relative ease and lower fabrication costs of DSSC have led to extensive research and experimentation in this field, positioning it as a compelling alternative to costly crystalline silicon technology.

A DSSC comprises five essential components: a conductive support, a semiconductor film, a suitable sensitizer (dye), an electrolyte acting as a redox couple, and a counter electrode [229]. Tailoring the optoelectronic properties of any of these components can significantly enhance the efficiency of DSSCs. This includes factors like the absorption coefficient of the sensitizer, energy band alignment matching the incident solar spectrum for maximum photon absorption, and solid-state properties of the dye such as its aggregation, morphology optimisation, and assembly mode on the TiO_2 photo-anode [230].

The first efficient DSSC developed in 1991, utilising mesoscopic titanium oxide as a photo-anode in the anatase phase. Since its inception, the efficiency of DSSCs has improved significantly, from 7.9% in 1991 to 15.2% in 2021 [231, 232]. However, challenges

such as long-term stability and potential electrolyte leakage after exposure to high temperatures remain areas of concern.

Interestingly, DSSCs are often regarded as the precursors to halide perovskite solar cells, marking an important milestone in the evolution of photovoltaic technology.

2.1.3.2 Perovskite Solar Cells

Perovskite, named after the mineral $CaTiO_3$ and the Russian mineralogist L.A. Perovski, refers to a class of compounds with a chemical formulae denoted as ABX_3 and the crystal structure illustrated in Figure 2.3 . In this structure, 'A' and 'B' represent cations, while 'X' stands for an anion species [233]. The valency states of cations in metal halide perovskites play a crucial role in their properties. In these compounds, the metal cations can have different valency states, affecting the electronic structure and overall behavior of the perovskites. For instance, in the context of metal halide perovskites like $CH_3NH_3MX_3$, the valency states of metal cations such as Cu, Zn, Ga, Ge, Sn, and Pb are significant. These cations can have fully or partially filled valence 3s, 4s, 5s, and 6s orbitals, which influence the band structure and the formation of valence band maxima. The presence of lone-pair electrons from these metal cations directly impacts the electronic structure of the perovskites, affecting properties like band gaps and carrier effective masses. Variations in the level of lone-pair states of these cations can lead to changes in band gaps, with wider band gaps observed when the level of lone-pair states increases. Additionally, the valency states of cations can influence the width of band gaps in perovskites, with different cations exhibiting distinct effects on the electronic properties of these materials [234].

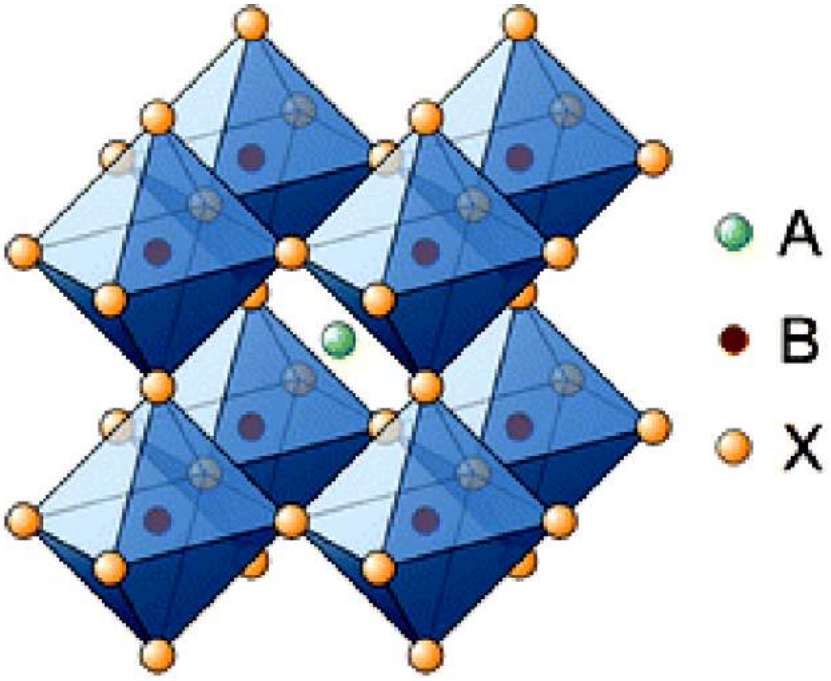


Figure 2.3: Schematic representation of the crystal structure of an organic-inorganic metal halide perovskite [235].

In the context of hybrid organo-lead perovskites used in solar cells, 'A' is typically a monovalent organic cation such as $CH_3NH_3^+$, 'B' is either Pb(II) or Sn(II), and 'X' is a halogen anion like iodide (I^-), bromide (Br^-), or chloride (Cl^-). Common semiconductor perovskite materials for solar cell applications are summarised in Table 2.1 [236–242]:

Table 2.1: Overview of common halide perovskite materials: bandgap energies, absorption coefficients, and peak power conversion efficiencies.

Halide Perovskite Type	Bandgap (eV)	Absorption Coefficient (cm^{-1})	PCE (%)
$MAPbI_3$	1.6	10^5	25.7
$FAPbI_3$	1.48	10^5	26.5
$CsPbI_3$	1.73	10^5	22
$MAPbBr_3$	2.3	10^5	19.1
$FAPbBr_3$	2.23	10^5	9.4

In the context of hybrid organo-lead perovskites used in solar cells, 'A' is typically a monovalent organic cation such as $CH_3NH_3^+$, 'B' is either Pb(II) or Sn(II), and 'X' is a halogen anion like iodide (I^-), bromide (Br^-), or chloride (Cl^-). The "MA" in $MAPbI_3$ stands for "Methylammonium", "Formamidinium" in $FAPbI_3$ and "Cesium" in $CsPbI_3$. Common semiconductor perovskite materials for solar cell applications include $CH_3NH_3PbI_3$, $CH_3NH_3PbBr_3$, and mixed halide structures like $CH_3NH_3PbI_{3-x}Cl_x$ or $CH_3NH_3PbI_{3-x}Br_x$ [236, 237].

These photoactive materials offer several advantages for solar cells, including low recombination losses, reduced material costs, extended charge carrier diffusion lengths, and the ability to tune the bandgap energy through cation and anion substitution [243]. Perovskite solar cells (PSCs) have seen a rapid increase in efficiency, surpassing other photovoltaic technologies in a short span [244]. The use of methylammonium lead halide ($CH_3NH_3PbX_3$) perovskites has led to the development of more stable and efficient solar cells, with high-quality perovskite films significantly impacting advanced solar cell technologies [245–247].

Perovskite solar cells commonly adopt two architectural designs: mesoscopic (Figure 2.4 (a)) and planar (Figure 2.4 (b)). In the mesoscopic design, a thin compact layer of TiO_2 (10-30 nm) is deposited onto a conductive transparent oxide like FTO or ITO material on glass, followed by a thicker porous layer of TiO_2 nanoparticles. This layer

is then sintered and infiltrated with a perovskite solution [248]. In contrast, the planar configuration does not include a mesoporous layer. Instead, a perovskite absorber layer is topped with a hole transport material (HTM) layer and a 60-80 nm thick layer of gold, deposited using techniques like spin coating and evaporation. In this setup, light passes through the photoanode (FTO), allowing the HTM and top contact layer to be opaque [249].

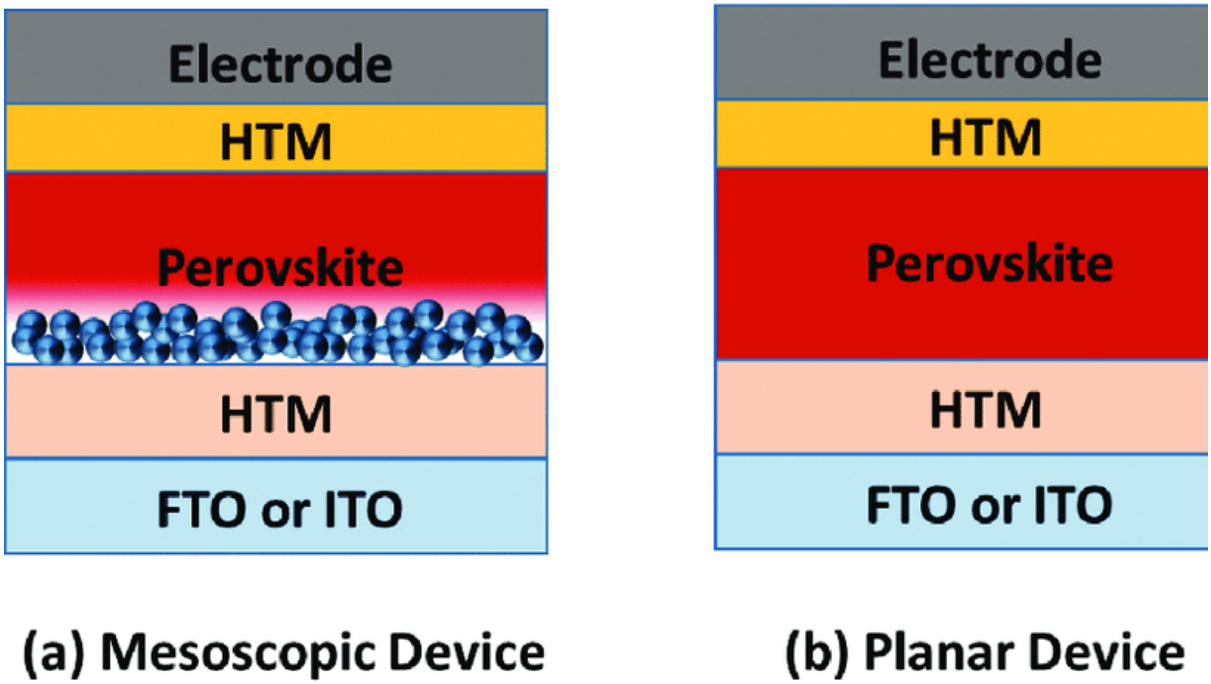


Figure 2.4: Device architecture of (a) mesoscopic perovskite solar cell and (b) planar perovskite solar cell [250].

Additives at the anion and cation sites, such as inorganic salts, organic halide salts, inorganic acids, fullerenes, polymers, and even water, have been used to improve the surface morphology of hybrid perovskite solar cells. These additives help in forming highly crystalline, smooth perovskite layers, thus enhancing the efficiency and stability of the cells [251–254]. Since 2015, researchers have been experimenting with replacing the methylammonium cation with formamidinium (FA) and/or cesium, and partially substituting iodide with bromide, to improve $MAPbI_3$'s water sensitivity and thermal stability [255, 256]. Recent advancements in perovskite materials, notably the introduction of formulations like $CsPbI_3$, have significantly improved the stability and efficiency of perovskite solar cells. These materials are particularly beneficial in the absorber layer, offering enhanced light absorption and charge transport properties, which are crucial for both mesoscopic and planar configurations [257, 258].

Encapsulation techniques help mitigate the effects of moisture and oxygen on PSCs [259–261].The main challenges with PSCs are the instability of the intrinsic bulk perovskite material and the interface between the perovskite material and charge transport layers. Instability factors include hygroscopicity, thermal instability, and ion migration. Hygroscopicity, related to environmental exposure, can be addressed through encapsulation [262–264].

2.1.4 Significance of Solar Cell Efficiency

The efficiency of a solar cell is defined as the ratio of power output from the solar cell to input power from the sun. It is the most commonly used parameter to compare the performance of one solar cell to another [265, 266]. Commercial manufacturers rate solar panels by their efficiency, which ranges from around 15-20% of conversion of the sun's energy transformed into usable electricity. High-efficiency solar panels can reach as much as nearly 23% [267]. Factors affecting photoconversion efficiency of the solar cell include efficiency include the amount of light reflected away from the device surface, the intensity of the sun, the amount of cloud cover, and heat build-up, which affects the conductivity in the photoactive layers of the solar cell [268]. Proper thermal management improves both efficiency and lifetime [269].

The efficiency of a solar cell is a critical factor that directly influences the amount of electrical power that can be generated by the incident photons illuminated on the surface of the device. Higher efficiency implies more power from smaller surfaces, which is essential for space-constrained applications. Moreover, the cost-effectiveness of solar power systems is closely linked to the efficiency of the solar cells, as higher efficiency can offset the initial investment in solar technology by providing more power output over the lifetime of the solar panel, thereby reducing the cost per kilowatt-hour of electricity generated. Efficient solar cells also contribute to a more sustainable energy solution by maximising power output while minimising the environmental footprint, leading to a reduction in the use of raw materials, energy, and land area required for solar installations [270,271].

The pursuit of higher efficiency drives innovations in research which include the integration of light management strategies using plasmonic and magnetoplasmonic nanostructures. Moreover, the tuning of the morphology with vertical phase segregation of the bulk heterojunction using eco-friendly co-solvents contributions to the increase in generation rate and thus the enhancement of the photocurrent through exciton dissociation and charge transport. These advancements can lead to the development of new materials and designs that offer improved performance and open up new applications for solar technology [272–276].

The PCE of solar cells is a crucial parameter that quantifies the efficiency with which a solar cell converts sunlight into electricity. The PCE is mathematically expressed as a percentage and is calculated using the formula:

$$PCE = \frac{P_{out}}{P_{in}} \times 100\% \tag{2.1}$$

where:

- P_{in} is the electrical power output from the solar cell (in watts).
- P_{out} is the power of the incident sunlight on the solar cell (in watts).

To further break down the components that determine P_{out}, the PCE can be related to critical measurement observables of the solar cell, namely the short-circuit current

density (J_{sc}), the open-circuit voltage (V_{oc}), and the Fill Factor (FF). The formula incorporating these variables is:

$$PCE = \frac{J_{sc} \times V_{oc} \times FF}{P_{in}} \times 100\% \tag{2.2}$$

The product of these three parameters, normalised by P_{in}, gives the efficiency of the solar cell. Improvements in materials, cell structure, and fabrication techniques focus on optimising these parameters to achieve higher efficiencies [277]. Specifically, increasing J_{sc} involves improving light absorption and charge separation [278]. Enhancing V_{oc} requires minimising recombination and optimising the energy band structure [279]. Improving FF involves reducing resistive losses and enhancing the electrical characteristics of the solar cell. Each of these factors is a critical area of research in the development of more efficient solar energy conversion technologies [280].

2.2 Efficiency Enhancement in Organic Solar Cells

Several challenges must be addressed before OPV devices become a viable commercial product. Currently, organic solar cells are hamstrung by TWO primary bottlenecks: low device efficiencies and device degradation in ambient air due to photo-oxidation or moisture [281, 282]. Exposure to the atmosphere decreases its power conversion efficiency, primarily due to water accumulation in the organic polymers and the breakdown of the polymer-cathode interface. Additionally, the limited absorption spectrum of the active layer material, stemming from the high bandgap energy of most organic semiconductors, results in low charge carrier concentration and, consequently, low efficiency [283–285]. Efforts to mitigate this limitation have included the integration of new polymers with lower bandgap energies into the photoactive layer, thereby extending the absorption spectrum [286]. Furthermore, the carrier lifetime of electron-hole pairs generated in the active layer poses another constraint on the efficiency of organic solar cells. Addressing these challenges is crucial for advancing the efficiency of organic solar cells and enhancing their commercial viability [166, 287, 288].One key aspect to consider is the carrier mobility imbalance, where discrepancies in the mobility of electrons and holes can limit overall device performance. Strategies to enhance carrier mobility through material design and device optimisation are essential for improving the efficiency and competitiveness of organic solar cells in the market [289–291].

2.2.1 The Role of Morphology in Organic Solar Cell Performance

The optimisation of the morphology of the BHJ in binary and ternary OPVs, is deemed to improve the performance of the OPV devices [65, 66]. One approach to tune morphology is by vacuum deposition of organic molecules to form layered devices. Alternatively, the co-deposition of organic molecules can be exploited to form BHJ with varying composition fraction across the device lateral area. This combinatorial material synthesis strategy has been explored as an alternative route for morphology optimisation at the nanoscale. Additionally, the selective combination of solvents with suitable solubility, miscibility and boiling points presents a potential approach to optimising morphology for new OPV materials [292]. The achievement of high PCEs in

organic solar cells is heavily reliant on the morphology of the BHJ. Thus, by tuning the nature of the interconnected network one can enhance exciton diffusion and dissociation processes. This may entail thermal annealing, solvent vapour annealing, or the use of co-solvents [69, 70].

2.2.1.1 Binary OPVs

The morphology of the active layer in binary OPVs plays a crucial role in determining the performance and efficiency of these devices. The nature of the donors and acceptors, including factors such as solubility, crystallinity, and miscibility, significantly influences the morphology of the active layer [293]. The tuning of the vertical morphology as illustrated in Figure 2.5 in binary organic solar cells has been identified as critical and challenging, particularly in the context of achieving high open-circuit voltage [294]. Understanding the fundamental origin of morphological degradation in non-fullerene acceptor-based organic solar cells is also recognised as a challenging yet essential aspect of improving the stability of these devices [295].

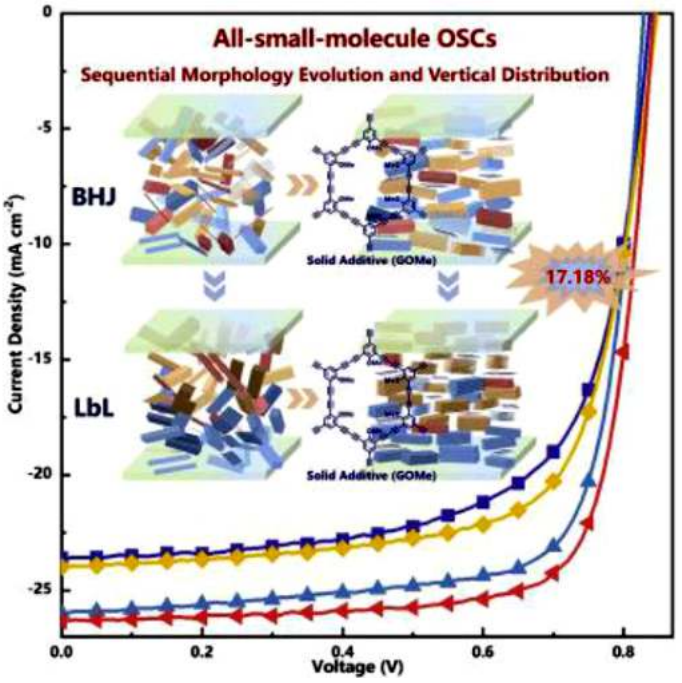


Figure 2.5: Visualising an effective strategy for optimising the active layer through sequential morphology evolution and enhancing vertical distribution [296].

The investigation of the metastable morphology of the bulk heterojunction in organic solar cells is crucial for understanding the performance and degradation mechanisms of these devices. Through advanced techniques like GIWAXS and GISAXS, researchers have delved into the temperature-induced morphology evolution in polymer/fullerene blends, shedding light on the intricate processes that occur post-deposition. The analysis has revealed fascinating phenomena such as spinodal decomposition leading to the formation of a fine-scale bi-continuous structure and the subsequent growth of large polycrystalline fullerene aggregates. Moreover, the co-existence of spinodal decomposition and nucleation-growth mechanisms has been observed, highlighting the

complexity of the transformation processes within the active layer. Additionally the molecular packing or orientation based on the H and J aggregation provides an indication of the nature of the interconnected network [297].

Furthermore, studies have shown that the morphology evolution in bulk heterojunctions goes through distinct phases, starting with spinodal decomposition of the donor:acceptor blend followed by the nucleation and growth of crystalline acceptor aggregates [298]. This unified thermodynamic and kinetic mechanism not only provides insights into the structural changes within the active layer but also correlates these changes with the degradation of organic solar cells during thermal annealing [299]. By understanding these intricate processes, researchers aim to optimise the morphology of organic solar cells, ultimately enhancing their efficiency and stability for practical applications.

Common methods used to control the morphology of the active layer in binary OPVs include thermal annealing, solvent annealing, post-solvent treatment [300–302]. Thermal annealing is a widely used method to optimise film morphology, leading to improved photovoltaic performance [303, 304]. Solvent annealing and post-solvent treatment are also common post-treatment methods to control the morphology of the active layer [305–307]. The effect of thermal annealing on the morphology of the active layer in binary organic solar cells is significant.

2.2.1.2 Ternary OPVs

Recent progress in the field of ternary blend OSCs has shed light on the critical role of not only the extending of the photon harvesting window but also that of morphology in determining device performance. Ternary blend organic solar cells, which consist of three components in the active layer, have garnered significant attention due to their potential for highly efficient solar energy conversion. A review of recent studies on ternary blends has emphasised the importance of understanding the morphology of these blends, particularly from the perspectives of molecular crystallinity, phase separation, and intermolecular interactions [308, 309].

The morphology of the active layer in ternary OPVs illustrated in Figure 2.6 (a) is a key determinant of device performance. The third component in the active layer has been shown to play a crucial role in controlling the crystallinity and phase separation of the blend, thereby influencing the formation of an interpenetrating network of electron-donor and acceptor domains. This network is essential for efficient exciton dissociation and charge transport, which are critical for achieving high device performance [311–318]. Each of the four configurations shown in Figure 2.6 (b) is discussed below:

1. **Donor1:Donor2:Acceptor1 (D1:D2:A1)**

   In this configuration, two donor materials are blended with one acceptor material. The rationale behind using two donors is often to broaden the absorption spectrum or to fine-tune the morphology of the active layer for improved charge transport [319]. The addition of a second donor can lead to complex phase separation behaviours and thus varied morphologies, as the interaction between the two donors and the acceptor can create multiple domains of different compositions and

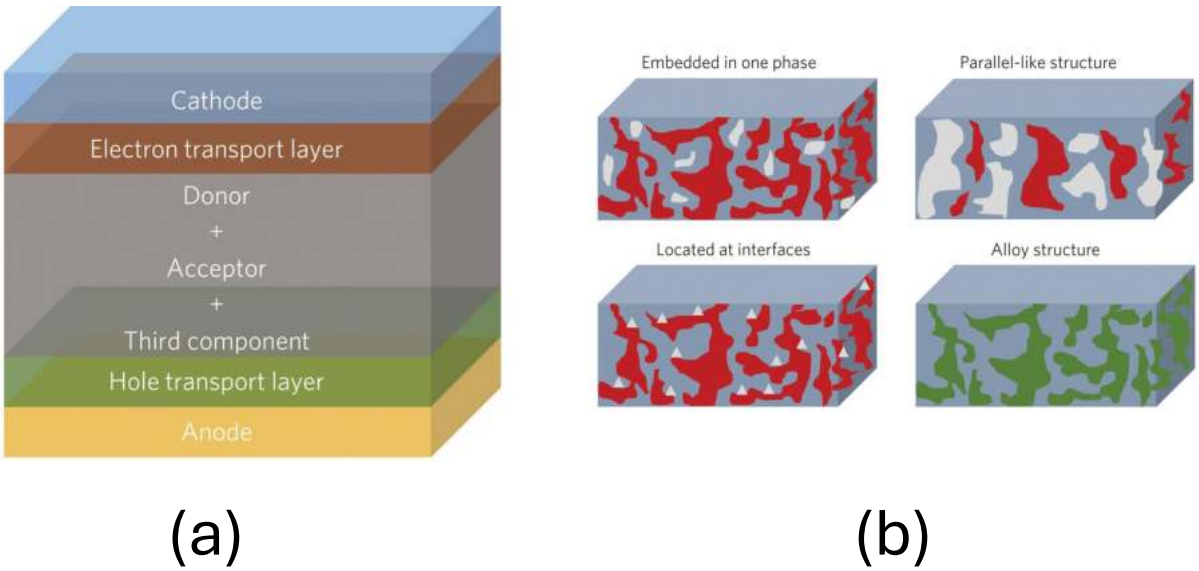


Figure 2.6: (a) Structure of three-component bulk heterojunction OSCs, and (b) Four distinct morphologies for the active layer, showcasing the integration of a third component: embedded within either the donor or acceptor phase, positioned at the interfaces, creating a structure parallel to the main donor or acceptor, and forming an amalgam with either the donor or acceptor material [310].

crystallinities [308,320]. The exact morphology will depend on the miscibility of the donors with each other and with the acceptor, as well as the processing conditions used [293].

2. **Donor1:Acceptor1:Acceptor2 (D1:A1:A2)**

   This configuration uses one donor material and two acceptor materials. Similar to the previous configuration, the aim is to enhance the absorption range and/or optimise the electronic levels for better energy level alignment. The two acceptors can facilitate the formation of a more complex morphology with varied domains that can potentially lead to improved charge separation and transport. The interaction between the different acceptor materials and the donor can result in diverse morphologies, influenced by the relative concentrations, the compatibility of the materials, and the processing techniques [321].

3. **Donor/Nonvolatile Additive/Acceptor (D/NA/A)**

   Introducing a nonvolatile additive into the active layer of an OSC can significantly affect its morphology and performance. Nonvolatile additives are used to influence the phase separation, crystallinity, and domain purity of the blend, leading to varied morphologies [322–325]. These additives can selectively solvate one component over the others, promoting a particular morphology that is conducive to efficient charge generation and transport. The specific effect on morphology depends on the nature of the additive, its concentration, and its interaction with the donor and acceptor materials [326].

4. **Parallel Linking or Alloying Structure**

   The parallel linking or alloying structure refers to a configuration where the donor and acceptor materials are mixed at the molecular level, often leading to a highly homogeneous interpenetrating network [327–329]. This configuration can result in a unique morphology where the donor and acceptor phases are finely intermixed, potentially reducing charge recombination and facilitating efficient charge transport [330]. The extent of phase separation and the resulting morphology can vary depending on the molecular design of the components and the processing conditions [331].

Each of these ternary configurations can indeed lead to varied morphologies within the active layer of organic solar cells. The specific morphology achieved is critical for the device's performance and is influenced by the choice of materials, their ratios, compatibility, and the processing methods used [332, 333].

In recent studies, a general strategy has been reported for better control of the morphology of ternary blend films composed of a polymer donor and two acceptors [334].This strategy involves incorporating a suitable third component into the blend, which is known as the ternary strategy. By adding this third component to the polymer donor and two acceptors, the performance of organic solar cells can be significantly improved in terms of efficiency and stability [334].

Recent research has underscored the importance of morphology in determining the performance of ternary blend organic solar cells. In ternary organic solar cells (TOSCs), morphology plays a crucial role in determining device performance by influencing key parameters like J_{sc}, V_{oc}, and FF. Research indicates that optimising the morphology of TOSCs can lead to significant efficiency improvements. For instance, a study reported an increase in power conversion efficiency from 8.82% to 11.20% by enhancing the morphology of ternary cells [335]. This enhancement is attributed to the improved distribution of photogenerated excitons and the optimisation of the active layer's morphology [336]. Moreover, FF in TOSCs can vary with the active layer thickness, showing an initial growth as the thickness increases from 50 to 200 nm, followed by a decline above 200 nm [337]. This demonstrates the intricate relationship between morphology, active layer characteristics, and device performance in TOSCs.

2.2.2 Morphology Control with Solvent Additives

Solvent additives are pivotal in determining the nanoscale organisation of the active layer in OSCs as their properties influence the drying kinetics, phase separation, and the solubility and miscibility of the photoactive components. This control over morphology is crucial for effective exciton generation and charge transport, ultimately enhancing power conversion efficiency [338]. The optimisation of domain sizes and purity within the active layer through solvent additives has been shown to lead to efficient exciton generation rate, exciton dissociation and charge collection [339–341]. A variety of additives, with high boiling point solvents, have been explored, such as 1,8-diiodooctane (DIO), 1-chloronaphthalene (1-CN), and Anisole, among others. Each additive has unique effects on the film-forming properties and can be chosen based on the desired

morphology and compatibility with the photoactive materials [342–345]. Achieving consistent and scalable morphological control using solvent additives across large-area production remains a challenge due to the variability in drying conditions and film formation dynamics [346].

Research is increasingly focused on understanding the underlying physics of film formation with solvent additives to enhance reproducibility [333]. Additionally, the environmental impact of solvent additives, including toxicity and the potential for safer, greener alternatives, is an important area of ongoing research [347–349]. The development of eco-friendly solvent additives that do not compromise on morphological control or device performance is gaining attention. Therefore, solvent additives play a critical role in enhancing OSC performance through morphology control, and ongoing research is focused on addressing challenges and developing sustainable solutions [350, 351].

2.2.2.1 Binary OPVs

The use of solvent additives for morphology control in binary OSCs has been a subject of extensive research and has shown promising results in enhancing device performance. By affecting film formation during the solution processing, solvent additives can provide fine control of the active layer morphology of organic photovoltaics, making them key morphology-directing agents for solution-processed organic solar cells [339]. Controlling the morphology of the active layer is essential for achieving high power conversion efficiency in OSCs, and processing BHJ layers with solvent additives has proven to be an effective strategy toward this goal [69]. Recent developments in morphology control and characterisation have provided valuable insights for further research in this area, emphasising the significance of morphology control in the development of binary organic solar cells [293]. Additionally, a general strategy for better control of the morphology of ternary blend films composed of a polymer donor and two acceptors has been reported, demonstrating the potential for enhanced device performance through morphology control [334]. When using additives in OSCs, the morphology controlled includes the phase separation between the donor and additive, which is critical for achieving the desired vertical phase-separation structure. This morphology control is verified in binary OPVs by assessing the miscibility between the polymer donor and the additive [352]. Therefore, the use of solvent additives for morphology control in binary organic solar cells has shown great promise and is expected to continue driving advancements in the field.

2.2.2.2 Ternary OPVs

Recent research has focused on the impact of solvent additives on the morphology and performance of ternary blend OSCs. A study by X. Weng et al. (2020) reported as a general strategy for better control of the morphology of ternary blend films, composed of a polymer donor and two acceptors, leading to improved device performance [353]. This study emphasised the importance of understanding and controlling the morphology of ternary blends for the development of highly efficient OSCs. The morphology control was verified in ternary OPVs by assessing the miscibility between the polymer donor and the additive. The Flory-Huggins interaction parameter χ_D is used to evaluate the miscibility, where a small χ_D indicates fine miscibility, while a large value suggests phase separation between the donor and additive. Additionally, contact angle measurements are employed to calculate the χ_D, providing insights into the miscibility of the components [354].

2.3 Plasmonic and Magnetoplasmonic Nanostructures for Photovoltaic Applications

The development of plasmonic and magnetoplasmonic nanostructures for photovoltaic applications has been a subject of research. These nanostructures have shown promise in enhancing the performance of solar energy utilisation. Recent studies have highlighted the potential of titanium nitride-based plasmonic NPs for photovoltaic applications, demonstrating their impact on solar cell performance [355]. Additionally, the combination of photonic and plasmonic nanostructures has been explored for developing high-efficiency solar energy systems, with a focus on applications such as photovoltaics, photo-thermal conversion, and photocatalysis [356–358]. Furthermore, the use of magnetoplasmonic nano-antennas has been identified as a rapidly expanding research field, with potential applications in solar energy utilisation [359]. The ongoing research in this area is expected to lead to significant advancements in the development of plasmonic and magnetoplasmonic nanostructures for enhanced photovoltaic performance.

2.3.1 Light-Matter Interaction

Plasmonics is the study that involves light-matter interactions at the sub-micron length scale and it continues to attract significant research attention due to its versatile applications such as optical communication, energy conversion and photovoltaic. Moreover, research has been extended to development of plasmonic and magnetoplasmonic nanostructures for solar cell applications leading to tuning of the size, aspect ratio, shape for multi-modal excitations [274]. In this section the collective oscillation of electrons also known as the surface plasmonic resonance is presented and discussed.

2.3.1.1 Surface Plasmonic Resonance

Surface Plasmon Resonance (SPR) has garnered attention for its potential applications in the field of photovoltaics. Plasmonic and magnetoplasmonic nanostructures have been explored for enhancing the performance of photovoltaic devices. These nanostructures, when integrated into solar cells, can facilitate light trapping, leading to improved light absorption and enhanced energy conversion efficiency [35, 360–364].

The review of properties and applications of plasmonic surface lattice resonances in ordered arrays of metal nanoparticles has highlighted their ability to scatter light and produce diffracted waves, which is relevant to the development of advanced photonic devices [365, 366].

Size The impact of nanoparticle size on SPR is a critical factor in the development of plasmonic and magnetoplasmonic nanostructures for enhancing PV performance. The size of plasmonic nanoparticles is directly linked to their SPR frequency, with smaller nanoparticles resonating at shorter wavelengths and larger particles at longer wavelengths. This size-dependent resonance tuning is essential for aligning plasmonic absorption with the solar spectrum to maximise light harvesting in solar cells [365]. Additionally, NP size influences the intensity and distribution of enhanced electromagnetic fields, with smaller nanoparticles producing more localised and intense field enhancements, beneficial for

light absorption in solar cells. On the other hand, larger nanoparticles are more efficient at scattering light [367]. Balancing absorption and scattering is crucial for optimising light trapping in solar cells. Varying the NP size can enable broadband light absorption, essential for capturing a wider range of the solar spectrum. However, it is important to carefully optimise NP size to ensure effective light absorption without excessive light scattering [368]. Incorporating a distribution of NP sizes can potentially create a more uniform and broadband enhancement of light absorption within the solar cell. Nevertheless, precise control over NP size is challenging but essential for consistent SPR effects, as variability in size can lead to inconsistent photovoltaic performance [369, 370]. Ongoing research is focused on developing reproducible synthesis methods that allow tight control over NP size. Furthermore, the size of NPs can affect the collective plasmonic behaviour in densely packed arrays, which is important for designing solar cell surfaces. The choice of material and fabrication techniques also imposes limitations on the achievable size range of NPs and their stability within the solar cell environment [371, 372].

Shape The effect of nanoparticle shape on SPR is a crucial aspect in the design of plasmonic and magnetoplasmonic nanostructures for various applications, including plasmonic sensors, nanolasers, biosensing, and energy harvesting [373, 374]. The shape of metal nanoparticles, such as nanorods, nanocubes, or nanostars, plays a significant role in determining their plasmonic properties and SPR characteristics. For instance, the measured localised surface plasmon resonance (LSPR) has been shown to broaden with the reduction of both the nanorod length and diameter, contrary to theoretical predictions [375]. When metal NPs are arranged in an ordered array, they may scatter light to produce diffracted waves, and the width of plasmon resonances depends on the number of particles that interact coherently [376–380]. The size-dependence of SPRs in metal nanostructures is critical for various applications, and SPRs are influenced by their size, morphology, composition, surface chemistry, and surrounding environment [381]. Therefore, the shape of metal NPs are interconnected factors that significantly influence the SPR properties and can be tailored to achieve specific plasmonic effects for diverse PV applications.

It is crucial to understand how different shapes impact their optical properties. Spherical NPs typically exhibit a single resonance mode due to their symmetry, while elliptically shaped NPs can have two oscillatory modes: longitudinal and transverse modes as depicted in Figure 2.7 [383].

In spherical NPs, the symmetry of the structure leads to a single resonance mode, resulting in a characteristic plasmonic response as shown in Figure 2.7 (a). On the other hand, elliptically shaped NPs lack this symmetry, allowing for the existence of multiple oscillatory modes. Specifically, elliptical NPs can support both longitudinal and transverse modes as depicted in Figure 2.7 (b), leading to a more complex optical behaviour compared to spherical NPs [384–386].

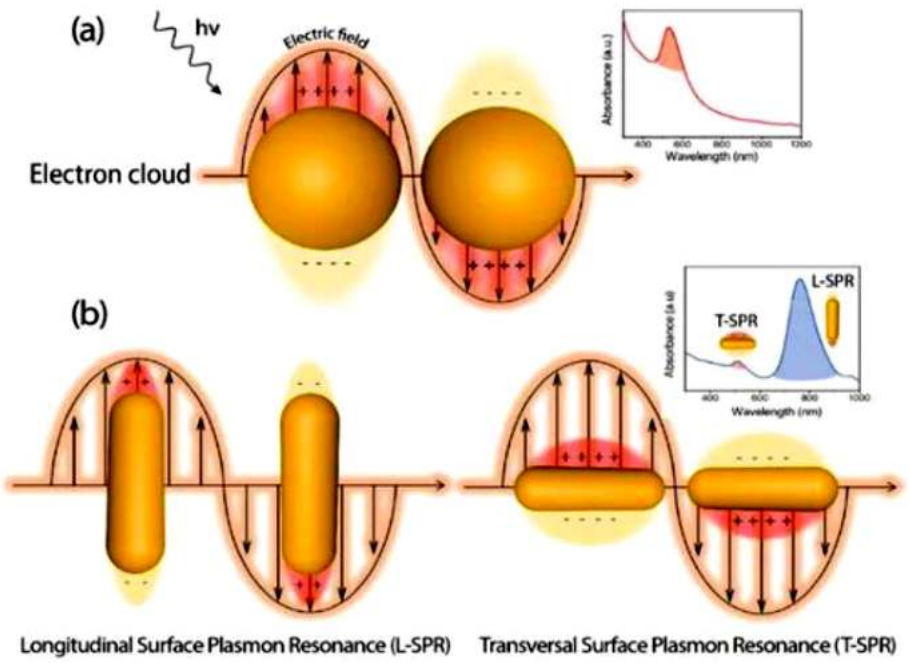


Figure 2.7: (a) Schematic diagram of (a) spherical shaped NPs illustrating a single resonance mode and (b) elliptically shaped NPs demonstrating multiple oscillatory modes [382].

Number Density of Plasmonic Nanostructures The effect of density on SPR is a fundamental aspect of plasmonics, influencing the behaviour of metal NPs and their applications in various fields. SPR can be used to observe density fluctuations and molecular absorption at the nanoscale [387, 388]. The density of metal NPs can affect their plasmonic properties and collective behaviour in densely packed arrays to enhance near field effects, which is important for designing plasmonic devices [389–391].

A higher density of NPs can enhance the SPR effects, leading to increased local electromagnetic field enhancement and improved light absorption in solar cells. However, beyond a certain density, NPs may begin to obstruct each other, reducing effective light absorption and scattering [392–394]. The spacing between NPs is crucial in defining their collective SPR behaviour. An optimal NP density is required to balance light trapping and minimise parasitic absorption, which can be beneficial for the overall efficiency of PV cells [395,396]. Studies have shown that a properly tuned NP density can maximise light trapping within the solar cell, leading to improved photocurrent generation [397–400]. Achieving and maintaining the optimal NP density during the fabrication process is challenging, as it influences the balance between light absorption and scattering and can affect the electrical properties of the PV cell [401–403].

Dielectric Layer In the realm of SPR for enhancing PCE in PV systems, the dielectric layer plays a pivotal role. It serves as a medium for the interaction between the plasmonic material and the incident light, significantly influencing the efficiency and localisation of the SPR [404]. The refractive index of the dielectric material determines the strength and wavelength of the SPR. Properly designing the dielectric layer can indeed maximise the electromagnetic field enhancement near the plasmonic NPs, leading to increased light

absorption in the active layer of solar cells. However, the shift in the resonance edge with the dielectric constant of the dielectric medium in which the NP is embedded is also significant. The dielectric constant of the medium influences the plasmonic resonance frequency and linewidth of the NPs, affecting their optical properties. A change in the dielectric constant can lead to a reversible shift in the plasmon resonance frequency and linewidth, impacting the overall performance of the plasmonic system [365, 405]. This, in turn, allows for the efficient conversion of a broader range of the solar spectrum [406,407]. The dielectric layer is particularly crucial for thin-film solar cells, where maximising light absorption per unit thickness is essential. It also provides a physical and chemical interface between the metallic NPs and the semiconductor material of the solar cell, vital for maintaining the structural and operational integrity of the cell. Selecting the appropriate dielectric material with the right optical and chemical properties is challenging but crucial for effective SPR. Recent advancements focus on exploring various materials, including silicon dioxide (SiO_2), titanium dioxide (TiO_2), and polymers, for their suitability as dielectric layers [408]. The thickness of the dielectric layer needs to be precisely controlled to optimise the SPR effect, with uniformity across the layer being essential for consistent solar cell performance. Integrating dielectric layers with emerging solar cell technologies like perovskite and organic solar cells is an area of active research, aiming to synergise the benefits of SPR with the unique properties of these materials [409–411].

2.3.1.2 Mechanism of Light Trapping Using Core-Shell Structures

Core-shell nanostructures consist of a core material encapsulated by a shell layer, typically comprising different materials with distinct optical properties. These structures are particularly effective in light trapping due to their unique ability to manipulate electromagnetic fields at the nanoscale [412, 413]. The core-shell configuration offers several pathways for enhancing light absorption in photovoltaic devices:

1. **Localised Surface Plasmon Resonance (LSPR):** When light interacts with the metallic core of the nanostructure, it induces collective oscillations of free electrons, known as localised surface plasmons [414,415]. These oscillations create strong electromagnetic fields near the surface of the core, which can be tuned by adjusting the size, shape, and material of the core-shell structure. The enhanced electromagnetic field increases the local light intensity, leading to higher absorption in the active layer of the photovoltaic device [416–418].

2. **Scattering and Near-Field Enhancement:** Core-shell structures can scatter incident light in multiple directions, effectively increasing the optical path length within the PV device. This scattering effect is particularly beneficial for thin-film solar cells, where the optical thickness is limited [419, 420]. The near-field enhancement around the core-shell structure also contributes to improved light absorption, as the intensified electromagnetic field can penetrate deeper into the active layer [421–424].

3. **Resonant Coupling:** Core-shell structures can support multiple resonant modes, including dipolar and higher-order multipolar resonances. These resonant modes can couple with the incident light, enhancing the absorption over a broad wavelength range [425, 426]. By carefully designing the core and shell materials, it is

possible to achieve resonant coupling at specific wavelengths that align with the absorption spectrum of the photovoltaic material [427, 428].

4. **Magnetoplasmonic Effects:** In magnetoplasmonic core-shell structures, the incorporation of magnetic materials introduces additional functionalities. The magneto-optical effects, such as the Kerr effect, can further enhance light trapping by modulating the polarisation and intensity of light within the photovoltaic device. This modulation can lead to improved absorption and charge carrier generation [429, 430].

Several studies have demonstrated the effectiveness of core-shell nanostructures in enhancing photovoltaic performance. For example, $Ag@SiO_2$ core-shell NPs have been shown to increase the light absorption in silicon-based solar cells significantly. The SiO_2 shell not only protects the metallic core from oxidation but also provides a dielectric environment that enhances the LSPR effect [431, 432].

Similarly, magnetoplasmonic core-shell structures, such as $Fe_3O_4@Au$, have been investigated for their dual functionality in light trapping and magnetic field-induced effects [433]. These structures exhibit tunable plasmonic properties and enhanced light absorption, leading to improved efficiency in photovoltaic devices.

2.3.2 Application of Magnetoplasmonic and Plasmonic Nanoparticles in Solar Cells

The application of magnetoplasmonic and plasmonic NPs in solar cells has garnered significant attention due to their potential in enhancing light-harvesting efficiency and improving overall performance. Metallic NPs exhibit LSPRs, which are associated with near-field enhancements [434]. These NPs have been proposed as a strategy to enhance the performance of dye-sensitized solar cells by designing omnidirectional light-harvesting layers with different shapes, inspired by the epidermal structures of various plants, resulting in enhanced capturing efficiency of obliquely incident light [435, 436]. The unique scattering properties of large metallic NPs can increase the optical path length, leading to effective light trapping within the semiconductor, addressing one of the main issues of thin-film solar cells, which is low absorption [437,438].

One of the main challenges in using these NPs is their integration into existing solar cell architectures without compromising the cell's electrical and structural integrity. There are considerations regarding the cost and scalability of incorporating these advanced materials into commercial solar cells. Research indicates that plasmonic and magnetoplasmonic NPs can significantly enhance the efficiency of various types of PV cells, including thin-film, organic, and perovskite solar cells [439, 440]. Furthermore, these NPs offer potential stability improvements, particularly in organic and perovskite solar cells, under varying environmental conditions [441–446]. Research has demonstrated that magnetic NPs can significantly enhance the performance of solar cells. One study showed that incorporating ferric oxide NPs into the active layers of solar cells, combined with a specific light-sensitive dye, can improve light absorption and reduce light loss due to reflection. This process boosts the PCE by generating an internal magnetic field that increases the dissociation of charge carriers, thereby increasing the V_{oc} [447].

2.4 Nanoparticles Simulation Techniques

The simulation of NPs has become an integral part of nanotechnology research, including in the field of photovoltaics and drug delivery systems. Advanced simulation techniques allow researchers to predict the behaviour, interactions, and effects of NPs under various conditions. The key simulation methods used in magnetoplasmonic and plasmonic NPs research. A discussion on the theoretical principles and their applications for energy conversion is provided in the subsequent subsections.

2.4.1 Simulations of Magnetoplasmonic NPs

The dynamic behaviour of magnetic moment in nanoparticles that exhibit exchange correlation is governed by the Landau-Lifshitz-Gilbert equation, explained in more detail in Chapter 3 [448–450]. For magnetoplasmonic NPs, simulations often need to couple both optical and magnetic properties, involving the integration of methods like finite-difference time-domain(FDTD) with micromagnetic simulations to study the interplay between plasmonic and magnetic effects [451, 452].

The study by Yuan et al. (2022) discusses the progress, opportunities, and challenges of magnetoplasmonic NPs under remote magnetic and light stimulation, emphasising the potential applications of these NPs in brain-tissue and cellular regeneration [453]. Furthermore, the work by Mikoliunaite et al. (2022) presents a novel method for the synthesis of magneto-plasmonic NPs with enhanced functionality, particularly for multi-wavelength surface-enhanced Raman spectroscopy (SERS) [454]. Additionally, the research by Han et al. (2017) focuses on a magnetic polypyrrole/iron oxide core/gold shell nanocomposite for multimodal imaging, demonstrating the multifaceted applications of these NPs [455].

2.4.2 Simulations of Plasmonic NPs

Finite-Difference Time-Domain (FDTD) is a widely used method for simulating the interaction of light with plasmonic NPs. It calculates the time-dependent electromagnetic fields, making it ideal for studying the dynamic optical response of various NP shapes and arrangements. FDTD simulations are crucial for optimising NP design for enhanced light absorption and scattering in photovoltaic cells [456–458]. This is explained in depth in Chapter 3.

The Discrete Dipole Approximation (DDA) is particularly effective for irregular and complex-shaped plasmonic NPs. It models the NPs as arrays of polarisable points, allowing for the calculation of their optical properties, such as scattering and absorption cross-sections [459].

The scattering cross-section (σ_{scat}) quantifies the area over which incident light is scattered by a particle. It represents the effectiveness of a particle in scattering light and is expressed in units of area. The absorption cross-section (σ_{abs}) measures the area over which incident electromagnetic radiation is absorbed by a particle. This parameter quantifies how effective a particle is at absorbing light, effectively removing it from the incident beam and converting it into other forms of energy. Like σ_{scat}, it is also expressed

in units of area.

The expressions for calculating σ_{scat} and σ_{abs} are derived from the electromagnetic response of the array of polarisable points that model the NP. The basic expressions involve the calculation of the electric and magnetic fields scattered by each dipole in response to an incident field, taking into account interactions between dipoles [460].

The scattering cross-section can be calculated from the far-field scattering pattern, typically involving the square of the amplitude of the scattered field, integrated over all scattering directions. The formula is given by:

$$\sigma_{scat} = \frac{1}{I_{inc}} \int |E_{scat}|^2 \, d\Omega \tag{2.3}$$

where:

I_{inc} is the intensity of the incident wave.
E_{scat} is the electric field of the scattered wave.
Ω is the integral is over the solid angle surrounding the particle.

The absorption cross-section is related to the total power absorbed by the particle and can be expressed as:

$$\sigma_{abs} = \frac{P_{abs}}{I_{inc}} \tag{2.4}$$

P_{abs} is the power absorbed by the nanoparticle, which can be calculated from the imaginary part of the polarisability of the dipoles and the intensity of the incident field.

These expressions are simplified and conceptual. The actual computation of σ_{abs} and σ_{scat} using DDA involves numerically solving the equations governing the interaction of electromagnetic waves with the discrete dipoles, accounting for factors like the complex refractive index of the material, the geometric arrangement of the dipoles, and the polarisation and wavelength of the incident light [461–463].

The suitability and accuracy of DDA depend on several underlying conditions and assumptions. Understanding these can help in determining when DDA is an appropriate tool for a given problem. Here are the key underlying conditions [464–467]:

1. **Volume Integral Method:**DDA belongs to the class of volume integral methods, making it suitable for calculating electromagnetic diffraction by objects with complex shapes and permittivity.
2. **Numerical Solution Requirement:**Due to the complexity of electromagnetic scattering problems involving objects with intricate shapes, the DDA method is essential for rigorously solving these scenarios numerically.

3. **Flexibility and Versatility:**DDA is known for its flexibility and versatility, allowing for a wide range of applications and developments over time to handle various electromagnetic diffraction scenarios effectively.

4. **Applicability to Sub-wavelength Particles:**DDA is particularly useful for studying the interaction between light and particles that are sub-wavelength in size, making it a valuable tool for analysing scenarios where traditional analytical solutions are not feasible

Simulations of plasmonic NPs are integral in designing materials for light management in PV cells. Studies focus on how NP size, shape, and material composition influence light trapping and conversion efficiency [468]. Simulating the coupled optical and magnetic responses of magnetoplasmonic NPs is computationally intensive, requiring advanced algorithms and high computational power. Achieving accurate simulations at a scale that is representative of practical applications remains challenging [469–471]. There is a continuous need for developing more efficient and accurate computational models. Correlating simulation results with experimental data is crucial for validating models and enhancing their predictive power [472–477]. This integration is key to advancing the practical application of NP technologies.

2.5 Morphology Tuning and Nanoparticle Integration

The integration of NPs in solar cells, particularly in the context of morphology tuning, has been a subject of significant research. OSCs with morphology control through the tuning of NP sizes have shown promise in achieving efficient photovoltaic performance [478]. The optimisation of the active layer morphology in OSCs remains a major challenge, and the manipulation of thin film morphology from the nano to micron length scales has been explored to enable strong light trapping and high carrier generation [479].

2.5.1 Morphology Control with Solvent Additives and Nanoparticle Integration

The morphology of the photoactive layer in OSCs, composed of donor and acceptor materials, is a critical determinant of their efficiency. Optimal morphology is essential for enhancing exciton dissociation, charge transport, and minimising recombination losses [480–482]. Studies focus on the nano-scale organisation of these materials, aiming to achieve a well-defined interpenetrating network for efficient charge separation. Key methods used for morphology control include solvent additives, annealing processes, and material selection, which significantly impact the crystallinity, domain size, and phase separation of the active layer [483].

The crystallisation process is crucial for achieving efficient charge transport and preventing recombination of charge carriers [484]. Faster crystallisation times promote the formation of well-ordered and interconnected networks, allowing for efficient charge transfer pathways. However, if the crystallisation occurs too quickly, it can hinder the phase separation of donor and acceptor materials, resulting in smaller domain sizes of low interfacial area and thus limiting the exciton dissociation as illustrated in Figure 2.8 [485–487]. On the other hand, larger domain sizes facilitate a higher donor-acceptor

interfacial area, favourable for efficient exciton dissociation and charge generation. However, excessively large domains can hinder charge transport and increase the likelihood of charge recombination [293]. Finding the right balance between crystallisation times and domain size is essential for optimising the PCE of OSCs. By fine-tuning these parameters, both efficient crystallisation for charge transport and optimal domain sizes for effective exciton dissociation can be achieved, ultimately maximising the overall device performance [488].

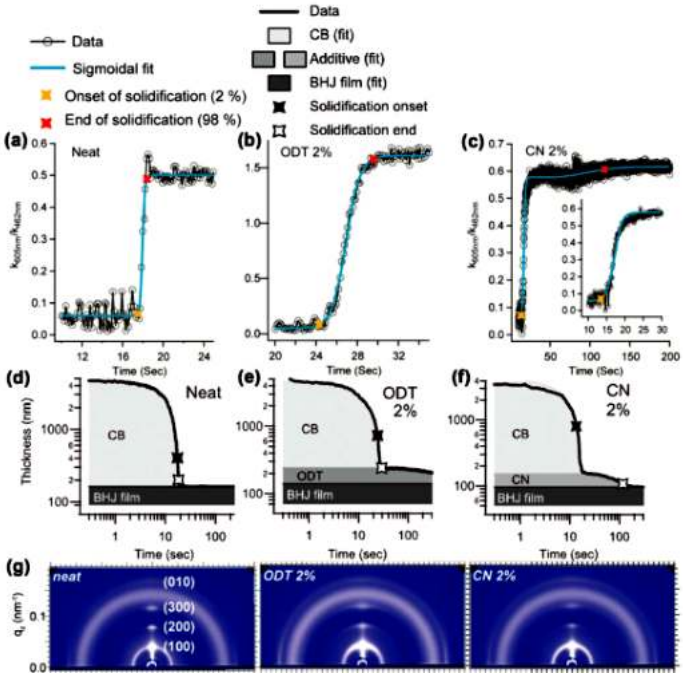


Figure 2.8: Capturing the film formation process of the P3HT/PCBM blend from CB solution: (a,d) without additives, (b,e) with 2% ODT, and (c,f) with 2% CN. Panels (a-c) illustrate the changes in the extinction coefficient (k) from 605 nm to 462 nm, while (d-f) detail the evolution of film thickness. Panel (g) showcases the GIWAXS diffraction patterns for various solid films [489, 490].

Domain size control focuses on manipulating the morphology through processing techniques. This involves invoking thermodynamic parameters such as the Hansen solubility parameters which aid in the selection of solvents or co-solvents to optimise the domain size and morphology. Both approaches are important for optimising OSCs and maximising their power conversion efficiency [491, 492].

The PCE of OSCs is largely determined by the nanoscale morphology of the photoactive layer, which plays a critical role in achieving optimal charge generation, carrier transport, and collection [293, 493, 494]. However, maintaining the thermally activated metastable phase in morphology required for an optimised blend morphology is challenging due to its sensitivity to high-temperature ageing, which can cause a shift toward a thermodynamic equilibrium state, leading to significant phase separation and a decrease in device efficiency [56, 495]. Thermal effects can induce drift from equilibrium to enhanced separation between donor and acceptor domains [55, 57, 59, 496–498].

There are various approaches to overcome the thermal instability of the D/A blends. Some methods include reducing the crystallinity of photovoltaic polymers or fullerenes [496, 499–501], selecting suitable D/A pairs, incorporating a "molecular lock", and cross-linking between D/A components in the active layers [59, 502–505]. However, one of the most effective and straightforward methods is blending host-active layers with additives. Chapter 5 offers a detailed explanation of how using Hansen solubility parameters as a criterion for adjusting morphology sheds light on the solubility, miscibility, and phase separation tendencies of BHJ.

2.5.2 Limitations and Challenges in Fabricating Organic Solar Cells with Fine-tuned Morphology

The optimisation of morphology in OSCs is essential for improving their efficiency, but it comes with several challenges. The challenges in defining the nanoscale morphology of the photoactive layer stem from significant factors such as the choice of spin casting solvent, the polymer-donor composition ratio, the solution's concentration, the materials' chemical structure affecting solubility and miscibility with organic solvents, and the control of crystallisation and phase segregation through the annealing process, which involves specific temperatures and heating rates [70, 506, 507]. Achieving the ideal phase separation between donor and acceptor materials significantly impacts charge transport and recombination processes. However, controlling the nanoscale morphology uniformly across the entire active layer is crucial for consistent device performance, posing a significant challenge [508–510]. The choice of materials also plays a vital role in the final morphology of the active layer, but finding compatible material combinations that lead to the optimal morphology while maintaining good electrical properties is difficult [511]. The morphological control of the photoactive layer using solvent/solid processing additives and post-deposition optimisation is a key focus for addressing these challenges [512].

The inherent variability in material properties adds to the complexity of achieving a reproducible and efficient morphology. Techniques successful in lab-scale experiments often face challenges when scaled up for industrial production, particularly in maintaining uniform morphology across large areas [513–516]. The transition from lab-scale techniques to large-scale production methods introduces additional challenges in morphology control. The sensitivity of OSC performance to slight variations in morphology necessitates stringent control over the fabrication process, which can be difficult to maintain consistently [517, 518].

Research is focused on developing new donor and acceptor materials that inherently form the desired morphology and are more tolerant to variations in processing conditions [330, 519]. Novel materials like non-fullerene acceptors have shown promise in forming stable and efficient morphologies. Optimising processing conditions such as solvent choice, drying temperature, and annealing processes is ongoing, as these parameters significantly impact the kinetics of film formation and, consequently, the morphology [520–522]. The use of solvent additives and processing aids to manipulate morphology is a common strategy, but finding the right combination remains an experimental challenge.

2.5.3 Potential Improvements and Advancements in Magnoplasmonic and Plasmonic Nanoparticle Integration

The integration of magnetoplasmonic and plasmonic NPs into devices, especially within the realms of morphology tuning and NP integration in solar cells holds transformative potential [523].The incorporation of plasmonic NPs into materials has been shown to significantly alter their photonic properties, enhancing light absorption and scattering [524]. Future improvements could focus on precise morphology control at the nanoscale, enabling the design of materials with highly optimised optical properties for specific applications, such as improved light management in solar cells [525]. Magnetoplasmonic NPs offer a unique avenue for dynamic morphology tuning through external magnetic fields. Advances in this area could lead to materials whose optical properties can be modulated in real-time, opening up new possibilities in smart photonic devices and adaptive solar energy harvesting systems [526, 527].

The development of advanced fabrication techniques that allow for the precise placement and orientation of nanoparticles within a host matrix is crucial. Techniques such as directed self-assembly and nano-print lithography could be further refined to achieve more complex and functional NP arrangements [528]. For both plasmonic and magnetoplasmonic NPs, scalable methods of integration into devices remain a challenge. Innovations in NP synthesis, such as greener synthesis methods and scalable chemical vapour deposition (CVD) techniques, could facilitate broader application in industrial-scale photovoltaics [529]. The efficient interfacing of NPs with silicon and other substrates is pivotal for enhancing the performance of PV cells and other semiconductor devices. Advances might include the development of novel linker molecules or surface treatments that improve the electrical and mechanical stability of NP-substrate interfaces [530, 531]. Future advancements could focus on creating hybrid systems that combine plasmonic or magnetoplasmonic NPs with other nanomaterials, such as quantum dots or 2D materials. Such systems could leverage the unique properties of each component to achieve synergistic effects, offering new pathways to ultra-high-efficiency PV cells [532].

Ensuring the long-term compatibility and stability of integrated nanoparticles within devices is essential. Research into corrosion-resistant coatings and more robust NP formulations could address these concerns [533, 534]. As the use of NPs expands, understanding their environmental impact and potential health risks becomes increasingly important. Advances in non-toxic, environmentally benign NPs, and thorough lifecycle assessments will be vital for sustainable deployment [535]. The future of NP integration will benefit from cross-disciplinary research that bridges materials science, electrical engineering, physics, and chemistry.

Chapter 3

3 Theoretical Foundation of Surface Plasmonic and Magnetoplasmonic Resonance Effects

The theoretical foundation of surface plasmonic and magnetoplasmonic resonance effects serves as a fundamental framework for understanding and controlling the optical properties of nanostructures through external mechanisms. This interdisciplinary field explores the interplay between plasmonic and magneto-optical (MO) phenomena, aiming to achieve a balance between SPRs and the MO response. The influence of SPRs on the MO properties of a system, as well as the ability of the magnetic field to modulate these properties, has been a subject of active research [373]. By exploiting the combined properties of hybrid plasmonic and ferromagnetic nanostructures, magnetoplasmonics is anticipated to play a significant technological role in various areas, including integrated optics and PV systems [536–538]. This emerging field utilises nanomaterials to combine the fields of magnetism and plasmonics, thereby creating completely new electromagnetic functionalities.

Conducting computational experiments on magnetoplasmonic nanoparticles is essential for several reasons. First, these simulations allow us to explore and predict the properties of magnetoplasmonic nanoparticles before synthesising them, saving time and resources. Computational models can provide detailed insights into how variations in nanoparticle size, shape, and composition influence their magnetic and plasmonic behaviour. This understanding is crucial for designing magnetoplasmonic nanoparticles with optimised properties for specific applications, such as solar cells.

Magnetoplasmonic nanoparticles have significant potential in enhancing the performance of solar cells. The ability to manipulate light absorption and scattering through the unique combination of magnetic and plasmonic properties can lead to improved photo-conversion efficiency. By tuning the size and shape of magnetoplasmonic nanoparticles, it is possible to maximise their effectiveness in enhancing light absorption in solar cells, thus increasing overall efficiency. This study aims to bridge the gap between theoretical predictions and practical applications by demonstrating how computationally optimised magnetoplasmonic nanoparticles can be used in photovoltaic systems.

3.1 Surface Plasmon Resonances

In order to grasp the characteristics of SPRs in various structures smaller than the wavelength in the visible range, it's essential to first understand how bulk or NPs react spectrally. The behaviour of metals across a broad frequency spectrum can typically be accounted for by the plasma theory. This theory posits that metals consist of a free electron gas that oscillates against a backdrop of stationary positive ions, while neglecting the interactions between electrons. The way this electron gas responds to an external electric field is what defines the optical attributes of metals. When these electrons are excited optically, their coherent oscillation is attenuated by collisions with the ion cores, characterised by a collision frequency (γ):

$$\gamma = \frac{1}{\tau} \tag{3.1}$$

which is roughly 100 THz and τ (10^{-14} s) describes the free time between collisions in the electron gas at ambient temperature. Through the application of the Drude model to metals, one can deduce their complex permittivity as a frequency-dependent function [539]:

$$\varepsilon(\omega) = \left(1 - \frac{\omega_p^2}{\omega^2 + i\gamma\omega}\right) \tag{3.2}$$

ω_p is the plasma frequency of the corresponding bulk metal, which depends primarily on the electron density and the effective mass of the electrons in the metal.

The plasma frequency, ω_p, for a bulk metal can be determined by the following formula:

$$\omega_p = \sqrt{\frac{n_e e^2}{\varepsilon_0 m^*}} \tag{3.3}$$

where:

n_e is the electron density (number of free electrons per unit volume),
e is the elementary charge (1.602×10^{-19} C),
ε_0 is the vacuum permittivity (8.854×10^{-12} F/m), m^* is the effective mass of the electron in the metal.

The effective mass m^* accounts for the fact that the motion of electrons in a solid is influenced by its interaction with the lattice ions and in other words: charge carriers are quasiparticles, which modifies its inertia compared to a free electron in vacuum [540].

The Drude model for metals treats the valence electrons as if they are not bound to atoms, essentially free. Upon the application of an electric field, these electrons accelerate, subsequently experiencing collisions with a specific scattering time. Assuming the medium to be without losses and disregarding the effects of collisions and scattering, the model simplifies the interaction as follows:

$$\varepsilon(\omega) = 1 - \frac{\omega_p^2}{\omega^2} \tag{3.4}$$

As a result, when the frequency falls below ω_p, the permittivity assumes a negative value and $\varepsilon(\omega)$ is expressed in terms of real quantities only, and there's no imaginary unit i involved in the expression provided.

When a metal characterised by negative permittivity interfaces with another material possessing positive permittivity, an electromagnetic (EM) wave is confined at their interface shown in Figure 3.1 in accordance with the Maxwell's equations in the frequency domain shown below:

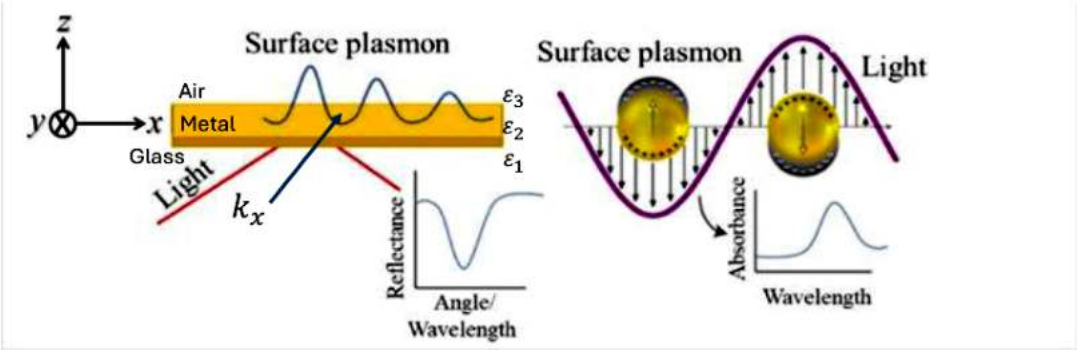


Figure 3.1: Schematic diagrams depicting localised (a) and travelling (b) surface plasmons arising from various noble metal NPs [541].

$$\nabla \times \mathbf{H} = -i\omega\mathbf{D} \tag{3.5}$$

This corresponds to a modified form of Faraday's law of induction, indicating that a time-varying magnetic field ($\mathbf{H}$) induces an electric displacement field ($\mathbf{D}$). The term $i\omega$ indicates the operation's dependence on the frequency of the time variation.

$$\nabla \times \mathbf{E} = i\omega\mathbf{B} \tag{3.6}$$

This is a form of Maxwell's addition to Ampère's law, showing how a time-varying electric field ($\mathbf{E}$) generates a magnetic field ($\mathbf{B}$). Again, $i\omega$ signifies the effect's dependence on the frequency.

$$\nabla \cdot \mathbf{H} = 0 \tag{3.7}$$

This equation states that the magnetic field ($\mathbf{H}$) has no divergence, meaning there are no "magnetic charges" or monopoles, consistent with Gauss's law for magnetism in the frequency domain.

$$\nabla \cdot \mathbf{E} = 0 \tag{3.8}$$

This suggests that the electric field ($\mathbf{E}$) in the scenario described has no divergence. This might be a simplification or a specific case where electric charges are not present or are evenly distributed, leading to no net electric flux density ($\mathbf{D}$) divergence in a region

of interest. However, in a more general context, this might not hold if electric charges are present; instead, you would have the following equation:

$$\nabla \cdot \mathbf{D} = \rho \tag{3.9}$$

ρ is the charge density.

In these equations, ($\mathbf{D}$) is the electric displacement field, which relates to the electric field ($\mathbf{E}$) as:

$$\mathbf{D} = \epsilon \mathbf{E} \tag{3.10}$$

ϵ is is the permittivity of the medium. Similarly, $\mathbf{B}$ is the magnetic flux density, related to $\mathbf{H}$ by:

$$\mathbf{B} = \mu \mathbf{H} \tag{3.11}$$

μ is the permeability of the medium.

The relevant transverse magnetic (TM) equations are expressed as follows:

$$-\frac{\partial H_y}{\partial x} = -i\omega\varepsilon_0\varepsilon E_z \tag{3.12}$$

H_y represents the transverse magnetic field component.
E_z represents the longitudinal electric field component.
ω is the angular frequency.
ε is the permittivity of the medium.

The boundary and continuity conditions that lead to equation (3.12) involve the tangential component of the electric field being equal to zero and the normal derivative of the tangential component of the magnetic field being equal to zero at the interface between different media. These conditions ensure the proper behaviour of electromagnetic fields at boundaries and interfaces.

$$-\frac{\partial H_y}{\partial z} = -i\omega\varepsilon_0\varepsilon E_x \tag{3.13}$$

E_z represents the electric field component in the x-direction.

$$\frac{\partial E_x}{\partial z} - \frac{\partial E_z}{\partial x} = i\omega\mu_0 H_y \tag{3.14}$$

Here, E_x and E_z are the components of the electric field in the x and z directions, respectively, H_y is the component of the magnetic field in the y direction μ_0 is the permeability of free space. This form of the equation is part of Maxwell's curl equations, which relate the curl of the electric field to the rate of change of the magnetic field, and vice versa.

The relative magnetic permeability is equal to 1 for non-magnetic materials at frequencies relevant to optics and radio wave propagation.

The associated TM wave equation is given by:

$$\frac{\partial^2 H_y}{\partial z^2} + (k_0^2 \varepsilon - k_x^2) H_y = 0 \tag{3.15}$$

k_0 is the free space wave number, also known as the propagation constant in vacuum. k_x is the wave number associated with the propagation of the wave in the x-direction, or it can be thought of as the component of the wave vector in the x-direction.

Hence, the expressions for the electric and magnetic components outside ($z > 0$) and within ($z < 0$) the metal surface are as follows:

$$E_x = -\frac{AC_1}{i\omega\varepsilon_0\varepsilon} e^{-C_1 z} e^{ik_x x} \tag{3.16}$$

$(z > 0)$ where; $C_1 = \sqrt{k_x^2 - k_0^2 \varepsilon_1}$

$$E_z = -\frac{Ak_x}{i\omega\varepsilon_0\varepsilon} e^{-C_1 z} e^{ik_x x} \tag{3.17}$$

$$H_y = A e^{-C_1 z} e^{ik_x x} \tag{3.18}$$

together with;

$$E_x = \frac{BC_2}{i\omega\varepsilon_0\varepsilon} e^{-C_2 z} e^{ik_x x} \tag{3.19}$$

$(z < 0)$ where; $C_2 = \sqrt{k_x^2 - k_0^2 \varepsilon_2}$

$$E_z = -\frac{Bk_x}{i\omega\varepsilon_0\varepsilon} e^{-C_2 z} e^{ik_x x} \tag{3.20}$$

$$H_y = B e^{-C_2 z} e^{ik_x x} \tag{3.21}$$

A and B are constants that need to be determined by applying the boundary conditions at the interface of the metal surface. Given the subsequent continuity condition at the

interface for the electric field component parallel to the interface:

$$E_{\parallel}^{1} = E_{\parallel}^{2} \tag{3.22}$$

$$D_{\perp}^{1} = D_{\perp}^{2} \tag{3.23}$$

This leads to the following:

$$A = B$$

$\therefore$

$$\frac{AC_1}{\varepsilon_1} + \frac{AC_2}{\varepsilon_2} = 0 \tag{3.24}$$

Taking into account the formulas for C_1 and C_2 as stated previously, the equations for the dispersion relation are as follows:

$$\frac{k_x^2 c^2}{\omega_p^2} = \frac{\frac{\omega^2}{\omega_p^2}\left(\frac{\omega^2}{\omega_p^2} - 1\right)}{\frac{2\omega^2}{\omega_p^2} - 1} \tag{3.25}$$

with,

$$\varepsilon_2 = 1 - \frac{\omega_p^2}{\omega^2} \tag{3.26}$$

and,

$$k_x^2 = \frac{\omega^2}{c^2}\left(\frac{\varepsilon_1 \varepsilon_2}{\varepsilon_1 + \varepsilon_2}\right) \tag{3.27}$$

As a result, the complex permittivity, which varies with frequency, is expressed as follows:

$$\varepsilon(\omega) = 1 - \frac{\omega_p^2}{\omega^2} \tag{3.28}$$

Furthermore, the complex wave vector:

$$k_x = k_x' + ik_x'' \tag{3.29}$$

which represents the direction of propagation can be derived from the preceding equations as follows:

$$k'_x = \frac{\omega}{c}\left[\frac{\varepsilon'_1\varepsilon_2}{\varepsilon'_1+\varepsilon_2}\right]^{\frac{1}{2}} \tag{3.30}$$

and,

$$k''_x = \frac{\omega}{c}\left(\frac{\varepsilon''_1}{2(\varepsilon'_1)^2}\right)\left[\frac{\varepsilon'_1\varepsilon_2}{\varepsilon'_1+\varepsilon_2}\right]^{\frac{1}{2}} \tag{3.31}$$

The complex permittivity is expressed as follows:

$$\varepsilon_1 = \varepsilon'_1 + i\varepsilon''_1 \tag{3.32}$$

ε'_1 is the real part, representing the dielectric constant of the medium, which affects the phase velocity of the wave.
ε''_1 is the imaginary part, representing the loss factor, which accounts for the energy lost due to the medium's absorption and leads to the attenuation of the wave as it propagates.

The complex wave vector is succinctly expressed as follows:

$$k_x = \frac{\omega}{c}\left[\frac{\varepsilon_m\varepsilon_d}{\varepsilon_m+\varepsilon_d}\right]^{\frac{1}{2}} \tag{3.33}$$

where ε_m and ε_d are the permittivities of metal and dielectric media, respectively. The direct generation of plasmon excitations from free space using a beam is not feasible due to a discrepancy in momentum [542]. As depicted in Figure 3.2, the dispersion curve comes close to the light line at smaller complex wave vector (k_x), explaining why the induced non-radiative plasmon resonances do not convert into light. At larger complex wave vector (k_x) and $\varepsilon'_1 \longrightarrow -\varepsilon_2$, the situation is as follows:

$$\omega_{SPR} = \sqrt{\frac{\omega_p}{1+\varepsilon_2}} \tag{3.34}$$

Within this domain, both the group and phase velocities markedly diminish, nearing zero. As a result, SPR appears as a localised oscillation of the electron plasma [543]. At a wavelength of 500 nm, the dielectric constant for Ag was ε_1 of -18 and an ε_2 of 0.55. For Au, it was ε_1 of -9.03 and ε_2 of 1.35.

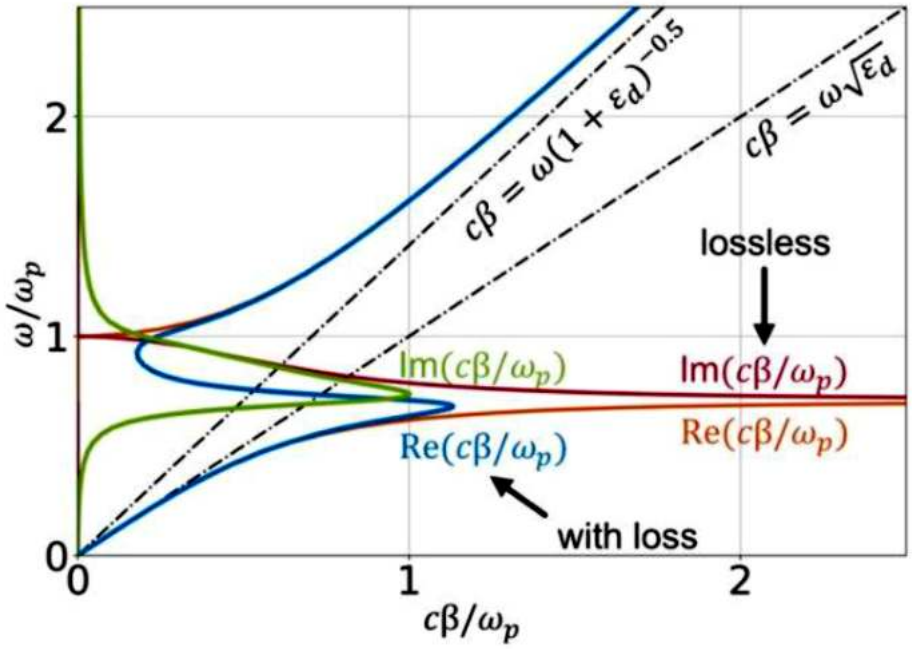


Figure 3.2: Layout of the dispersion relation diagram for non-radiative plasmons. The dispersion relation is plotted against the real component and the imaginary component of the wave vector [544].

3.2 Magnetoplasmonics

Magnetoplasmonics is a field of study that focuses on the interconnection of magnetic and plasmonic properties, either within the same material or through a combination of pure plasmonic and pure magnetic systems [545]. The use of nanostructured quasi free-electron metals, such as Au and Ag, as plasmonic materials is well-established. However, their weak magneto-optical response limits their efficiency in light manipulation. On the other hand, pure ferromagnetic nanostructures are poor plasmonic candidates. To overcome these limitations, the combined properties of hybrid plasmonic and ferromagnetic nanostructures are being explored in the field of magnetoplasmonics, which is expected to have significant technological applications [526, 546]

3.2.1 Magneto-Optical Effects

The interaction between light and matter is influenced by the magnetic state of the medium and depends on the electronic structure of the material. This interaction gives rise to phenomena known as magneto-optic effects, which occur when electromagnetic radiation interacts with magnetically polarised materials [547, 548]. The interaction of a material with incoming electromagnetic fields is characterised by its optical and magneto-optical traits, which are influenced by its composition, structure, and the symmetry of its components. Typically, these properties are quantified by examining how reflectance, absorbance, and polarisation rotation depend on frequency. The dielectric function stands out as a crucial characteristic that delineates the electronic and optical behaviour of the material. Furthermore, it facilitates the comparison of how different materials react upon encountering photons, electrons, and their associated fields [549].

When light strikes a magnetic material, the way it's polarised, meaning the direction and phase of its waves changes. This alteration can be described mathematically using the dielectric function. Specifically, the off-diagonal components of this function are what changes. To understand how and why this happens, we turn to Maxwell's equations, which are a set of equations that govern how electromagnetic fields behave. When we write these equations in Gaussian units, we can precisely describe how the polarisation of light is modified upon interacting with a magnetic material. This mathematical framework allows us to predict and understand the complex ways light and magnetic materials interact. This can be expressed as [550–553]:

$$\nabla \cdot \mathbf{D} = 4\pi\rho^{total} \tag{3.35}$$

$$\nabla \times \mathbf{E} = -\frac{1}{c}\frac{\partial \mathbf{B}}{\partial t} \tag{3.36}$$

$$\nabla \cdot \mathbf{B} = 0 \tag{3.37}$$

$$\nabla \times \mathbf{H} = \frac{4\pi}{c}\mathbf{J}^{total} + \frac{1}{c}\frac{\partial \mathbf{D}}{\partial t} \tag{3.38}$$

In this context, E and B represent the electric and magnetic fields, respectively, while ρ^{total} and $\mathbf{J}^{total}$ denote the total charge density and total current density, respectively. These fields are considered on a macroscopic level. Moreover, the total charge density is described as the sum of the contributions due to free and bound electrons in the form:

$$\rho^{total} = \rho^{free} + \rho^{bound} = \rho^{ext} + \rho^{bound} \tag{3.39}$$

whereas the total current density is defined as the sum of free and bound current densities:

$$\mathbf{J}^{total} = \mathbf{J}^{free} + \mathbf{J}^{bound} = \mathbf{J}^{cond} + \mathbf{J}^{ext} + \mathbf{J}^{bound} \tag{3.40}$$

By incorporating the characteristics of the medium, such as polarization (P) - the electric dipole moment per unit volume, and magnetisation (M) - the magnetic dipole moment per unit volume, we obtain:

$$\rho^{bound} = \rho^{pol} = -\nabla \cdot \mathbf{P} \tag{3.41}$$

and;

$$\mathbf{J}^{bound} = \mathbf{J}^{pol} + \mathbf{J}^{Mag} = \frac{\partial \mathbf{P}}{\partial t} + c\nabla \times \mathbf{M} \tag{3.42}$$

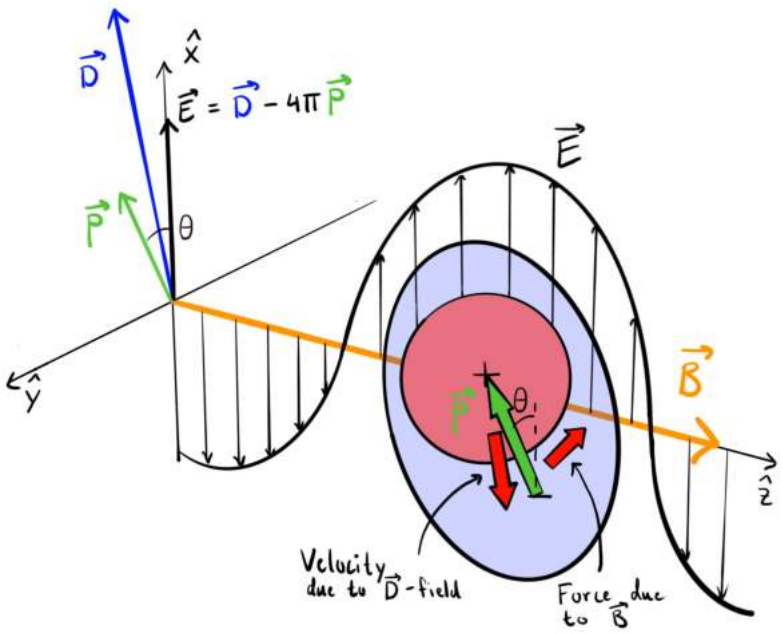


Figure 3.3: A traditional representation of the process by which a magnetic field induces rotation in the polarisation and, consequently, alters the electric field within a material [551].

The magnetisation affecting the polarisation by rotation is illustrated classically in Figure 3.3 and can be described in terms of the electric displacement D by Maxwell's law:

$$D = \varepsilon E \tag{3.43}$$

where ε is the electric permittivity of the material and E is the applied electric field. The parameter ε is frequency dependent and, in general, complex. In Figure 3.3 , the external D-field prompts the electron density to shift in the reverse direction, influenced by the B-field and the resulting Lorentz force:

$$\mathbf{F} = q(\mathbf{v} \times \mathbf{B}) \tag{3.44}$$

Consequently, the electron density begins to migrate in a direction perpendicular to the D-field. This movement is represented by vectors in the x-y plane, clearly illustrating how the external D-field is transformed into the E-field by the material.
In a three-dimensional material that is neither magnetic nor optically active, the electric permittivity is represented by the tensor with only the diagonal elements as shown below:

$$\varepsilon_\omega = \begin{pmatrix} \varepsilon_{xx} & 0 & 0 \\ 0 & \varepsilon_{yy} & 0 \\ 0 & 0 & \varepsilon_{zz} \end{pmatrix} \tag{3.45}$$

For isotropic materials, the permittivity components:

$$\varepsilon_{xx} = \varepsilon_{yy} = \varepsilon_{zz}$$

whereas, in anisotropic materials, the ε components vary along different symmetry axes. When subjected to a magnetic field, the permittivity tensor of magnetic materials transforms into a non-diagonal matrix:

$$\varepsilon_{\omega} = \begin{pmatrix} \varepsilon_{xx} & a\Pi_z & a\Pi_y \\ -a\Pi_z & \varepsilon_{yy} & -a\Pi_x \\ -a\Pi_y & a\Pi_x & \varepsilon_{zz} \end{pmatrix} \tag{3.46}$$

where:

$$a\Pi_i = \varepsilon_{MO}$$

denotes the magneto-optical constant of the material, and Π_i represents the components of the applied magnetic field (for paramagnetic and diamagnetic materials) or the material's magnetisation (for ferromagnetic materials) [545]. It's also noted that the effect of the external magnetic field is contingent upon its orientation relative to the material. Specifically, the non-diagonal elements come into play when the medium is magnetised in a direction perpendicular to the plane in which these elements are defined [554, 555].

3.2.2 The Oscillatory Electron According to the Lorentz Model

The combination of the refractive index and the attenuation coefficient creates what is known as the complex refractive index, which can be obtained from various microscopic models, usually employing a linear response theory. For the purpose of deriving the optical response and demonstrating the application of a microscopic model to ascertain the complex refractive index, a Lorentz oscillator model will be employed. This approach includes incorporating a magnetic field oriented along the z-axis [556]. Additionally, the derivation will highlight how the introduction of magnetism contributes off-diagonal elements to the dielectric function.

In this basic model, the electron is considered a classical entity, tethered to the immobile nuclei by a restoring force:

$$\mathbf{F}_{res} = -m\omega_0^2\mathbf{r} \tag{3.47}$$

The electron is subjected to a damping force:

$$\mathbf{F}_{damp} = -m\gamma\frac{\partial\mathbf{r}}{\partial t} \tag{3.48}$$

which varies with velocity, as increased speeds result in a higher frequency of collisions. Consequently, the equation of motion is expressed as:

$$m\frac{\partial^2 \mathbf{r}}{\partial t^2} + m\gamma\frac{\partial \mathbf{r}}{\partial t} + m\omega_0^2\mathbf{r} + e\left(\mathbf{E}(t) + \frac{\partial \mathbf{r}}{\partial t} \times \mathbf{B}\right) = 0 \tag{3.49}$$

In this context, γ represents the damping factor, ω_0 the system's resonance frequency, m the effective mass of the electron, or electron rest mass and $e\mathbf{E}(t)$ the driving force exerted by the electric field E(t). The final term accounts for the Lorentz force in the presence of a steady magnetic field.

By assuming plane waves and doing a simple Ansatz for $\mathbf{r}$:

$$\mathbf{E} = \mathbf{E}_0 e^{-i\omega t} \tag{3.50}$$

$$\mathbf{r} = \mathbf{r}_0 e^{-i\omega t} \tag{3.51}$$

$$\mathbf{B} = (0, 0, B) \tag{3.52}$$

provides:

$$m(\omega_0^2 - \omega^2 - i\omega\gamma)r_{0x} + iq\omega B r_y = qE_{0x} \tag{3.53}$$

$$m(\omega_0^2 - \omega^2 - i\omega\gamma)r_{0y} - iq\omega B r_y = qE_{0y} \tag{3.54}$$

$$m(\omega_0^2 - \omega^2 - i\omega\gamma)r_{0z} = qE_{0z} \tag{3.55}$$

equations 3.53 - 3.55 can be resolved with:

$$\mathbf{r} = \alpha(\omega)\mathbf{E} \tag{3.56}$$

For a system of charged particles of charge -e and displaced relative to their equilibrium position by r is defined as:

$$\mathbf{p} = -e\mathbf{r} \tag{3.57}$$

Taking into account the atomic density N and combining equations (3.56) and (3.57) leads to the macroscopic polarisation of the form:

$$\mathbf{P} = N\mathbf{p} = -Ne\alpha\mathbf{E} = \varepsilon_0\chi\mathbf{E} \tag{3.58}$$

χ being the susceptibility of the medium due to the application of the **E** and **B** fields. The tensor suggests an anisotropic medium with distinct susceptibilities in different directions. The off-diagonal terms (χ_{xy} and $-\chi_{xy}$) imply that the polarisation in the x-direction affects the y-direction and vice versa, which is characteristic of certain anisotropic or non-linear materials.

$$\chi = \begin{pmatrix} \chi_{xx} & \chi_{xy} & 0 \\ -\chi_{xy} & \chi_{xx} & 0 \\ 0 & 0 & \chi_{zz} \end{pmatrix} \tag{3.59}$$

as well as:

$$\chi_{xx} = -\left(\frac{Ne^2}{m\varepsilon_0}\right)\left(\frac{\omega^2 + i\gamma\omega - \omega_0^2}{(\omega^2 + i\gamma\omega - \omega_0^2)^2 - \omega_c^2\omega^2}\right) \tag{3.60}$$

$$\chi_{zz} = -\left(\frac{Ne^2}{m\varepsilon_0}\right)\left(\frac{i\omega_c\omega_c}{(\omega^2 + i\gamma\omega - \omega_0^2)^2 - \omega_c^2\omega^2}\right) \tag{3.61}$$

$$\chi_{xy} = -\left(\frac{Ne^2}{m\varepsilon_0}\right)\left(\frac{1}{\omega^2 + i\gamma\omega - \omega_0^2}\right) \tag{3.62}$$

In this instance,

$$\omega_c = \frac{eB}{m}$$

signifies the cyclotron frequency. The off-diagonal components χ_{xy} are characteristic of a magnetic medium and vanish in the absence of a magnetic field. When B is minimal and only first-order terms in B are considered, it follows that:

$$\chi_{xx} = \chi_{zz}$$

making χ_{xy} proportional to B.

By applying equation (3.58) and referencing the definition of the D-field, the linear response is thus determined as:

$$\mathbf{D} = \varepsilon_0 \mathbf{E} + \mathbf{P} = \varepsilon_0(1 + \chi)\mathbf{E} = \varepsilon \mathbf{E} \tag{3.63}$$

In Gaussian units, it is expressed as:

$$\mathbf{D} = \mathbf{E} + 4\pi \mathbf{P} = (1 + 4\pi\chi\varepsilon_0)\mathbf{E} = \varepsilon \mathbf{P} \tag{3.64}$$

with the final expression for the dielectric function being:

$$\varepsilon_{ij} = \delta_{ij} + 4\pi\varepsilon_0 \chi ij \tag{3.65}$$

The relationship between the refractive index and the dielectric function is given by:

$$\varepsilon = n^2$$

The assumption here is that resonance occurs at frequencies near the natural frequency, leading to the refractive index's dependency on frequency, which accounts for the phenomenon of refraction.

3.3 Simulation Technique for Magnetoplasmonic NPs

Micromagnetic simulations involve working with significantly larger length scales by employing a continuum approximation. These simulations assume that the systems are sufficiently large to disregard atomic ordering, yet small enough to resolve domains [557]. The system is partitioned into micromagnetic cells or volume elements, with the assumption of uniform magnetisation, thereby approximating it as a single moment. Subsequently, the energies associated with exchange, anisotropy, magnetostatics, and Zeeman effects can be computed based on the orientation of magnetisation within each volume element [558]. Simulations can be conducted to determine the static equilibrium of a system by solving the spatial distribution of the magnetisation (M). Alternatively, the dynamic equilibrium can be explored by applying the Landau-Lifshitz-Gilbert (LLG) equation:

$$\frac{\partial \mathbf{S}_i}{\partial t} = \frac{-\upsilon}{(1 + \beta^2)} \left[\mathbf{S}_i \times \mathbf{H}_{eff} + \beta \mathbf{S}_i \times (\mathbf{S}_i \times \mathbf{H}_{eff}) \right] \tag{3.66}$$

where:

$\mathbf{S}_i$ is a unit vector representing the direction of the magnetic spin moment on site i.

υ is the gyromagnetic ratio.

β is the Gilbert damping constant.

$\mathbf{H}_{eff}$ represents the effective field that influences the spin moment and its relaxation, resulting from the direct transfer of angular momentum between the spin and a heat bath, thereby aligning the spin along the field direction.

Micromagnetic simulations are well-suited for investigating macroscopic systems characterised by a low surface-to-volume ratio, where the intricate analysis of microstructure or surface effects plays a lesser role in influencing the overall magnetic behaviour of the system.

Atomistic spin simulations serve as a link between micromagnetic and ab initio methods. In these simulations, atoms are considered to have a local magnetic moment, and the electron theory is integrated with the equation of motion of atomistic spins. This approach effectively integrates the behaviour of individual atoms into the larger magnetic framework, providing a valuable middle ground between micromagnetic and ab initio techniques [559, 560].

As outlined in section 3.2.2, the origin of magnetism lies in the electrons possessing discrete energy levels, highlighting the inherently quantum mechanical nature of magnetic systems. Moreover, the characteristics of these materials are significantly impacted by thermal influences. To accurately simulate magnetic materials, it is imperative to integrate quantum mechanical aspects with thermodynamic principles. The system's energetics are dictated by quantum mechanics, while its temporal progression and thermal behaviours are approached through classical means. Given that atoms are treated as dynamic entities, modelling complex magnetic phenomena like antiferromagnetic coupling, which poses challenges for micromagnetic modelling, is seamless. The parameters for atomistic simulations can either be derived from fundamental principles or adapted from the macroscopic properties of materials [561].

The open-source atomistic spin simulation software package VAMPIRE, currently undergoing active development, was employed to create particles with specific geometric forms, including spheres, cubes, and various other polygonal shapes. Control over the simulations is achieved via a straightforward text file system, necessitating only a material file and an input file to execute numerous magnetic simulations. These test simulations are instrumental in identifying the code's limitations and determining the optimal utilisation of computational resources.

In VAMPIRE, a crystalline network of sufficient size to accommodate the simulated shape is established. The exchange interaction of the unit cell is pre-determined. Subsequently, the unit cell is duplicated until its dimensions align with the initial step, after which atoms are selectively extracted from the crystalline structure until the desired geometric shape is achieved. The atoms within this modified crystalline framework are then allocated to one or more materials. This process also facilitates the creation of core-shell structures, although the feasibility of such structures depends on the specific core, shell, and interfacial exchange interactions.

The VAMPIRE program was utilised for the computation, incorporating a diverse range of simulation methods to facilitate the study of spin dynamics and equilibrium properties. In this study, a Heisenberg-type spin Hamiltonian and Monte Carlo (MC) integrator were employed. Within the MC simulations, involving 10,000 equilibrium steps. Following this, the system underwent 10,000 averaging steps before being incrementally heated in 10 K intervals until the complete M(T) curve was derived. New states were generated from old states by randomly selecting a single spin and updating it to a new trial position.

Subsequently, a transition probability, contingent on the energy difference between the initial and final state, was utilised to accept or reject the new state. The newly obtained state then became the new initial state, and this process continued. The Hinzke-Nowak combinational algorithm, known for its efficient sampling of all available phase space while maintaining a reasonable trial move acceptance rate, was adopted as one of the most effective Monte Carlo algorithms for classical spin models [562]. Consequently, M-T plots were obtained for each system under investigation. To assess the finite-size effects on curie temperature T_c, the equilibrium magnetisation for various sizes of spherical, cubic and other polygons NPs was computed as a function of temperature, M(T). The Heisenberg-type spin Hamiltonian employed in this study is represented by the following form [563, 564]:

$$H = -\sum_{i \neq j} J_{ij} S_i \cdot S_j - \sum k_u S_{i,z}^2 \tag{3.67}$$

The first term in the expression represents the exchange interaction, while the second term denotes the uniaxial anisotropy. The coefficient J_{ij} denotes the exchange coupling constant between the spins i and j. This constant is negative for antiferromagnetic materials, causing the moments at sites i and j to align anti-parallel, and positive for ferromagnetic materials, resulting in the alignment of moments at sites i and j in a parallel manner. The symbols S_i and S_j represent the local spin moment at site i and j, respectively, aiming to minimise the energy in each scenario. Additionally, k_u stands for the uniaxial anisotropy constant, which induces spins to align along the easy axis, representing the direction of minimum energy. The term S_{iz} indicates that the easy axis is directed parallel to the z direction. The magnetic material parameters for Fe, Ni and Fe_3O_4 in Table 3.1 [561].

Table 3.1: Table of constants used in the material file

Atom	μ_B	k_u	J_{ij}
		$J/atom$	$J/link$
Fe	2.22	5.65×10^{-25}	7.050×10^{-21}
Ni	0.606	5.47×10^{-26}	2.757×10^{-21}
O	1.0	-1.54×10^{-24}	0

The exchange integral (J) is established according to mean field theory as:

$$J = \frac{3k_B T_c}{\xi z} \tag{3.68}$$

In the given context, k_B represents the Boltzmann constant, z denotes the number of nearest neighbours, ξ is a correction factor derived from the mean-field expression and T_c is the Curie temperture.

When considering magnetic core-shell NPs, the Hamiltonian employed is expressed as:

$$H_{ex} = H_{FM1} + H_{AFM} + H_{FM2} \tag{3.69}$$

$$H_{ex} = \sum_{i \neq j} J_{FM1} S_i \cdot S_j + \sum_{i,\nu} J_{AFM} S_i \cdot S_\nu + \sum_{\nu,i} J_{AFM} S_\nu \cdot S_i$$

$$+ \sum_{i \neq j} J_{FM2} S_i \cdot S_j + \sum_i k_u S_{i,z}^2 \tag{3.70}$$

S represents the spin unit vector, with the first term pertaining to the core material, the last term to the shell material, and the second and third terms representing the interfacial exchange energies, which are assumed to have the same value in the VAMPIRE software [565, 566]. This implies that Equation 3.66 exclusively describes the exchange coupling between the two ferromagnetic (FM) structures, with other interactions such as dipole-dipole, anisotropy, and Zeeman energies being considered negligible in the total magnetic energy. The dipolar interaction was disregarded under the assumption that the nanoparticles (NPs) are non-interacting, while magnetic anisotropy was omitted due to the temperature-dependent magnetic properties of the nano-hybrid core-shell system being primarily linked to the strong relationship between T_c and J as defined by Equation 3.64. The Zeeman contribution was neglected as it has not yet been incorporated into the VAMPIRE software using the MC approach. The model also takes into account interfacial exchange and direct exchange in the FM core and shell. Furthermore, the model assumes that the NPs are monodisperse, and it is expected that the impact of magnetic interactions will be insignificant [567].

To ascertain T_c, three approximations were utilised:

(i) Curie-Bloch Equation:

$$m(T) = \left(1 - \frac{T}{T_c}\right)^{\iota} \tag{3.71}$$

(ii) Kuzmin relation Equation:

$$m(T) = \left[1 - b\tau^{\frac{3}{2}} - (1-b)(\tau)^c\right]^{\iota} \tag{3.72}$$

(iii) Derivative criteria followed by polynomial fitting the temperature-dependent magnetisation data.

In the context an ideal FM, it is proposed that ι, a universal exponent, typically around 0.34, while:

$$\tau = \frac{T}{T_c}$$

b is set to 1, and c is assigned a value of 3/2 for a pure Bloch FM [565].

3.4 Simulations Results for Magnetoplasmonic NPs

The Curie temperature is a crucial physical characteristic that indicates the temperature at which magnetic materials lose their permanent magnetism. The manipulation and comprehension of this temperature in NPs have the potential to drive significant progress in solar energy conversion technologies. For magnetic NPs intended for use in solar cells, understanding their Curie temperature is essential to ensure the preservation of their magnetic functionality within the solar cell operational temperature range. This understanding is instrumental in predicting and optimising the magnetic properties of the nanoparticles under operating conditions. The integration of magnetic NPs with silicon solar cells offers the opportunity to improve the efficiency of photovoltaic devices [568–571]. Furthermore, the Curie temperature of NPs is influenced by their size and shape, and this understanding is pivotal for customising the magnetic properties of the NPs to meet the specific requirements of silicon solar cell applications [572].

3.4.1 Ni, Fe and Fe_3O_4 Bare NPs

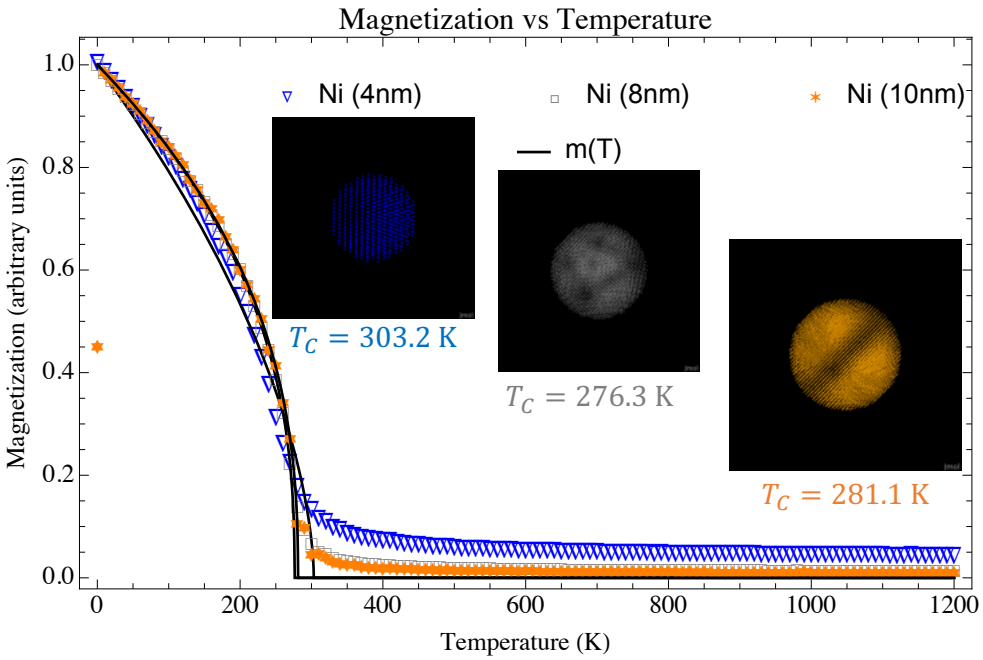


Figure 3.4: Simulation of the mean temperature-dependent magnetisation for Ni NPs in a size range of 4 nm to 10 nm.

Understanding the variation in magnetic properties across different materials such as Fe, Ni and Fe_3O_4 within identical NP size ranges holds significant importance. Analysis of

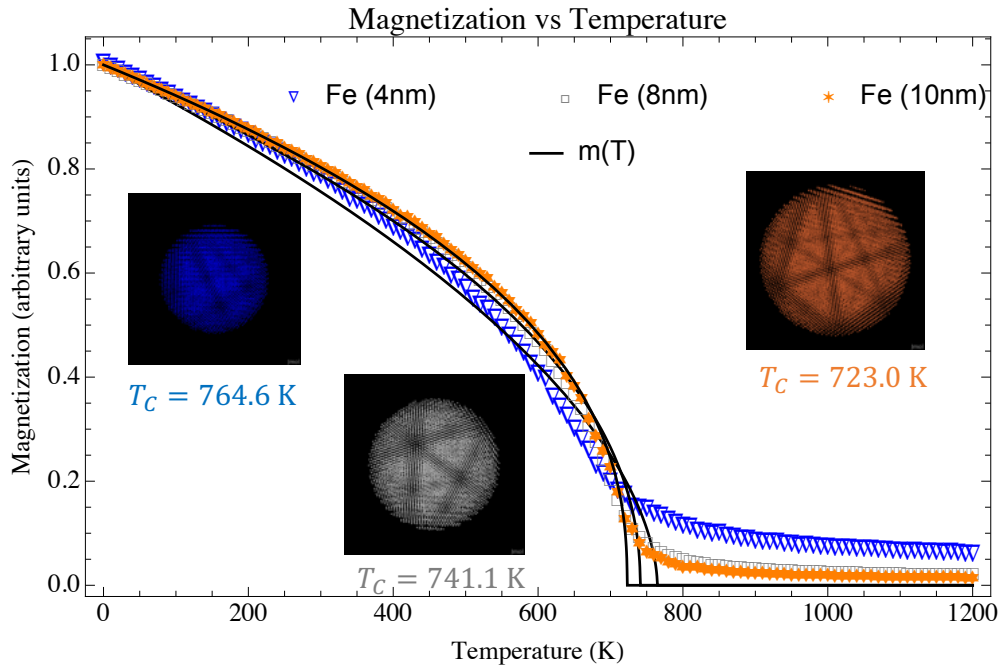


Figure 3.5: Simulation of the mean temperature-dependent magnetisation for Fe NPs in a size range of 4 nm to 10 nm.

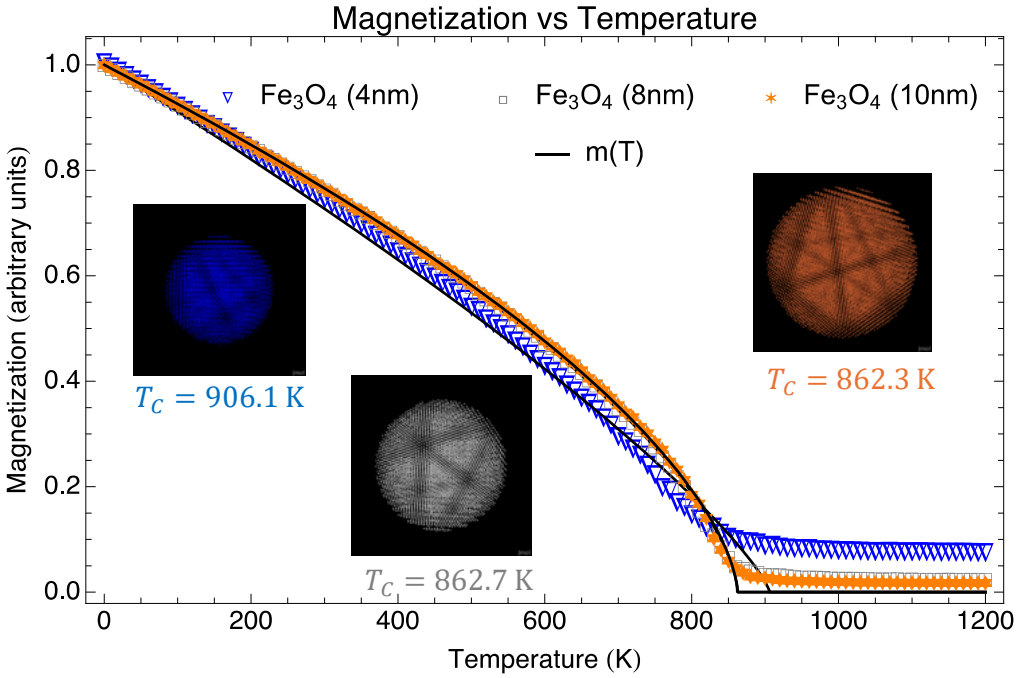


Figure 3.6: Simulation of the mean temperature-dependent magnetisation for Fe_3O_4 NPs in a size range of 4 nm to 10 nm.

Figures 3.4 through 3.6 demonstrates that Fe nanoparticles manifest the highest T_c in comparison to Ni NPs. This finding suggests the intrinsic magnetic strengths of these materials at nanoscale dimensions.

Notably, within these figures, it's observed that the magnetisation for the smallest NP

size examined (4nm) does not reduce to zero. This observation implies a sufficiently strong exchange interaction, capable of maintaining short-range spin magnetic moment correlations at temperatures surpassing the magnetic-ordering threshold [573, 574]. Moreover, a trend is discernible across these figures wherein a decrease in NP size leads to a broadening of the magnetic behaviour at the transition point, diminishing the criticality typically observed.

A further distinction can be seen in the behaviour of Ni NPs, where an increase in size results in a noticeable decrease in the magnetic ordering temperature, as exemplified by the 8 nm (446 K) and 10 nm (442 K) Ni NPs. This phenomenon can be attributed to the increased surface area of larger nanoparticles, which diminishes exchange coupling due to a higher proportion of atoms without adjacent neighbours, thereby lowering the magnetic-ordering temperature [574, 575].

In exploring the magnetic properties of NPs, a key focus is their T_c. Remarkably, the 4 nm Fe_3O_4 NP is identified to possess the highest T_c value of 906.1 K among the NPs simulated. This observation underscores the importance of examining significant properties like T_c to grasp the complex magnetic behaviours of NPs, particularly in understanding how these properties are influenced by NP size and material composition.

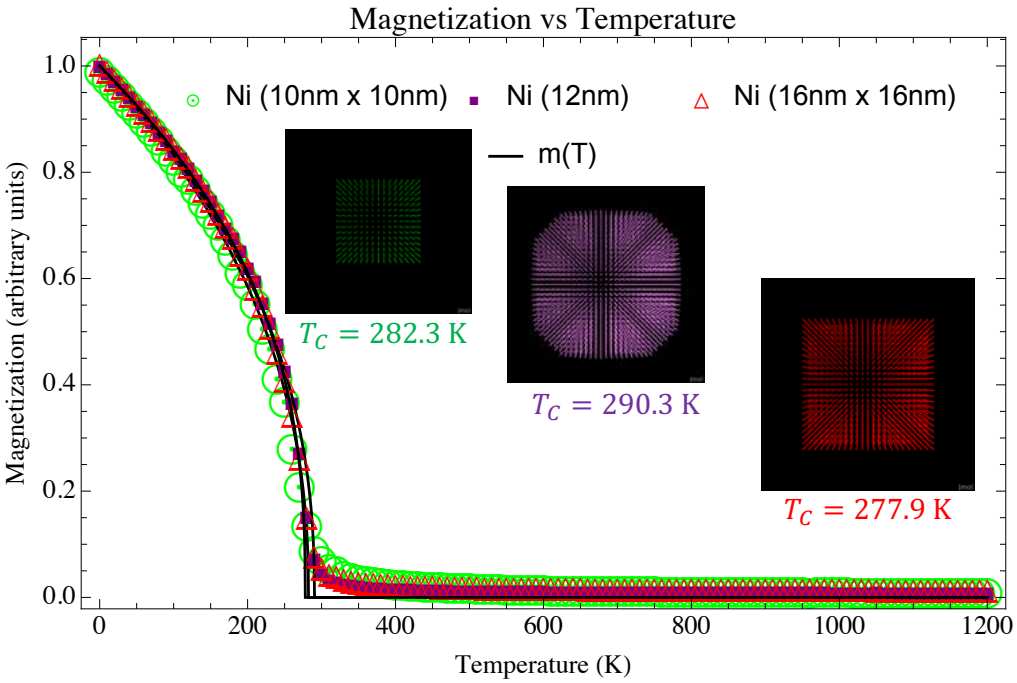


Figure 3.7: Simulation of the mean temperature-dependent magnetisation for complex shapes of bare Ni NPs in a size range of 10 nm to 16 nm.

3.4.2 Pure Magnetic Core-Shell NPs

Pure Magnetic core-shell NPs offer a unique platform for exploring magnetic phenomena at the nanoscale due to their distinct core and shell materials, which can be tailored to exhibit specific magnetic properties. The simulations of such NPs,

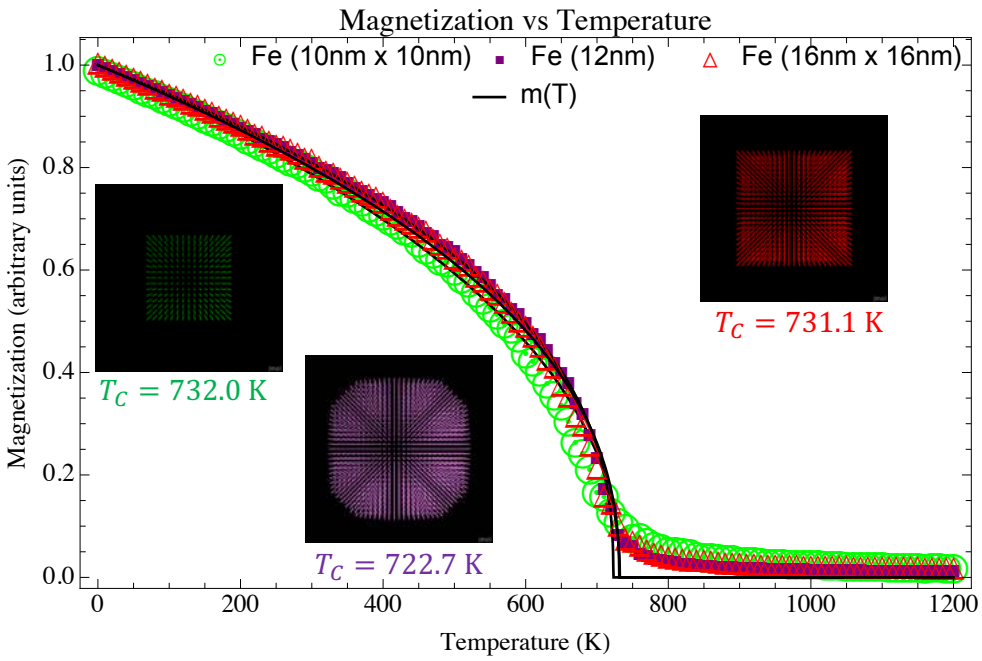


Figure 3.8: Simulation of the mean temperature-dependent magnetisation for complex shapes of bare Fe NPs in a size range of 10 nm to 16 nm.

particularly those consisting of purely magnetic materials (e.g., Ni@Fe and Fe@Ni), are crucial for several reasons. Firstly, they allow for the investigation of magnetic interactions and exchange coupling between the core and shell, which are essential for understanding and enhancing the magnetic properties of the NPs. These properties include superparamagnetism, enhanced coercivity and magnetic anisotropy [576,577].

The simulations of pure magnetic core-shell NPs can provide insight into the optimisation of synthesis processes and the tailoring of NP properties for specific applications by predicting the outcomes of modifying various parameters. This predictive capability is essential for reducing the need for extensive empirical testing, thereby accelerating the development of new materials and technologies.

3.4.2.1 Ni@Fe Core-Shell NPs

The results presented in Figures 3.9, 3.10, 3.11 and 3.12 showcase the Ni@Fe NPs within the size range of 4 nm to 16 nm exhibiting various shapes. Notably, these NPs exhibit intriguing trends based on the Fe/Ni (fractional radius) ratios, particularly in relation to the mean temperature-dependent magnetisation. For instance, the 4 nm core-shell NP with Ni(0.25)@Fe(1) composition demonstrates a stable mean temperature-dependent magnetisation despite transitioning from a 4 nm Fe NP to a 4 nm Ni(0.25)@Fe(1) NP. This behaviour is expected due to the majority of Fe atoms in the structure and the minority Ni atoms occupying inner atomic sites.

Furthermore, the 4 nm Ni(0.25)@Fe(1) NP displays a T_c of 754.0 K, with T_c decreasing as the Ni radius ratio increases. The magnetic properties analysis reveals that minor variations in core position have negligible impact on overall magnetic properties of core-shell NPs. However, a significant shift occurs in Ni(0.5)@Fe(1) NPs where an increase in

core atoms and decrease in shell atoms lead to a notable reduction in magnetic-ordering temperature and temperature-dependent magnetisation. This reduction is attributed to the substitution of high magnetic moment Fe atoms with low spin magnetic moment Ni atoms, given their respective atomic spin moments.

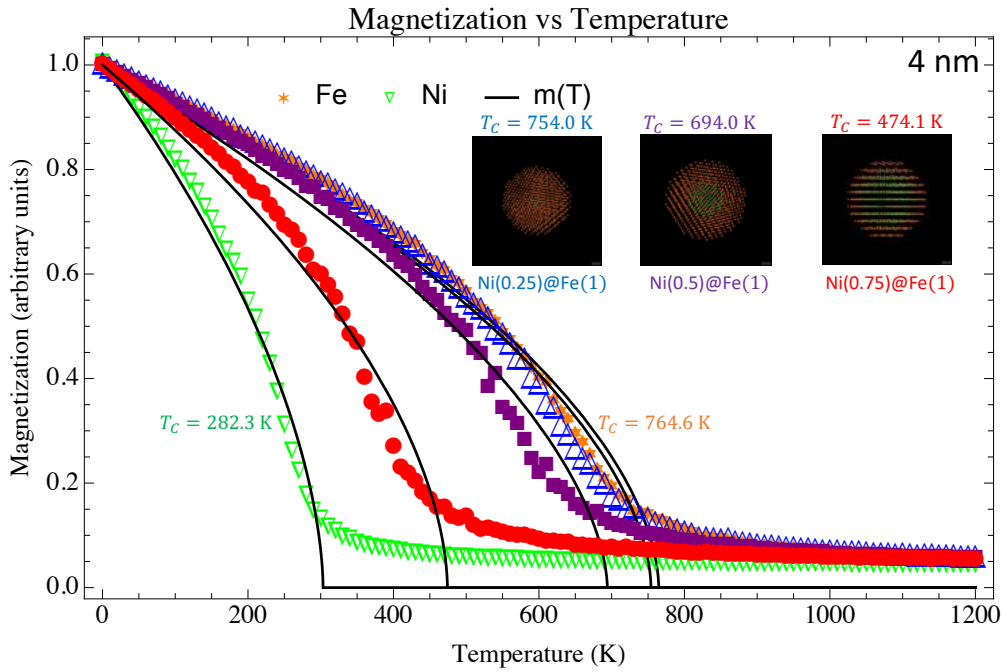


Figure 3.9: Simulation of the mean temperature-dependent magnetisation for 4 nm Ni@Fe core-shell NPs with varying core-shell ratios.

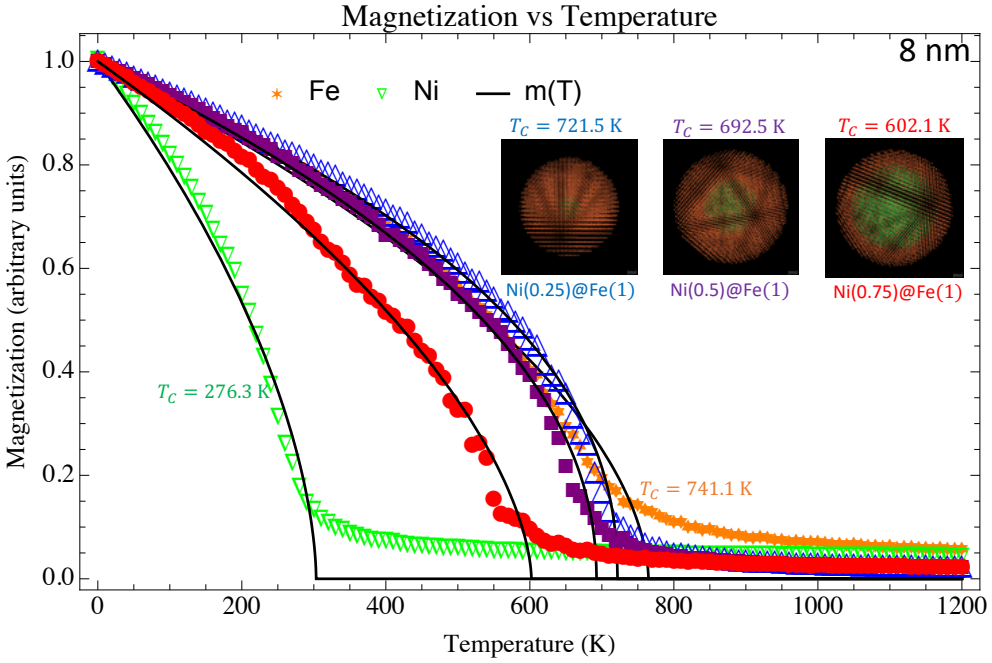


Figure 3.10: Simulation of the mean temperature-dependent magnetisation for 8 nm Ni@Fe core-shell NPs with varying core-shell ratios.

Moreover, for Ni(0.5)@Fe(1) ratio in 4 nm NPs, T_c is measured at 694.0 K and decreases to 474.1 K for Ni(0.75)@Fe(1). Despite varying Fe/Ni radii ratios, zero magnetisation is not achieved for the 4 nm NPs. In the case of Ni(0.75)@Fe(1) 4 nm core-shell NP, significant magnetic modulations are observed with reductions in mean temperature-dependent magnetisation and magnetic ordering temperature compared to other Ni@Fe radii ratios.

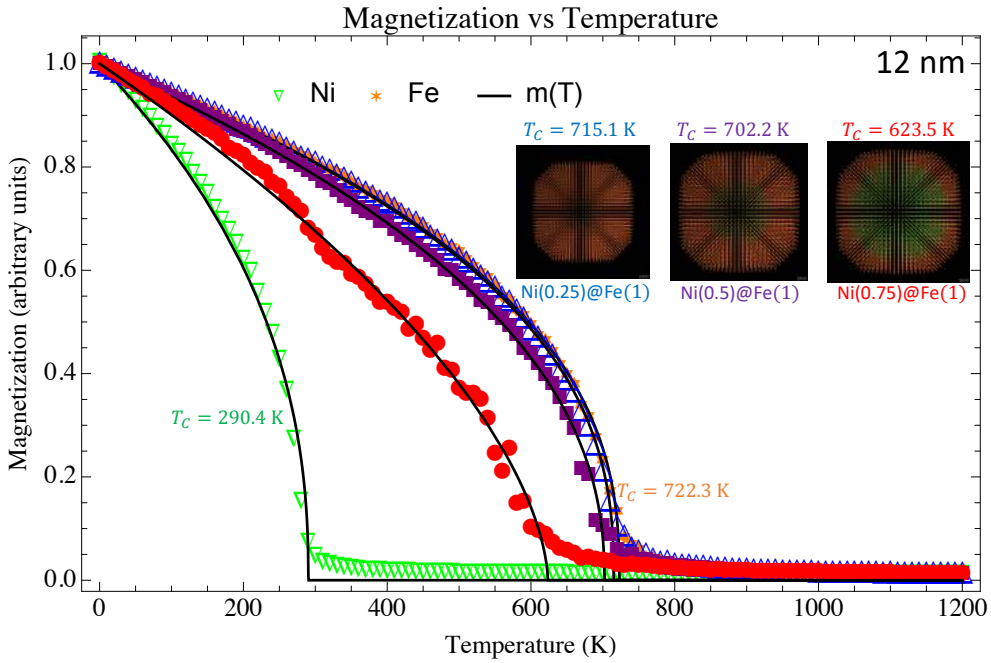


Figure 3.11: Simulation of the mean temperature-dependent magnetisation for octahedron 12 nm Ni@Fe core-shell NPs with varying core-shell ratios.

Additionally, oscillations in magnetisation within the temperature range of 0-300 K are attributed to canted spin structures at specific temperatures, leading to reduced magnetisation levels. Interestingly, a smooth variation is noted in mean temperature-dependent magnetisation for 4 nm Fe NPs. The trends observed in 8 nm Ni@Fe core-shell NPs mirror those of 4 nm NPs with systematic decreases in magnetic-ordering temperature: Ni(0.25)@Fe(1) (T_c= 721.5 K) → Ni(0.5)@Fe(1) (T_c= 692.5 K) → Ni(0.75)@Fe(1) (T_c= 602.1 K).

Overall, these findings highlight the intricate interplay between composition, size, and magnetic properties in Ni@Fe NPs across different shapes and sizes, underscoring the importance of understanding these relationships for tailored applications in nano-magnetism and related fields.

3.4.2.2 Fe@Ni Core-Shell NPs

The investigation into chemically reversed structures involving Fe@Ni core-shell NPs is anticipated to yield comparable insights to those observed in Ni@Fe NPs. Specifically, the 4 nm Fe(0.25)@Ni(1) NP exhibits a mean temperature-dependent magnetisation profile that closely resembles that of the 4 nm Ni NP. This similarity can be attributed to the lower presence of Fe atoms within the system, leading to analogous trends as seen

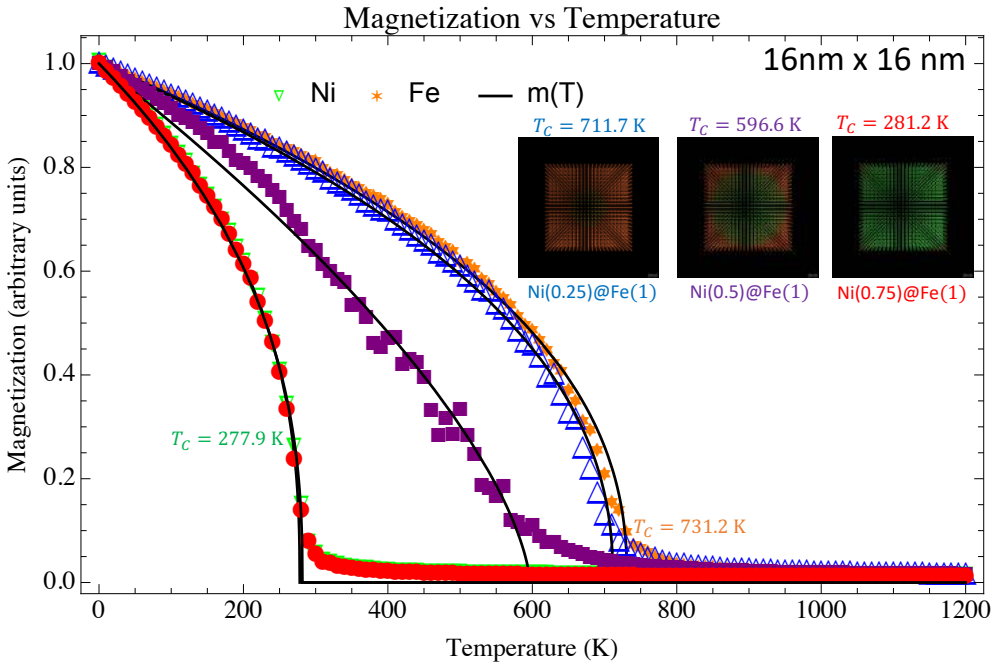


Figure 3.12: Simulation of the mean temperature-dependent magnetisation for cubic 16 nm x 16 nm Ni@Fe core-shell NPs with varying core-shell ratios.

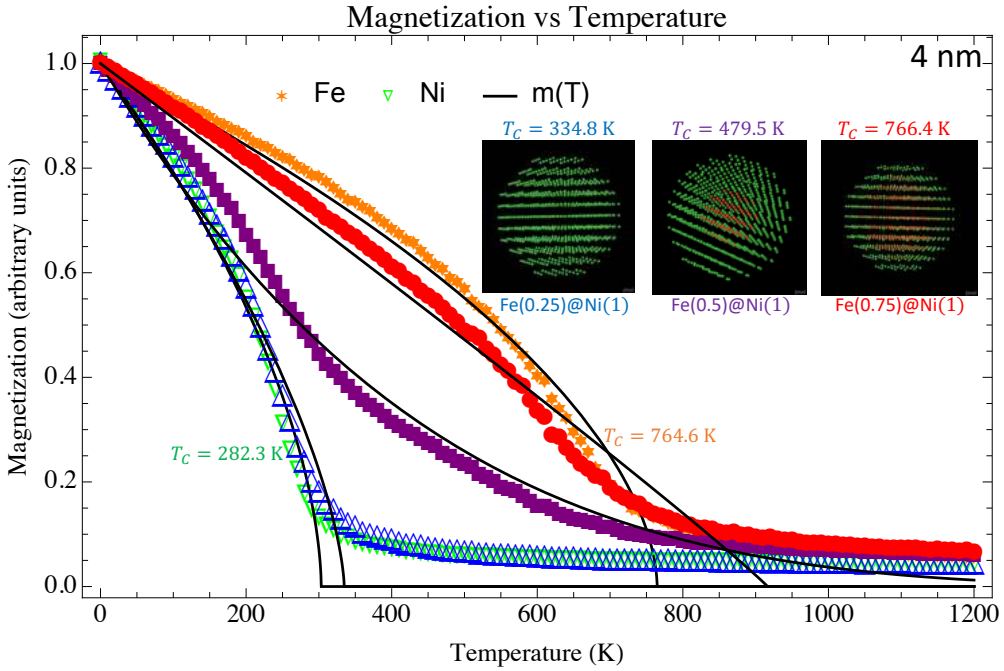


Figure 3.13: Simulation of the mean temperature-dependent magnetisation for 4 nm Fe@Ni core-shell NPs with varying core-shell ratios.

in Ni@Fe NPs.

Noteworthy deviations begin to manifest with the Fe(0.5)@Ni(1) NPs, where significant modulations emerge in temperature-dependent magnetisation below the magnetic-ordering temperature (453 K), with T_c measured at 479.5 K. Figures 3.13 through

3.16 illustrate substantial magnetisation oscillations within the temperature range of 0-380 K due to canted spins. Conversely, Fe(0.75)@Ni(1) NPs exhibit relatively smooth magnetisation variations without pronounced oscillations.

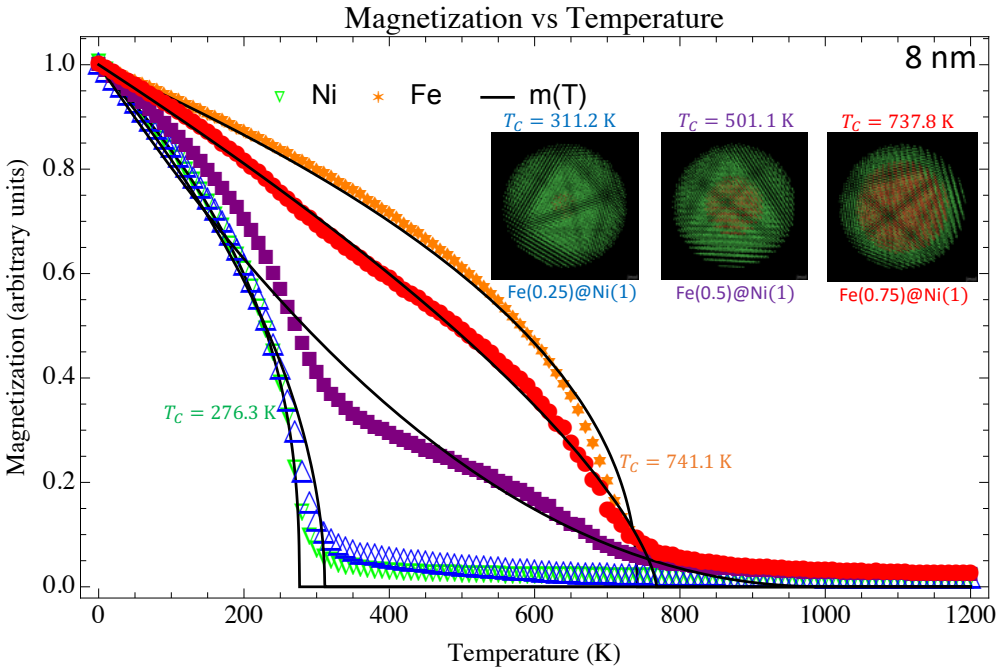


Figure 3.14: Simulation of the mean temperature-dependent magnetisation for 8 nm Fe@Ni core-shell NPs with varying core-shell ratios.

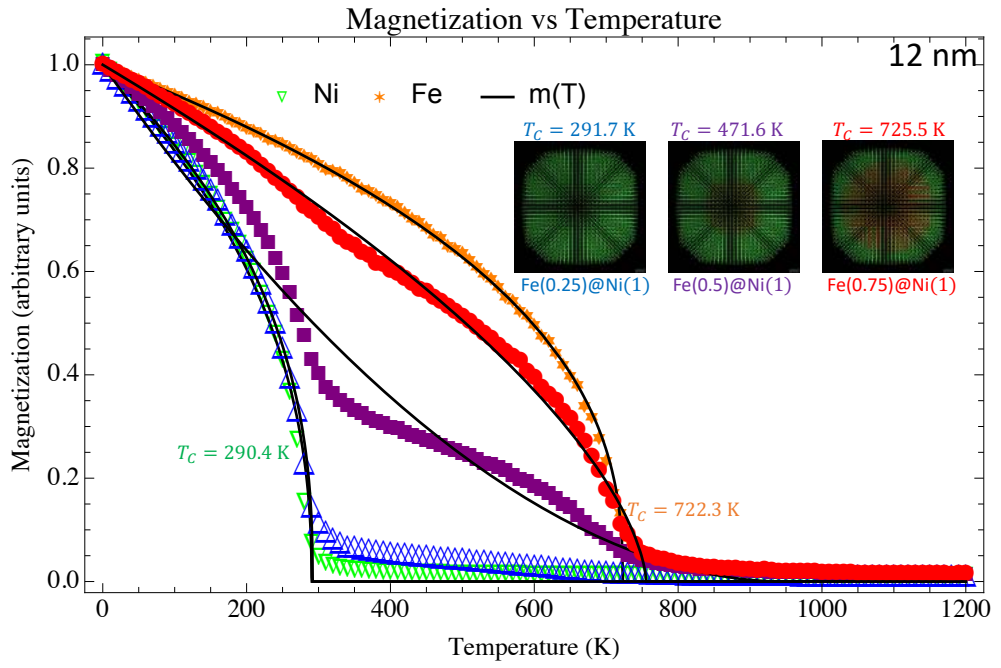


Figure 3.15: Simulation of the mean temperature-dependent magnetisation for octahedron 12 nm Fe@Ni core-shell NPs with varying core-shell ratios.

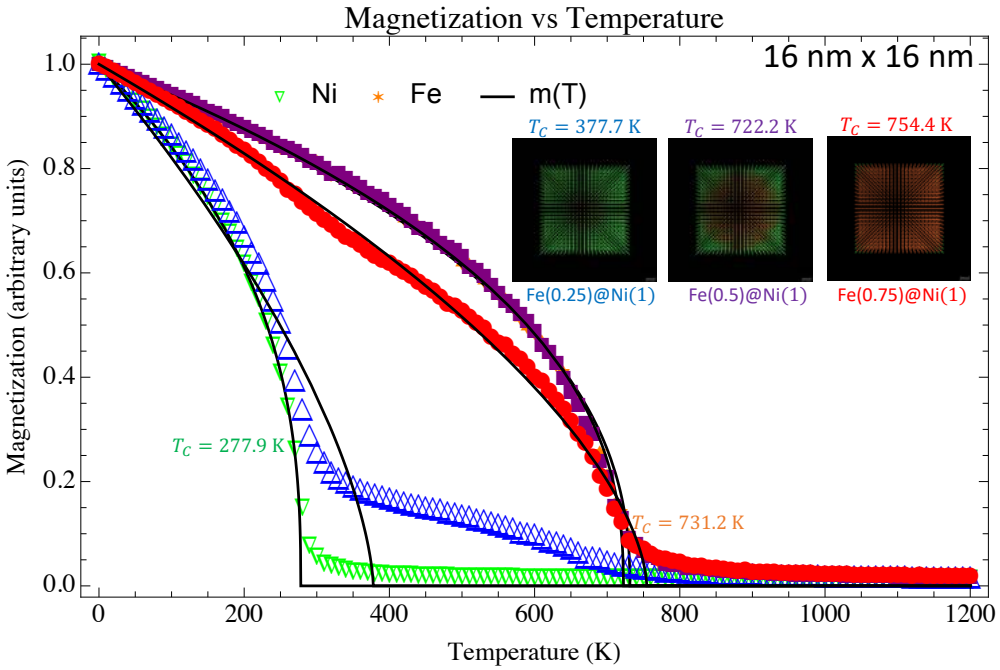


Figure 3.16: Simulation of the mean temperature-dependent magnetisation for cubic 16 nm x 16 nm Fe@Ni core-shell NPs with varying core-shell ratios.

Similarly, larger Fe@Ni NPs demonstrate comparable magnetisation variations concerning temperature, mirroring trends observed in smaller NPs. The Curie temperature also aligns with this consistent trend across different sizes and compositions of Fe@Ni core-shell NPs.

These findings underscore the importance of understanding the interplay between composition, size, and magnetic properties in both Ni@Fe and Fe@Ni core-shell NPs, emphasising the need for further exploration to elucidate the underlying mechanisms governing their magnetic behaviour and potential applications in nano-magnetism and related fields.

Chapter 4

4 Plasmonics and Magnetoplasmonics Effects for Photovoltaic Applications: Silicon Solar Cell

This chapter presents the results of a comprehensive study on the effects of plasmonics and magnetoplasmonics on the efficiency of silicon solar cells. The chapter highlights the potential of plasmonic and magnetoplasmonic nanostructures to enhance the optoelectronic properties of silicon based photovoltaic devices and subsequently their performance.

The chapter presents the methods employed for the fabrication of the plasmonic and magnetoplasmonic nanostructures with tunable physical properties. The nanostructures were either synthesised as pristine single-component systems or embedded within a SiO_2 shell structure. The physical properties of these nanostructures, such as their optical, electrical, and magnetic characteristics, were thoroughly examined and correlated with the J-V (current-voltage) characteristics of the PV devices.

The chapter concludes by showing that plasmonic effects lead to enhancement in photo-absorption as well and increase in photocurrent for Plasmonic nanostructures from 7.64% - 10.7%. On the other hand magnetoplasmonics nanostructures further exhibit that light matter interaction effects enhance the fill factor of the silicon solar cells.

4.1 Methodology

4.1.1 Materials and Chemicals

All materials and chemicals used in this study were of analytical grade and purchased from Sigma Aldrich. The commercial devices (a-Si) were purchased at MR WATT shop based in Italy. The following materials were used:

- Gold(III) chloride trihydrate ($HAuCl_4 \cdot 3H_2O$) ($\geq$ 99.9%, Sigma-Aldrich)
- Silver nitrate ($AgNO_3$) ($\geq$ 99.9%, Sigma-Aldrich)
- Tri-sodium citrate dihydrate ($C_6H_5Na_3O_7 \cdot 2H_2O$) ($\geq$ 99.0%, Sigma-Aldrich)
- Nickel(II) chloride hexahydrate ($NiCl_2 \cdot 6H_2O$) ($\geq$ 98.0%, Sigma-Aldrich)
- Ferric chloride hexahydrate ($FeCl_3 \cdot 6H_2O$) ($\geq$ 97.0%, Sigma-Aldrich)
- Sodium acetate (CH_3COONa) ($\geq$ 99.0%, Sigma-Aldrich)
- Tetraethyl orthosilicate (TEOS) ($\geq$ 98.0%, Sigma-Aldrich)
- Ethanol ($\geq$ 99.8%, Sigma-Aldrich)
- Ethylene glycol ($C_2H_6O_2$) ($\geq$ 99.8%, Sigma-Aldrich)

- Hydrazine hydrate ($N_2H_4 \cdot H_2O$) ($\geq$ 80.0%, Sigma-Aldrich)
- Sodium hydroxide (NaOH) ($\geq$ 98.0%, Sigma-Aldrich)
- Deionized water
- Concentrated ammonia aqueous solution (28 wt%, Sigma-Aldrich)

4.1.2 Synthesis of Nanoparticles

4.1.2.1 Synthesis of Au and $Au@SiO_2$ Nanoparticles

The synthesis of gold (Au) nanoparticles begins with dissolving 1 mM $HAuCl_4 \cdot 3H_2O$ in a 1% $C_6H_5Na_3O_7 \cdot 2H_2O$ aqueous solution. Sodium chloride (NaCl) is then added as a stabilising agent. This mixture is heated to 80° C under vigorous stirring and is allowed to reflux for 15 minutes before cooling down to room temperature, yielding Au nanoparticles.

To synthesise $Au@SiO_2$ core-shell nanoparticles, 10 mL of the Au precursor solution is mixed with 40 mL of ethanol. Subsequently, 2 mL of ammonia and TEOS are added drop-wise while stirring continuously for approximately 3 hours. The resulting mixture is then centrifuged at 6000 rpm for 6 minutes and washed with deionized water. The purified NPs are dried in an oven at70° C for 24 hours, resulting in $Au@SiO_2$ core-shell nanoparticles.

4.1.2.2 Synthesis of Ag and $Ag@SiO_2$ Nanoparticles

Silver (Ag) nanoparticles are synthesiSed by dissolving 0.001 M $AgNO_3$ in deionized water, followed by the addition of 0.5 g of sodium citrate under vigorous stirring at 60° C until a pale yellow colour forms. The mixture is centrifuged at 6000 rpm for 5 minutes, and the NPs are washed four times with distilled water to remove excess reactants.

For the $Ag@SiO_2$ core-shell nanoparticles, 5 mL of the Ag precursor solution is mixed with 40 mL of ethanol. Then, 2 mL of ammonia and TEOS are added drop-wise while stirring continuously for approximately 3 hours. The mixture is centrifuged at 6000 rpm for 6 minutes and washed with deionized water. The purified nanoparticles are dried in an oven at 70° C for 24 hours, resulting in $Ag@SiO_2$ core-shell nanoparticles.

4.1.2.3 Synthesis of Fe_3O_4 and $Fe_3O_4@SiO_2$ Nanoparticles

The synthesis of Fe_3O_4 NPs starts by dissolving 0.55 g of $FeCl_3 \cdot 6H_2O$ in 30 mL of ethylene glycol at 100° C with magnetic stirring. To this solution, 0.45 g of sodium acetate is added and stirred for 1 hour and 40 minutes. Following this, 0.1 g of tri-sodium citrate is introduced and stirred for an additional 20 minutes. The mixture is then transferred to a stainless steel autoclave and heated at 200° C for 11 hours. After heating, the mixture is centrifuged at 8000 rpm for 10 minutes, washed with ethanol and deionized water, and dried under vacuum at 70° for 12 hours to obtain Fe_3O_4 nanoparticles.
To create $Fe_3O_4@SiO_2$ core-shell nanoparticles, 0.1 g of Fe_3O_4 nanoparticles is dispersed in a mixture of 45 mL ethanol, 15 mL deionized water, and 1 mL ammonia solution. This solution is ultrasonicated for 1.5 hours. Following this, 0.45 mL TEOS is added drop-wise and stirred continuously for 2.5 hours. The nanoparticles are washed with deionized water and dried under vacuum at 70° C to form $Fe_3O_4@SiO_2$ core-shell nanoparticles.

4.1.2.4 Synthesis of Ni and $Ni@SiO_2$ Nanoparticles

Nickel (Ni) nanoparticles are synthesised by preparing a solution of 5 mL of 0.1 M $NiCl_2 \cdot 6H_2O$ in ethylene glycol. To this solution, 3 mL of ethylene glycol is added and mixed at 80° C with magnetic stirring. Subsequently, 0.5 mL of hydrazine hydrate is added drop-wise, followed by 1.5 mL of NaOH. The solution is stirred until it turns black, indicating the formation of Ni nanoparticles.

To produce $Ni@SiO_2$ core-shell nanoparticles, 0.1 g of Ni nanoparticles is dispersed in a mixture of 45 mL ethanol, 15 mL deionized water, and 1 mL ammonia solution. The solution is ultrasonicated for 1.5 hours. Then, 0.45 mL TEOS is added drop-wise and stirred continuously for 2.5 hours. The nanoparticles are washed with deionized water and dried under vacuum at 70°, resulting in $Ni@SiO_2$ core-shell nanoparticles.

4.2 Characterisation of Nanoparticles

Characterisation of the synthesised nanoparticles was conducted using the following techniques:

4.2.1 Transmission Electron Microscopy (TEM)

The TEM instrument used is a FEI Tecnai T12a, operating with an accelerating voltage up to 120 kV. The microscope features a LaB^6 electron source, known for its bright and stable emission, which contributes to the high-quality imaging capabilities of the system. With a point-point resolution of 0.34 nm and a line resolution of 0.2 nm. The Tecnai T12 supports magnifications up to 110,000x, allowing for samples at the nanoscale to be explored. It also boasts a specimen tilt range from $-50°$ to $+50°$, enabling different viewing angles for comprehensive analysis. The TEM is equipped with various specimen holders to accommodate single tilt, cryo, and room temperature samples, addressing a broad spectrum of experimental setups. Furthermore, with a drift rate of less than 1 nm per minute, it ensures stability and accuracy in imaging over extended periods.

4.2.2 Ultraviolet-Visible Spectroscopy (UV-Vis)

The UV-Vis- NIR - 500 Cary Spectrometer was used to characterise the optical properties of the plasmonic and magnetoplasmonic nanoparticles. The instrument operates using the dual beam method to allow for baseline calibration in the absorption, transmission and reflection modes. This instrument provided detailed information on the optical absorption properties across the UV, visible, and NIR regions. For plasmonic nanoparticles, we measured the surface plasmon resonance (SPR) to gain insights into their size, shape, and dielectric environment. For magnetoplasmonic nanoparticles, we analysed shifts and changes in the SPR peak under applied magnetic fields to understand the interplay between plasmonic and magnetic properties.

4.2.3 X-ray Diffraction (XRD)

The Bruker D2 PHASER XRD was used to determine the structural phases of magnetoplasmonic nanoparticles due to its superior alignment at an accuracy of $\pm 0.02°$ in 2θ over the entire angular range, ensuring precise and accurate data. The detector offers

an energy resolution better than 380 eV, which is four times the efficiency of traditional detectors. This high-resolution detector allows for fast data acquisition and superior filtering of unwanted radiation, leading to outstanding peak-to-background ratios and improved detection limits.

The D2 PHASER supports a 2θ range from $-5°$ to $150°$ and ϕ rotation of $360°$. The detector has 192 channels, making it ideal for a variety of applications, including particle sizing for nano-powders and phase identification.

4.2.4 Raman Spectroscopy

Raman spectroscopy was used for studying NPs and due to its ability to provide detailed information about molecular vibrations, crystal structures, and chemical compositions. It can assess the crystalline quality of the nanoparticles, revealing changes in crystallinity through peak shifts and widths, and detect strain and stress induced by nanoparticles. Raman spectroscopy also aids in studying plasmonic effects, with surface-enhanced Raman scattering (SERS) providing insights into light-nanoparticle interactions. Electron-phonon interactions at nanoparticle interfaces, crucial for charge carrier dynamics, can also be investigated.

The Raman spectra were measured using the 514.5 nm line from a Lexel Model 95-SHG argon ion laser, paired with a Horiba LabRAM HR Raman spectrometer and an Olympus BX41 microscope attachment. The incident laser beam was focused onto the sample with a 100x objective (N.A. = 0.90), and the backscattered light was dispersed through a 600 lines/mm grating onto a liquid nitrogen-cooled CCD detector. Data capture and processing were performed using LabSpec v5 software. To prevent a heat-induced phase transition to haematite, the laser power at the sample was maintained at a very low level (0.04 mW) for the magnetite samples. The spectrum acquisition time for these low-power measurements was set to 120 seconds and averaged over three measurements.

4.2.5 Vibrating Sample Magnetometry (VSM)

The magnetic properties of Fe_3O_4 NPs and $Fe_3O_4@SiO_2$ core-shell nanostructures were characterised using the vibrating sample magnetometer of the DynaCool 12T Physical Property Measurement System (PPMS). Hysteresis loops were obtained over a temperature range from 0 K to 300 K to examine the magnetisation mechanisms within the NPs. Furthermore, zero-field-cooled (ZFC) magnetisation was analysed as a function of increasing temperature at an external magnetic field strength of 100 Oe.

4.3 Results and Discussion

4.3.1 Morphology of Plasmonic and Magnetoplasmonic Nanostructures for Shape and Size Dependence (TEM)

The morphology of these nanostructures is related to the aspect of quantum confinement in which the size, shape and monodispersity determines the optoelectronic properties of these materials in the embedded media. Hence in this subsection, the size, shape and dimensions of the core and shell will be discussed to establish the physical and

geometrical characteristics of these nanostructures.

4.3.1.1 Plasmonic NPs

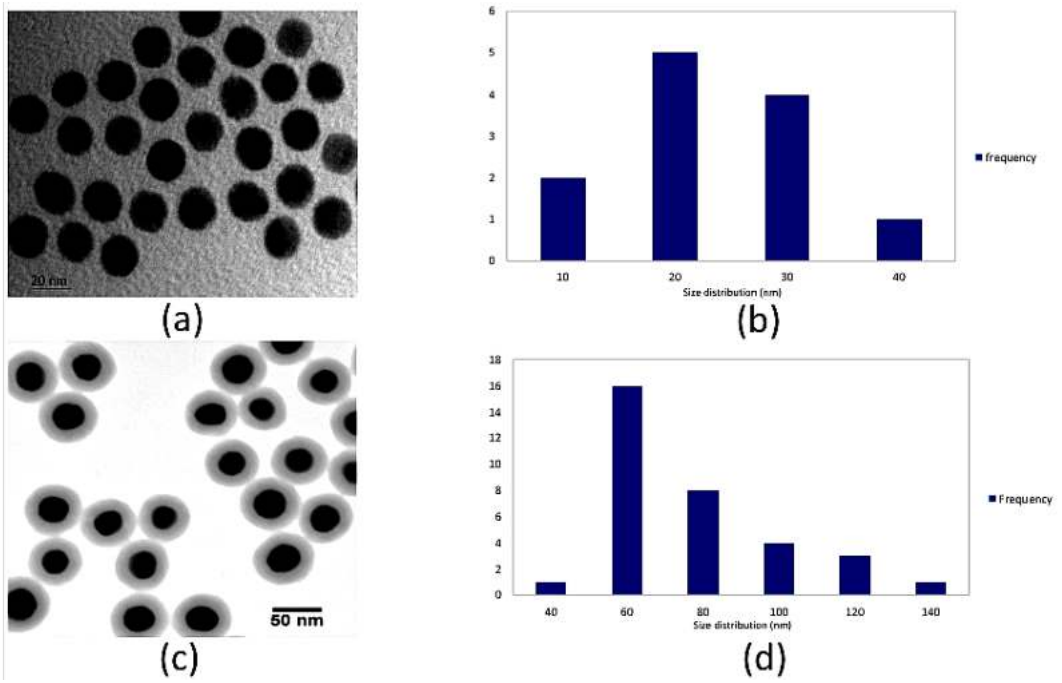


Figure 4.1: Image (a) shows image of Au NPs with 20 nm diameter, (b) shows how the Au NPs are distributed on the surface, (c) shows the image of $Au@SiO_2$ spheres having an average diameter of 69.8 nm and (d) shows the size distribution of the core-shell $Au@SiO_2$ NPs.

The TEM images provide detailed insights into the morphology of the plasmonic nanostructures under investigation. The Au NPs depicted in Figure 4.1 (a) exhibit a uniform dispersion across the substrate, with a predominantly spherical morphology. This uniformity in shape is crucial for plasmonic applications, as it ensures consistent shallow absorption profiles with reduced broadening optical properties across the sample. The size distribution of these Au NPs have been determined using ImageJ software from a chosen distribution of nanoparticles. The average size of the core in the NP is in the range 26 ± 3.56 nm. The dispersion in the size of the Au NPs enables the investigation of size dependent plasmonic resonances. The dependence of size on the optical absorption in an ensemble of NP is to increase the number of localised surface plasmonic resonance leader to broader peaks. In the case where the spherical symmetry is broken then more than one mode is observed. For an elliptical shaped Au NPs, this can be imagined as two spherical nanoparticles that are in close proximity (a tight fit), there will be a longitudinal and a transverse plasmonic mode coexisting in the excitation.

Magnetic nanoparticles have been found to be sensitive to their surrounding and their surface requires passivation, which is usually carried using a shell, predominant of an oxide such as SiO_2. This prevents further reactivity of the surface and changes in the properties of the NP. The same can also be considered for Au NPs which are stabilised using shell structures around their core. Figure 4.1 (c) reveals a variety of sizes for these complex

structures. The corresponding size distribution is shown in Figure 4.1 (d), emphasising the diversity in dimensions that can be achieved through careful synthesis. The TEM images of these core-shell NPs highlight their composite nature, where the core (dark) is encapsulated by a silica shell (brighter material). A notable observation from these images is that the NPs predominantly consist of single core structures, with only a minor fraction forming aggregates containing more than one core. This observation suggests a high degree of control in the synthesis process, minimising the formation of aggregates that could adversely affect the uniformity and reproducibility of the plasmonic properties.

The morphology analysis of these Au plasmonic nanostructures via TEM images show that these nanoparticles have near spherical shape with an average diameter of 20 ± 3.56 nm. Their size distribution is homogeneous for both Au and $Au@SiO_2$ nanoparticles. The ability to achieve a uniform dispersion of spherical Au NPs and to control the size distribution of both Au NPs and $Au@SiO_2$ core-shell NPs underlines the sophistication of the synthesis techniques employed, paving the way for the development of advanced regular plasmonic nanomaterials with tailored optical functionalities.

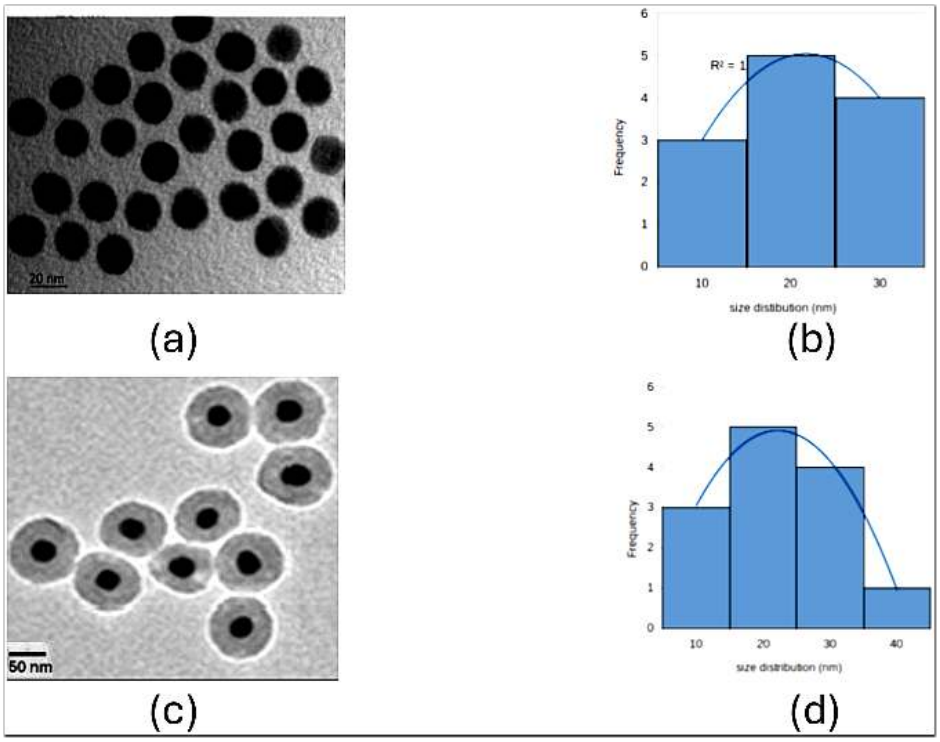


Figure 4.2: Image (a) shows image of Ag NPs with 20 nm diameter, (b) shows how the Ag NPs are distributed on the surface, (c) shows the image of $Ag@SiO_2$ spheres having a diameter of ≈ 24 nm and (d) shows the size distribution of the core-shell $Ag@SiO_2$ NPs.

The morphology studies presented in Figure 4.2 underscore the synthesis of well-defined, regular-shaped nanoparticles of pure Ag. A notable feature of these NPs is their low degree of agglomeration, which is critical for applications requiring uniform dispersion and consistent inter-particle distances for reproducible plasmonic responses.

The comparison of the bare Ag NPs to Au NPs reveals that both types of NPs possess an identical diameter of around 20 ± 3.56 nm. This uniformity in size between different

metallic NPs allows for a direct comparison of their plasmonic properties. Here the electron density and the effective mass of the electrons in these nanostructures should provide the distinct optical property contrast.

On the other hand, the $Ag@SiO_2$ core-shell NPs exhibit an average diameter of approximately 24 nm. This size is significantly smaller than that of the $Au@SiO_2$ core-shell NPs, indicating a distinct difference in the size increase due to the silica coating process. This discrepancy suggests that the silica shell thickness might be controlled differently or that the core material influences the efficiency of silica deposition. The phenomenon of the core Ag NPs appearing smaller after adding a shell of SiO_2 using the Stöber method can be attributed to the process of adding the shell. When a shell of SiO_2 is deposited onto the Ag NPs, it can lead to changes in the overall size perception due to the addition of the SiO_2 layer around the core [578, 579]. This process is commonly observed in core-shell SiO_2 synthesis methods like Stöber's method [580, 581].

The size comparison between the bare and core-shell nanoparticles of Ag and Au highlights the influence of both the core material and the shell thickness on the final size of the nanostructures, which in turn affects their plasmonic properties.

4.3.1.2 Magnetoplasmonic NPs

Magnetoplasmonic Properties of Fe_3O_4 and $Fe_3O_4@SiO_2$

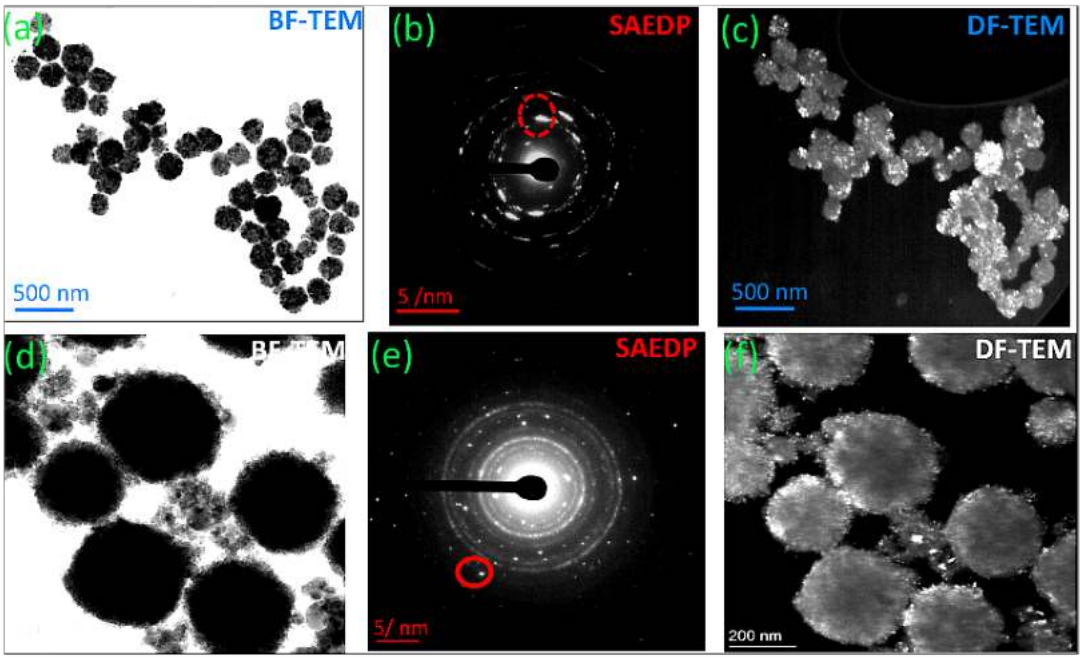


Figure 4.3: (a) Bright Field TEM (BFTEM) showing the distribution of Fe_3O_4 NPs on a carbon film, (b) the Selected Area Electron Diffraction Pattern (SAEDP), (c) Dark Field TEM (DFTEM) showing the distribution of Fe_3O_4 NPs on a carbon film, (d) BFTEM showing the distribution of $Fe_3O_4@SiO_2$ core-shell NPs on a carbon film, (e) SAEDP of $Fe_3O_4@SiO_2$ core-shell NPs and (f) DFTEM showing the distribution of $Fe_3O_4@SiO_2$ core-shell NPs on a carbon film.

Figure 4.3 (a) presents the bare Fe_3O_4 NPs, showcasing their well-defined spherical

morphology with an average diameter of approximately 150 nm. This observation is crucial for evaluating the size-dependent magnetic properties of the NPs, which are influenced by their diameter.

The Selected Area Electron Diffraction Pattern (SAEDP) depicted in Figure 4.3 (b) reveals distinct diffraction rings. These rings correspond to the various reflections characteristic of polycrystalline Fe_3O_4, thus confirming the crystalline phase of spinel structure attributed to the Fe_3O_4 NPs. Notably, the red circles in both Figures 4.3 (b) and (e) highlight the reflection spot used for acquiring Dark-Field TEM (DFTEM) images, underscoring the methodological approach taken for detailed structural analysis.

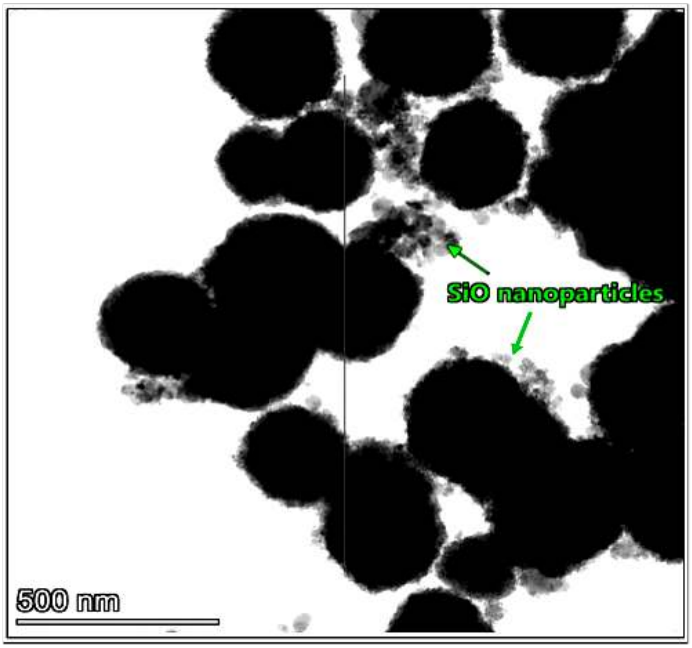


Figure 4.4: High-resolution BFTEM images showing the distribution of the SiO_2 NPs on the surface of the magnetite NPs. These NPs have an average particle size of about 20 nm in diameter.

In Figure 4.3 (c), the Dark Field Transmission Electron Microscope image showcases a diffraction spot that aligns with the prominently featured NPs, corroborating their composition as Fe_3O_4. This alignment between the diffraction spot and the NPs substantiates the polycrystalline nature of the Fe_3O_4 NPs. Conversely, the spots observed in Figure 4.3 (e) do not correspond to any Fe_3O_4 reflections but rather emanate from smaller NPs adjacent to the Fe_3O_4 NPs. This discrepancy in DFTEM analysis suggests the presence of a new phase within the sample, potentially indicating the formation of composite or hybrid structures.

The BFTEM in Figure 4.4 shows the particle size distribution and structural pattern of the nanoparticles. The SiO_2 NPs exhibit a spheroidal morphology with an average particle size of approximately 20 nm in diameter where they coalesce to form the shell structure. The intimate contact between the SiO_2 and magnetite NPs observed

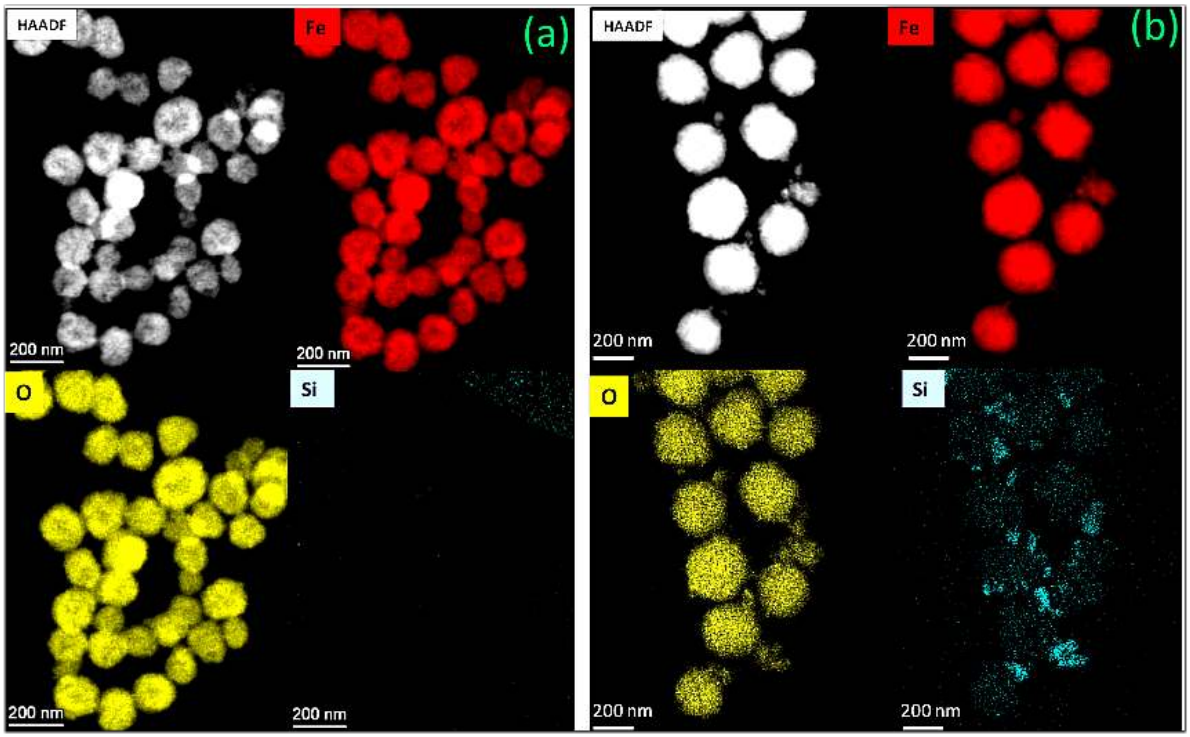


Figure 4.5: (a) High Angle Annular Dark Field (HAADF) image and the corresponding energy dispersive x-ray spectroscopy (EDXS) maps for Fe_3O_4 NPs and (b) High Angle Annular Dark Field image and the corresponding EDXS maps for $Fe_3O_4@SiO_2$ core-shell NPs.

indicates the possibility of a synergistic interaction between the magnetic and plasmonic components, which is hypothesised to result in enhanced performance for applications that exploit their combined properties.

The elemental composition analysis, illustrated in Figure 4.5 (a), demonstrates a uniform distribution of iron (Fe) and oxygen (O) within the NPs. This uniformity is critical for ensuring consistent magnetic and optical properties across the sample. Importantly, there is no detectable silicon (Si) elemental map in this sample, indicating the absence of silica in the bare NPs.

Furthermore, Figure 4.5 (b) showcases the (STEM-EDS) maps for the $Fe_3O_4@SiO_2$ samples. These maps confirm the uniform distribution of Fe and O within the core of the NPs, while also detecting the presence of Si on the surface/shell of the NPs.

Magnetoplasmonic Properties of Ni and $Ni@SiO_2$

For sample preparation for TEM, the bare Ni NPs were first dispersed in ethanol. To ensure a uniform distribution, the solution was sonicated for 30 minutes. This sonication step is critical as it prevents agglomeration, allowing for more accurate morphology characterisation. After sonication, the Ni NPs were deposited onto a TEM copper grid that was coated with a carbon (C) film. This C film provides a stable background for TEM imaging. The grid was left to air dry for 15 minutes to evaporate the ethanol

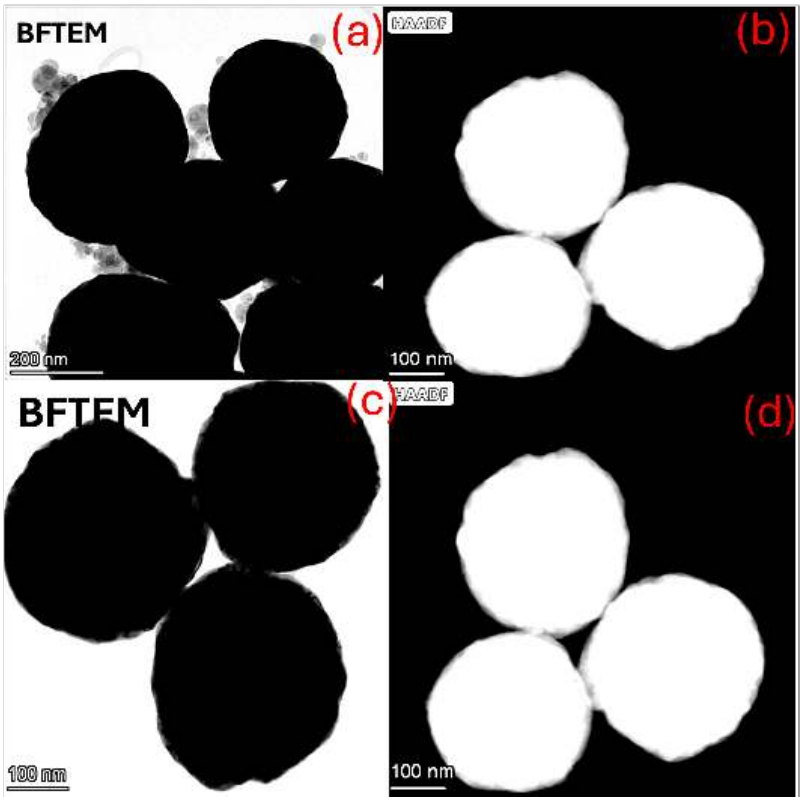


Figure 4.6: BFTEM showing the distribution of aggregated Ni NPs on a carbon film, (b) HAADF image of Ni NPs, (c) BFTEM showing the distribution of $Ni@SiO_2$ core-shell NPs on a carbon film (d) HAADF image of $Ni@SiO_2$ core-shell NPs.

solvent, which ensures that only the NPs remain on the grid. Subsequently, the grid was placed in the TEM for imaging.

BFTEM and HAADF imaging techniques were employed to study the Ni NPs. These imaging modes provide different contrast mechanisms, thereby giving complementary information about the NPs. The BFTEM images in Figure 4.6 (a) displayed the size and morphology of the NPs, while HAADF imaging in Figure 4.6 (b) offered additional detail due to its sensitivity to variations in atomic number.

Following a similar preparation procedure as the bare Ni NPs, the $Ni@SiO_2$ core-shell NPs were dispersed in ethanol and sonicated for 30 minutes. The sonication process not only aids in dispersion but also helps in the detachment of any loosely bound aggregates. The $Ni@SiO_2$ NPs were then applied onto a TEM copper grid with a C film and left to air dry for 15 minutes. The reduction in the melting point of Ni and the presence of eddy currents could contribute to the agglomeration of the NPs due to the competition between surface and bulk energies/effects [582].

The lack of contrast in the shell layer surrounding the Ni-NPs could be attributed to the similarity in electron density between Ni and SiO_2. This similarity is evident when considering the atomic numbers, where $Z_{Ni} = 28$ and $Z_{SiO_2} = 24$ [583]. The comparable electron densities of these elements, influenced by their atomic numbers, may lead to a lack of noticeable contrast in the shell layer surrounding the Ni NPs.

It is not possible to see the SiO2 shell with HAADF imaging technique because SiO_2 is a low atomic number material that does not provide sufficient contrast in HAADF imaging. HAADF imaging relies on the atomic number of elements to generate contrast, and since SiO_2 has a low atomic number, it appears transparent or does not produce a strong signal in HAADF images [584].

Imaging of the core-shell NPs was conducted using BFTEM and HAADF and the resulting images are presented in Figures 4.6 (c) and (d), respectively. The images reveal a core-shell structure of $Ni@SiO_2$ in which Ni forms the core of the structure of diameter 350 nm while the SiO_2.

The uniform size and shape of these NPs are indicative of the controlled synthesis process, which is needed for the correlation of morphology and physical properties requisite for magnetoplasmonic applications.

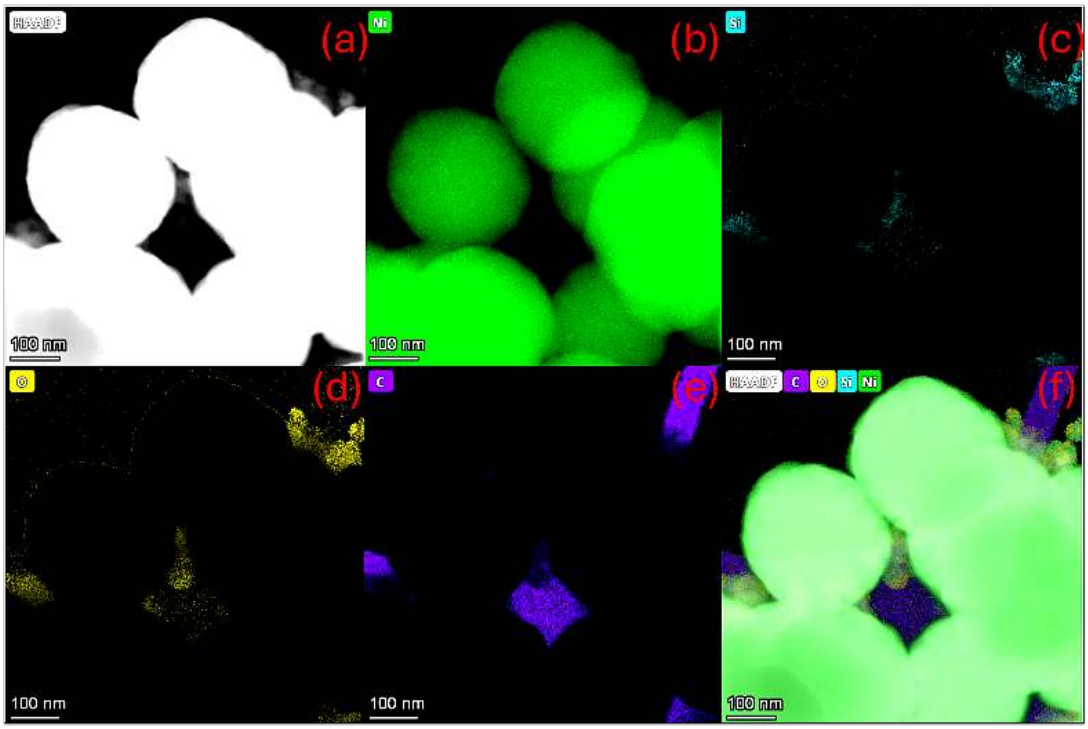


Figure 4.7: (a) HAADF imaging alongside EDXS mappings, (b) for Ni, (c) Si, (d) O, (e) C, and (f) the aggregate weight percentages within Ni NPs.

The HAADF image of Figure 4.7 (a) provides a clear representation of the morphology of the NPs, by decoupling the elemental distribution within the NP. This is crucial for the verification of the shell coverage and homogeneous distribution of the electron density in the NPs. Concurrently, the STEM-EDS maps furnish a detailed picture of the elemental distribution within these structures. The maps indicate that the NPs have a predominant composition of Ni in Figures 4.7 (b) and (f), which is consistent with the designed synthesis parameters aimed at creating Ni-based magnetoplasmonic characteristics.

However, the presence of Si and O in Figures 4.7 (c) and (d) signals in the EDXS maps could suggest either contamination or oxidation events that may have transpired during sample preparation. Such occurrences are not uncommon in sample handling and may arise from various sources, including environmental exposure or interaction with preparation materials [585, 586]. On a related note, the C map clearly in Figure 4.7 (e) delineates the carbonaceous film utilised to support the NPs during their transfer onto the copper grid. This carbon layer is instrumental in stabilising the sample and is a routine inclusion in TEM sample preparation.

These findings are pivotal in understanding the nuances of nanostructure formation and the potential implications of sample handling and environment on the integrity and purity of the nanostructures. Further investigations could elucidate the specific origins of the Si and O signals and confirm whether they are indeed artefacts of sample preparation or integral components of the NPs. Such insights would be beneficial in refining the synthesis and handling processes to enhance the purity and performance of these magnetoplasmonic structures in their respective applications.

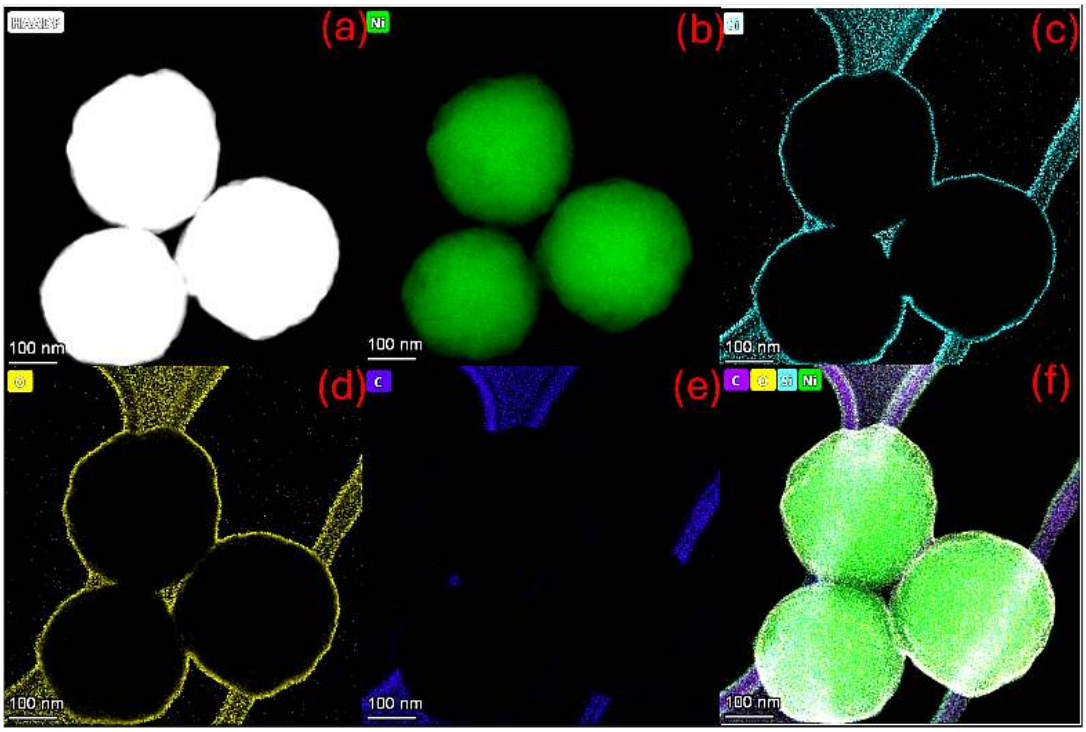


Figure 4.8: (a) HAADF imaging alongside EDXS mappings, (b) for Ni, (c) Si, (d) O, (e) C, and (f) the aggregate weight percentages within $Ni@SiO_2$ core-shell NPs.

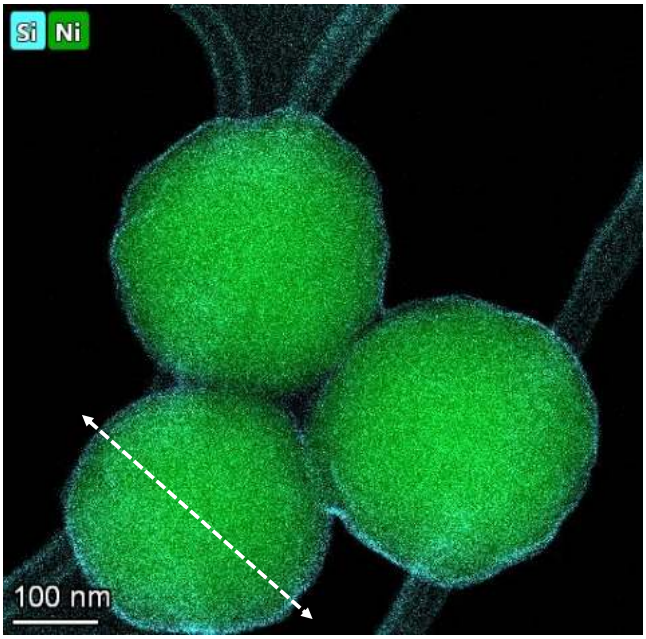
The HAADF image in Figure 4.8 (a) reveals the structural outline of the NPs, while the corresponding EDXS maps in Figures 4.8 (b) to (f) delineate the elemental distribution within these entities. From these mappings, it is evident that the core of the NPs is predominantly Ni, as shown by the intensity of the signals in the Ni map in Figure 4.8 (b). Surrounding the nickel core is a shell composed of Si and O, constituents of SiO_2, which manifests as a concentric layer enveloping the Ni core.

In comparison to the observations made in Figure 4.7, there is a notable increase in the elemental percentages of Si and O, suggesting a more substantial presence of the SiO_2 shell in these particular NPs. The uniformity of the Si-O shell is remarkable, and the EDXS maps indicate a homogeneous distribution of these elements across the entire shell region. The thickness of the SiO_2 shell is measured to be approximately 40 nm, contributing to the overall stability and morphological integrity of the NPs. Furthermore, the C map highlights the carbonaceous film utilised during sample preparation.

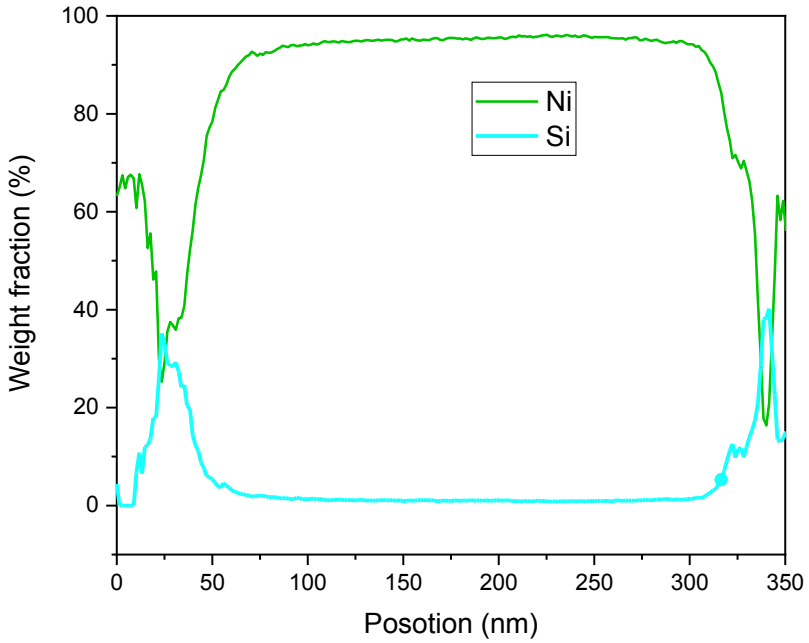
Further analysis was carried out for the $Ni@SiO_2$ core-shell NPs. The acquired TEM images provided insight into the elemental distribution within the samples. EDXS mapping was used to elucidate the spatial presence of Ni and Si elements within the NPs.

Figure 4.9 (a) presents the EDXS map overlaid on the TEM image, highlighting the regions rich in Ni (green) and Si (turquiose). As seen from the colour coded image, Ni is distributed homogeneously from the core extending radially outward up to the thin shell of Si(SiO_2). To further determine the elemental distribution with the nanoparticle, a line scan was measured across the NP. This is depicted by the white broken line which quantifies by weight percent of the constituent elements in the NP. The data extracted from this analysis, shown in Figure 4.9 (b), reveals a pronounced increment in the weight percentage of Si, reaching approximately 35% at the surface of the NP in contrast to the core. This gradient confirms the formation of a SiO_2 shell around the Ni core.

Figure 4.10 (a) showcases a HAADF image with a red point indicating where the electron beam was centered during the EDXS measurement. The corresponding EDXS spectrum, detailed in Figure4.9 (b), qualitatively illustrates the elemental composition of the sample from their respective X-ray lines, substantiating the presence of Ni and Si. It is notable that the spectrum includes a Cu-K line associated with the Cu TEM grid on which the NPs are supported.

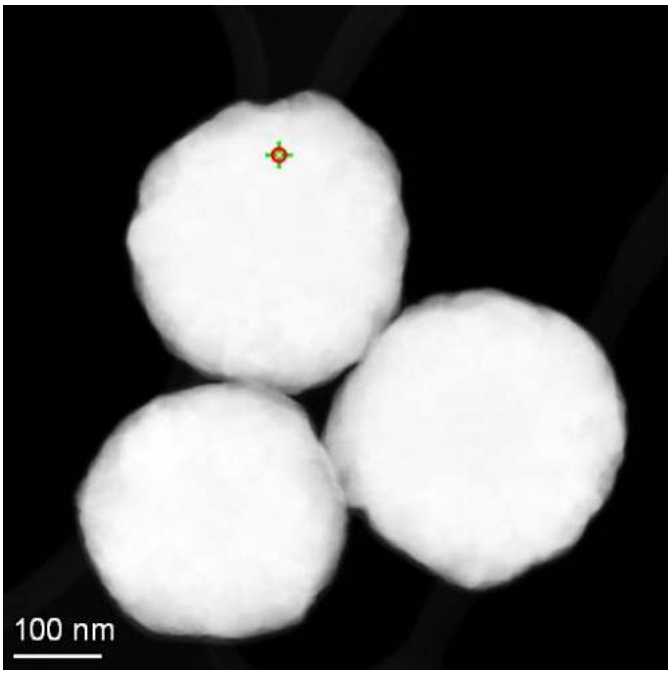


(a)

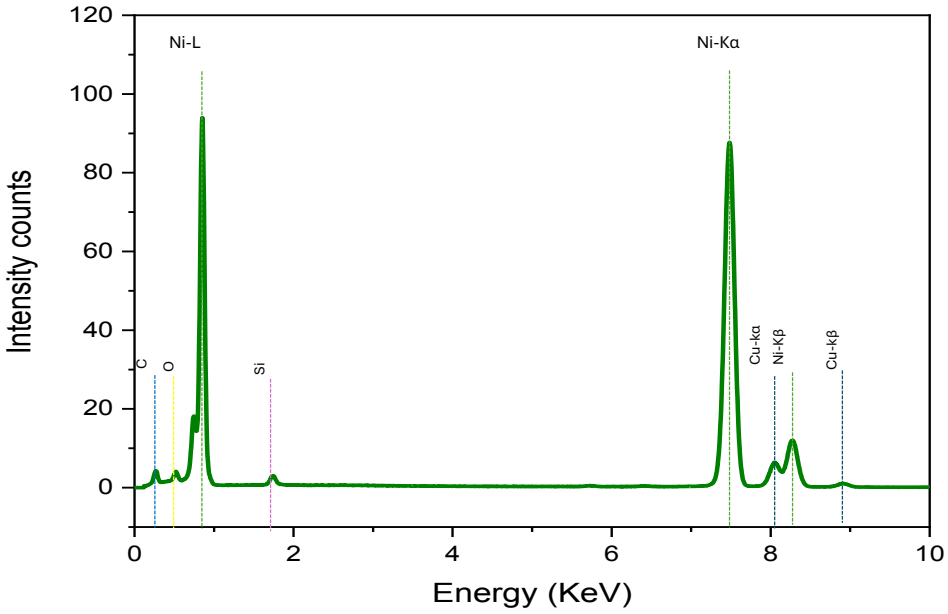


(b)

Figure 4.9: The images labeled (a) illustrate the STEM-EDS mapping of samples containing Ni and Si elements, as well as the associated line scan denoted by a white line. Image (b) depicts the plot of the atomic weight percentages of these elements.



(a)



(b)

Figure 4.10: In image (c), we observe the electron beam targeted at the red mark seen in the HAADF image. Lastly, image (d) presents the EDS spectrum that reveals the elemental makeup of the$Ni@SiO_2$ core-shell NPs.

4.3.2 Optical Spectroscopy

4.3.2.1 Plasmonic NPs

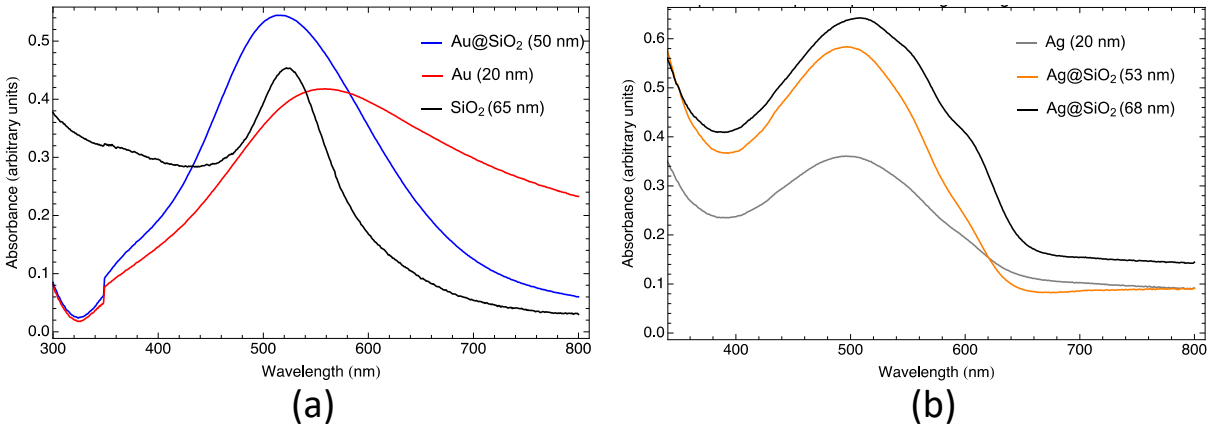


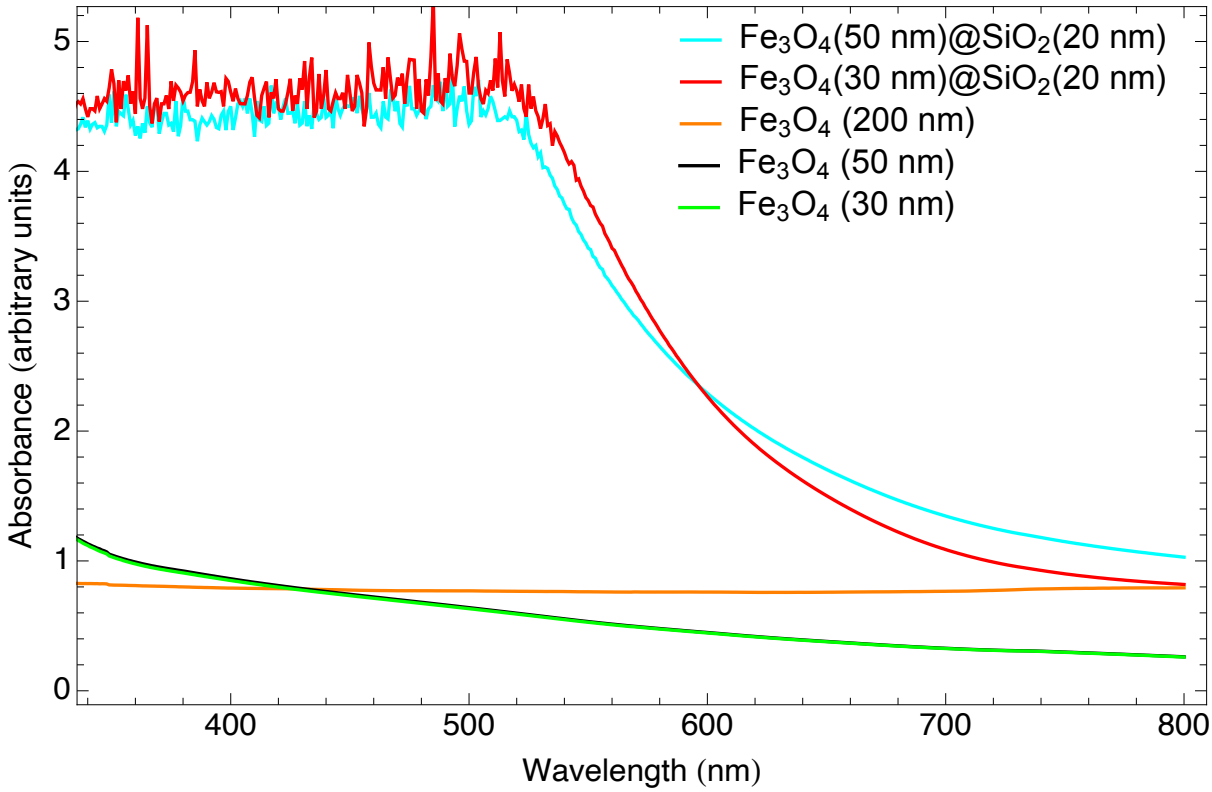
Figure 4.11: Optical absorption spectra of (a) SiO_2 , Au and $Au@SiO_2$ NPs, and (b) Ag and $Ag@SiO_2$ NPs.

The absorption spectra depicted in Figure 4.11 (a) for the Au NPs exhibit a broad LSPR peak at 550 nm. To determine the formation and the optical properties of the $NP@SiO_2$ co-shell structures, SiO_2 NP were also investigated. In contrast, the characteristic LSPR of SiO_2 NPs was observed around 510 nm, but with a higher peak intensity compared to that of the Au NPs. The $Au@SiO_2$ core-shell NPs show a LSPR peak at approximately 510 nm, yet with a significantly enhanced peak intensity relative to the bare Au and SiO_2 NPs. This phenomenon indicates that the LSPR peak position is blue-shifted by the SiO_2 coating. This effect can be attributed to the alteration of the dielectric constant of the surrounding medium upon encapsulation, as supported by references [587, 588].

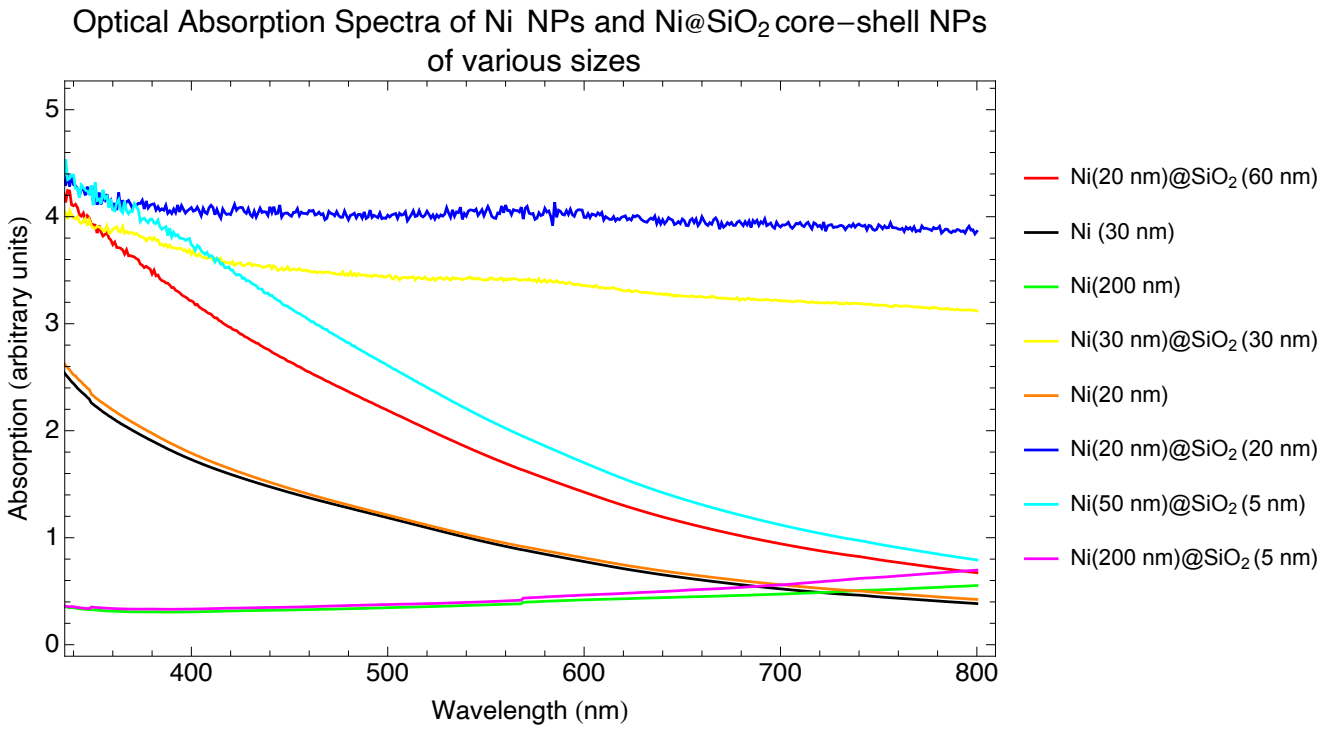
This trend is further corroborated in Figure 4.11 (b), where the absorbance of Ag NPs is observed to increase upon the addition of a SiO_2 shell, even when the shell's size is augmented by 15 nm, from 53 nm to 68 nm. This increase in size enhances the spectrum's peak of the core-shell nanostructures, suggesting that the presence of the SiO_2 shell not only affects the peak intensity but also potentially modifies the optical properties of the NPs through changes in the local dielectric environment. These observations underscore the critical role of the dielectric coating in modulating the optical properties of plasmonic NPs, pointing towards a tunable approach for optimising their plasmonic responses for various applications.

4.3.2.2 Magnetoplasmonic NPs

Figure 4.12 (a) presents the optical absorption characteristics of Fe_3O_4 and $Fe_3O_4@SiO_2$ NPs, as determined through Diffuse Reflectance Spectroscopy. Notably, the plasmonic



(a)



(b)

Figure 4.12: Optical absorption spectra of (a) Fe_3O_4 and $Fe_3O_4@SiO_2$, (b) Ni and $Ni@SiO_2$ NPs of various sizes.

resonance of the core-shell structures is situated within the visible spectrum. A clear

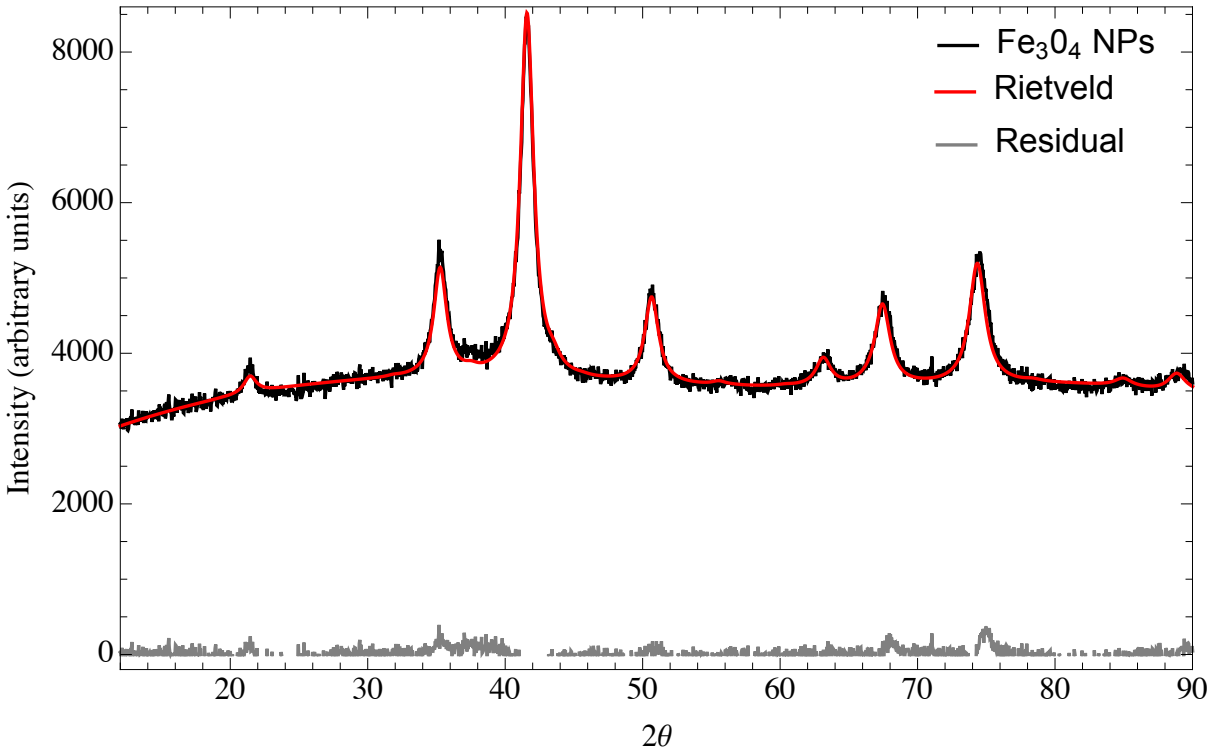
size-dependent behaviour in the plasmonic effects is observed, with larger NPs (200 nm Fe_3O_4) demonstrating reduced absorbance. This pattern is indicative of a transition where scattering becomes more dominant than absorption in these larger magnetoplasmonic nanostructures. For NPs sized at 30 nm and 50 nm, a consistent monotonic increase in absorbance is noted as the wavelength of incoming light decreases, with only a marginal difference in the optical absorption profiles between the two sizes, both peaking in the UV region. The integration of a SiO_2 shell around the Fe_3O_4 core modifies the absorbance profile similarly for both 30 nm and 50 nm cores, although the 30 nm core-shell NPs show a more pronounced increase in absorbance from the red end of the spectrum. This behaviour suggests an enhanced electromagnetic field and magneto-activity around the NPs upon resonance, reflecting a general trend seen in noble metals like gold and silver where larger NPs primarily scatter light, while smaller ones are more absorbent.

Remarkably, the optical absorption of $Fe_3O_4@SiO_2$ NPs under 500 nm wavelength is enhanced by three orders of magnitude compared to the uncoated Fe_3O_4 NPs. This indicates a significant improvement in absorption at shorter wavelengths for core-shell nanostructures with the SiO_2 layer. However, at lower wavelengths, the optical response of the core-shell NPs exhibits considerable noise, potentially due to interface roughness.

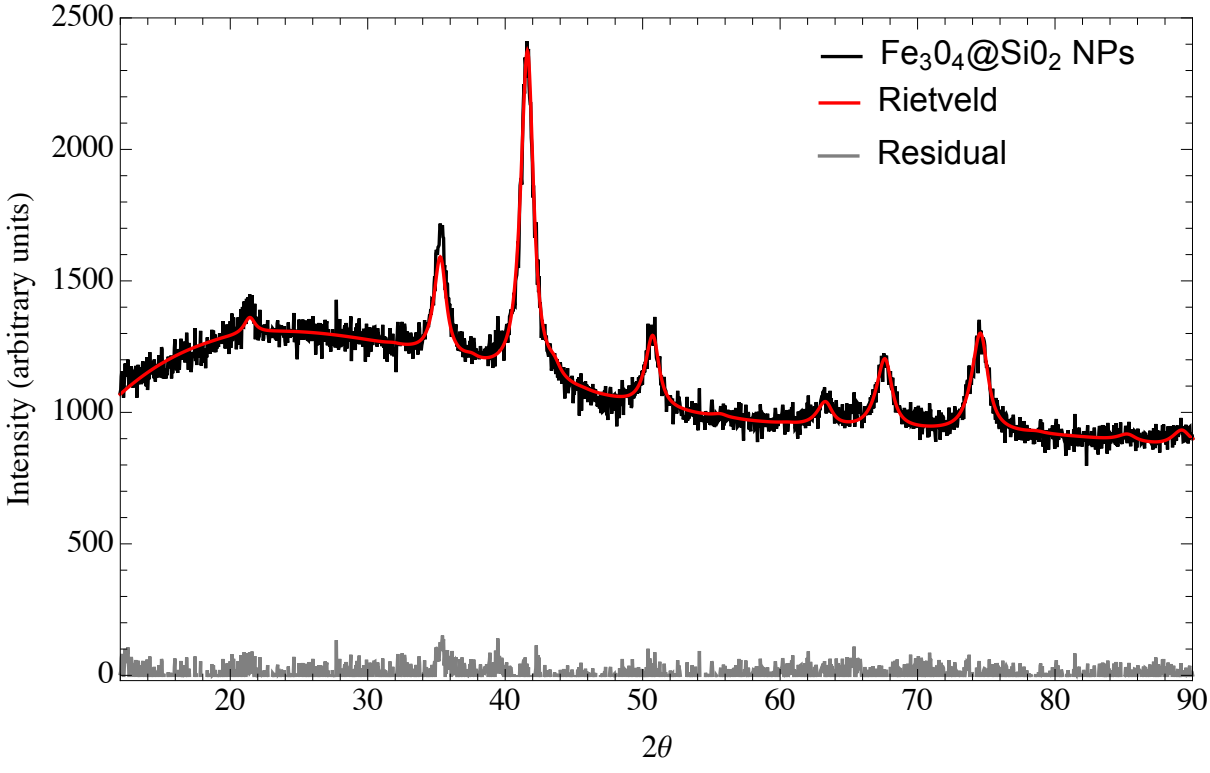
Subsequent findings pertaining to Ni NPs and their composite forms with SiO_2 coatings are detailed in Figure 4.12 (b). The spectral analysis showcases distinctive resonance phenomena within specific frequency ranges, characterised by substantial absorption or scattering of certain light frequencies. The variation in NP size reveals pronounced plasmonic effects, with some absorption peaks surpassing the geometrical absorption of the NPs.

The addition of SiO_2 coatings to the magnetic NPs results in red-shifted and broadened LSPR peaks, as opposed to the spectra of the bare magnetic NPs. This finding highlights the significant role of the SiO_2 coating in modulating the optical response of the magnetoplasmonic NPs, suggesting a substantial impact on their plasmonic behaviour. The conducted optical spectroscopy of magnetoplasmonic NPs elucidates the influence of NP size and surface coatings on their light absorption and scattering properties.

4.3.3 X-Ray Diffraction Measurements



(a)



(b)

Figure 4.13: XRD pattern of (a) Fe_3O_4 and (b) $Fe_3O_4@SiO_2$ NPs. The diffraction patterns were compared to the known spectra of Fe_3O_4 [589–592].

The crystalline structure and purity of powdered magnetic nanoparticles were scrutinised through X-ray diffraction (XRD) analysis. Specifically, the XRD patterns of the Fe_3O_4 NPs are depicted in Figure 4.13 (a), alongside the Rietveld refined pattern. The observed diffraction peaks were indexed to correspond to the face-centered cubic (FCC) structure, underpinning the magnetite's Fd-3m space group, as per the standards of the Inorganic Crystal Structure Database (ICSD) reference number 26410.

Through Rietveld refinement, it was possible to deduce the average particle size and the lattice parameter with a significant degree of accuracy. The average crystallite particle size of the Fe_3O_4 NPs was estimated to be 8.68 $\pm$ 0.0843 nm. Concurrently, the lattice parameter was determined to be $a = 8.37 \pm 0.0110$ $\mathring{A}$.

Moreover, the analysis extended to the Fe_3O_4 NPs encapsulated with a SiO_2 shell, as showcased in Figure 4.13 (b), which demonstrates their dielectric environment compared to non-encapsulated NPs. The average particle size for the Fe_3O_4@SiO_2 NPs was calculated to be 12.14 $\pm$ 0.472 nm. This increase in size, compared to the uncoated Fe_3O_4 NPs, can be attributed to the SiO_2 shell enclosing the Fe_3O_4 NP core.

XRD measurements provided insightful data on the crystalline structure, purity, and particle size of the magnetic NPs.

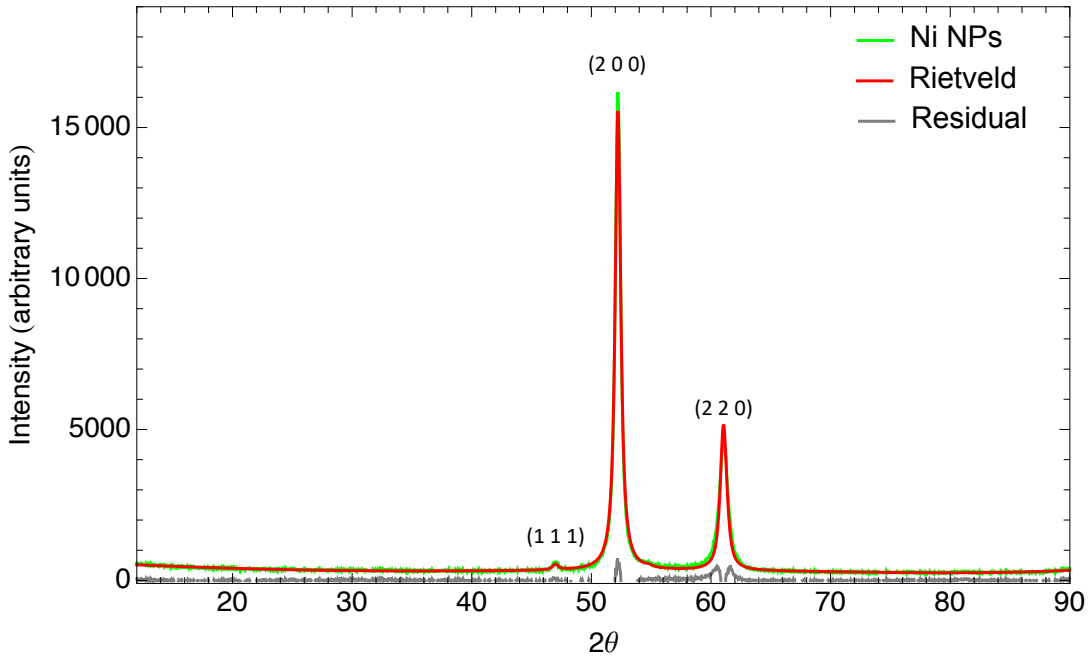


Figure 4.14: XRD patterns of Ni NPs. The pattern was compared with the known spectra of Ni [593–596], confirming the composition of the resulting NPs.

Figure 4.14 illustrates the typical XRD pattern for the prepared Ni NPs. The diffraction peak observed within this pattern can be accurately indexed to an FCC crystal structure lattice parameters, characterised by the Fm-3 space group. This structural identification corresponds with the entries for nickel in the ICSD-52265, confirming the crystalline nature of the synthesised sample.

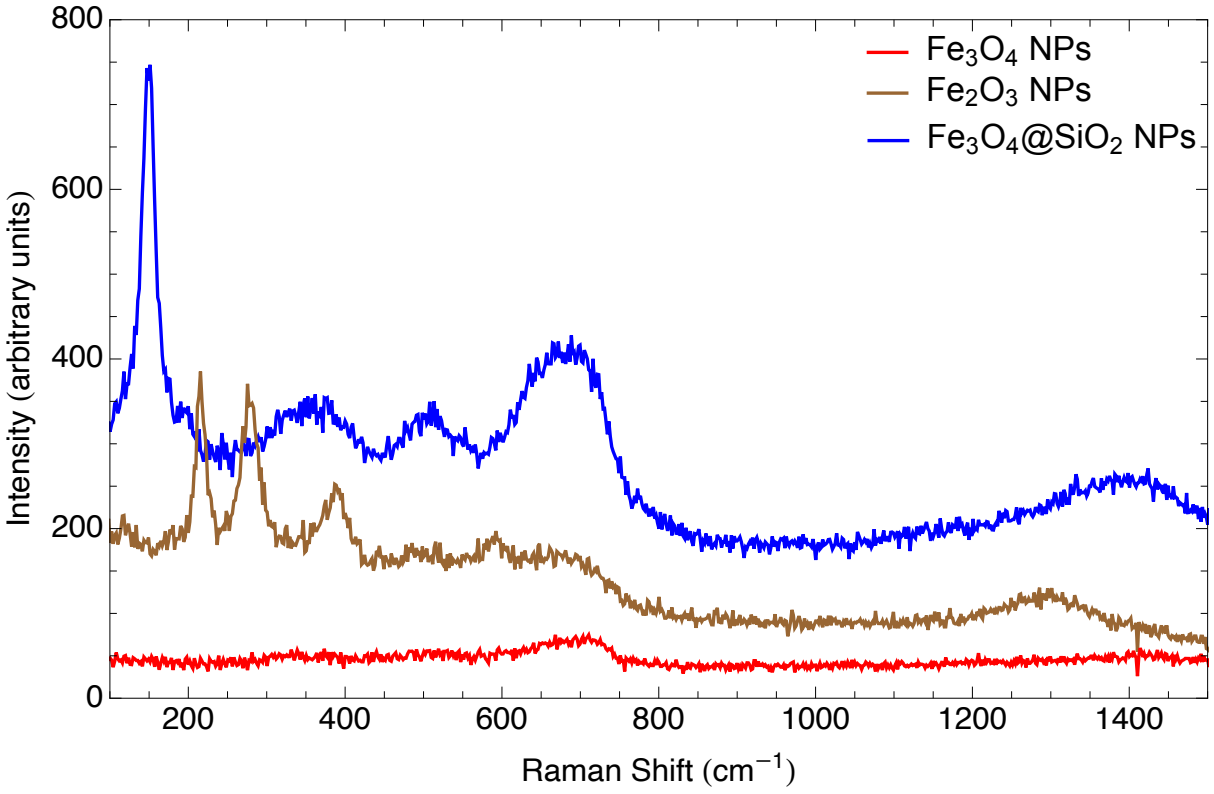
The outcome of the refined XRD analysis reveals that the average particle size of the Ni NPs is 19.2 nm. Furthermore, it underscores their nano-scale dimensionality, highlighting the effectiveness of the synthesis and refinement methods employed in accurately characterising the materials at the nanoscale.

4.3.4 Structural Properties by Raman Spectroscopy

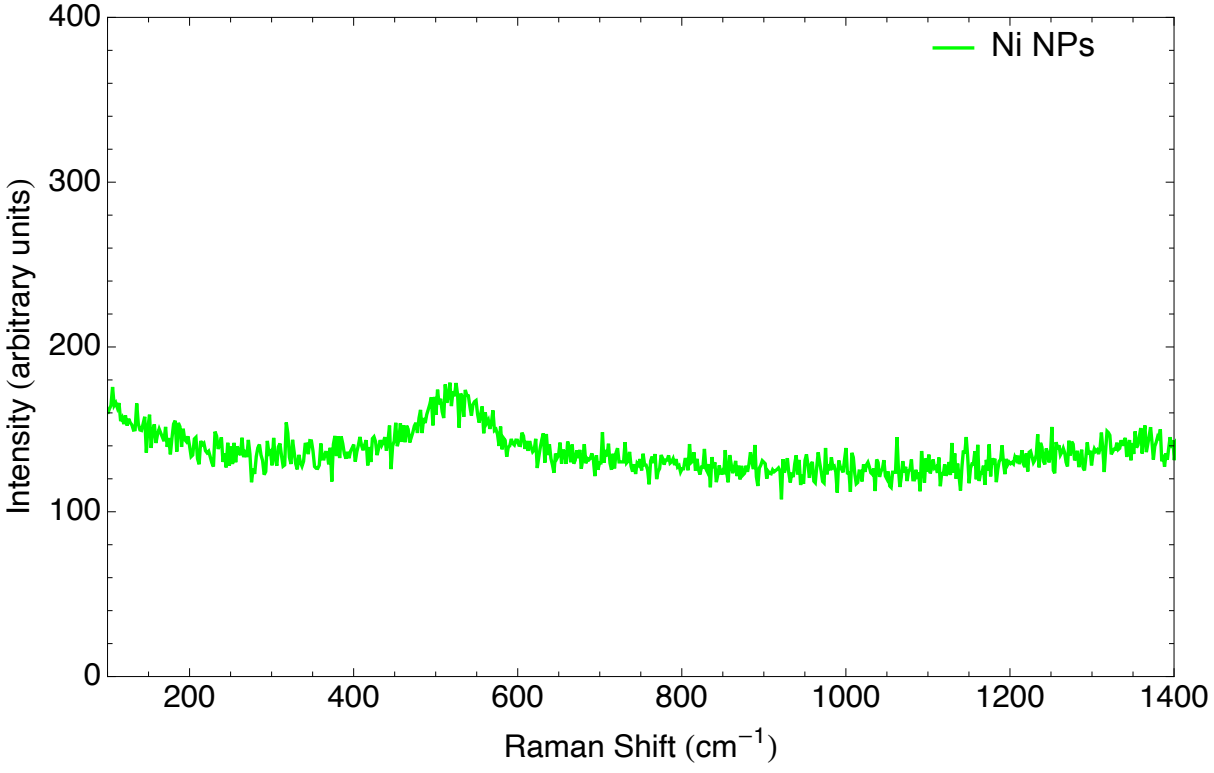
Raman spectroscopy was utilised to verify the presumed crystalline structure of iron oxides across varied compositions. Magnetite belongs to the O_h^7 space group, encompassing 14 vibrational modes. Out of these, A_{1g}, E_g and $3T_{2g}$ represent the five Raman active modes [597]. The spectra collected at ambient temperature reveal a pronounced peak around 684 cm^{-1} and it is associated with the A_{1g} mode. This peak signifies the symmetric stretching of oxygen atoms along the Fe-O bond. The E_g and $3T_{2g}$ modes, observed at 380 cm^{-1} and 370 cm^{-1} respectively, are too faint to be distinguished within the spectra. The presence of these vibrational modes is indicative of magnetite and corroborates with modes related to a cubic phase, as documented in the literature [598–600].

Moreover, core-shell nanostructures exhibit broader peaks in comparison to the pure magnetite spectrum. This amplification in Raman intensity is likely due to the surface-enhanced Raman scattering (SERS) effect, which enhances the local electromagnetic field owing to plasmon resonances in $Fe_3O_4@SiO_2$ core-shell NPs. In the realm of thermal stability, the magnetite phase initially transitions into maghemite and ultimately transforms into hematite upon heating in air [601]. Such a transformation is readily facilitated by excessively high laser power. This phenomenon is conspicuously observed in Figure 4.15 (a), where the magnetite (depicted in red spectrum) transitions into hematite (illustrated in brown spectrum) following an increase in laser power from 0.04 mW to 0.4 mW, with the excitation wavelength maintained at 514.5 nm for both instances.

The Raman spectrum of Ni, as presented in Figure 4.15 (b), showcases a notable Raman band at approximately 522 cm^{-1}. This finding is consistent with earlier research by Gellini et al. (2017) [602], which documented a Raman band for Ni within the 505-530 cm^{-1} range. Thus, the observed Ni spectrum concurs with existing literature [603–607], affirming the presence of characteristic spectral features related to the Ni stretching mode. Collectively, the identified spectral characteristics within the Ni spectrum offer critical insights into the chemical composition of the material under examination and substantiate its characterisation as Ni.



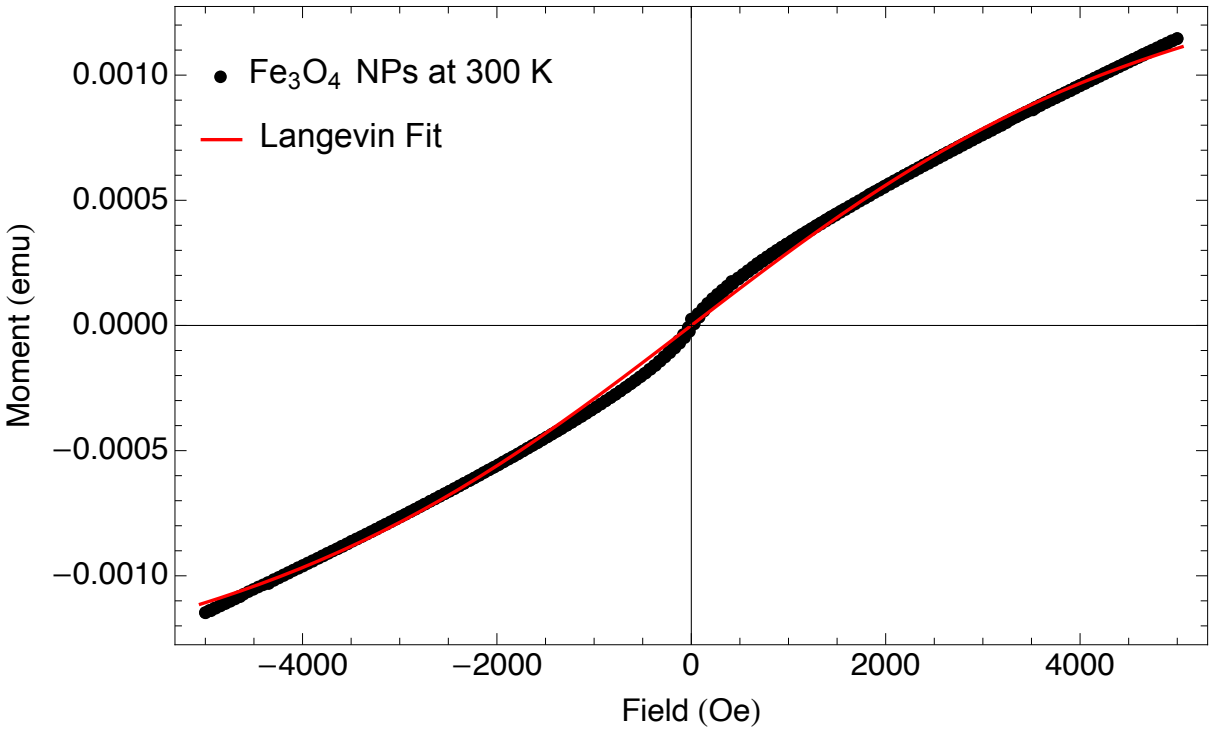
(a)



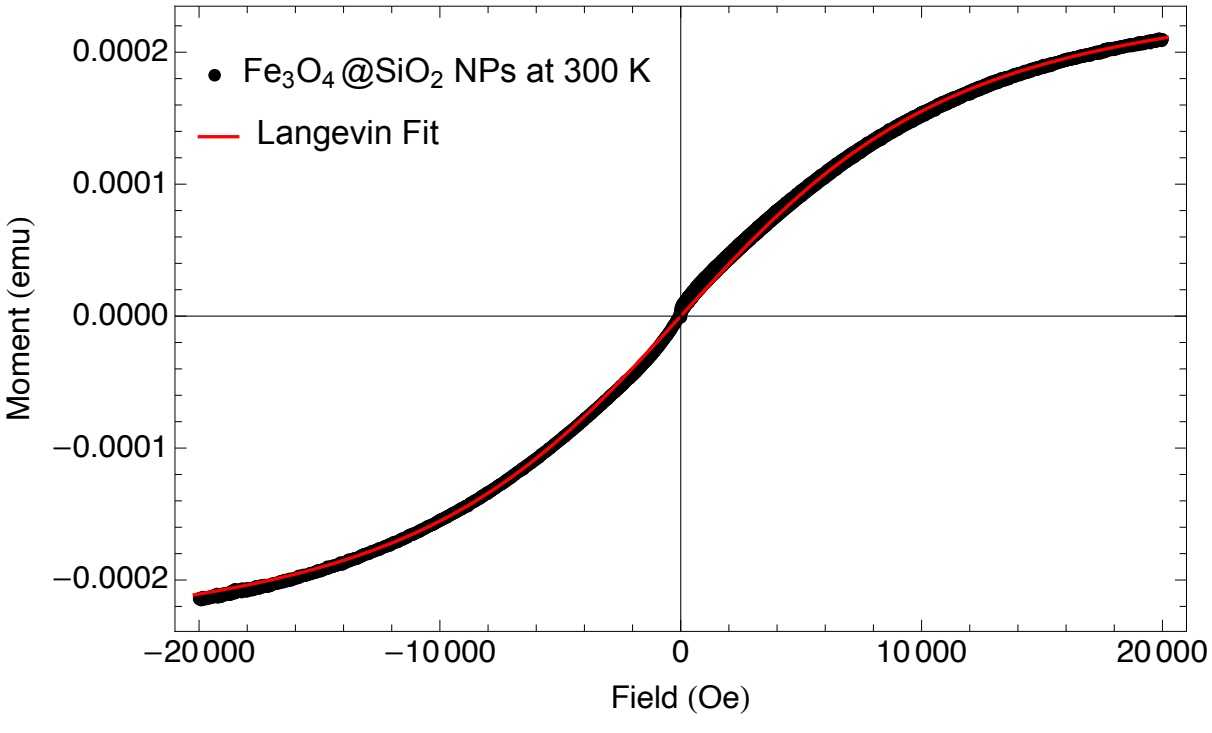
(b)

Figure 4.15: XRD pattern of (a) Fe_3O_4 and (b) $Fe_3O_4@SiO_2$ NPs. The diffraction patterns were compared to the known spectra of Fe_3O_4 [589–592].

4.3.5 Magnetic Measurements



(a)



(b)

Figure 4.16: Magnetic hysteresis loop of (a) Fe_3O_4 NPs and (b) $Fe_3O_4@SiO_2$ core-shell NPs. The fit uses a modified Langevin function at 300 K.

From the hysteresis loops depicted in Figure 4.16, we could deduce several key parameters employing the $\frac{1}{H}$ law [608] and incorporating the Langevin function for data analysis.

These parameters include the saturation magnetisation (M_s) and the average particle diameter (D). By integrating a paramagnetic term into the Langevin function, the following relation was derived [609]:

$$M(H) = M_s \left[\coth\left(\frac{\mu_p H}{k_B T}\right) - \frac{k_B T}{\mu_p H} \right] + \chi_a H \tag{4.1}$$

Here, μ_p, the magnetic moment per particle, is given by:

$$\mu_p = \frac{M_s \pi D^3}{6} \tag{4.2}$$

In equation (4.1), k_B represents the Boltzmann constant, and χ_a denotes the high-field susceptibility, which correlates to the assumed paramagnetic surface contributions within the NPs. Consequently, equation (4.1) simplifies to:

$$M(H) = M_s \left[\coth\left(\frac{\mu_p H}{k_B T}\right) - \frac{k_B T}{\mu_p H} \right] \tag{4.3}$$

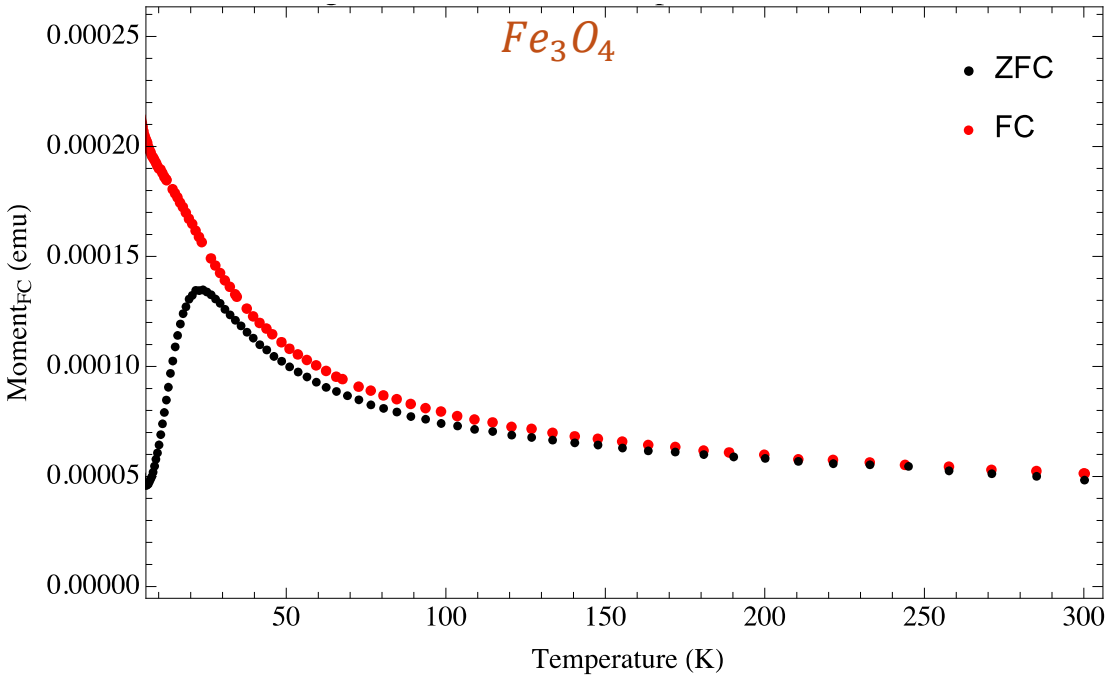
Analysis of Figure 4.16 (a) for Fe_3O_4 NPs revealed that M_s is 0.280 emu/g, μ_p is $173.7\mu_B$, and the average diameter (D) is 22.2 ± 2.1 nm. For the $Fe_3O_4@SiO_2$ core-shell nanostructures, as shown in Figure 4.16(b), the findings were $M_s = 0.0339$ emu/g , $\mu_p = 78.2\mu_B$, and $D = 34.4 \pm 2.3$ nm.

It is important to note that nanometer-sized ferrimagnetic or ferromagnetic particles exhibit superparamagnetic behaviour, characterised by a significant magnetic moment and unstable orientation due to thermal fluctuations. This instability arises when the thermal ambient energy exceeds the magnetic anisotropy energy [610]. In the regime where the ratio $\frac{\mu_p H}{k_B T}$ is much less than 1, at high temperatures, equation (4.3) simplifies further to [611]:

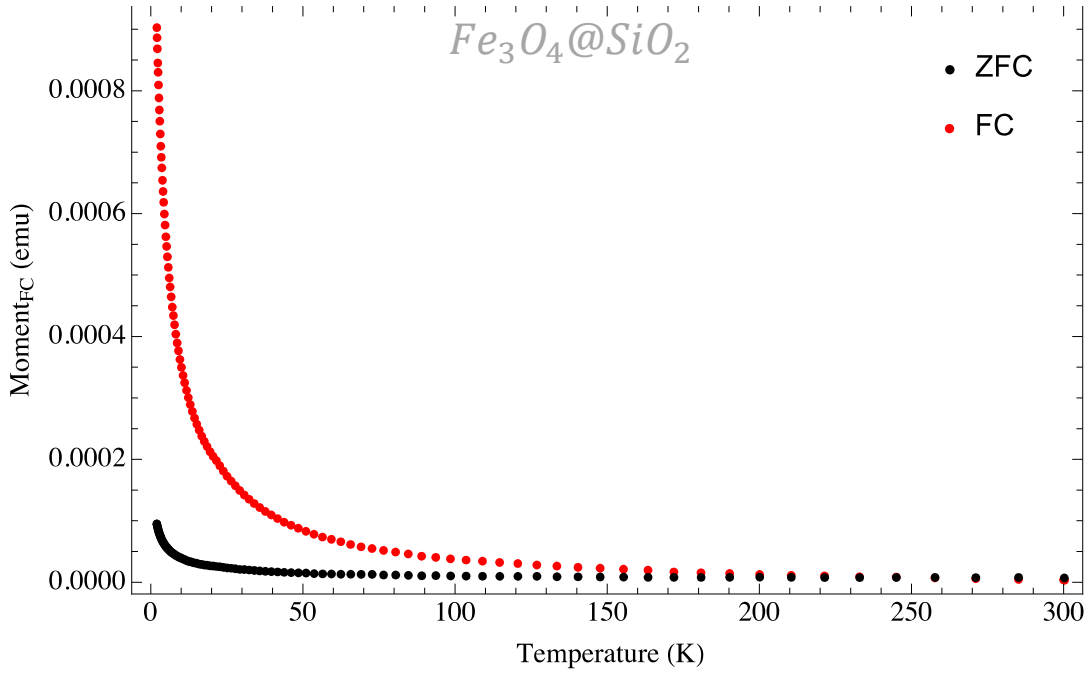
$$M(T) = \frac{H M_s^2}{3 k_B T} \tag{4.4}$$

This simplification aids in understanding the thermal behaviour and magnetic properties of these NPs at elevated temperatures, highlighting their potential applications and the physics governing their magnetic responses.

Each individual magnetic NP possesses a characteristic temperature known as the blocking temperature (T_B), which signifies the transition from a state where the magnetic moment is kinetically responsive to one where it is kinetically unresponsive as the temperature (T) decreases. The magnetic moment M(T) is null for temperatures below T_B ($T < T_B$) and increases for thermally unblocked NPs at temperatures above T_B



(a)



(b)

Figure 4.17: Temperature dependence of the zero-field-cooled (ZFC) and field-cooled (FC) magnetisation in a 0 and 100 Oe measuring field of (a) Fe_3O_4 NPs and (b) Fe_3O_4@SiO_2 core-shell NPs.

($T > T_B$). The plots displayed in Figure 4.17 illustrate the Zero-Field Cooled (ZFC) and Field Cooled (FC) conditions, enabling the determination of the distribution parameters of the blocking temperatures for individual particles in a non-interacting scenario. Analysis of Figure 4.17 reveals that, with increasing temperature, the particles acquire

sufficient thermal energy to surmount the energy barrier, altering their magnetisation direction to align with the external magnetic field. Consequently, an initial increase in magnetisation with rising temperature is observed for the ZFC curve. Upon reaching a certain temperature, the particles exhibit superparamagnetic behaviour, leading to a net decrease in magnetisation. This phenomenon is ascribed to the particles obtaining ample thermal energy to oscillate between parallel and antiparallel states with respect to the applied magnetic field.

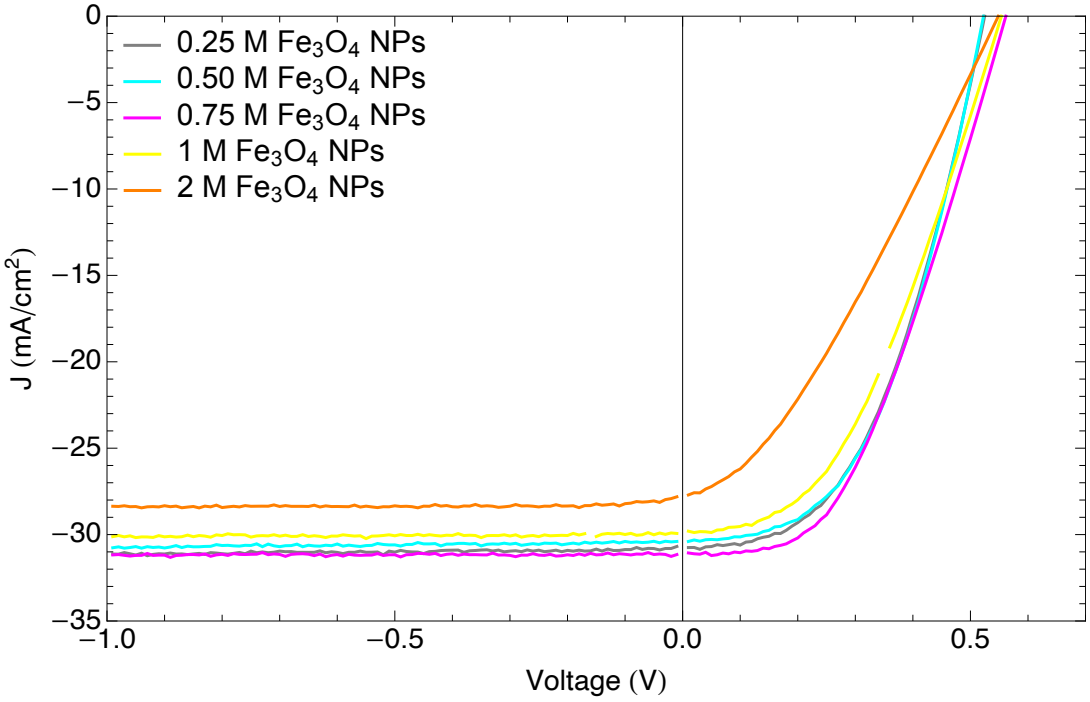
A notable peak in the ZFC magnetisation curve is identified at a blocking temperature of 28.1 K, with the breadth of the ZFC data predominantly influenced by the NP size distribution within the sample, as illustrated in Figure 4.17 (b). A discernible trend emerges, where smaller NPs attain a blocked state at lower temperatures, while larger NPs remain unblocked at elevated temperatures. It is critical to acknowledge that at high temperatures, the ZFC and FC curves exhibit a near-identical profile. However, as temperature diminishes nearing T_B, a divergence between the curves becomes evident. This behaviour suggests that below T_B, NPs exhibit ferrimagnetic characteristics, whereas above T_B, they transition to a superparamagnetic state.

4.3.6 J-V Characterisation of Magnetoplasmonic and Plasmonic Incorporated Si PV Devices

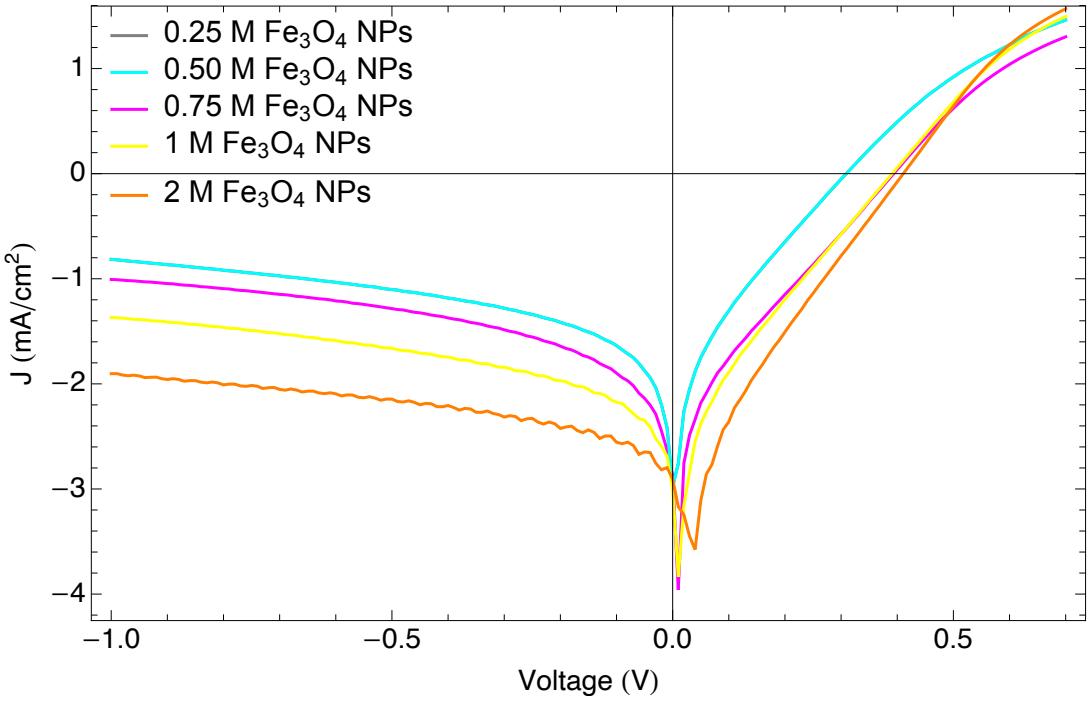
The investigation into the optimum concentration of Fe_3O_4 NPs for enhancing the efficiency of Si PV devices is critical for maximising their power conversion efficiency. In this study, Fe_3O_4 NPs were deposited onto the surface of pristine Si PV devices at five different concentrations, as detailed in Table 4.1. The effect of these concentrations on the photovoltaic performance was meticulously analysed, focusing on the key parameters of J-V characteristics such as short-circuit current (J_{sc}) and open-circuit voltage (V_{oc}).

The increase in built-in voltage for a silicon solar cell with a high concentration of Fe_3O_4 NPs (2M) can be attributed to several factors involving the properties and interactions of the NPs with the silicon substrate. Firstly, Fe_3O_4 NPs possess strong optical properties, including enhanced light absorption in the visible spectrum, which can increase the generation of electron-hole pairs, thus boosting the photo-generated voltage [612, 613]. Additionally, at higher concentrations, these NPs might improve surface passivation of the solar cell, reducing recombination losses and increasing efficiency. The presence of Fe_3O_4 NPs can also alter charge carrier dynamics by introducing localised electric fields or acting as trap sites, which affects charge separation and collection [614]. Furthermore, interactions at the NP-silicon interface might modify the semiconductor's band structure, influencing the built-in electric field. While an increase in series resistance could occur due to NP aggregation at very high concentrations, this effect might be offset by other benefits such as enhanced light trapping or improved passivation [367,615].

The dark current in Figure 4.18 (b) in the reverse bias condition increases with higher concentrations, which in turn leads to a decrease in photocurrent. This trend can be crucial in understanding efficiency losses in solar cells. Additionally, the characteristic of dark current density versus voltage indicates that the built-in voltage predominantly exists around $V = 0$. However, higher concentrations are associated with a shift in the built-in field, which may be a contributing factor to the observed reduction in



(a)



(b)

Figure 4.18: (a) shows the J-V characteristics for the pristine device and when it is incorporated with Fe_3O_4 NPs at different concentrations illuminated with light (1 sun through 1.5 AM filter). (b) shows the J-V dark conditions for all the samples.

open-circuit voltage (V_{oc}). In the forward bias case, the J-V characteristics reveal distinct regimes: there is a linear regime followed by a field-dependent mobility regime, characterised by a quadratic dependence on voltage (V^2). These findings suggest

complex interactions between material properties and device performance under different electrical.

Table 4.1: Summary of the performance of a-Si solar cells incorporated with optimised magnetoplasmonic NPs at different concentrations.

Device	$J_{sc}(mA/cm^2)$	V_{oc}(V)	FF(%)	PCE(%)	R_s	R_{sh}
	±3.6	±0.02	±1.2		$(\Omega \cdot cm^2)$	$(\Omega \cdot cm^2)$
Pristine	35.5	0.57	37.7	7.64	9.55	119
				±0.8	±0.04	±1.9
0.25 M Fe_3O_4	30.8	0.52	48.2	7.79	13.1	122
				±0.8	±0.02	±1.6
0.50 M Fe_3O_4	30.4	0.52	49.5	7.86	5.86	157
				±0.8	±0.02	±1.7
0.75 M Fe_3O_4	30.0	0.56	46.9	7.89	8.43	195
				±0.9	±0.03	±3.3
1 M Fe_3O_4	29.9	0.55	44.0	7.12	9.25	115
				±0.5	±0.04	±1.9
2 M Fe_3O_4	27.8	0.55	32.7	4.97	14.3	123
				±0.1	±0.06	±1.9

Table 4.1 that increasing the concentration of Fe_3O_4 superparamagnetic NPs beyond a 0.75 M concentration led to a degradation in photovoltaic device performance. This deterioration is primarily manifested through a reduction in J_{sc} and a slight decline in V_{oc} compared to the pristine device. The augmentation of J_{sc} observed in devices with Fe_3O_4 NPs suggests an enhancement in light absorption due to the plasmonic effects

induced by the NPs. However, this benefit is counterbalanced by the adverse impacts of high NP concentration.

This complex interplay between the beneficial plasmonic effects and the detrimental impacts of excessive nanoparticle concentrations underscores the need for a carefully optimised Fe_3O_4 NP deposition strategy. The results indicate that while a certain level of NP incorporation can enhance light absorption and thus the photovoltaic performance, there exists a critical concentration beyond which the adverse effects outweigh the benefits. Understanding and controlling the mechanisms by which Fe_3O_4 NPs influence Si PV devices are essential for the development of highly efficient and stable plasmonic and magnetoplasmonic photovoltaic systems [616, 617].

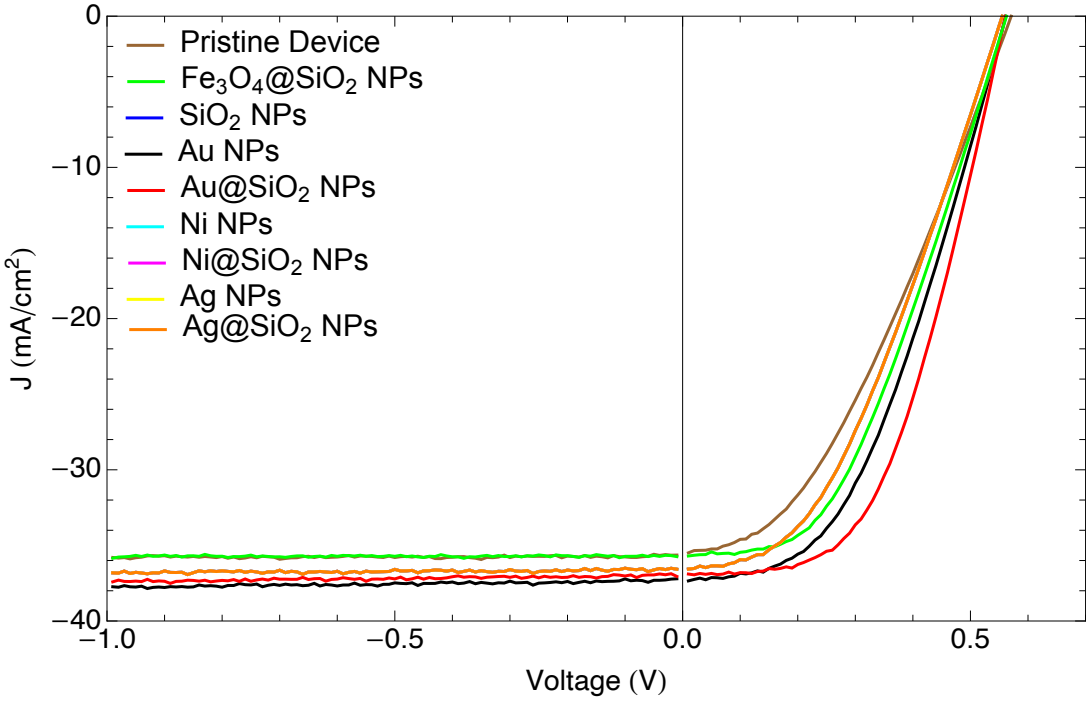
Figures 4.18 and 4.19 present the J-V characteristics of pristine a-Si solar cells with dimensions of 5 cm x 2.5 cm, and a similar device enhanced with plasmonic NPs, respectively. These measurements were conducted under illumination over an area of $2cm^2$. The device incorporating plasmonic NPs exhibited a noteworthy increase in photocurrent, achieving a total enhancement of 10.7%. This improvement is attributed to the enhanced light absorption facilitated by the NPs.

Table 4.2: Summary of the performance of commercial a-Si solar cells incorporated with plasmonic/magnetoplasmonic NPs and their core-shell nanostructures with SiO_2.

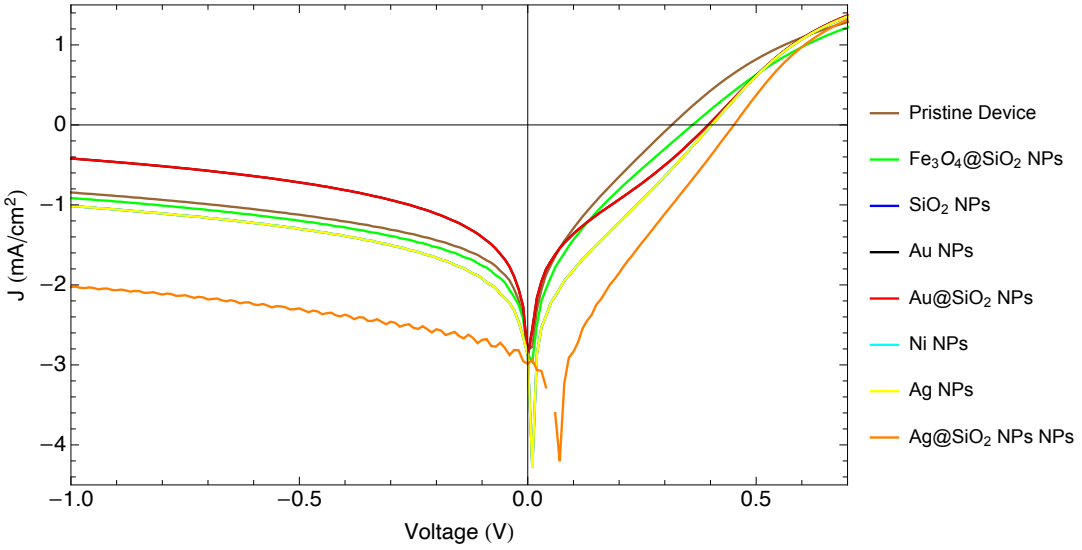
Device	$J_{sc}(mA/cm^2)$	V_{oc}(V)	FF(%)	PCE(%)	R_s	R_{sh}
	±3.6	±0.02	±1.2		$(\Omega \cdot cm^2)$	$(\Omega \cdot cm^2)$
Pristine	35.5	0.57	37.7	7.64	9.55	119
				±0.8	±0.04	±1.9
SiO_2	36.5	0.56	40.7	8.24	8.34	166
				±0.9	±0.03	±2.6
0.75 M Fe_3O_4	30.0	0.56	46.9	7.89	8.43	195
				±0.9	±0.03	±3.3
Fe_3O_4@SiO_2	31.0	0.53	46.9	8.27	12.7	263
				±0.3	±0.05	±4.4

Ni	36.5	0.56	40.7	8.24	8.32	246
				±0.6	±0.05	±4.6
$Ni@SiO_2$	36.6	0.57	42	8.72	8.19	126
				±0.2	±0.04	±2.6
Ag	35.5	0.55	46.5	9.15	7.03	168
				±0.2	±0.05	±3.6
$Ag@SiO_2$	32.9	0.58	51.3	9.69	6.67	123
				±0.3	±0.04	±3.3
Au	36.7	0.56	47.8	9.88	6.50	312
				±0.6	±0.03	±5.0
$Au@SiO_2$	36.9	0.56	51.4	10.7	5.60	122
				±0.7	±0.02	±1.9

Significantly, the addition of a SiO_2 shell to the plasmonic NPs resulted in the highest observed J_{sc} among the tested configurations, surpassing both the standard plasmonic and the magnetoplasmonic Si-cell devices. This enhancement can be attributed to the optimal alignment between the nanoparticle's resonance absorption and the optical bandgap of the Si solar cells. Key performance parameters extracted from the J-V curves, such as J_{sc}, V_{oc}, FF, and PCE are summarised in Tables 4.1 and 4.2. The incorporation of plasmonic NPs uniformly improved these metrics compared to the reference device. Notably, PCE of the reference a-Si solar cell, initially recorded at 7.64%, increased to 9.88% upon integrating Au NPs at the front end of the device. The highest J_{sc}, measuring 36.9 mA/cm^2, was observed for $Au@SiO_2$ core-shell NPs, which also exhibited the highest PCE at 10.7%. This increment in PCE aligns with the augmented absorption capabilities of these core-shell nanostructures, as demonstrated in Figure 4.11 (a). The presence of Au NPs enhances light absorption through preferential



(a)



(b)

Figure 4.19: (a) shows the J-V characteristics for the pristine device and when it is incorporated with plasmonic, magnetoplasmonic and core-shell NPs illuminated with light (1 sun through 1.5 AM filter). (b) shows the J-V dark conditions for all the samples.

scattering into the substrate, leveraging the LSPR effect to minimise optical losses and improve charge transport.

Additionally, the J-V characteristic curves under dark conditions reveal notable differences in leakage current among the devices. The pristine device showed the highest leakage, followed by those incorporating Au, SiO_2, and $Au@SiO_2$ NPs, respectively. The disparity in leakage currents may be linked to the NPs deposition method and the

interplay between nanoparticle thickness and device architecture.

Figure 4.18 further explores the J-V characteristics of devices enhanced with magnetoplasmonic NPs and their core-shell counterparts. Devices incorporating $Fe_3O_4@SiO_2$ NPs demonstrated superior efficiency compared to those with bare magnetite NPs. The PCE of devices augmented with magnetite NPs increased by 1.93%, 2.80%, and 3.16% for concentrations of 0.25 M, 0.50 M, and 0.75 M, respectively. However, higher concentrations of magnetite NPs (1 M and 2 M) diminished the PCE of the pristine device to 6.81% and 34.9%, respectively. The application of a SiO_2 shell on magnetite NPs effectively reduced recombination losses by exploiting light scattering and LSPR, leading to significant improvements in device performance metrics such as PCE and V_{oc}.

The integration of plasmonic layers, specifically those comprising $Au@SiO_2$ and $Fe_3O_4@SiO_2$ NPs, significantly enhanced the J_{sc}, FF, and PCE of commercial a-Si PV devices. However, the incorporation of bare Fe_3O_4 NPs at higher concentrations adversely affected the device's performance.

4.4 Conclusion

The comprehensive study detailed in Chapter 4 has underscored the potential of plasmonic and magnetoplasmonic nanostructures in enhancing the efficiency of silicon PV devices. By meticulously synthesising and characterising various nanostructures, including pristine single-component systems and SiO_2-embedded core-shell structures, significant insights into their optoelectronic properties were gained. The incorporation of plasmonic and magnetoplasmonic nanostructures into silicon solar cells has resulted in notable efficiency improvements. For instance, devices integrated with $Au@SiO_2$ core-shell NPs exhibited a substantial increase in photocurrent, achieving a PCE enhancement of up to 10.7%. This improvement is attributed to the enhanced light absorption and scattering facilitated by the LSPR effect of the NPs.

The study demonstrated that the efficiency of silicon PV devices could be maximised by optimising the concentration of magnetoplasmonic NPs. Specifically, $Fe_3O_4@SiO_2$ NPs at a concentration of 0.75 M yielded the highest efficiency gains without the detrimental effects observed at higher concentrations. This finding highlights the importance of precise (optical absorption losses) control over NP concentration to balance the beneficial plasmonic effects with the potential adverse impacts of excessive NP incorporation.

Core-shell nanostructures, particularly those with SiO_2 shells, have shown superior performance compared to their bare counterparts. The SiO_2 shell not only enhanced the stability and uniformity of the NPs but also played a crucial role in modulating their optical properties, leading to improved light absorption and reduced recombination losses. The study highlighted the importance of controlling the size, shape, and dispersion of NPs to achieve consistent and reproducible plasmonic and magnetoplasmonic properties. TEM and other characterisation techniques confirmed the uniformity and well-defined morphology of the synthesised NPs.

The incorporation of plasmonic and magnetoplasmonic NPs uniformly improved key

performance metrics, J_{sc}, V_{oc}, FF and PCE. For instance, the J_{sc} of devices incorporating $Au@SiO_2$ NPs reached 36.9 mA/cm^2, the highest observed among the tested configurations. The presence of Au NPs enhances light absorption through preferential scattering into the substrate, leveraging the LSPR effect to minimise optical losses and improve charge transport.

In conclusion, the research presented in this chapter provides compelling evidence that plasmonic and magnetoplasmonic nanostructures are viable candidates for enhancing the performance of silicon-based solar cells. The findings lay a strong foundation for future work aimed at further optimising NP synthesis, integration strategies, and device architectures to achieve even higher efficiencies in solar energy technologies. These advancements hold significant promise for the development of high-efficiency, cost-effective PV systems, contributing to the broader goal of sustainable energy solutions.

Chapter 5

5 Morphology Tuning of OSCs with Co-Solvent Additives

5.1 Introduction

The pursuit of efficient, cost-effective, and environmentally friendly energy solutions has placed organic solar cells (OSCs) at the forefront of renewable energy research [348]. OSCs offer the promise of lightweight, flexible, and easily scalable photovoltaic devices, making them an attractive alternative to traditional silicon-based solar cells [618, 619]. However, the performance of OSCs is critically dependent on the nanoscale morphology of their photoactive layers, which plays a pivotal role in charge generation, transport, and collection [620].

Achieving the optimal morphology in OSCs involves carefully balancing the intermolecular interactions between donor and acceptor materials within the photoactive layer. This balance is crucial for forming an interpenetrating network that facilitates efficient charge separation and minimises recombination losses [621]. However, the desired metastable morphology is often thermally sensitive, prone to phase separation, and difficult to maintain under operating conditions. This instability poses a significant challenge to the long-term performance and reliability of OSCs [622].

One promising approach to overcoming these challenges is the use of co-solvent additives during the fabrication process. Co-solvent additives can influence the solubility, miscibility, and crystallisation behaviour of the active materials, thereby allowing for precise control over the morphology of the photoactive layer [623]. By tuning these parameters, it is possible to enhance the PCE and stability of OSCs.

This chapter will first discuss the fundamental principles underlying the use of co-solvents, focusing on the Hansen solubility parameters (HSPs) and their application in predicting and controlling the solubility and miscibility of OSC materials. The chapter will then provide a detailed analysis of how these parameters can be leveraged to achieve desired morphologies by selecting appropriate co-solvents. By employing HSP, we can visualise and quantify the compatibility between different materials, facilitating the optimisation of blend morphology and enhancing electronic performance. The research will explore the underlying principles of co-solvent interactions using HSPs as a theoretical framework. Through a combination of theoretical computations and experimental validation, the study will identify optimal co-solvent systems that promote the formation of favourable morphologies in OSCs.

The objectives of this chapter are threefold:

1. To develop and validate a predictive model based on HSP for selecting effective co-solvent systems.
2. To elucidate the fundamental mechanisms by which co-solvent additives influence

the morphology of OSCs.

3. To experimentally demonstrate the enhancement in PCE and stability of OSCs through the application of optimised co-solvent additives.

5.2 Hansen Solubility Parameters

The PCE of OSCs is largely determined by the nanoscale morphology of the photoactive layer, which plays a critical role in achieving optimal charge generation, carrier transport, and collection [293, 493, 494]. However, maintaining the thermally activated metastable phase in morphology required for an optimised blend morphology is challenging due to its sensitivity to high-temperature ageing, which can cause a shift toward a thermodynamic equilibrium state, leading to significant phase separation and a decrease in device efficiency [56, 495]. Thermal effects can also induce drift from equilibrium to enhanced separation between donor and acceptor domains [55, 57, 59, 496–498].

There are various approaches to overcome the thermal instability of the D/A blends. However, one of the most effective and straightforward methods is blending host-active layers with additives. The gain of which is optimal blend morphology, improved electronic performance and device stability [314, 624, 625]. The formation of the interconnected network of the bulk heterojunction in an organic solar cells is attained after mixing of separately dissolved donor and acceptor solutions at a given temperature and for a given time. Therefore the effect of component solubility, miscibility and annealing will determine the metastable morphology of the blend. The application of Hansen solubility parameters as a criteria for tuning morphology provide insights into the solubility, miscibility, and phase separation behaviour of BHJ. Hansen solubility parameters have thus been used to predict the solubility of a polymer in a particular solvent or solvent mixture based on the similarity of their respective Hansen parameters as demonstrated in Figure 5.1. The Hansen solubility sphere provides a quantitative way to predict the solubility of materials by considering three primary forces: dispersive (δd), polar (δp), and hydrogen bonding (δh) interactions. Each material is represented by a point in this three-dimensional space, and the closer two materials are within this space, the more compatible or miscible they are. The three primary forces can be expressed as solubility parameter distance R_a:

$$R_a = \sqrt{4(\delta_{d2} - \delta_{d1})^2 + (\delta_{p2} - \delta_{p1})^2 + (\delta_{h2} - \delta_{h1})^2} \tag{5.1}$$

By leveraging this principle, co-solvents can be identified that match the solubility profile of specific OSC materials, promoting more effective morphology control during film formation. The relative energy difference (RED) number is often used to quantify the ratio of R_a to the interaction radius R_0 [626]:

$$RED = \frac{R_a}{R_0} \tag{5.2}$$

The interaction radius is a measure used to quantify the characteristic distance at which the solvent molecules interact with the solute molecules in a solution. This parameter reflects the effective range over which the solvent can influence the solute's properties, such

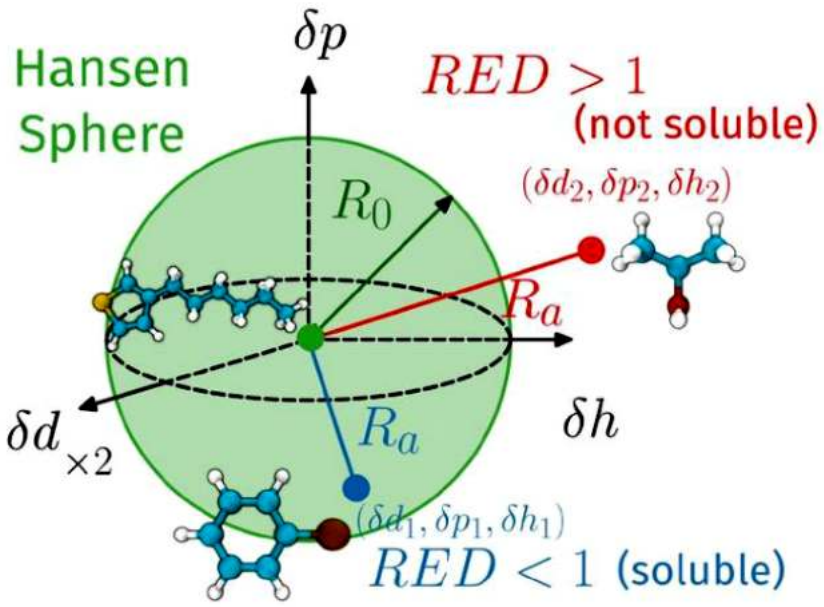


Figure 5.1: Visualising Compatibility: The Hansen solubility sphere maps the universe of solvents in a 3D space defined by dispersion, polar, and hydrogen bonding forces.

as solubility or molecular orientation. In the context of OSC materials and their processing, understanding R_0 is crucial for selecting appropriate co-solvents that can tailor the device's morphology by promoting or inhibiting specific interactions at the molecular level

By this definition, $RED = 0$ is equivalent to no energy difference, $RED < 1$ indicates high solute-solvent affinity, $RED > 1$ indicates low affinity and $RED = 1$ (or around 1) reflects a boundary condition. Experimental results have demonstrated that manipulating the RED between the donor and acceptor materials in BHJ OSCs can significantly impact their performance, with smaller RED values leading to improved device efficiency and enhanced charge generation and collection [627–629].

In Figure 5.2, we illustrate the results of the Hansen solubility parameter (HSP) calculations. The initial column lists the donor and acceptor materials, while columns two through ten detail the solvents along with their corresponding RED values, showcasing how these solvents interact with the OSC materials.These calculations are instrumental in the development of the morphology of the bulk heterojunction in OSCs, guiding the selection of compatible solvents. By analysing the solubility parameters of various active layer materials, these calculations help in pinpointing suitable solvents that can function effectively as co-solvents or additives. This selection is critical for optimising the fabrication process, ensuring that the materials involved in the OSC construction are not only compatible with each other but also conducive to the production of efficient and durable solar cells. Through this meticulous pairing of materials and solvents, based on their solubility parameters, the calculations lay the groundwork for advancing OSC technology by enhancing the performance and reliability of the devices.

The solvents used for the calculations in the table in Figure 5.2 are:

- Chloroform (CF)
- Chlorobenzene (CB)
- ortho-Dichlorobenzene (o-DCB)
- 1,8-Diiodooctane (DIO)
- 1-Chloronapthalene (1-Chloro)
- Toulene
- Eucalyptol (Eu)
- 2-Methylanisole (2-MEA)
- 2-Methyltetrahydrofuran (2-MeTHF)

	CF	CB	o-DCB	DIO	1-Chloro	Toulene	Eu	2-MEA	2-MeTHF
$PC_{70}BM$	RED= 0.8071	RED= 0.4221	RED= 0.2349	RED= 0.6585	RED= 0.2792	RED= 0.9002	RED= 1.24	RED= 1.005	RED= 0.583
$PTB7$	RED= 0.5188	RED= 0.3080	RED= 0.2194	RED= 0.3635	RED= 0.5695	RED= 0.3743	RED= 0.6427	RED= 0.4658	RED= 0.824
$PTQ10$	RED= 0.548	RED= 0.765	RED= 0.728	RED= 0.436	RED= 0.849	RED= 1.005	RED= 1.174	RED= 1.24	RED= 0.850
$Y6$	RED= 0.245	RED= 0.543	RED= 0.50	RED= 0.224	RED= 0.678	RED= 1.85	RED= 0.458	RED= 1.574	RED= 1.15
$PM6$	RED= 0.316	RED= 0.534	RED= 0.50	RED= 0.224	RED= 0.648	RED= 1.806	RED= 0.412	RED= 1.539	RED= 0.245
$ITIC-Th$	RED= 0.6545	RED= 0.8950	RED= 0.8889	RED= 0.7786	RED= 1.2271	RED= 1.2682	RED= 0.6266	RED= 1.012	RED= 0.346

Figure 5.2: HSP Analysis for Active Layer Materials in OSC Fabrication: Green values indicate solubility of the material in the solvent, while red values signify insolubility.

5.3 Tuning of Morphology of OSCs by Co-Additives

Device fabrication, particularly in the context of OSCs, involves a multitude of intricate processes tailored to optimise the performance characteristics of the final device. A pivotal aspect of this optimisation involves the morphology tuning of OSCs, where co-solvent additives play a significant role.

5.3.1 Fabrication Techniques for OSCs

The fabrication of thin films for OSCs is a critical aspect of their performance and efficiency. Various techniques are employed in laboratories and industrial settings to deposit organic semiconductor materials onto substrates, each with its own advantages and limitations. Key fabrication techniques are Spin Coating, Doctor Blading, Dip Coating, Inkjet Printing, Slot-Die Coating, Spray Coating, Screen Printing, and Vacuum Deposition. Each method is evaluated based on its ability to control film thickness, scalability for large-scale production, uniformity of film deposition, and suitability for specific applications [630–632].

Spin coating, while precise in controlling film thickness, may lack scalability for industrial production [633, 633, 634]. Doctor blading offers scalability and uniformity, making it suitable for large-area applications [635]. Dip coating provides flexibility in thickness adjustment but may not be as efficient for mass production [508, 630, 636–638]. Inkjet printing allows for precise patterning and reduced material waste, ideal for complex multilayer structures [639–641].

Slot-die coating proves efficient for continuous processes and large-scale manufacturing, while spray coating covers large areas quickly but may result in less uniform films [642, 643]. Screen printing is advantageous for creating thick layers and is widely used in large-scale production [644]. Vacuum deposition, although offering thin and uniform layers, is costlier and less suitable for flexible substrates [645, 646].

The fabrication process of the OSC devices in this study employed the spin-coating technique, with speeds ranging from 1500 rpm to 2000 rpm for durations of 40 to 60 seconds, as detailed in Table 5.2. This method allows precise control over film thickness by adjusting the spin speed and duration, which is crucial for the performance of OSCs.

5.3.2 Methodology

The devices were designed with an inverted structure, a configuration that differs from the traditional architecture by reversing the positions of the electron-donor and electron-acceptor layers. This structural arrangement, depicted in Figure 5.3, was chosen for its benefits in enhancing the operational stability and efficiency of the solar cells. The inverted structure is instrumental in optimising the interface between layers, thereby improving the overall photovoltaic performance of the OSCs.

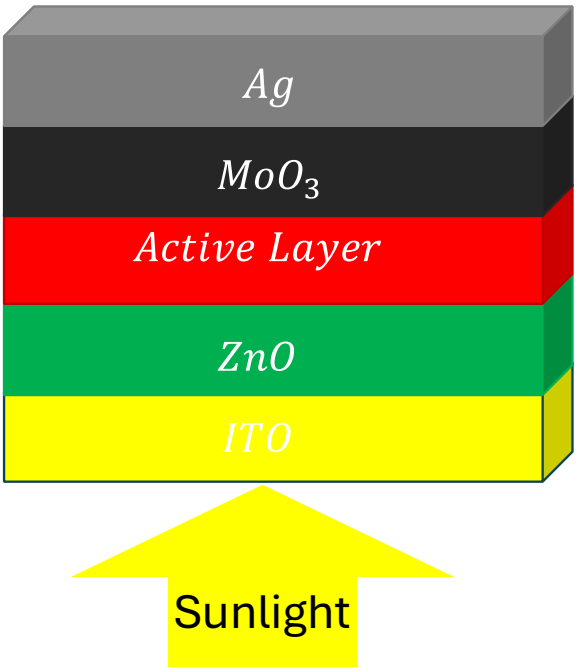


Figure 5.3: The structure of the standard inverted device architecture constituting MoO_3 and ZnO as the hole and electron transport layers, respectively.

Device Fabrication

The sequential steps towards device fabrication in this work are outlined below:

1. **Substrate Preparation:**

   The process begins with the preparation of ITO-coated glass substrates, each measuring 30 mm x 30 mm. These substrates are initially sonicated in a detergent solution to ensure thorough cleaning. Following this, they are sequentially rinsed with deionized water, acetone, and isopropyl alcohol (IPA), dedicating 15 minutes to each rinse to guarantee the removal of contaminants. To further eliminate any residual organic matter, the substrates undergo a 20-minute oxygen plasma treatment.

2. **ZnO Layer Deposition:**

   The next step involves depositing a ZnO layer via spin-coating performed in ambient air. This process ensures a uniform ZnO layer with a thickness ranging between 25 and 30 nm. The spin-coating parameters include a pipette volume of 200 μL, a spin speed of 4000 rpm, an acceleration of 2000 rpm/s, and a duration of 60 seconds. Post-deposition, the substrates are subjected to annealing at 200° C for 30 minutes to enhance the layer's properties.

3. **Active Layer Deposition:**

   The deposition of the active layer is conducted inside a glovebox, where the oxygen level is maintained below 0.2 ppm to preserve an inert atmosphere. This spin-coating process is meticulously controlled, with specific speeds and durations adjusted to accommodate the unique blend of materials and co-solvents used. After spin-coating, thermal annealing is performed, with temperatures and times fine-tuned according to the blend composition to optimise the layer's performance.

4. MoO_3 **Layer Deposition:**

   A uniform 10 nm MoO_3 layer is deposited using thermal evaporation. This step is carried out in a high vacuum environment, with a base pressure of 10^{-9} mbar maintained throughout the process to ensure the quality and consistency of the MoO_3 layer.

5. **Silver Electrode Deposition:**

   Finally, the deposition of the silver electrode is achieved through an automated thermal evaporation process, aiming for a layer thickness of 100 nm. The deposition is conducted in stages, starting with a rate of 0.2 $\mathring{A}/s$ for the first 15 minutes, followed by 0.8 $\mathring{A}/s$ for the next 20 minutes, and concluding with 1.5 $\mathring{A}/s$ for the final 10 minutes. Throughout this process, the base pressure is kept at 10^{-9} mbar to ensure a high-quality deposition of the silver electrode.

Organic Solar Cell Device Configurations

The selection of the three active layer compositions ($PTB7 : PC_{70}BM$, PTQ10:Y6, and $PM6 : Y6 : PC_{70}BM$) for studying their device configuration in the inverted device structure was based on specific solvent pairings and additives guided by the Hansen Solubility Parameters. These selections were made to optimise the morphology and

performance of the OSCs by controlling the interfaces, exciton dissociation, and charge transport efficiency, ultimately enhancing the power conversion efficiency and stability of the devices.

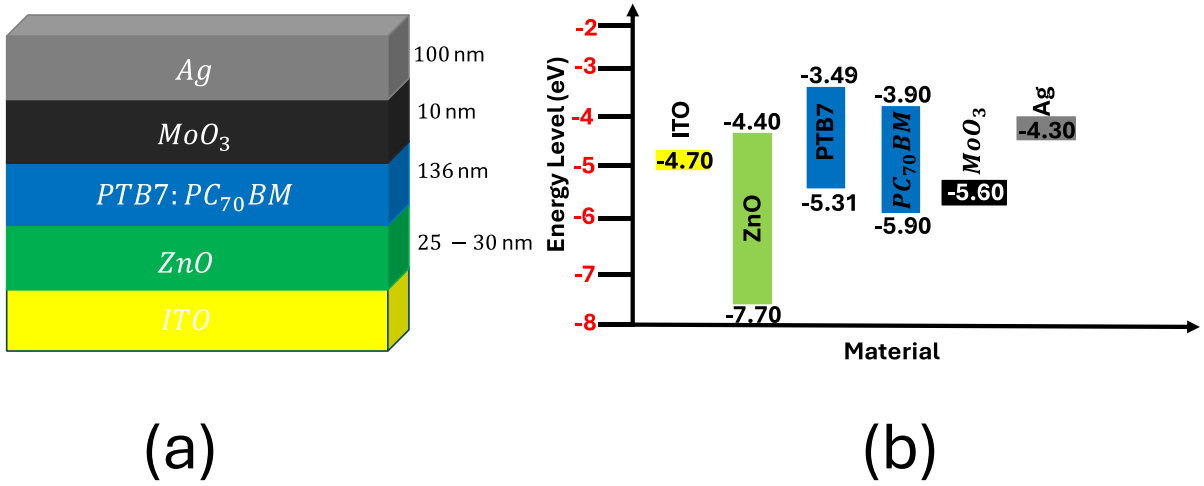


Figure 5.4: (a)Device architecture with the active layer of $PTB7 : PC_{70}BM$ and (b) the energy level diagram of the devices layers comprising of the work-function for the electrodes, the valence and conduction band of the oxides layers, the HOMO and LUMO of the photoactive layers.

Figure 5.4 (a) illustrates the architecture of an inverted configuration comprising of $PTB7 : PC_{70}BM$ blend. The role of dual solvents on the morphology of the photoactive layer and subsequently on the device properties was investigated. In this respect, a green solvent (2-MEA) was paired with an industrial solvent (Toluene) based on HSP calculations in Figure 5.2. The choice 2-MEA and toluene as a co-solvent system due to their ability to dissolve both components effectively while enabling a favourable morphology upon drying. Toluene is a non-polar solvent that can dissolve $PC_{70}BM$ well, and 2-MEA, being more polar, helps in dissolving PTB7 [647, 648]. The combination of green (2-MEA) and industrial (toluene) solvents considers both environmental impact and the practical aspects of solvent evaporation rates and solubility parameters. The material selection PTB7 as it is widely used donor polymer in OPVs due to its broad absorption spectrum and good charge transport properties. $PC_{70}BM$ is a common acceptor material known for its ability to efficiently dissociate excitons into free carriers [649].

In an energy diagram shown in Figure 5.4 (b), the LUMO level of $PC_{70}BM$ and the conduction band minimum of ZnO are typically aligned close in energy, facilitating electron transfer from the active layer to ZnO. Similarly, the HOMO level of PTB7 and the energy level of MoO3 are aligned to enhance hole transport. The overall diagram shows a step-wise energy level alignment from the HOMO of PTB7 to the work function

of ITO for holes, and from the LUMO of $PC_{70}BM$ to the work-function of Ag for electrons, driving the efficient separation and collection of charge carriers.

The field of OPVs has seen a significant evolution with the transition from fullerene-based acceptors to non-fullerene acceptors (NFAs), marking a pivotal shift in the design and efficiency of solar cells. Fullerene acceptors, once dominant in the OPV landscape, exhibit limitations such as suboptimal morphological compatibility with donors, susceptibility to photooxidation and oxidation, and constrained optical and electronic properties [650–652]. These limitations have spurred the search for more robust alternatives, leading to the emergence of NFAs like Y6. The material, Y6 distinguishes itself by offering superior optical absorption, enhanced electronic properties, and improved morphological stability, which significantly mitigates the issues associated with fullerene acceptors. Furthermore, Y6's compatibility with a broader range of donor materials allows for the creation of devices with higher efficiency and stability [56, 653].

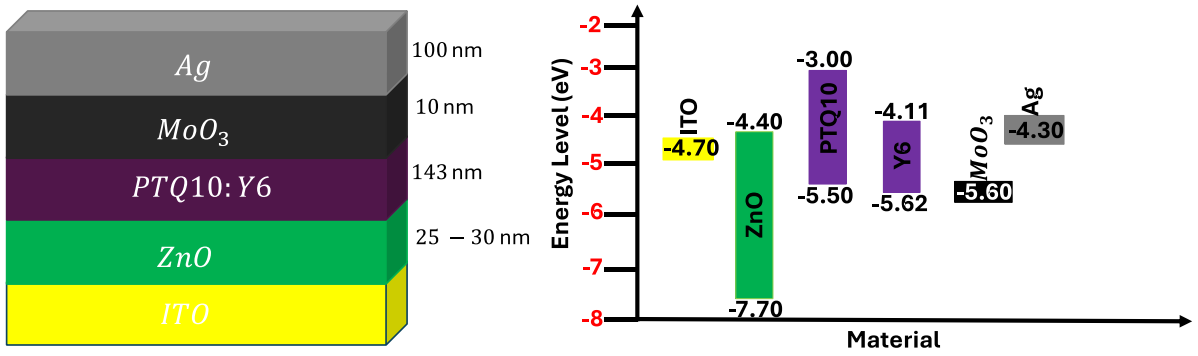


Figure 5.5: (a)Device architecture with the active layer of $PTQ10:Y6$ and (b) the energy level diagram of the devices layers comprising of the work-function for the electrodes, the Valence and Conduction band of the oxides layers, the HOMO and LUMO of the photoactive layers.

When comparing the properties of donor materials in two device configurations, the shift from $PTB7:PC_{70}BM$ in the first device configuration in Figure 5.4 (a) to PTQ10:Y6 in Figure 5.5 (a) is noteworthy. PTQ10, used in conjunction with Y6, exemplifies the advancements in donor material design aimed at optimising the interaction between donor and acceptor components. This pairing not only leverages the strengths of Y6 but also capitalises on PTQ10's tailored electronic properties and absorption characteristics, resulting in a device that potentially surpasses its predecessor in both efficiency and operational stability. This transition underscores the ongoing refinement and sophistication in OPV device architectures, promising a future of more efficient and durable solar

energy solutions.

Figure 5.5 presents the non-fullerene acceptor (NFA) based device, utilising $PTQ10 : Y6$ as the active layer. The figure compares the efficacy of environmentally benign solvents, Eu and 2-MeTHF, against a pair of chlorinated solvents, CF and 1-CN. The study's aim was to assess the performance trade-offs associated with transitioning to greener solvent systems.

The use of CF with 1-CN as an additive aims to achieve a specific interaction and solvation effect that benefits the morphology of the active layer. The comparison with green co-solvents like 2-MeTHF and Eu is significant for exploring more environmentally friendly alternatives that still provide the necessary solvation properties for both PTQ10 and Y6, likely based on their Hansen Solubility Parameters.

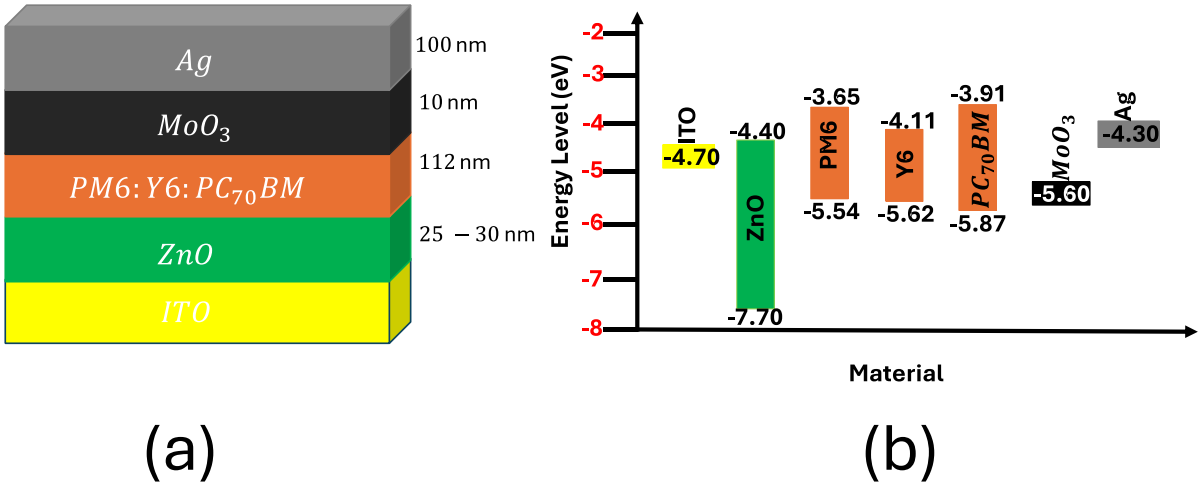


Figure 5.6: (a)Device architecture with the active layer of $PM : Y6 : PC_{70}BM$ and (b) the energy level diagram of the devices layers comprising of the work-function for the electrodes, the valence and conduction band of the oxides layers, the HOMO and LUMO of the photoactive layers.

Lastly, Figure 5.6 delineates the device employing a third component ($PC_{70}BM$) into the PM6:Y6 system within the active layer, which is aimed at further optimising the phase separation and morphological distribution within the active layer to enhance charge transport and collection efficiencies. The ternary blend is processed using a mixture of chloroform and co-additives DIO:1-CN. This arrangement was explored to understand the effects of solvent mixtures on the morphological distribution of the ternary constituents and their corresponding impact on the photovoltaic performance.

In the fabrication of OPVs, the solvents listed in Table 5.1 can be strategically chosen to fine-tune the solubility and mixing of donor and acceptor materials, crucial for achieving

Table 5.1: Comparative Properties of Selected Organic Solvents [654–658].

Solvent	Chemical Formula	Boiling Point (° C)	Melting Point (° C)	Flash Point (° C)	Toxicity Level	Dielectric Constant	Density (g/mL)
Chloroform	$CHCl_3$	61.2	-63.5	Non-Flammable	High	4.81	1.48
DIO	$C_8H_{16}I_2$	Variable	Variable	Variable	Moderate	N/A	N/A
1-Chloronaphthalene	$C_{10}H_7Cl$	258	-6	113	Moderate to High	N/A	1.19
Toulene	C_7H_8	110.6	-95	4	Moderate	2.38	0.87
Eucalyptol	$C_{10}H_{18}O$	176-177	1.5	48.5	Low to Moderate	N/A	0.92
2-MEA	$C_8H_{10}O$	173	N/A	> 38	Moderate	N/A	N/A
2-MeTHF	$C_5H_{10}O$	80	-136	-11	Moderate	7.58	0.86

optimal morphological characteristics. For instance, solvents with appropriate boiling points and evaporation rates are selected to control the drying kinetics, influencing the domain size and purity in the blend films [346]. Similarly, the dielectric constant of a solvent affects the dissociation of excitons and the formation of free charge carriers in the active layer [659]. The density and viscosity of solvents also play roles in the coating and printing processes, determining the uniformity and thickness of the film [660]. Moreover, understanding the toxicity and environmental impact of these solvents is essential for adopting greener and safer alternatives in the production process.

Therefore, the properties listed Table 5.1 are not just mere physical constants; they are critical factors that determine the efficiency, stability, and scalability of OSCs. By carefully selecting solvents based on these parameters and HSP calculations, the phase morphology of the active layer can be tuned, ultimately impacting the power conversion efficiency and the overall performance of OSCs. This holistic approach to solvent selection, grounded in the principles of HSP and informed by the detailed solvent properties, underscores the intricate interplay between high-performance and sustainable organic photovoltaics.

Characterisation Techniques

1. **Morphological Analysis:**

   - **Grazing Incidence Wide-Angle X-ray Scattering (GIWAXS):**Thin film samples designated for GIWAXS measurements were fabricated on Si substrates measuring 15 mm by 15 mm. The fabrication process employed was consistent with the established recipe used for device fabrication, ensuring uniformity and reproducibility across samples. This approach facilitated a direct comparison between the structural characteristics of the thin films and their performance in devices.

     GIWAXS analysis was conducted to elucidate the crystalline structure and orientation within the $PTB7 : PC_{70}BM$ thin films. The measurements were carried out on the ID-10 beamline at the European Synchrotron Radiation Facilities located in Grenoble, France. The diffraction patterns obtained during the GIWAXS measurements were recorded using a detector, of pixel size of 172×172 μm allowing for high-resolution capture of diffraction patterns. A wavelength of 1.24 $\mathring{A}$ was selected for the measurements, optimising the interaction between X-ray photons and the sample materials. These measurements were performed on the thin films affixed to Si substrates, positioned at an incidence angle of 0.2° to enhance the sensitivity of the method to surface and near-surface structural features.

2. **Optoelectronic Properties:**

   - **UV-Vis Spectroscopy:** To characterise the optical properties of the fabricated photovoltaic devices, optical absorption measurements were conducted using a Cary 500 UV-Vis Spectrophotometer. This instrument is well-suited

for precise and reliable spectral analysis across a wide wavelength range, typically spanning from 175 nm to 3300 nm. The Cary 500 UV-Vis Spectrophotometer operates based on the principles of ultraviolet-visible (UV-Vis) spectroscopy, which involves measuring the intensity of light before and after it passes through a sample to determine the absorbance at specific wavelengths.

Prior to measurement, the samples were prepared by depositing the active layers onto cleaned and treated ITO-coated glass substrates as described in the previous sections. These substrates, now coated with the various layers required for device functionality, were carefully mounted in the sample holder of the spectrophotometer. The instrument was calibrated using a blank ITO-coated glass substrate to establish a baseline for absorbance. This baseline measurement accounted for any inherent absorbance due to the substrate itself, ensuring that subsequent measurements reflected the optical properties of the deposited layers exclusively.

For the measurement process, the following parameters were set on the Cary 500 UV-Vis Spectrophotometer: The absorbance spectra were recorded over a range of 300 nm to 1000 nm. This range is particularly relevant for photovoltaic materials, as it encompasses the significant portion of the solar spectrum where these materials are expected to absorb light. A moderate scan speed was selected to balance measurement time and data resolution. Typically, a scan rate of 600 nm/min was employed. The slit width was set to 2 nm to ensure an appropriate balance between signal intensity and spectral resolution. Absorbance data were recorded at 1 nm intervals to provide a detailed absorption profile of the materials.

The Cary 500 UV-Vis Spectrophotometer software facilitated the acquisition of absorbance spectra. Each sample's spectrum was obtained by averaging multiple scans to minimise noise and improve data reliability. The resulting absorbance spectra were then analysed to identify characteristic peaks and shoulders corresponding to the optical transitions of the active materials. Key parameters extracted from the absorbance spectra included the onset of absorption, peak absorption wavelengths, and the overall shape of the absorption profile. These parameters provided insights into the electronic structure and light-harvesting efficiency of the photovoltaic materials.

- **Active Layer Thickness:** After deposition, accurately measuring the film thickness is crucial for characterising the device's performance, as the thickness of the active layer significantly impacts the absorption of light and the charge transport within the solar cell. In this case, a Dektak profilometer (Dektak 150) was employed to measure the thickness of the thin films. The film thickness was determined by measuring the average height difference over a specific area, typically performed in dried films at room temperature. This process involved making three scratches on the thin film deposited and then taking the average of the measurements from these three scratches to ensure accuracy and reliability in the thickness measurement process. The parameters of the fabrication of the active layers are displayed in Table 5.2.

- **Current-Voltage (J-V) Characteristics:** For the evaluation of current-voltage (J-V) characteristics and the determination of the maximum power point (MPP), a Keithley Instruments 2400 series Source Meter Unit (SMU) was utilised, conducting experiments in ambient air conditions, both under illumination and in darkness. Illumination was provided by a Wavelabs SINUS-220 simulator, simulating AM 1.5 irradiance, while darkness was ensured by a light-tight enclosure. The solar cell's effective exposure area was carefully defined by employing a mask with apertures for three sections of 0.25 cm^2 and one of 1 cm^2, constructed from black-anodised metal and positioned within the enclosure. The accuracy of these mask dimensions was verified via optical microscopy, confirming a deviation tolerance of $\pm$ 0.5%.

3. **Stability:**

   - Testing degrading of PCE.

5.3.3 Morphology and Optical Properties of the Active Layers

The performance of the OPV device is highly dependent on the morphology of the interconnected network of the donor and acceptor polymer. However, the optical properties of the active layer is the first limiting step towards device performance since it determines the maximum photon flux to be absorbed and subsequently limits photocurrent in the device. Besides, the optical absorption is determined by the optical density of the active layer thickness and complex refractive index. Although the light-matter interaction is intuitive, the nature of the optical properties in a blended active layer become rather a complex phenomena. In this section, effect of morphology on the optical properties of the blend layer formed from spin coating with various combination of solvents is presented.

The optical properties of the active layers in organic photovoltaic materials were investigated through the use of various solvents and their co-solvent mixtures. The absorption spectra shown in Figure 5.7 of chlorinated solvents, specifically CB and o-DCB, alongside their co-solvent blend (CB:o-DCB), revealed a distinct absorption peak centered around 370 nm. The absorption peak of $PC_{70}BM$ at 370 nm originates from the $\pi - \pi^*$ transition [661]. This peak is not solely dependent on the solubility or conformational change of the acceptor with different solvents but is influenced by the interaction between the solvent and the solute in both ground and excited states, affecting the transition energies and causing peak broadening [662]. This feature is highlighted by the dotted red circle in the spectroscopic data representing chlorinated co-solvents. In contrast, a broader absorption peak at approximately the same wavelength was observed for the green solvent (2-MEA) and the industrial solvent toluene, as well as their combined solvent system (2-MEA:Toluene), which is red shifted. The notable peak observed in the co-solvent mixture of 2-MEA and toluene suggests that the organic photovoltaic material, $PC_{70}BM$, is partially soluble in this solvent combination. This finding indicates a significant interaction between the solvents and the $PC_{70}BM$ material.

The optoelectronic properties of PTB7 involve transitions between different energy levels, as observed in the two peaks between 600 - 700 nm. These peaks correspond

Table 5.2: Parameters for Active Layer Fabrication.

Donor: Acceptor	Solvents	Solution Concentration (mg/mL)	Spin Speed (rpm)	Thickness (nm)
$PTB7 : PC_{70}BM$ (1:1.5)	$2-MEA : Toulene$ (7:3)	20	1500	136
$PTB7 : PC_{70}BM$ (1:1.5)	$2-MEA$ (1)	20	1500	113
$PTB7 : PC_{70}BM$ (1:1.5)	$Toulene$ (1)	20	1500	134
$PTB7 : PC_{70}BM$ (1:1.5)	$CB : o-DCB$ (1:1)	20	1500	149
$PTB7 : PC_{70}BM$ (1:1.5)	CB (1)	20	1500	142
$PTB7 : PC_{70}BM$ (1:1.5)	$o-DCB$ (1)	20	1500	138
$PTQ10 : Y6$ (1:1.2)	$CF : 1-CN$ (199:1)	16	1500	143
$PM6 : Y6 : PC_{70}BM$ (1:1:0.2)	$CF : DIO : 1-CN$ (194:5:1)	16	1500	114

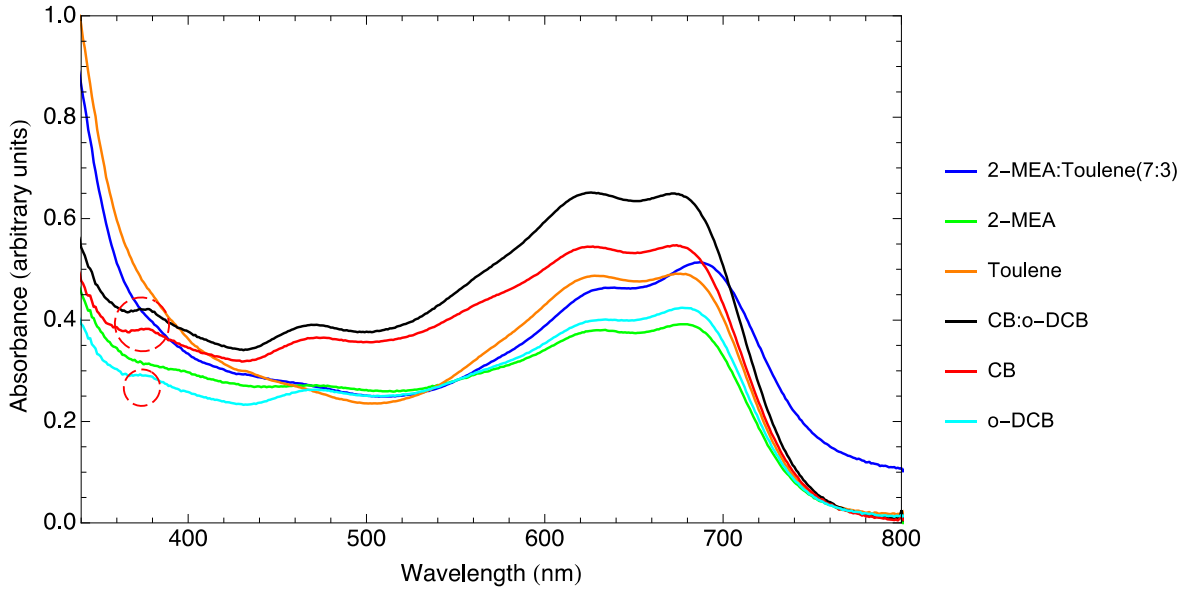


Figure 5.7: Optical absorbance spectra for the $PTB7 : PC_{70}BM$ active layer thin film on glass, showcasing results using chlorinated solvents, industrial-grade solvents, eco-friendly solvents, and their respective blends.

to transitions between the ground state and the first two vibronic levels A_{0-0} and A_{0-1} of excited states of the donor, E_{0-0} and E_{0-1}. These transitions are crucial in understanding the behaviour of PTB7 in optoelectronic applications.

Further insights were provided by HSP calculations as depicted in Figure 5.2. The solubility of $PC_{70}BM$ in toluene is characterised by a RED value of 0.9002, while the donor material PTB7 has an RED value of 0.3743, leading to a blend RED value of 0.6373 for the $PC_{70}BM$/PTB7 combination. In the case of 2-MEA, the RED values for $PC_{70}BM$ dissolution are notably higher at 1.005, reinforcing the notion of partial solubility. The increased absorbance intensity observed with the co-solvent (2-MEA:Toluene) mixture is likely due to the presence of undissolved $PC_{70}BM$ particles, suggesting an elevated absorption from the spectra of the thin film.

Conversely, the RED values for $PC_{70}BM$ in chlorinated solvents showcase variation; in CB the RED is 0.9899, while in o-DCB it decreases to 0.4168. PTB7 presents RED values of 0.3080 in CB and a lower 0.2194 in o-DCB. The differences in these values suggest that the active layer components, $PC_{70}BM$ and PTB7, achieve a more effective dissolution in chlorinated solvents as opposed to green solvents. Consequently, the co-solvent mixture (CB:o-DCB) exhibits superior absorbance characteristics compared to the individual chlorinated solvents, underscoring its enhanced potential for use in organic photovoltaic applications.

Chlorinated co-solvents can influence the band-gap energies of systems they are involved in, affecting the electronic transitions within these systems. The presence of chlorinated solvents can lead to changes in the absorption spectra and morphology of

materials, particularly in systems like OSCs [663–666]. The use of co-solvents, such as chlorinated ones, in processing OPVs can impact the aggregation and phase separation behaviour of the materials. Specifically, the presence of co-solvents like o-DCB can affect the onset of polymer aggregation and the formation of large domains in the material [667].

Chlorinated solvents enhance the photoabsorption of blends through various molecular interactions. Their high polarity improves solubility and uniformity of the blend, while their higher refractive indices can increase light absorption by reducing scattering. Chlorinated solvents also facilitate the formation of charge transfer complexes, leading to new or enhanced absorption bands [668, 669]. Additionally, they influence molecular packing and aggregation, which can improve electronic interactions and enhance absorption. The introduction of new vibrational modes and the stabilisation of conformations that are conducive to light absorption are further mechanisms through which these solvents contribute to photoabsorption [670–672]. These effects vary with the specific blend and solvent used, highlighting the complexity of their interactions at the molecular level.

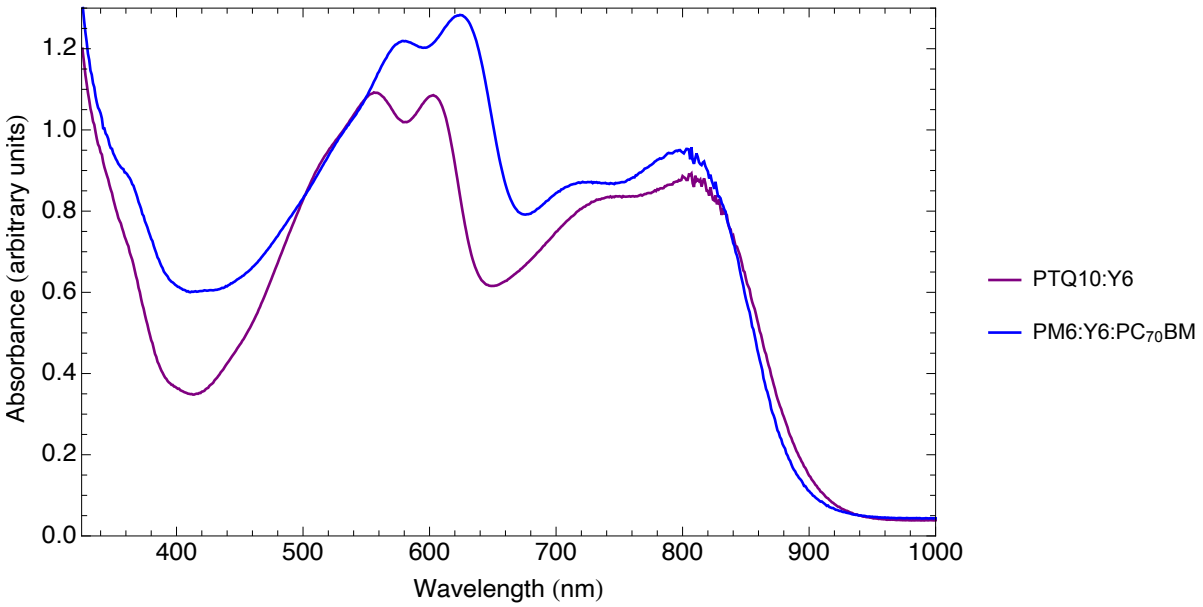


Figure 5.8: Optical absorbance spectra for the PTQ10:Y6 and $PM6 : Y6 : PTB7 : PC_{70}BM$ active layers.

The study of absorbance spectra within the realm of OPV materials is a pivotal aspect of advancing solar energy technology, offering deep insights into the electronic structure, energy levels, and potential efficiency of these materials. The focus on specific active layer compositions, such as PTQ10:Y6 dissolved in a solvent mixture of CF:1-CN, alongside $PM6 : Y6 : PC_{70}BM$ dissolved in CF: DIO:1-CN, represents a sophisticated approach in tailoring the physical and chemical properties of the active layers to optimise solar energy conversion efficiency.

PTQ10 and Y6, when dissolved in CF:1-CN, create an active layer that capitalises on the synergistic effects of both materials' absorption characteristics, potentially leading to a broadened absorption spectrum and improved photovoltaic performance. PTQ10, known for its wide absorption range and high charge mobility, combined with

Y6, a non-fullerene acceptor with excellent electron-accepting capabilities, suggests a promising path toward high-efficiency OPV cells [673–675]. The choice of CF:1-CN as a solvent plays a crucial role in achieving a homogeneous solution, facilitating optimal film formation and morphological stability.

On the other hand, the ternary blend of PM6, Y6, and $PC_{70}BM$, dissolved in a mixture of CF:DIO:1-CN, introduces an additional component, $PC_{70}BM$, a fullerene derivative, into the active layer. This blend aims to not only capture a wide range of the solar spectrum through the complementary absorption profiles of PM6 and Y6 but also to enhance the charge transport and collection efficiency through the well-established electron-accepting properties of $PC_{70}BM$. The inclusion of DIO in the solvent mixture is a strategic choice, known to influence the morphology of the active layer positively, promoting phase separation at the nanoscale, which is critical for efficient charge separation and transport.

Optical characterisation of active layer blends was performed, and the outcomes are presented in Figure 5.8. The figure illustrates the features in the spectra of a PTQ10 and Y6 blend. The blend has a mass ratio of 1:1.2 and is formed from a co-solvent mixture of chloroform and 0.5% 1-CN. Two strong absorption peaks are observed within the range of 400 to 610 nm for the PTQ10:Y6 blend and they correspond to $\pi - \pi^*$ transitions. The extrapolation of the absorption peak at 610 nm to the wavelength axis leads to an estimated band edge of 684 nm corresponding to an energy gap of 1.90 eV. This is really interesting because one could also have photoabsorption in the acceptor, Y6. The range 700 -900 nm is associated with the aggregation of the Y6 NFA, there are reports of the time dependent crystallisation process after solvent volatilisation, which is associated with the $\pi - \pi^*$ stacking and the red shifting of these bands [676].

A comparative analysis with a ternary blend composed of PM6, Y6, and $PC_{70}BM$ (with a ratio of 1:1:0.2) in a co-solvent mix of chloroform and 3% DIO: 0.5% reveals a more pronounced absorption peak than that observed in the binary blend of PTQ10:Y6. This enhanced absorbance is accompanied by a noticeable peak at 370 nm, which is typically linked to the presence of $PC_{70}BM$. Furthermore, the addition of the DIO:1-CN co-additives to the $PM6 : Y6 : PC_{70}BM$ blend results in a notable redshift of Y6 absorption peak, from approximately 810 nm to around 830 nm. This shift suggests that the co-additives play a significant role in modifying the absorption properties of the Y6 material.

The shift in the absorption peak, especially with the introduction of co-additives, suggests a change in the molecular arrangement and interactions within the blend. In ternary blends like $PM6 : Y6 : PC_{70}BM$ with co-additives like DIO and 1-CN, the interaction between the molecules can lead to a more favourable alignment and spacing for electronic transitions. This alignment can modify the electronic states of the materials, resulting in a redshift of the absorption peak.

The process is largely influenced by the molecular orbital interactions between the donor (PM6), acceptor (Y6), and the $PC_{70}BM$, which acts as an additional acceptor or morphological control agent. The co-additives play a crucial role in optimising these interactions by adjusting the microstructure, possibly by promoting a more ordered phase or affecting the crystallinity of the blend.

The ternary blend film's absorption spectrum is broad, extending from 450 to 900 nm. Within this spectrum, the peak situated at the long wavelength of 812 nm is identified as originating from the Y6 component. Conversely, the peak at the shorter wavelength of 625 nm is assigned to the PM6. This broad absorption range and the distinctive peaks within the ternary blend underscore the complex interaction between the constituent materials and the influence of additive treatment on the optical properties of the active layer. The presence of a broad absorption range and distinctive peaks from both donor and acceptor materials suggests a synergistic blend that aims to utilise the strengths of both components. This implies a configuration that could be thought of DA-DA, where both donor and acceptor materials are blended to achieve a wide absorption spectrum and efficient charge transfer [677,678].

5.3.4 Formulation Effect on Morphology

Grazing Incidence Wide-Angle X-ray Scattering (GIWAXS) is a powerful technique widely employed in the analysis of thin films and surfaces. It provides detailed information about the structural organisation, crystallinity, and orientation of materials at the nanoscale. This technique is particularly useful in the study of active layers of OSCs. In the context of examining the effects of chlorinated co-solvents and green co-solvents on specific materials or reactions, particularly those based on the $PTB7 : PC_{70}BM$ blend, represents a pivotal advancement in optimising the photovoltaic performance through nanostructural control. GIWAXS offers unique insights into how these solvents influence the structural properties of thin films and interfaces.

The results presented in Figures 5.9 to 5.12 offer a detailed insight into the morphological evolution of $PTB7 : PC_{70}BM$ blend thin films subjected to annealing at 120° C for 10 minutes, utilising different chlorinated solvent environments. Specifically, Figures 5.9 and 5.10 depict the effects of individual solvents, CB and o-DCB, respectively, on the film's structure. The 1D and 2D grazing incidence X-ray scattering (GIXS) data for all the these chlorinated solvent films reveal a prevalent amorphous phase, characterised by a disordered "halo" pattern indicating an aggregate morphology that is primarily amorphous in orientation and the GIWAXS images display a ring-like pattern spanning Q values from -0.5 to 0.5 $\mathring{A}^{-1}$.

In the case of CB (Figure 5.9), the GIWAXS image display a Q_z value of 1.44 $\mathring{A}^{-1}$ and Q_{xy} of 0.32 $\mathring{A}^{-1}$. This suggests an intermediate level of crystallinity and phase separation within the film. The alignment of CB's HSP with the solubility characteristics of PTB7 and $PC_{70}BM$ promotes efficient $\pi - \pi$ stacking conducive to effective charge transport, albeit with the need to modulate the aggregation to prevent excessive H-aggregation, which can dampen fluorescence and limit exciton diffusion [666].

Conversely, films processed with o-DCB (Figure 5.10) exhibit a Q_z of 1.33 $\mathring{A}^{-1}$ and Q_{xy} of 0.27 $\mathring{A}^{-1}$, indicating the formation of larger crystalline domains and more pronounced phase separation. The sharpness of the observed peaks suggests the presence of J-aggregation, which, while beneficial for light absorption, must be finely balanced to prevent adverse effects on charge separation [679–681].

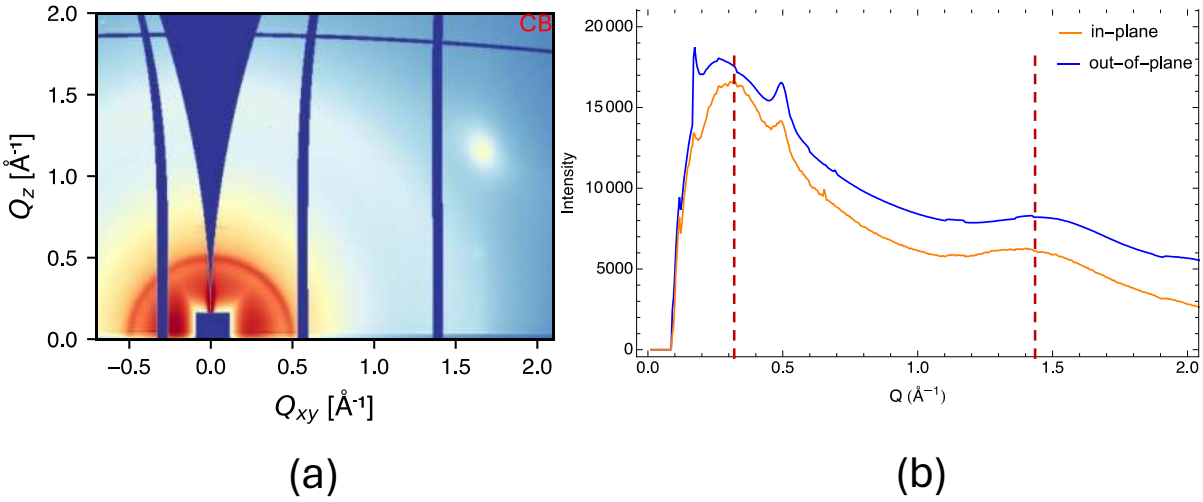


Figure 5.9: (a) shows the ex-situ pattern of the morphology of the $PTB7$: $PC_{70}BM$(1:1.5) formed from a chlorinated solvent (CB) and (b) the corresponding intensity profiles along Q_{xy} (in-plane) and Q_z (out-of-plane) directions. The thin fims were annealed at 120° C for 10 minutes.

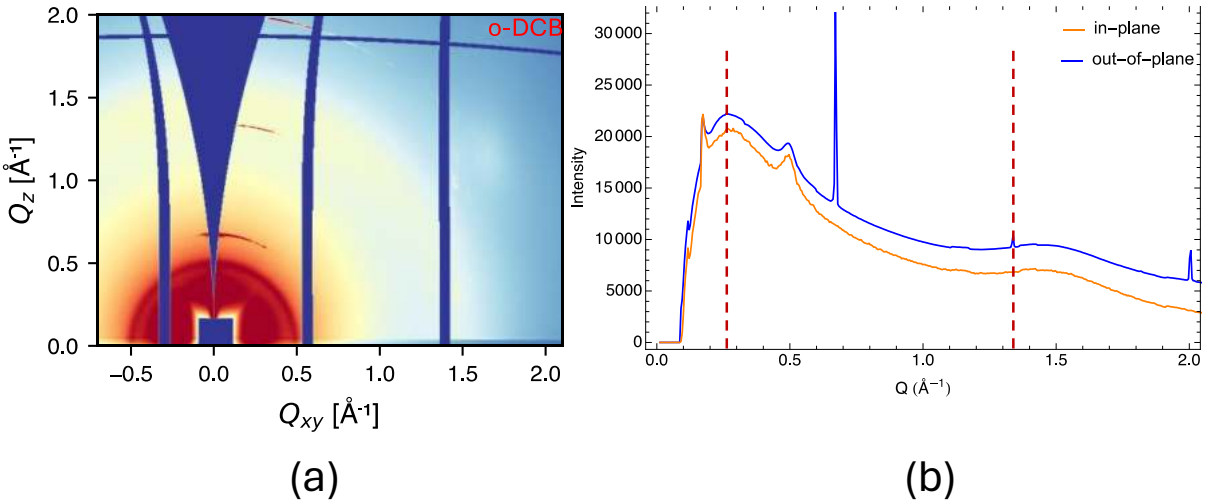


Figure 5.10: (a) shows the ex-situ pattern of the morphology of the $PTB7$: $PC_{70}BM$(1:1.5) formed from a chlorinated solvent (o-DCB) and (b) the corresponding intensity profiles along Q_{xy} (in-plane) and Q_z (out-of-plane) directions. The thin fims were annealed at 120° C for 10 minutes.

Figure 5.11 illustrates the influence of a co-solvent system (CB:o-DCB), revealing a Q_z

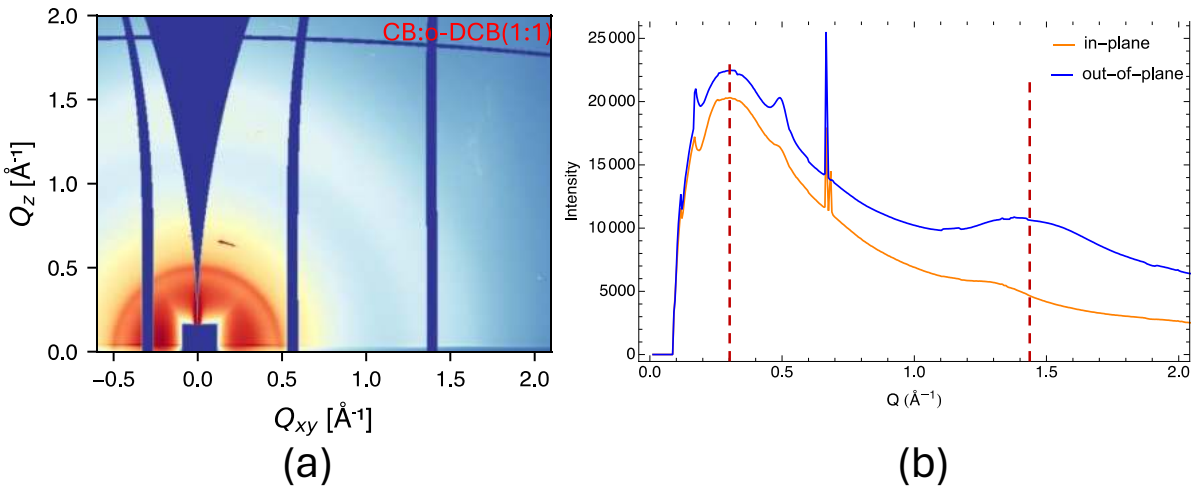


Figure 5.11: (a) shows the ex-situ pattern of the morphology of the $PTB7$: $PC_{70}BM$(1:1.5) formed from chlorinated co-solvents (CB:o-DCB) and (b) the corresponding intensity profiles along Q_{xy} (in-plane) and Q_z (out-of-plane) directions. The thin fims were annealed at 120° C for 10 minutes.

of 1.45 $\mathring{A}^{-1}$ and Q_{xy} of 0.30 $\mathring{A}^{-1}$. This configuration seems to favour out-of-plane $\pi - \pi$ stacking, enhancing vertical phase separation and thereby improving the interconnectivity between domains, which is crucial for efficient charge transport to the electrodes [493,682].

The introduction of an additive, DIO, in the solvent mixture (CB:DIO, Figure 5.12) results in a morphology that supports both H- and J-aggregation, as indicated by the Q_z and Q_{xy} values similar to those of the co-solvent system but with a slight increase in Q_{xy} to 0.31 $\mathring{A}^{-1}$. The presence of DIO promotes a refined nanoscale morphology and enhanced donor-acceptor intermixing, critical for balancing exciton generation, separation, and charge transport processes crucial to the performance of OSCs [293,343,480,683–685].

These observations underscore the profound impact of solvent choice and additive use on film morphology and, consequently, on the performance of OSCs. The preference for out-of-plane $\pi - \pi$ stacking, particularly evident in the co-solvent system, aligns with findings from the literature emphasising the importance of vertical phase separation for efficient charge transport pathways [686–688]. The sharp peaks in films processed with o-DCB reflect a well-defined molecular arrangement, which is advantageous for charge separation and collection. These insights resonate with previous studies, such as those by Liao et al [69]. and Zheng et al [689]., demonstrating the influence of solvent quality and additives on domain purity, crystallinity, and overall device efficiency. The GIWAXS analysis not only confirms the intricate effects of chlorinated solvent interactions on the microstructural morphology of the $PTB7$: $PC_{70}BM$ blends but also highlights the critical role of thoughtful solvent and additive selection in optimising the nanoscale architecture of the active layer in OSCs.

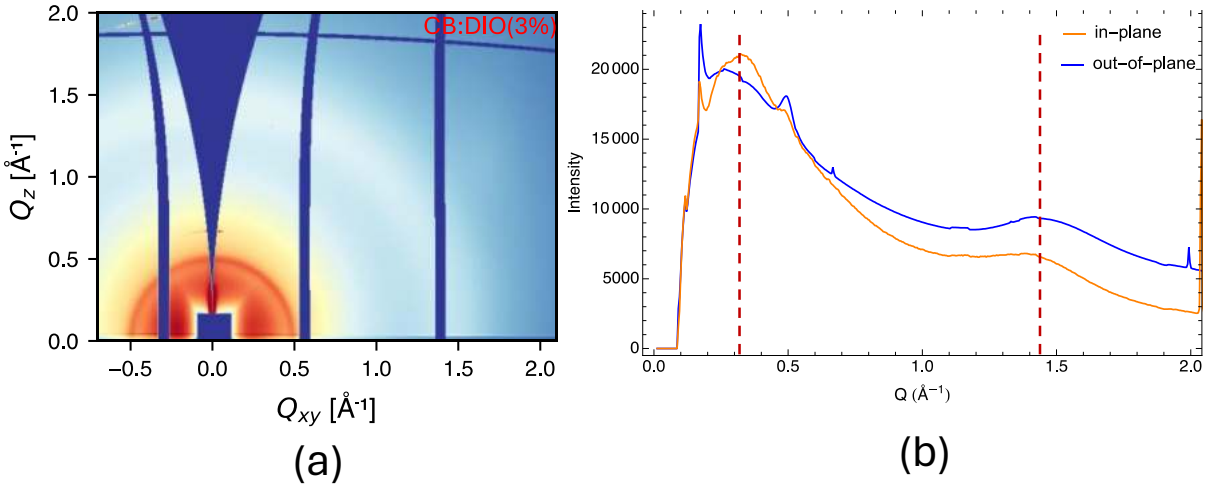


Figure 5.12: (a) shows the ex-situ pattern of the morphology of the $PTB7$: $PC_{70}BM$(1:1.5) formed from chlorinated co-solvents (CB:DIO) and (b) the corresponding intensity profiles along Q_{xy} (in-plane) and Q_z (out-of-plane) directions. The thin fims were annealed at 120° C for 10 minutes.

The GIWAXS analysis of $PTB7$: $PC_{70}BM$ thin films processed with eucalyptol (Eu) shown in Figure 5.13, limonene (Lim) in Figure 5.14, and their combination (Eu:Lim) in Figure 5.15, assessing their impact on the morphology and performance of OSCs. The use of green solvents has shown promising potential in altering the molecular morphology of $PTB7$: $PC_{70}BM$ blends. The GIWAXS results indicate distinct in-plane (Q_{xy}) and out-of-plane (Q_z) coherence for the films cast with each solvent.

The thin films processed with Eu in Figure 5.13 demonstrated a Q_z value of 1.41 $\AA^{-1}$ and Q_{xy} of 0.29 $\AA^{-1}$, suggesting a well-balanced crystalline and amorphous phase morphology. The HSPs of Eu, which emphasise a moderate dispersion force with minimal polar and hydrogen-bonding interactions, likely facilitate favourable $\pi - \pi$ stacking without leading to excessive H-aggregation.

The Lim treated thin films exhibited a Q_z of 1.42 $\AA^{-1}$ and Q_{xy} of 0.28 $\AA^{-1}$. Similar to Eu, limonene appears to encourage effective $\pi - \pi$ stacking but may lead to slightly different crystallite sizes or a degree of H-aggregation, as indicated by the comparable Q_z but slightly lower Q_z values. The terpenic nature of Lim could influence the solvent evaporation rate, affecting the kinetics of film formation and domain size [690].

The combination of Eu and Lim resulted in a Q_z of 1.42 $\AA^{-1}$ and an increased Q_{xy} of 0.32 $\AA^{-1}$. This suggests an enhanced in-plane ordering, which may correspond to improved $\pi - \pi$ stacking. Co-solvent systems can modulate the film formation dynamics, potentially leading to a morphology that encourages a mixture of H- and J-aggregates,

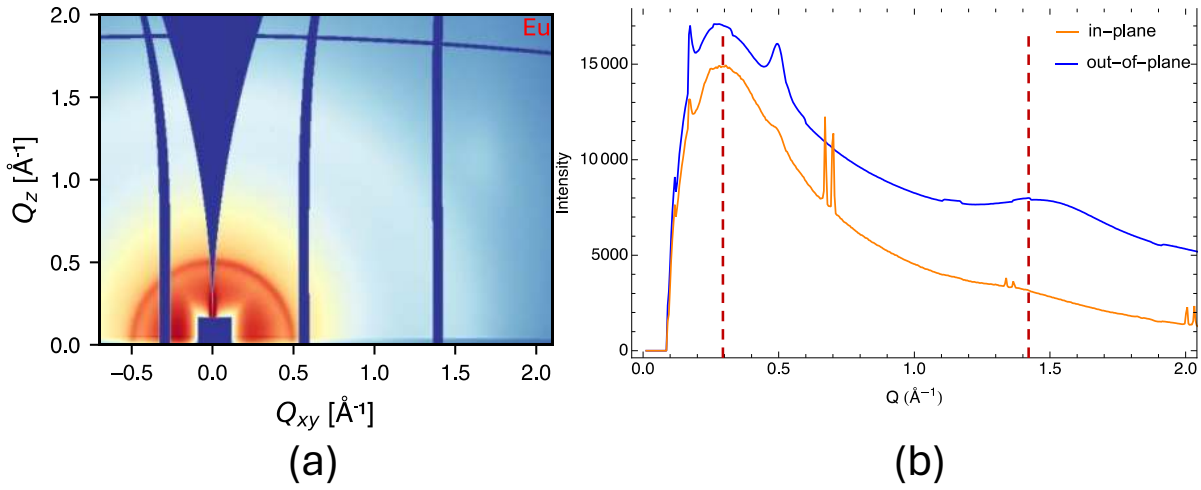


Figure 5.13: (a) shows the ex-situ pattern of the morphology of the $PTB7$: $PC_{70}BM$(1:1.5) formed from a green solvent (Eu) and (b) the corresponding intensity profiles along Q_{xy} (in-plane) and Q_z (out-of-plane) directions. The thin fims were annealed at 120° C for 10 minutes.

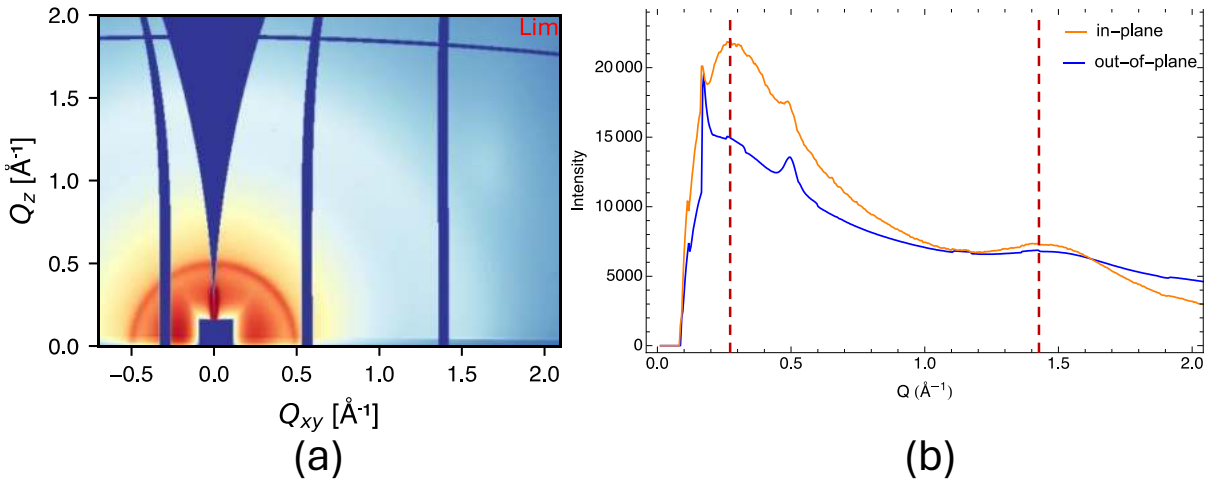


Figure 5.14: (a) shows the ex-situ pattern of the morphology of the $PTB7$: $PC_{70}BM$(1:1.5) formed from a green solvent (Lim) and (b) the corresponding intensity profiles along Q_{xy} (in-plane) and Q_z (out-of-plane) directions. The thin fims were annealed at 120° C for 10 minutes.

which are desirable for balanced charge transport and absorption properties [691].

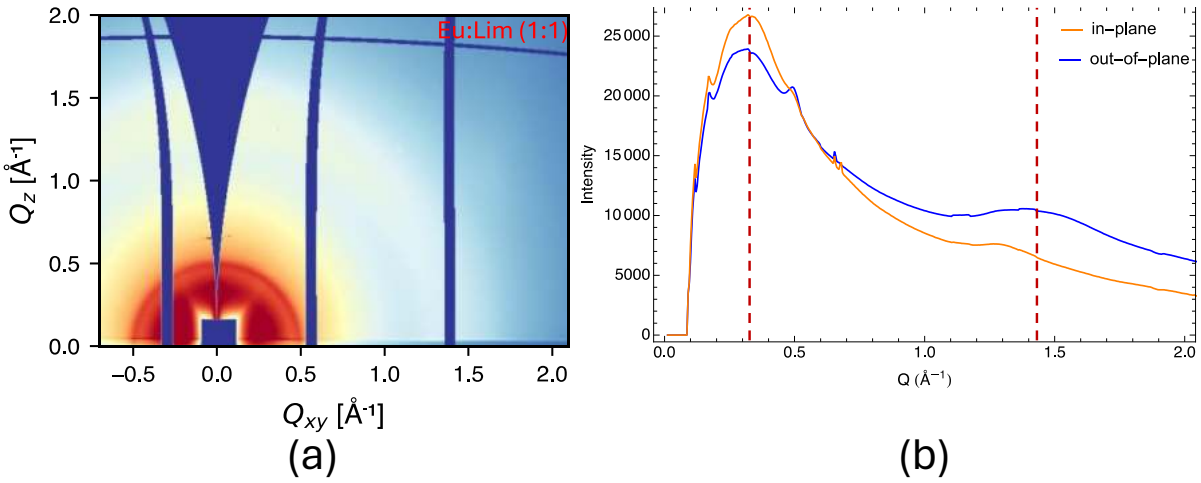


Figure 5.15: (a) shows the ex-situ pattern of the morphology of the $PTB7$: $PC_{70}BM$(1:1.5) formed from green co-solvents (Eu:Lim) and (b) the corresponding intensity profiles along Q_{xy} (in-plane) and Q_z (out-of-plane) directions. The thin fims were annealed at 120° C for 10 minutes.

The subtle variations in Q_z and Q_{xy} values between the different solvent systems provide insights into the tuning of morphology. Literature corroborates that the fine-tuning of $\pi - \pi$ stacking and control over aggregate formation are integral for achieving optimal solar cell performance [692–695]. For instance, the work by Huang et al [696]., underscores the role of solvent-solute interactions in directing the film nanostructure, thereby affecting the PCE of OSCs.

The exploration of green solvents like Eu and Lim in the fabrication of $PTB7 : PC_{70}BM$ thin films has demonstrated their capacity to influence the morphological characteristics pivotal for OSC performance. GIWAXS analysis has revealed that both green solvents, and particularly their combination, can be harnessed to achieve a desirable balance of molecular ordering and aggregation. This balance is vital for facilitating efficient exciton dissociation and charge transport, which are essential for high-performing photovoltaic devices.

The use of 2-MEA and toulene (Figure 5.16) as well as Eu and toulene (Figure 5.17) in terms of HSPs. These parameters are critical in determining the solubility and phase behaviour of polymer blends like $PTB7 : PC_{70}BM$.
For the films using 2-MEA:Toulene, $Q_z = 1.38\ \AA^{-1}$ and $Q_{xy} = 0.28\ \AA^{-1}$ indicate a certain degree of vertical and horizontal molecular ordering. This suggests moderate $\pi - \pi$ stacking and possibly some degree of H-aggregation, where molecules align side by side with their π-faces parallel but slightly offset.

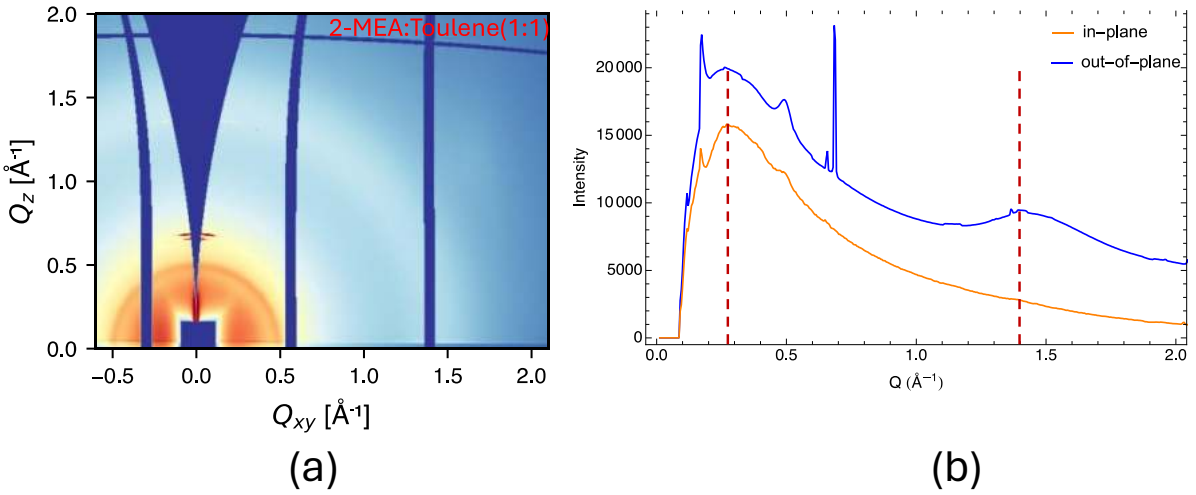


Figure 5.16: (a) shows the ex-situ pattern of the morphology of the $PTB7$: $PC_{70}BM$(1:1.5) formed from an industrial solvent an green solvent (2-MEA:Toulene) and (b) the corresponding intensity profiles along Q_{xy} (in-plane) and Q_z (out-of-plane) directions. The thin fims were annealed at 120° C for 10 minutes.

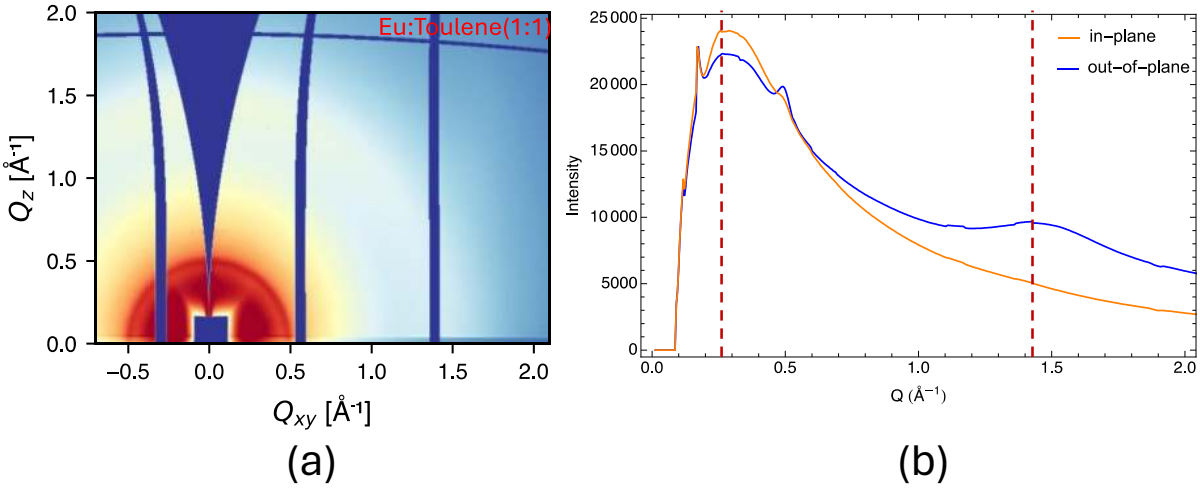


Figure 5.17: (a) shows the ex-situ pattern of the morphology of the $PTB7$: $PC_{70}BM$(1:1.5) formed from an industrial solvent an green solvent (Eu:Toulene) and (b) the corresponding intensity profiles along Q_{xy} (in-plane) and Q_z (out-of-plane) directions. The thin fims were annealed at 120° C for 10 minutes.

For the films using Eu:Toulene, $Q_z = 1.42$ $\AA^{-1}$ and $Q_{xy} = 0.27$ $\AA^{-1}$ suggest slightly

higher vertical ordering and a comparable horizontal order. The higher Q_z value can be indicative of increased $\pi - \pi$ stacking and a tilt in molecular orientation relative to the substrate, which may also imply a transition towards more J-aggregation, where the π-conjugated backbones are more co-facially aligned.

The observed differences in molecular stacking and orientation are closely related to the morphology of the active layer in OSCs. Better $\pi - \pi$ stacking can enhance charge carrier mobility, thereby improving the photovoltaic performance [697–699]. Moreover, the balance between H and J aggregation influences the exciton diffusion and dissociation processes. Efficient exciton dissociation at the donor-acceptor interface is essential for high photocurrent generation [700].

The comprehensive GIWAXS analysis of $PTB7 : PC_{70}BM$ blend thin films processed using various chlorinated solvents and green solvent systems offers profound insights into the molecular morphologies that govern the performance of OSCs. The study elucidates how different solvent environments influence the crystallinity, phase separation, and aggregation behaviour within the films, thereby impacting charge transport and overall device efficiency.

5.3.5 Electrical Properties by J-V Measurements

The morphology of OSCs plays a crucial role in determining their electrical properties, particularly the J-V characteristics, which describe the relationship between the current density (J) and the applied voltage (V) making them essential essential for evaluating their performance. These characteristics encompass key parameters such as the short-circuit current (J_{sc}), open-circuit voltage (V_{oc}), fill factor (FF), and PCE [701, 702]. The morphology directly influences these parameters through its effect on the charge carrier dynamics within the cell. For instance, a well-optimised morphology can lead to higher J_{sc} and FF by minimising recombination losses and maximising charge carrier extraction [703, 704].

The significance of morphology control in OSCs, particularly through the judicious selection and manipulation of co-solvents, lies in its ability to influence the electrical properties, J-V characteristics, and ultimately, the overall performance of these photovoltaic devices. By understanding and optimising the interplay between morphology and J-V characteristics, the boundaries of OSC performance, making them a more viable and competitive option in the global energy market.

The evaluation of statistical device parameters derived from the JV curves presents an indispensable approach in quantifying the performance and efficiency of OSCs. These parameters are essential as they provide a comprehensive understanding of the efficiency and performance of OSCs.

The graphical representation of these statistical device parameters typically employs the x-axis to denote sample labeling, thereby providing a structured overview of the data. For instance, in Figure 5.20, sample labels such as CF61, DO45, CD40, B35, DD40, A32, and CD4B are depicted. These labels correspond to seven substrates, within which four

pixels were scrutinised per substrate. This methodological approach underscores the comprehensive nature of the data collection, ensuring a robust analysis of device performance.

Significantly, the pixel exhibiting the highest PCE is highlighted, with the average PCE being computed from the top-performing pixels across the seven substrates as shown in Table 5.4. This strategy not only accentuates the peak performance metrics but also provides a balanced view by considering the highest efficiencies achieved, thereby encapsulating the potential and limitations of the OSCs under investigation.

The Mott-Gurney analysis, also known as the Mott-Gurney law or Mott-Gurney equation, is a simple empirical expression used to describe the current density-voltage (J-V) characteristics of thin-film devices such as OSCs, organic light-emitting diodes (OLEDs), and thin-film transistors (TFTs). It was first proposed by Sir Nevill Mott and Frederick Gurney in 1940 [705].

Space-charge limited current (SCLC) regime is an efficient way for determining the value of charge carrier mobility of injected charge carriers in diode devices and has been applied to organic devices with success [706]. By neglecting the diffusive component in the total electric current, Mott-Gurney derived a simple analytical relation in which the electric current varies linearly with the mobility (μ) and quadratically with the bias voltage [707]:

$$J = \frac{9\varepsilon\varepsilon_0\mu V^2}{8L^3} \tag{5.3}$$

where:

- J is the current density (mA/cm^2).
- ε = 3.0 is the dielectric constant of the material for the active layer $PTB7 : PC_{70}BM$ [708].
- ε_0 = 8.854 $\times 10^{-12}$ F/m is the vacuum permittivity.
- μ is the charge carrier mobility ($cm^2/V \cdot s$).
- V is the applied voltage (V).
- L is the thickness of the active layer of $PTB7 : PC_{70}BM$

$PTB7 : PC_{70}BM$ Based Organic Solar Cells

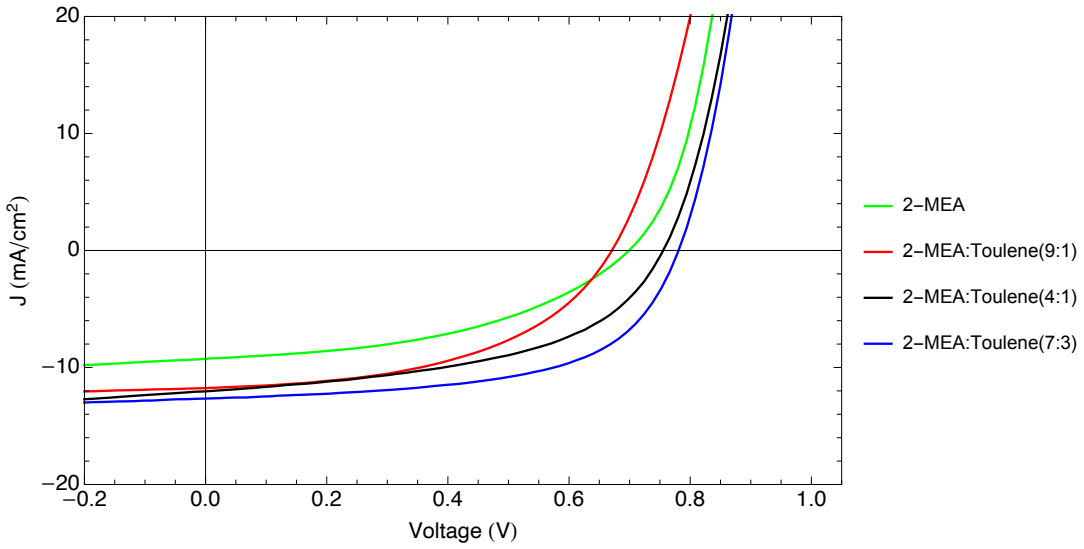
Several studies have been carried out on the efficiency of an OPV device with a bulk heterojunction comprising of the PTB7 and $PC_{70}BM$. In all instances, chlorinated solvents were used to tune the morphology of the bulk heterojunction thereby correlating the molecular orientation with J-V characteristics, specifically the photocurrent, $J_(sc)$ and FF. Figure 5.18 shows the J-V characteristics of the $PTB7 : PC_{70}BM$ bulk heterojunction solar cell formed from a mixture of green solvent, 2-MEA and the industrial solvent, Toluene in varying proportions but for a constant mass ratio (1:1.5)

of the donor (D) and Acceptor (A) materials in a total concentration of 20 mg/mL. The data shows that solvent mixing ratio of 7:3 by volume yields the device with the enhanced device performance metrics. The J_{sc} of 12.66 mA/cm^2, and FF of 58.5% have been evaluated from the J-V curve for a device of area 0.25 cm^2. The PCE of this device is calculated as 5.77 %. The solvent mixing ratio can be linked to the optical properties of a device using an active layer of $PTB7 : PC_{70}BM$ with 2-MEA:Toluene solvents, the study observed improved device parameters with the addition of Toluene to 2-MEA, with an optimal concentration of 7:3. This enhancement in optical absorption in the region of the absorption peaks at around 623 and 677 nm, attributed to the characteristic $\pi - \pi^*$ transition of PTB7, indicates that the co-solvent mixtures modify the BHJ to enhance photon harvesting more effectively. The extracted shunt and series resistance values from current density - voltage characteristics are given in Table 5.5. It is evident that the use of a co-solvent mixtures reduces the series resistance of the OPV device. The dark J-V in Figure 5.18 (b) shows the device with the solvent ratio 9:1 (2-MEA:Toulene) with a high leakage current density and lower rectification ratio compared to the other 3 devices.

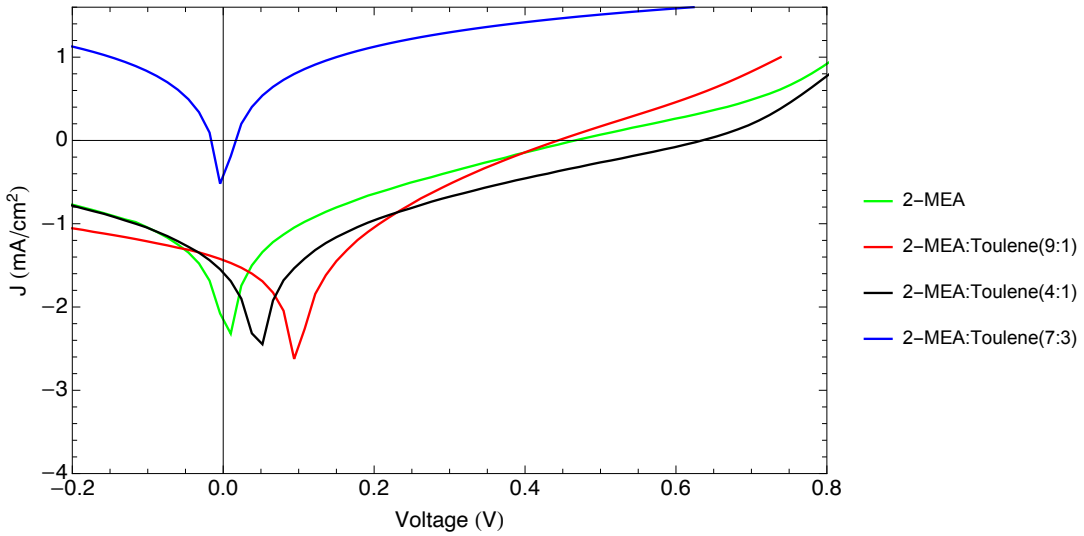
Further investigations demonstrated a notable trend: the progressive addition of Toluene to 2-MEA led to a consistent improvement in the device's electrical parameters. This trend was visually documented across Figures 5.20 through 5.23, underscoring the positive impact of Toluene on the device's overall efficiency. Particularly, at the identified optimal concentration, the PCE saw a significant increase to 5.77%, which was also accompanied by improvements in J_{sc}, V_{oc}, and FF metrics. These enhancements are largely attributable to the improved miscibility of the active materials in the solvent mixture, which effectively facilitates better charge transport and extraction within the photovoltaic device. However the homogeneous dispersion of the fullerene derivative in the donor to enhance the Donor-Acceptor interface cannot be ruled out [709].

The observed performance variations in devices fabricated with different solvent mixtures highlight the significant influence of solvent characteristics on the efficiency of organic photovoltaic devices. Specifically, devices fabricated using pure 2-MEA as the solvent exhibited the lowest PCE, suggesting that 2-MEA alone may not effectively dissolve both components of the blend PTB7 and $PC_{70}BM$ or promote a microstructure conducive to efficient charge generation and transport. This inefficacy could stem from the polarity, boiling point, or solvation power of 2-MEA, which might not adequately control the domain sizes or the distribution of donor and acceptor materials. Conversely, the gradual improvement in PCE observed upon adding toluene to 2-MEA underscores toluene's crucial role in optimising the active layer's morphology. Being less polar than 2-MEA, toluene likely enhances the solubility of the hydrophobic component $PC_{70}BM$ and may alter the solvent evaporation rate, facilitating better phase separation and domain purity essential for efficient charge transfer and extraction [710].

The performance variations observed in Figure 5.19 can be attributed largely to the interplay between solvent solubility parameters and the resulting film morphology. Toluene, when mixed with 2-MEA, enhances the solubility of the fullerene component and possibly affects the polymer as well, optimising the dissolution of both components. The ratio of MEA:Toluene (7:3) that yielded the highest PCE likely provides an ideal balance, allowing for a high-quality film formation without excessive phase separation or aggregation. This optimal solvent mixture not only aids in achieving better film thickness,



(a)



(b)

Figure 5.18: (a) J-V curves of devices with the $PTB7 : PC_{70}BM$ (1:1.5) mass ratio with a green solvent (2-MEA) and with various concentration of an industrial solvent (Toulene) being added to the blend. (b) shows the J-V dark conditions for the devices.

which was observed to increase with higher toluene content but also improves molecular ordering within the film. On the aspect of charge carrier mobility, the observed variations highlight the nuanced impact of the solvent mixture on both the generation of charge carriers and their transport within the material. The charge carrier mobilities of the devices also vary with the solvent concentration. The device with the MEA:Toulene(7:3) concentration has a higher charge carrier mobility ($2.76 \times 10^{-5}\ cm^2/V \cdot s$) compared to the device with only 2-MEA($\mu = 1.70 \times 10^{-5}\ cm^2/V \cdot s$) and the other co-solvents with lower toulene concentrations which are depicted in Table 5.3, underscores a more intricate interplay between morphology, film thickness, and the pathways through which charge carriers traverse, pointing to the delicate balance required in optimising these parameters for enhanced device performance. This suggests that the morphology of the active layer may be more important for charge carrier transport than the charge carrier mobility itself.

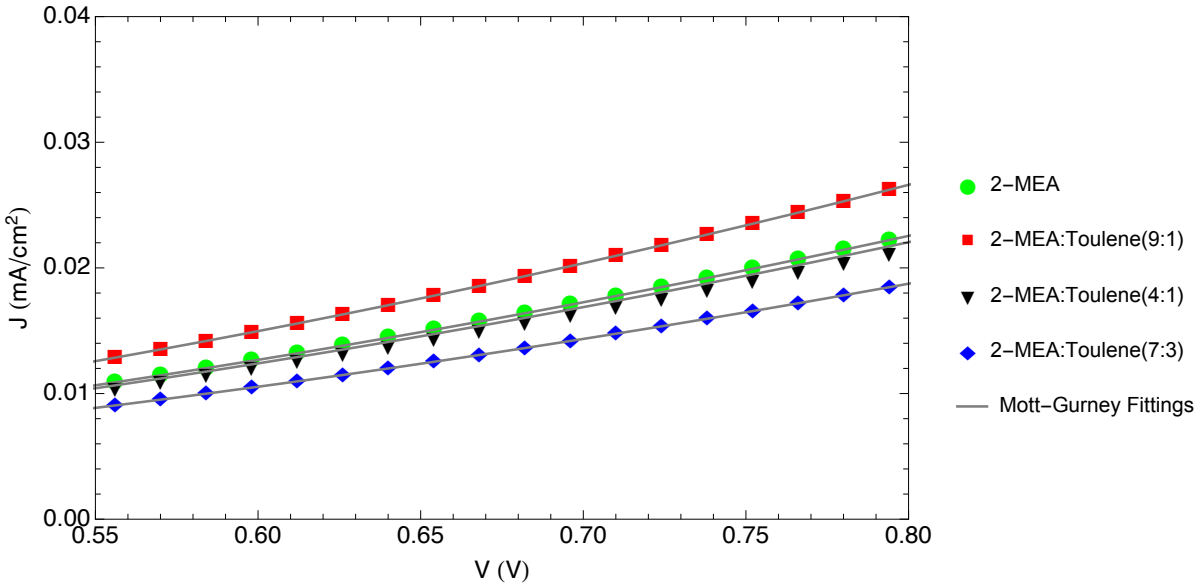


Figure 5.19: Fittings performed by Equation (5.3) over the dark J-V measurements (range of 0.55-0.8 V) for devices with the active of $PTB7 : PC_{70}BM$ in (2-MEA:Toulene) co-solvents at different concentrations.

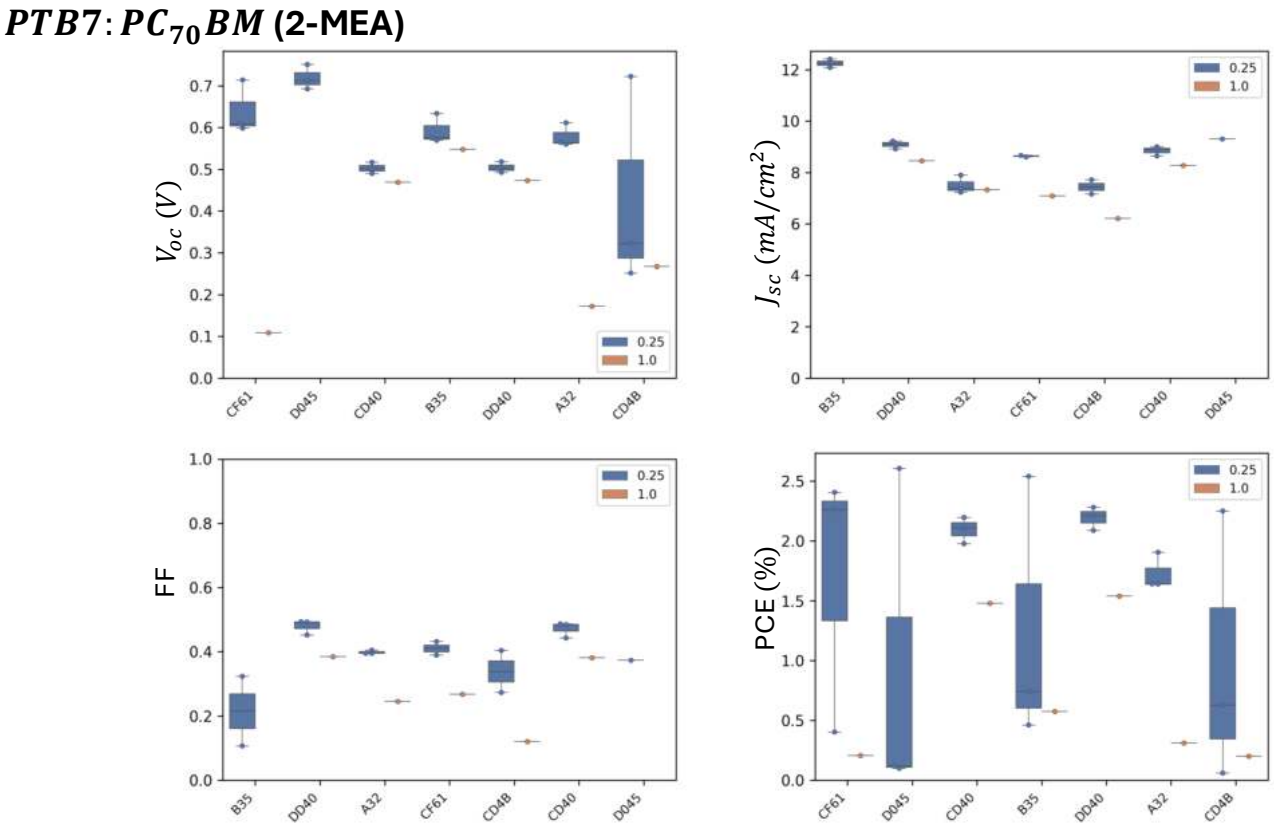


Figure 5.20: Statistical device parameters of the active layer in $PTB7 : PC_{70}BM$(1:1.5) using a green solvent (2-MEA).

The synergistic effect of the solvent blend on the device's performance is further

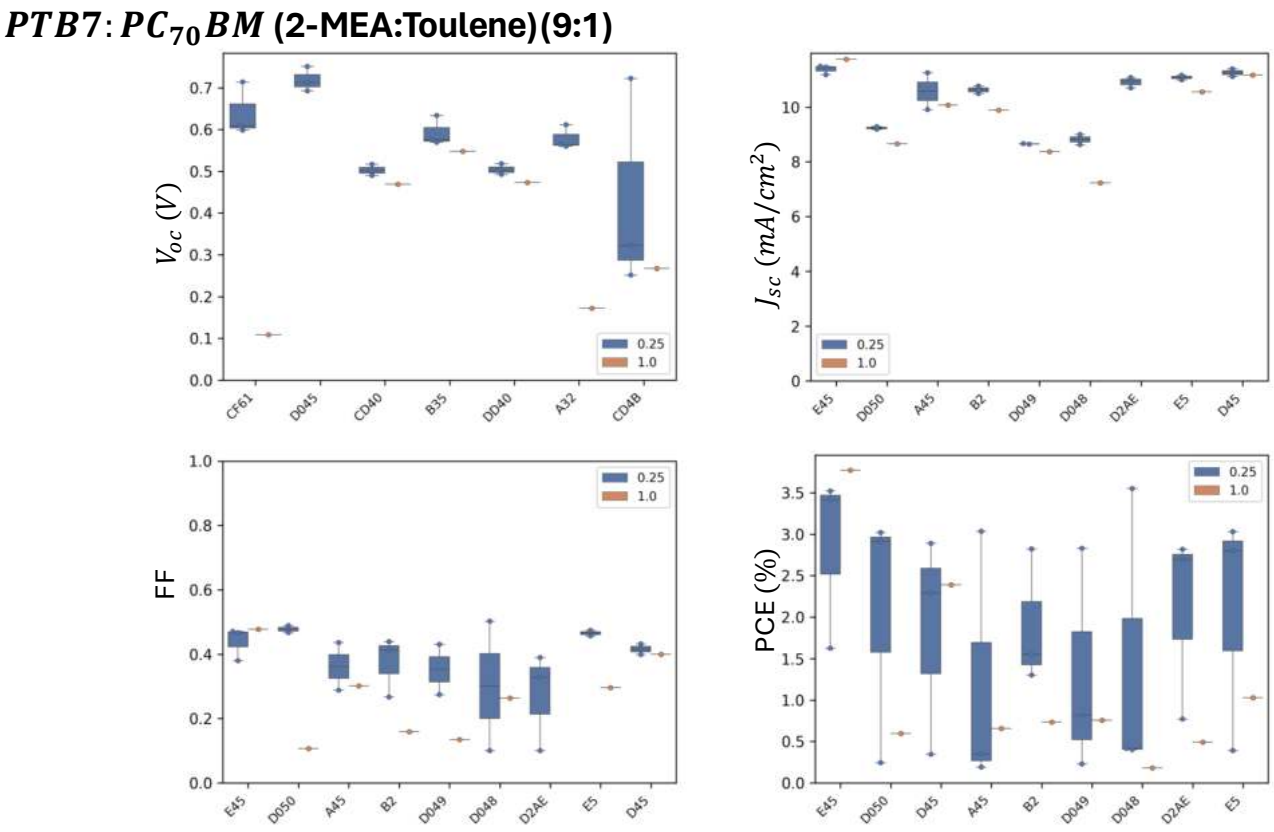


Figure 5.21: Statistical device parameters of the active layer in $PTB7 : PC_{70}BM$ (1:1.5) using co-solvents (2-MEA:Toluene) in a 9:1 ratio (900 μL of 2-MEA and 100 μL of Toulene). The total concentration is 20 mg/mL.

supported by optical characterisation data in Figure 5.7. The addition of Toluene to the solvent mix resulted in increased miscibility, as predicted by the HSP calculations (Figure 5.2). This increase in absorbance is typically attributed to more extensive delocalisation of π-electrons across the stacked molecules, which can lower the energy gap between the HOMO and LUMO. As a result, the material can absorb photons with lower energy (longer wavelength), broadening the absorbance spectrum. This is advantageous for OPVs as it allows the active layer to harvest a wider range of the solar spectrum [711]. Both donor and acceptor materials can be influenced by π-stacking. For donors, π-stacking can enhance light absorption and facilitate charge transfer to the acceptor. For acceptors, efficient π-stacking is crucial for accepting and transporting electrons away from the donor [712]. Thus, the addition of Toulene has an influence on both donors and acceptors.

The initial lower performance metrics observed with devices utilising solely green solvents like 2-MEA were attributed to the limited solubility of the active materials in these solvents. The RED value for $PC_{70}BM$ is 1.005, making it partially soluble in 2-MEA and the RED value of for $PC_{70}BM$ is 0.9002, making it soluble in Toulene. Despite using 2-MEA only the V_{oc} is very large (Figure 5.20) and so is the J_{sc}, yet the device efficiency is low. This could be attributed to factors other than large fullerene domains, especially considering the significant J_{sc}. The small FF may be influenced by issues related to charge carrier recombination, trap-assisted recombination, or other

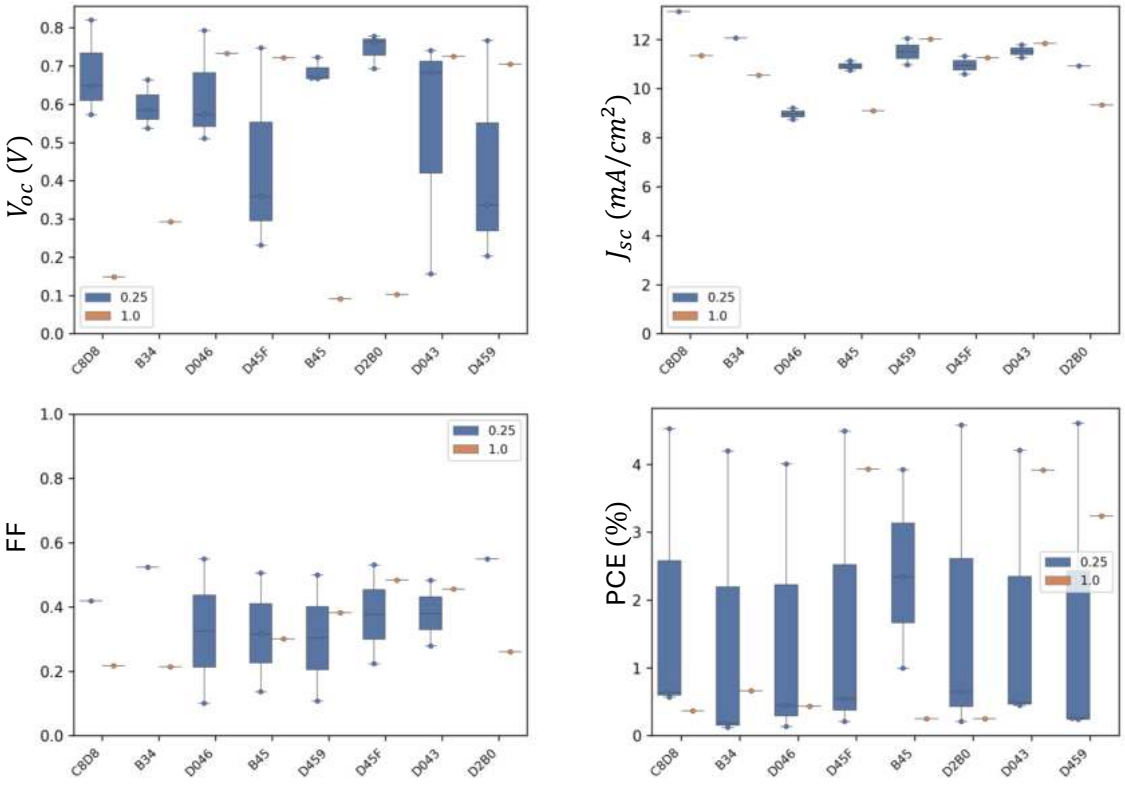


Figure 5.22: Statistical device parameters of the active layer in $PTB7 : PC_{70}BM$ using co-solvents (2-MEA:Toluene) in a ratio of 4:1 (800 μL of 2-MEA and 200 μL of Toulene). The total concentration is 20 mg/mL.

morphological factors affecting the device's performance. Furthermore, inappropriate solubility can promote excessive crystallinity or aggregation, introduce defects, or result in residual solvent in the film, all of which can act as barriers to charge transport or sites for increased recombination. The nuanced interplay between solvent and processing conditions underscores the complexity of achieving a balance that supports both high charge generation and efficient charge collection.

Larger domains in the $PTB7 : PC_{70}BM$ blend can be beneficial up to a point, as they can facilitate efficient charge transport to the electrodes. However, excessively large domains can reduce the interfacial area between the donor and acceptor materials, which is critical for the dissociation of excitons into free charge carriers [713]. Thus, there's a balance to be struck in achieving the optimal domain size that promotes both exciton dissociation at the donor-acceptor interface and efficient charge transport to the electrodes.

While Toluene can produce larger domains due to its slower drying rate (Boiling point of 110.6° C) compared to the boiling point of 2-MEA (173° C) and different solubility parameters for PTB7 and $PC_{70}BM$, the exact effect on domain size and performance also depends on other processing conditions, such as solution concentration, drying temperature, and annealing processes [714, 715].

This solubility challenge was effectively addressed by incorporating Toluene, highlighting its role not only as a solvent but also as a performance-enhancing additive. The choice of Toluene is particularly noteworthy due to it allowing for the formation of a morphology with a large donor acceptor interface, which aids in charge transport. Lastly, due to its lower toxicity compared to traditional chlorinated solvents, aligning with environmental and safety considerations. Moreover, Toluene's established use in industrial applications underscores its practical viability as an additive, offering a sustainable and less hazardous alternative for improving the solubility and, consequently, the performance of photovoltaic devices as indicated in Table 5.4.

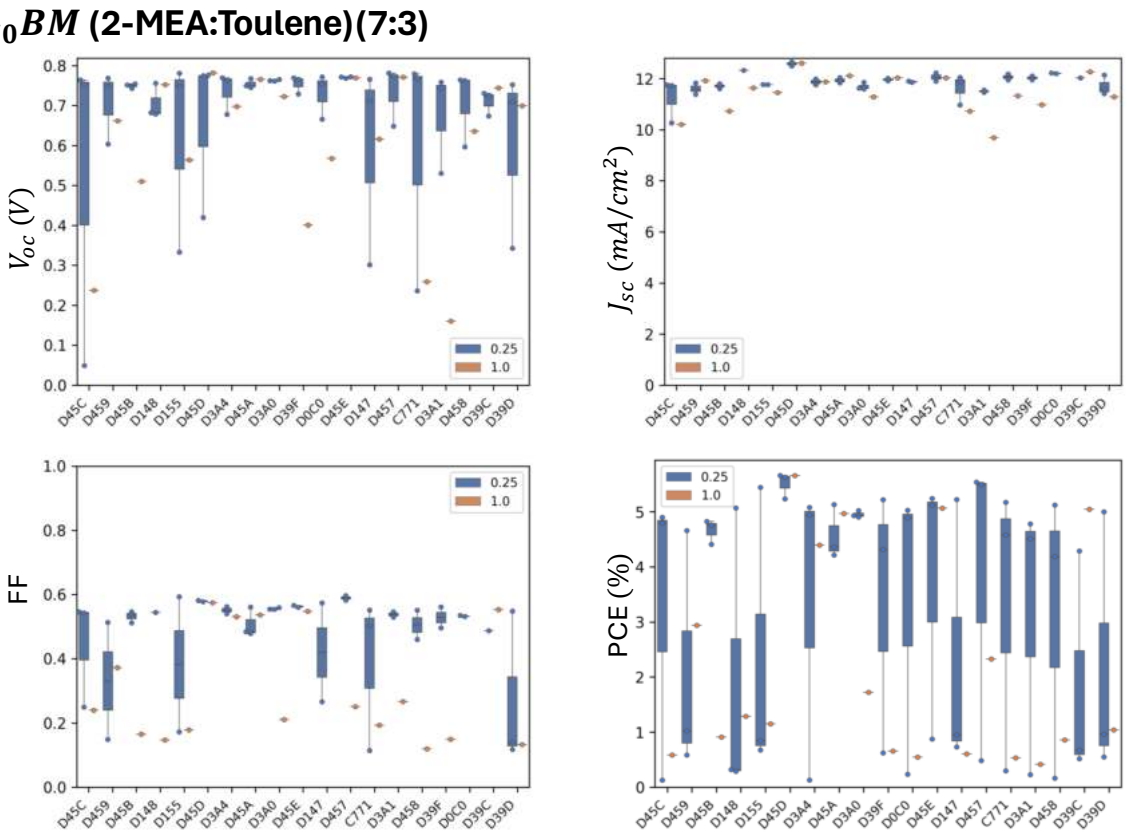


Figure 5.23: Statistical device parameters of the active layer in $PTB7 : PC_{70}BM$ using co-solvents (2-MEA:Toluene) in a ratio of 7:3.

Table 5.3: Charge carrier mobilities of the device with the active layer $PTB7 : PC_{70}BM$ using green and industrial co-solvents at different concentrations.

Donor:Acceptor(1:1.5)	Solvents	Thickness (nm)	μ ($\times 10^{-5}\ cm^2/V \cdot s$)
$PTB7 : PC_{70}BM$	$2-MEA$ (1)	113	1.70
$PTB7 : PC_{70}BM$	$2-MEA : Toulene$ (9:1)	122	2.53
$PTB7 : PC_{70}BM$	$2-MEA : Toulene$ (4:1)	128	2.34
$PTB7 : PC_{70}BM$	$2-MEA : Toulene$ (7:3)	136	2.76

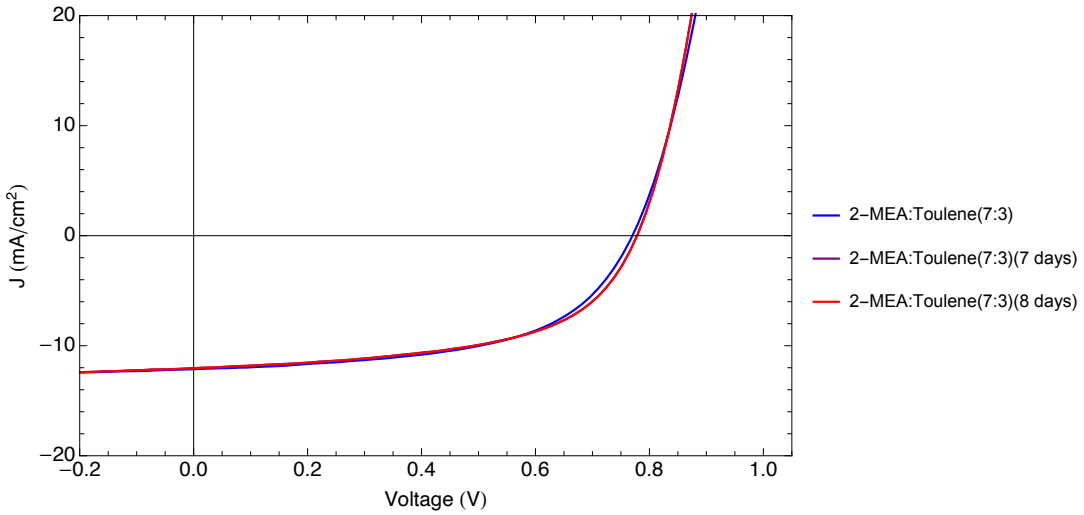
The results of the $PTB7 : PC_{70}BM$ bulk heterojunction based device in Figure 5.23 show that the solvent ratio 7:3 (2-MEA:Toulene) has the superior performance metric. Subsequently further analysis on the lifetime of these devices were carried out as follows: the devices were categorised into two distinct groups. The first group comprised devices preserved within a moisture-free glovebox environment. The electrical characteristics, specifically J-V measurements, for this set were conducted on two occasions: firstly, after a period of 7 days and subsequently after 8 days.

The second group involved devices that were encapsulated to protect them from environmental factors. Initial measurements for these encapsulated devices were carried out after 24 hours, followed by another set after 96 hours. Subsequently, these devices underwent a light ageing process within an ageing box, exposed to air at a consistent temperature of 85° C for a duration of 22 hours, with measurements taken immediately afterward. This cycle of ageing and measuring was repeated under varying conditions: after 165 hours exposed to air, the devices were subjected to light and air within the ageing box at 85° C for 25 hours; following a storage period of 284 hours, they were again placed in the ageing box under similar conditions for 72 hours. After a cumulative duration of 365 hours post-initial storage, the devices were aged for an extended period of 88 hours in the ageing box. The devices were then rested for 72 hours. Finally, the devices were aged at a temperature of 85° C for a further 172 hours, with the final measurements recorded thereafter.

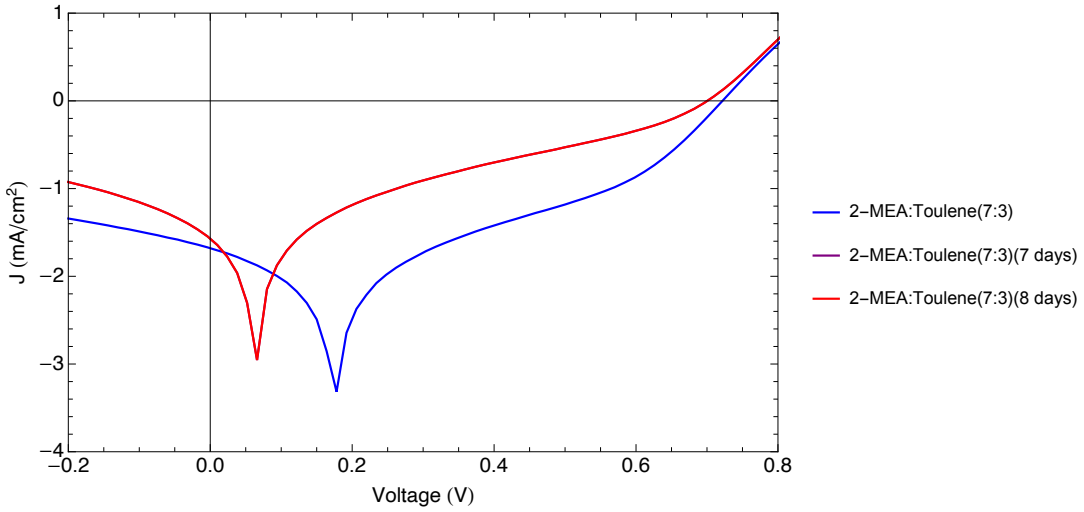
The stability observed in the charge carrier mobility of the encapsulated devices over an 8-day period in Figure 5.25, all processed using the 2-MEA:Toluene (7:3) co-solvent system, underscores the effectiveness of this solvent mix in both optimising and maintaining the electronic properties and morphology of the active layer. The charge carrier mobility increased slightly from 2.54 $\times 10^{-5}\ cm^2/V \cdot s$ for the reference device to 2.73 $\times 10^{-5}$

Table 5.4: Photovoltaic parameters of the $PTB7 : PC_{70}BM$ devices with various concentrations of Toulene.

Solvents	J_{sc} (mA/cm^2)	V_{oc} (V)	FF (%)	R_{sh} $(\Omega \cdot cm^2)$	R_s $(\Omega \cdot cm^2)$	$PCE_{max}(Avg)$ (%)
2-MEA	9.26	0.70	45.1	1417	80.3	2.92 (2.70)
2-MEA:Toulene (9:1)	11.76	0.67	49.5	629.5	11.7	3.90 (3.53)
2-MEA:Toulene (4:1)	12.0	0.76	50.2	1251	41.3	4.56 (4.43)
2-MEA:Toulene (7:3)	12.66	0.78	58.4	2750	30.0	5.77 (5.65)



(a)



(b)

Figure 5.24: (a) J-V curves of non-encapsulated devices with the $PTB7 : PC_{70}BM$ with optimal co-solvents (2-MEA:Toulene) concentration and (b) shows the J-V dark conditions for the devices.

$cm^2/V \cdot s$ for devices measured after 7 and 8 days, possibly due to further molecular ordering or mild annealing effects within the film. This improvement indicates that the film morphology, initially established by the solvent mix, remains robust, not degrading or undergoing adverse phase separation with time. Co-solvents like 2-MEA and toluene significantly influence the solubility dynamics and drying kinetics during film formation, affecting both initial film quality and its long-term stability. The chosen ratio of 2-MEA to toluene seems particularly adept at fostering a well-mixed phase that supports both high performance and stability, crucial for the longevity and efficacy of organic photovoltaic devices.

The J-V curves illustrated in Figures 5.24 (a) and (b) indicate that the electrical parameters of these devices remained unchanged over an 8 day observation period. This finding is significant, suggesting that the absence of encapsulation does not detrimentally affect the short-term stability of the device's electrical performance when stored in a

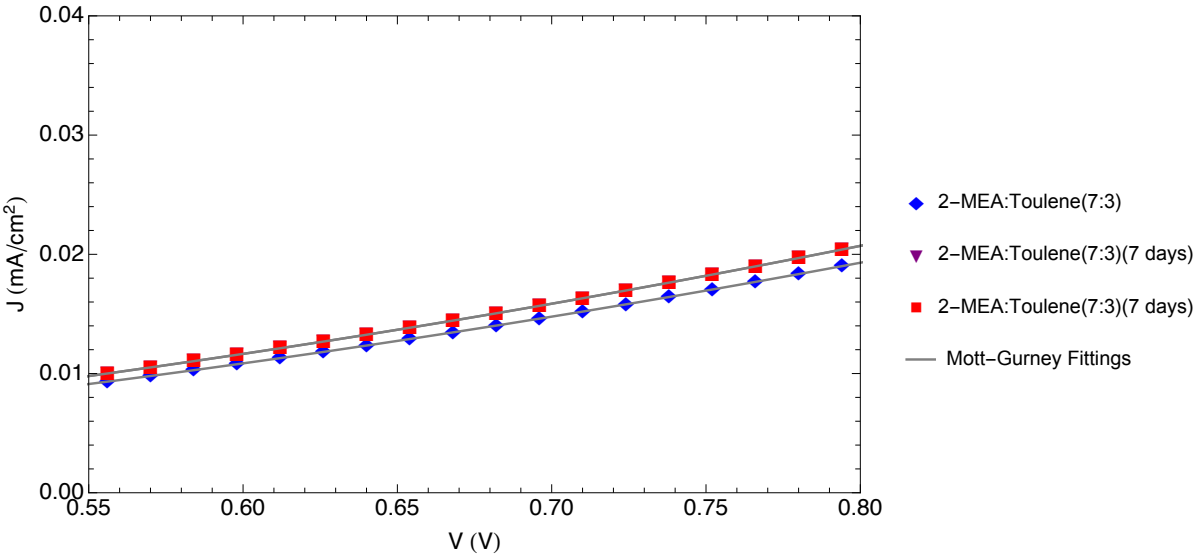


Figure 5.25: Fittings performed by Equation (5.3) over the dark J-V measurements (range of 0.55-0.8 V) for non-encapsulated devices with the active of $PTB7 : PC_{70}BM$ in (2-MEA:Toulene) as the optimal concentration.

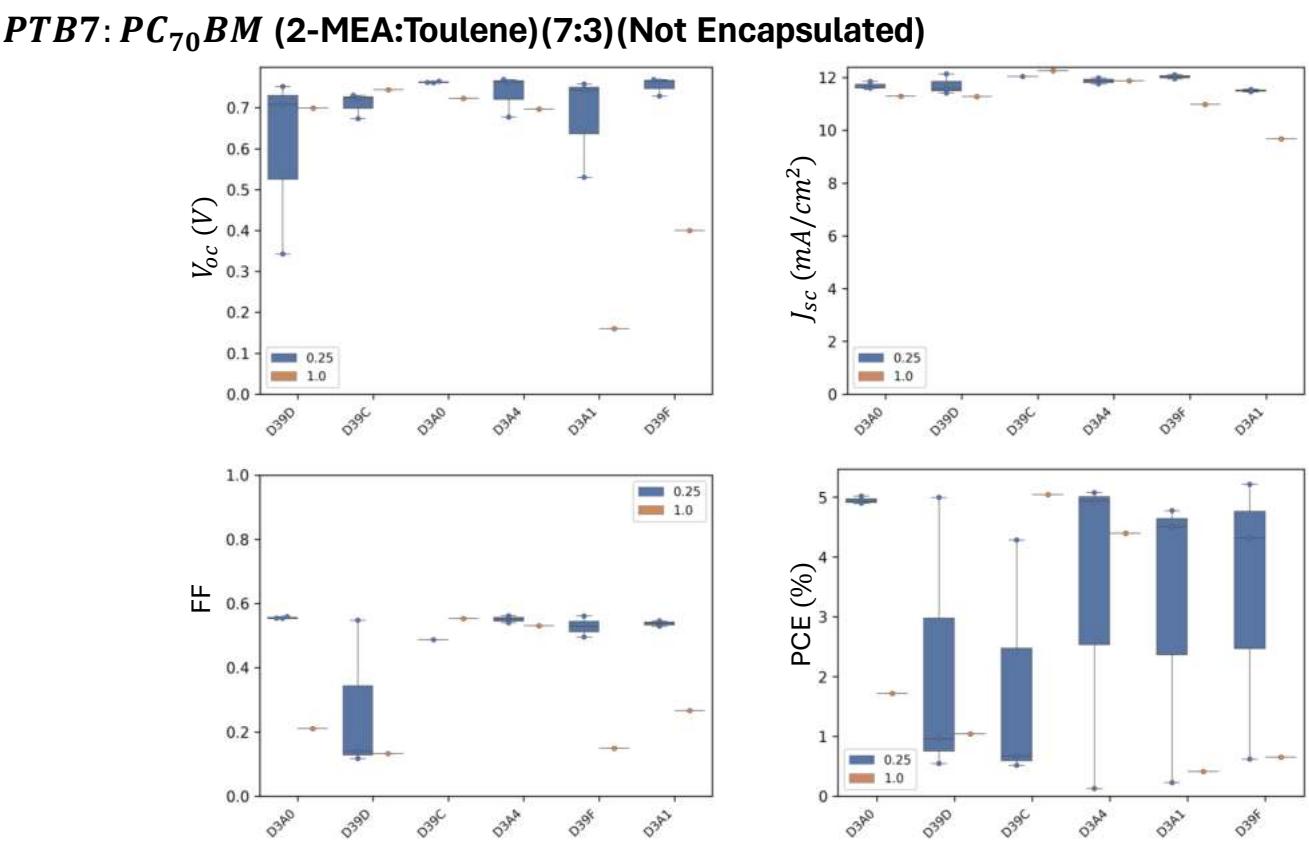


Figure 5.26: Statistical non-encapsulated device parameters of the active layer in $PTB7 : PC_{70}BM$ (1:1.5) using the optimal co-solvents (2-MEA:Toluene) ratio.

controlled environment, such as a glove box. The consistent behaviour of the electrical properties is not limited to the observations made in Figure 5.24 (a) but is also evident across Figures 5.26 to 5.28. These additional figures further substantiate the initial

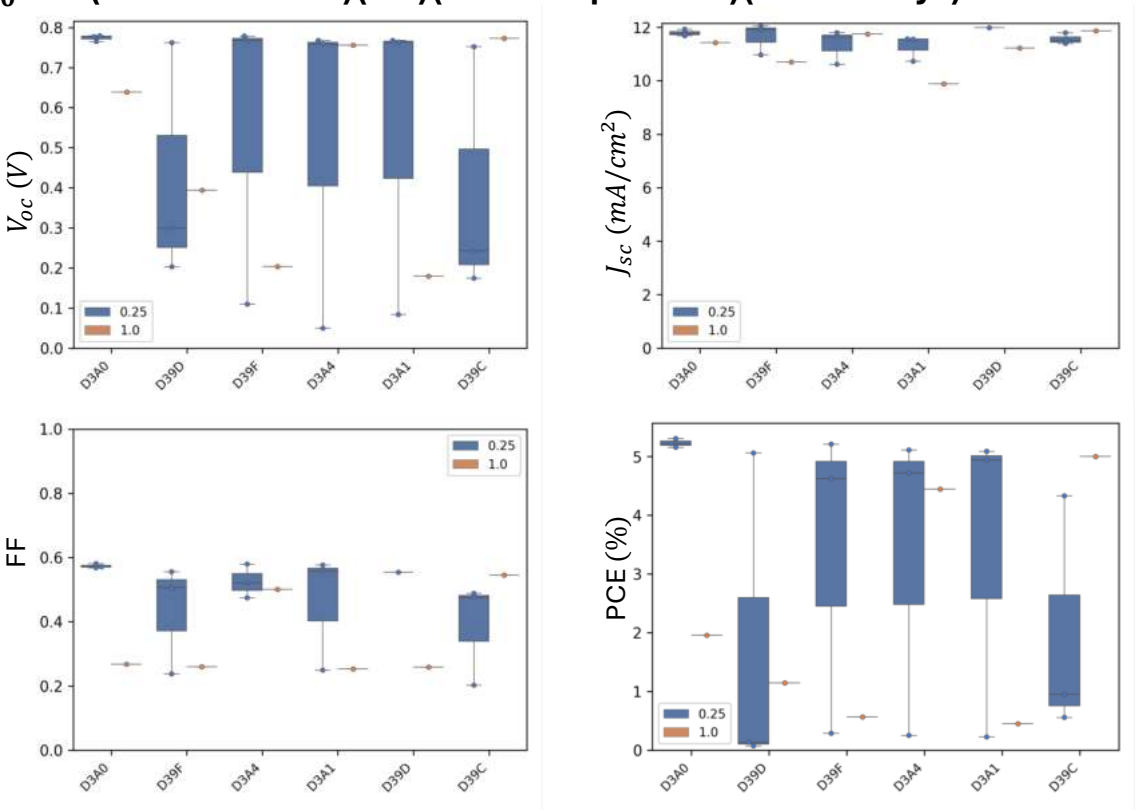


Figure 5.27: Statistical non-encapsulated device parameters of the active layer in $PTB7$: $PC_{70}BM$ (1:1.5) using the optimal co-solvents (2-MEA:Toluene) after 7 days.

observation, presenting a broader view of the devices' stability by showcasing consistent electrical performance across multiple samples and measurement conditions. This consistency highlights the potential for these non-encapsulated devices to maintain their performance under stable environmental conditions, an important consideration for their practical application and longevity.

$PTB7:PC_{70}BM$ (2-MEA:Toulene)(7:3)(Not Encapsulated)(After 8 Days)

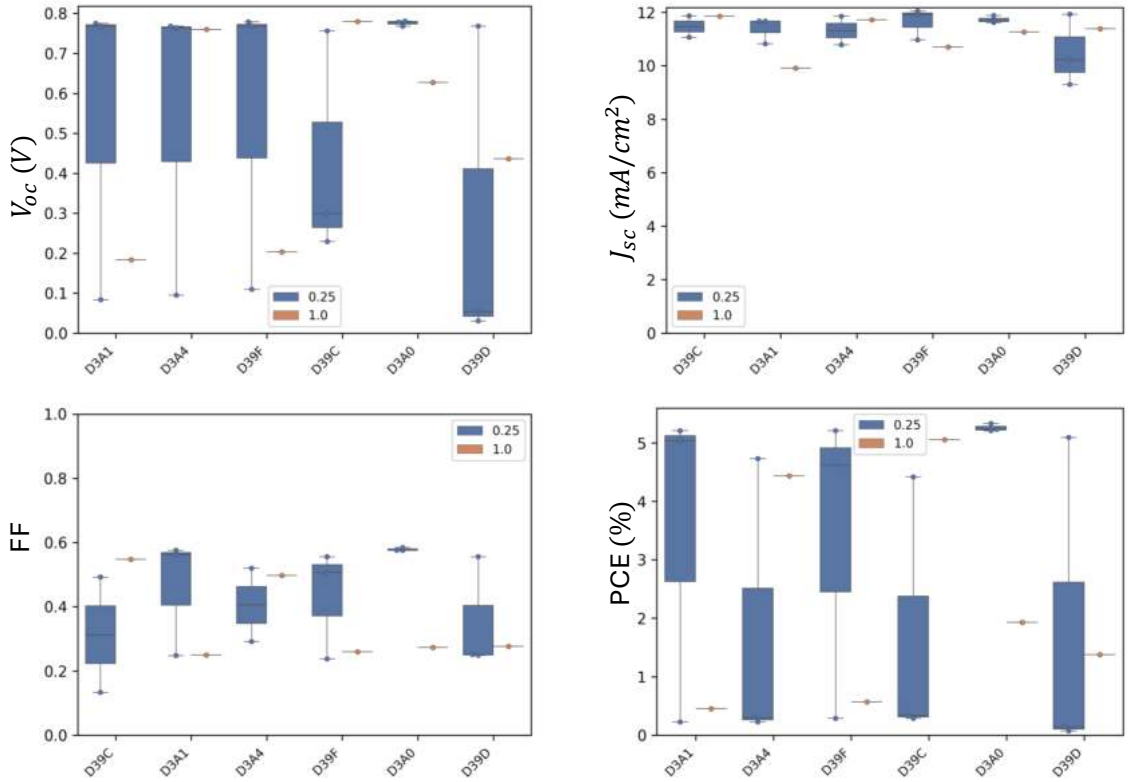


Figure 5.28: Statistical non-encapsulated device parameters of the active layer in $PTB7:PC_{70}BM$ (1:1.5) using the optimal co-solvents (2-MEA:Toluene) after 8 days.

Table 5.5: Photovoltaic parameters of the $PTB7:PC_{70}BM$ (1:1.5) non-encapsulated devices with optimal co-solvent concentration of 2-MEA:Toulene (7:3) measured for a period of 8 days.

Time (Days)	J_{sc} (mA/cm^2)	V_{oc} (V)	FF (%)	R_{sh} $(\Omega \cdot cm^2)$	R_s $(\Omega \cdot cm^2)$	$PCE_{max}(Avg)$ (%)
0	12.13	0.77	55.8	2097	37.8	5.21 (5.10)
7	12.04	0.78	55.9	1724	33.6	5.24 (5.11)
8	12.04	0.78	55.9	1724	33.6	5.24 (5.10)

The effect of relaxation of the metastable interconnected network is mainly observed in the changes of the V_{oc}, FF, R_{sh}, R_s, PCE and J_{sc} Table 5.5 shows that these values remain constant over time as illustrated in Figure 5.29 experienced a marginal

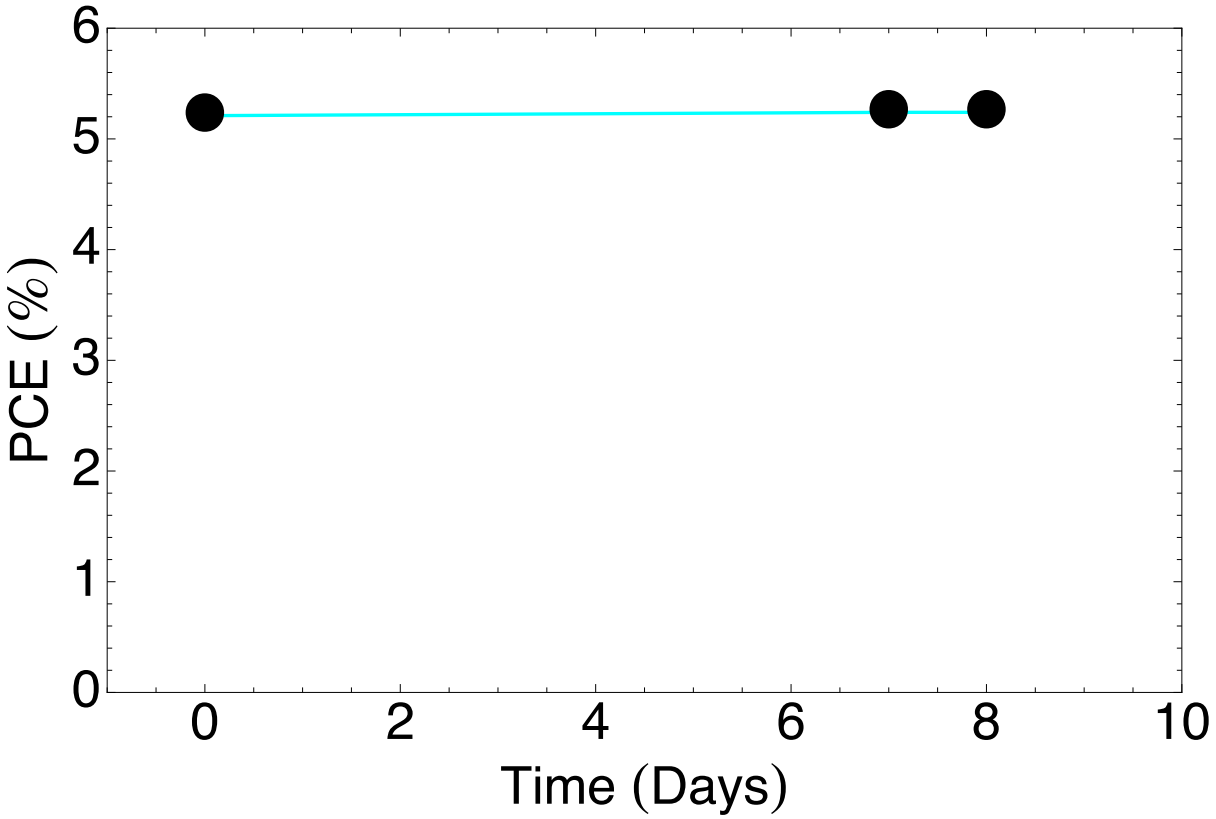
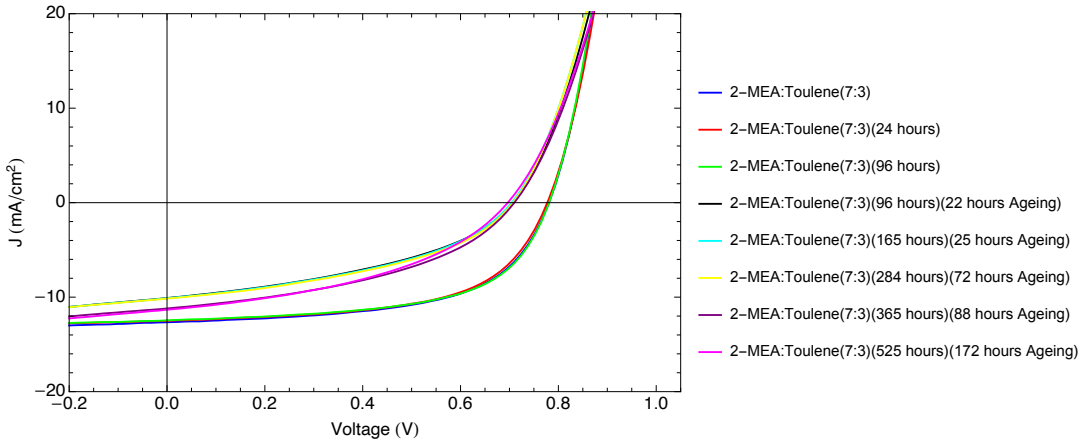


Figure 5.29: Evolution of PCE over 8 days for the non-encapsulaled $PTB7 : PC_{70}BM$ devices.

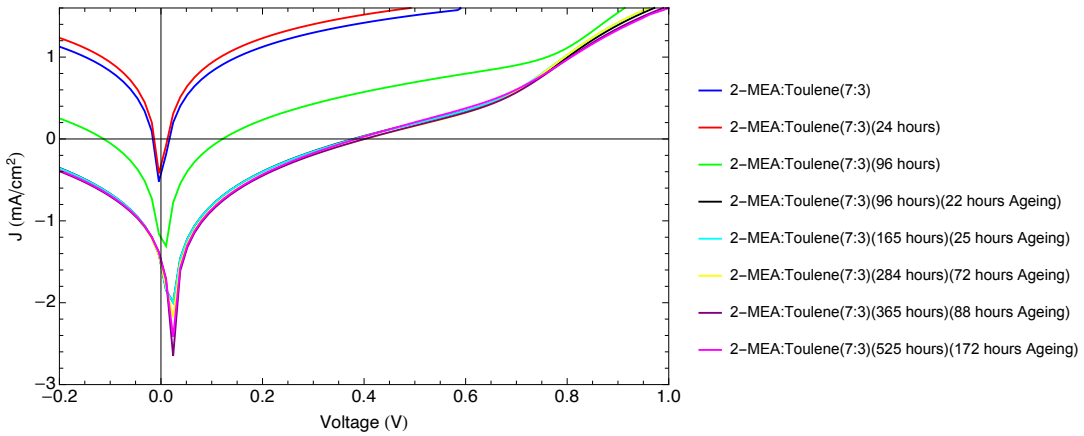
increase of 0.3% upon measurements conducted over a period of 7 days, with a notable observation on the 8th day. This enhancement in device efficiency can be attributed to several environmental influences, including light exposure, fluctuations in temperature, or subtle alterations in the cell's architecture resulting from handling [515, 716]. Such factors are known to induce slight yet positive changes in the device's operational parameters. The dependability and efficacy of OSCs are determined by a myriad of factors, such as the choice of materials, the process of fabrication, and the conditions under which they are stored. These observations are in consonance with existing studies that emphasise the critical role of precise measurement protocols and the consideration of stability in assessing the efficiency of organic solar cells across varied environmental conditions [717–719].

Encapsulation is crucial for protecting solar cells from environmental factors like oxygen and moisture, which can degrade the cell components and reduce PCE over time. However, the encapsulation process itself can introduce additional challenges that impact performance. Issues such as encapsulation-induced defects, material compatibility challenges, degradation over time, encapsulation thickness effects, and encapsulation process quality variations can collectively impact the performance of encapsulated OSCs as observed in the statistical data of encapsulated (Figure 5.32) and non-encapsulated (Figure 5.26) devices.

The Mott-Gurney analysis long-term stability tests on encapsulated $PTB7 : PC_{70}BM$ devices in Figure 5.31 using an 2-MEA:Toluene (7:3) co-solvent system reveal insight-



(a)



(b)

Figure 5.30: (a) J-V curves of encapsulted devices with the $PTB7 : PC_{70}BM$ (1:1.5) mass ratio with a green solvent (2-MEA) and with various concentration of an industrial solvent (Toulene) being added to the blend. (b) shows the J-V dark conditions for the devices.

ful trends in charge carrier mobility over 697 hours of ageing. Initially, charge carrier mobility exhibits slight fluctuations but generally shows an upward trend as depicted in Table 5.7, possibly due to enhanced molecular ordering within the film, likely influenced by post-fabrication annealing effects induced by the high temperatures [631]. However, after reaching a peak, μ begins to decrease, suggesting the onset of thermal degradation or adverse effects from prolonged exposure to air, reflecting changes in the film's morphology. The initial stability and later decline in mobility highlight the role of film morphology, which seems initially well-configured for stability due to the optimal solvent mix promoting good solubility and interaction between PTB7 and $PC_{70}BM$. This configuration withstands environmental stresses initially but shows limits under prolonged harsh conditions. Despite these mobility changes, the efficiency of the devices remains stable, suggesting that encapsulation effectively protects the active materials from some degradative effects, such as moisture and oxygen ingress. This underscores the significant influence of the chosen co-solvent system in establishing a morphology conducive to both initial high performance and substantial resilience over time, though with noted limitations under extended stress, providing crucial insights for further material and process

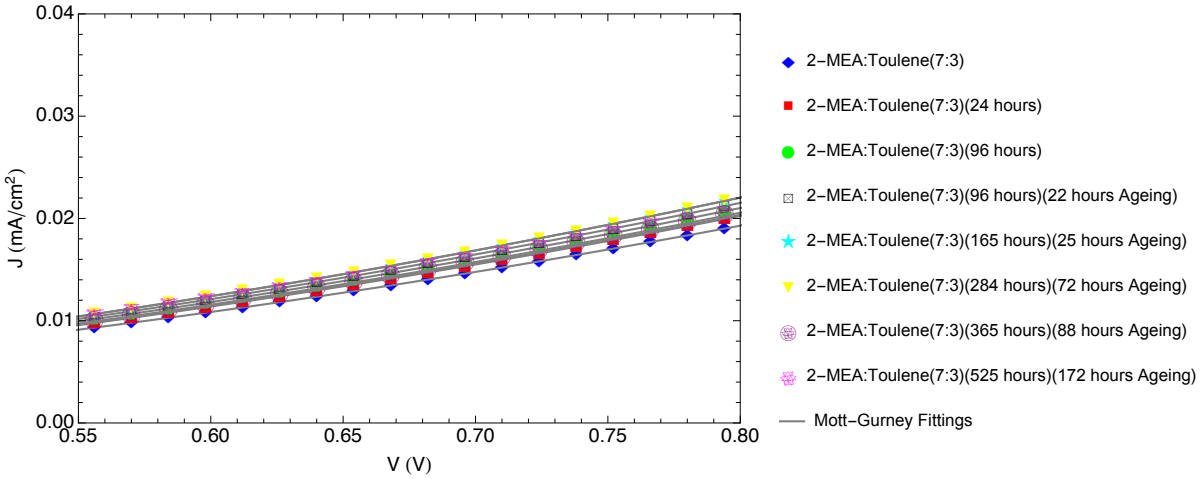


Figure 5.31: Fittings performed by Equation (5.3) over the dark J-V measurements (range of 0.55-0.8 V) for encapsulated devices with the active layer of $PTB7 : PC_{70}BM$ (1:1.5) in (2-MEA:Toulene) as the optimal concentration with a thickness of 136 nm measured over 697 hours.

optimisation in OSCs.

$PTB7 : PC_{70}BM$ (2-MEA:Toulene)(7:3)(Encapsulated)

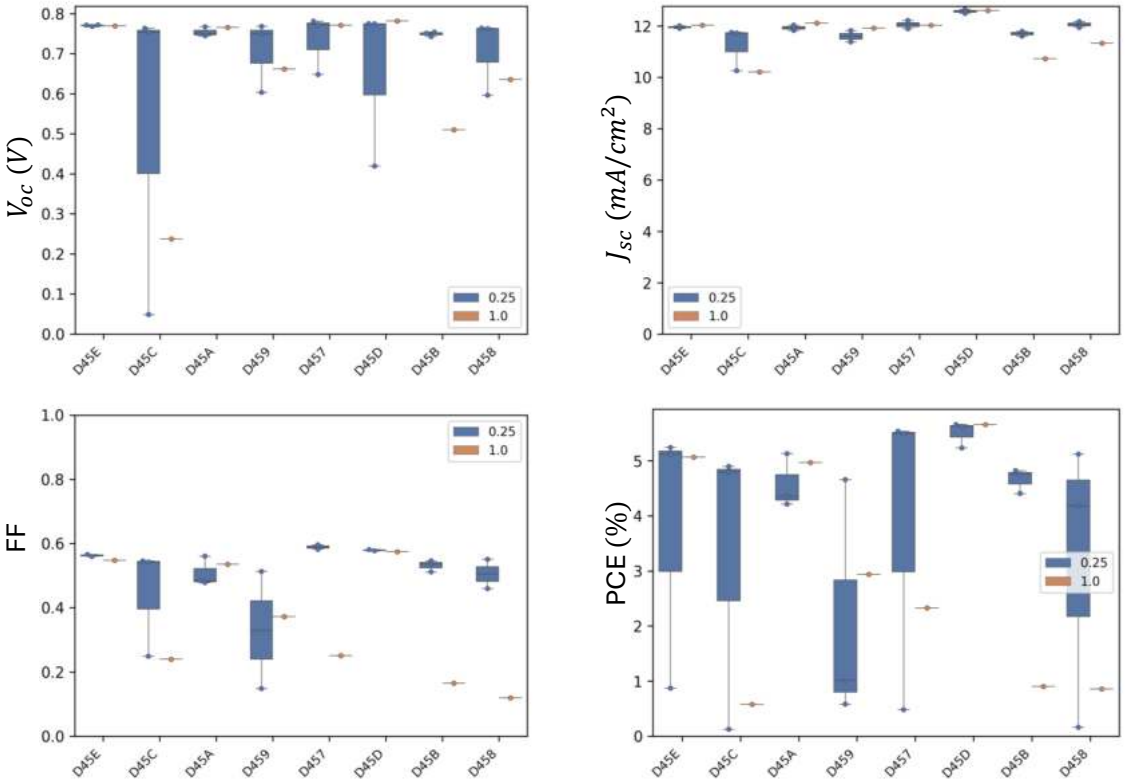


Figure 5.32: Statistical encapsulated device parameters of the active layer in $PTB7 : PC_{70}BM$ (1:1.5) using the optimal co-solvents (2-MEA:Toluene) ratio.

$PTB7:PC_{70}BM$ (2-MEA:Toulene)(7:3)(Encapsulated)(24 Hours)

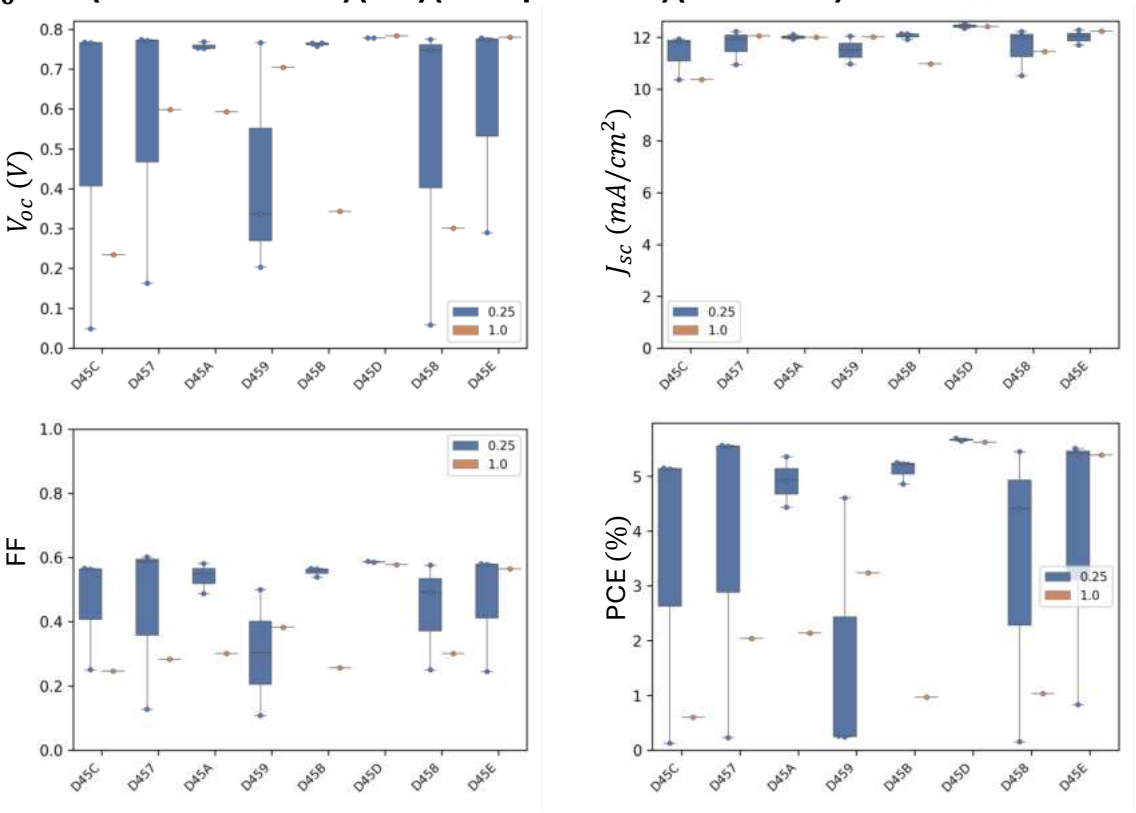


Figure 5.33: Statistical encapsulated device parameters of the active layer in $PTB7$: $PC_{70}BM$ (1:1.5) using the optimal co-solvents (2-MEA:Toluene) ratio after 24 hours.

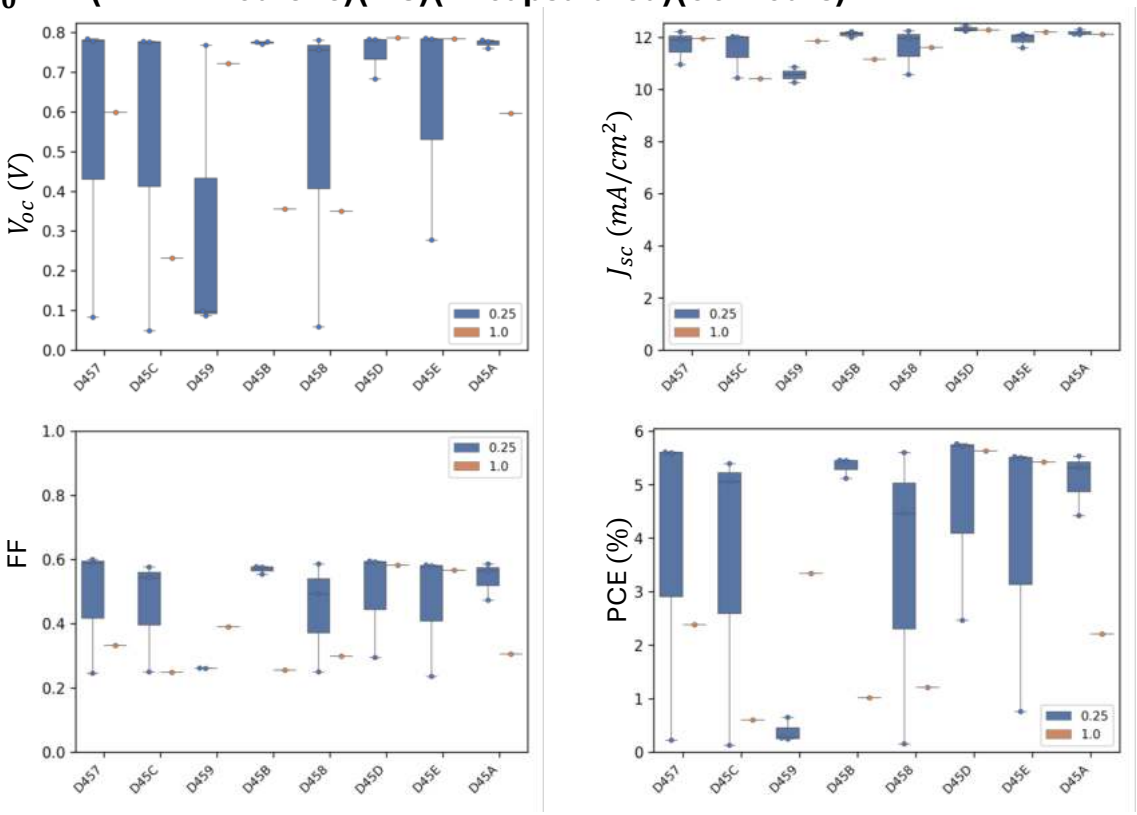


Figure 5.34: Statistical encapsulated device parameters of the active layer in $PTB7$: $PC_{70}BM$ (1:1.5) using the optimal co-solvents (2-MEA:Toluene) ratio after 96 hours.

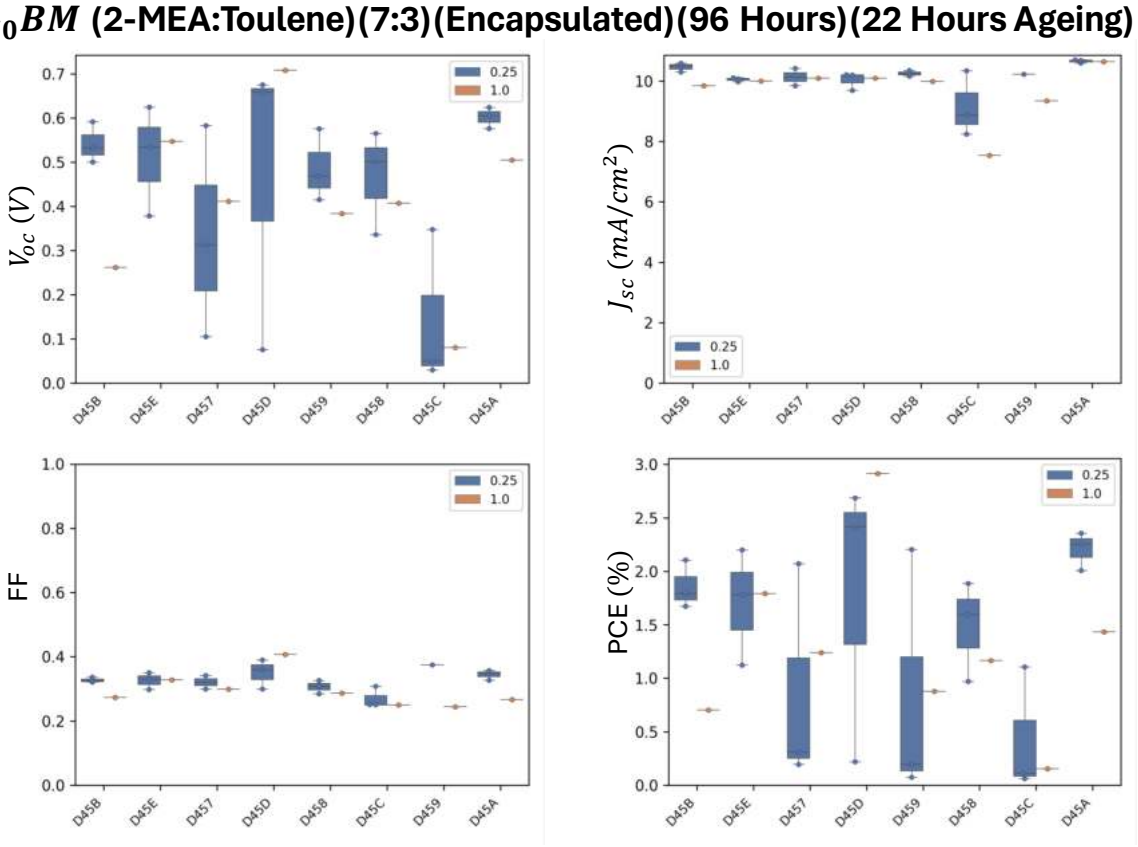


Figure 5.35: Statistical encapsulated device parameters of the active layer in $PTB7$: $PC_{70}BM$ (1:1.5) using the optimal co-solvents (2-MEA:Toluene) ratio after light ageing at 85° C for 22 hours in air, 96 hours post fabrication.

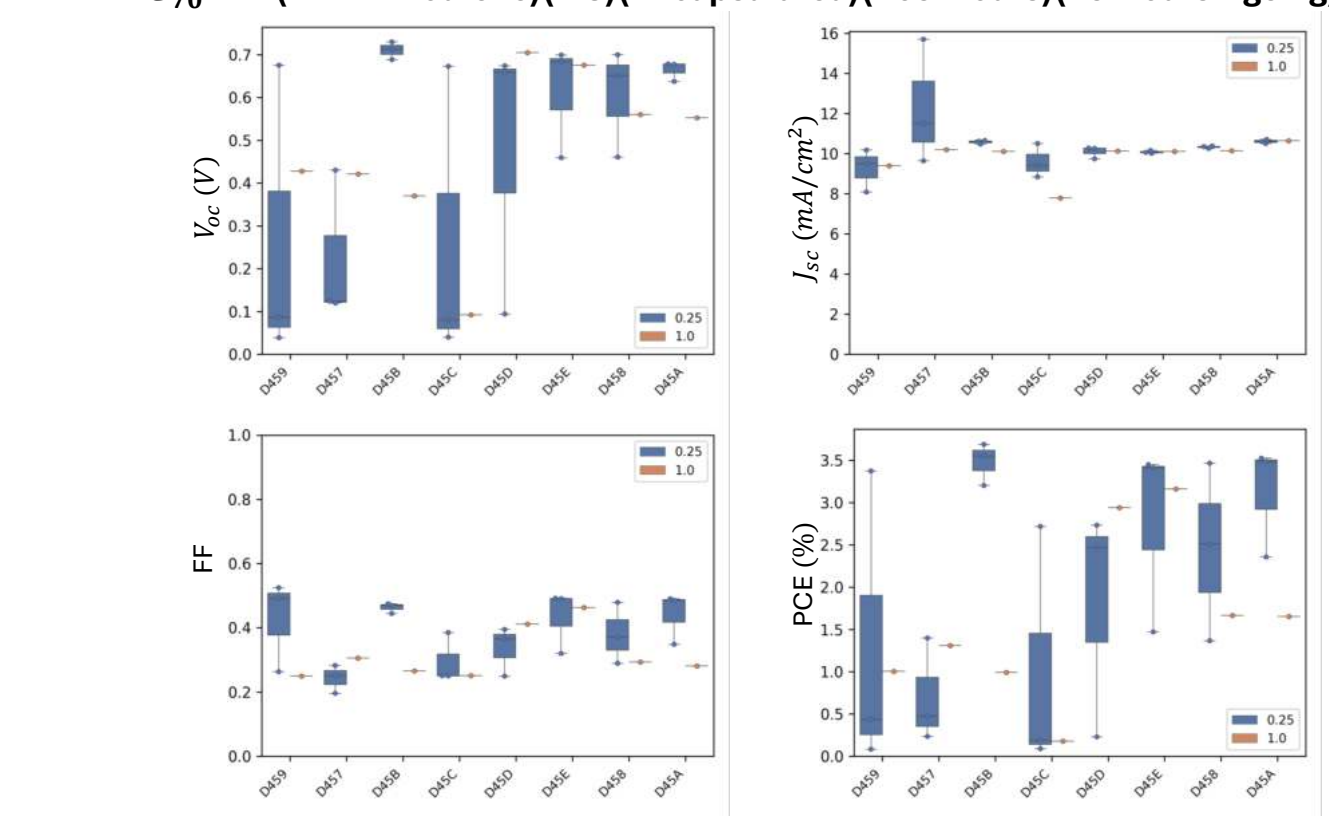


Figure 5.36: Statistical encapsulated device parameters of the active layer in $PTB7$: $PC_{70}BM$ (1:1.5) using the optimal co-solvents (2-MEA:Toluene) ratio after being stored for 47 hours for the devices to recover, then light ageing at 85° C for 25 hours in air, 165 hours post fabrication.

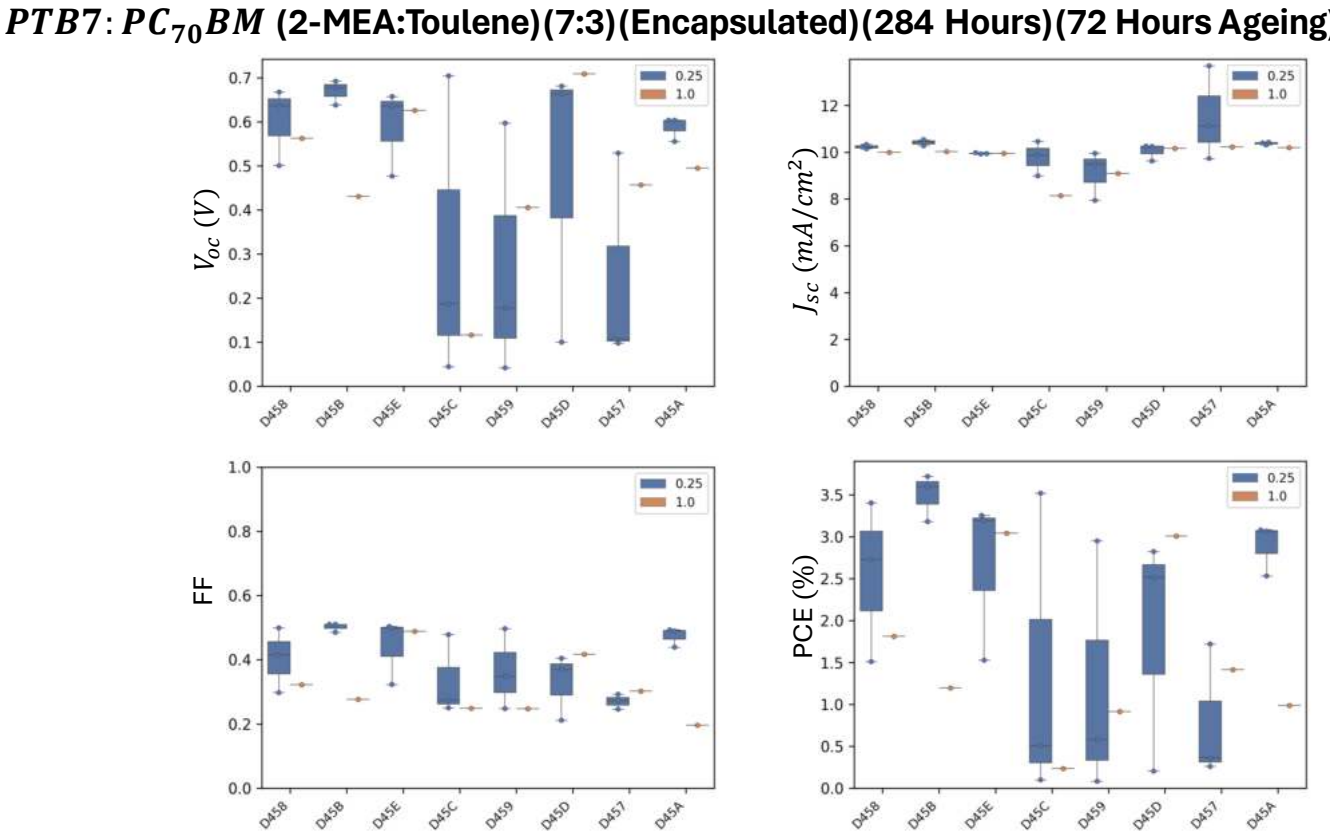


Figure 5.37: Statistical encapsulated device parameters of the active layer in $PTB7$: $PC_{70}BM$ (1:1.5) using the optimal co-solvents (2-MEA:Toluene) ratio after being stored for 94 hours for the devices to recover, then light ageing at 85° C for 72 hours in air, 284 hours post fabrication.

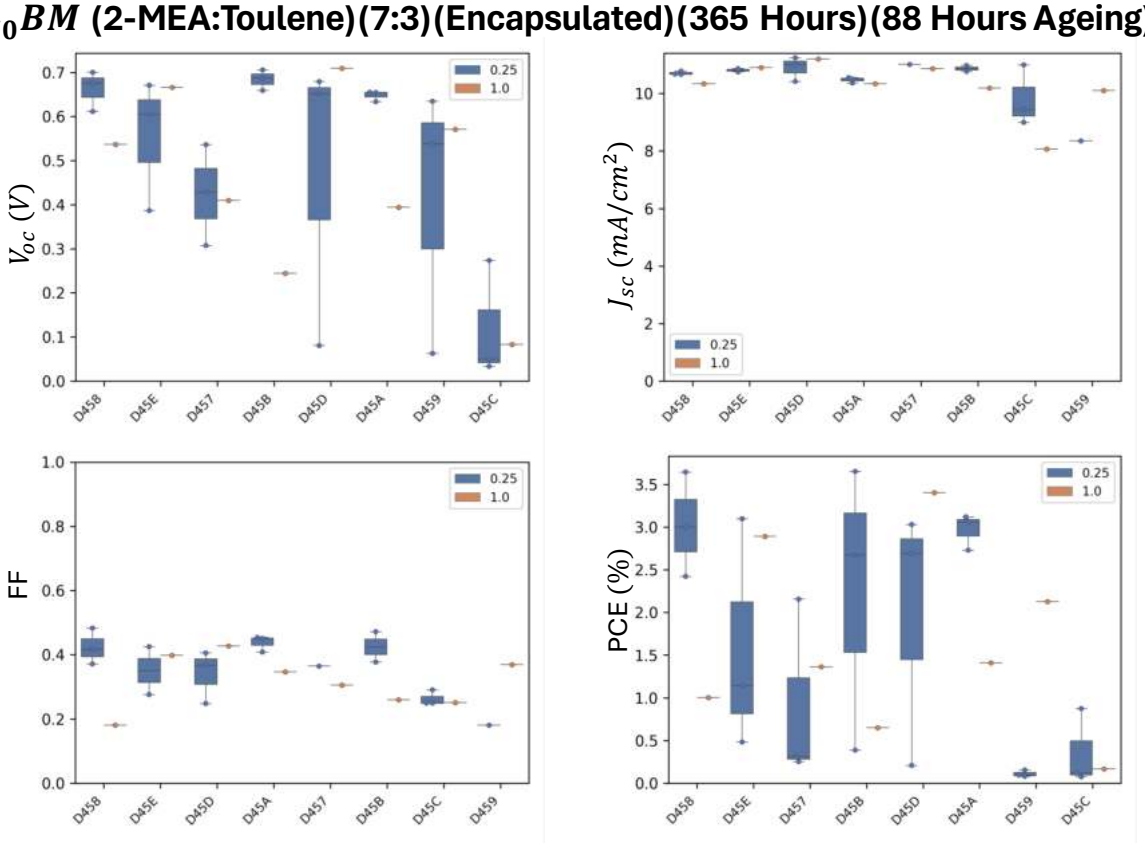


Figure 5.38: Statistical encapsulated device parameters of the active layer in $PTB7$: $PC_{70}BM$ (1:1.5) using the optimal co-solvents (2-MEA:Toluene) ratio after light ageing at 85° C for 72 hours in air, 365 hours post fabrication.

$PTB7:PC_{70}BM$ (2-MEA:Toulene)(7:3)(Encapsulated)(525 Hours)(172 Hours Ageing)

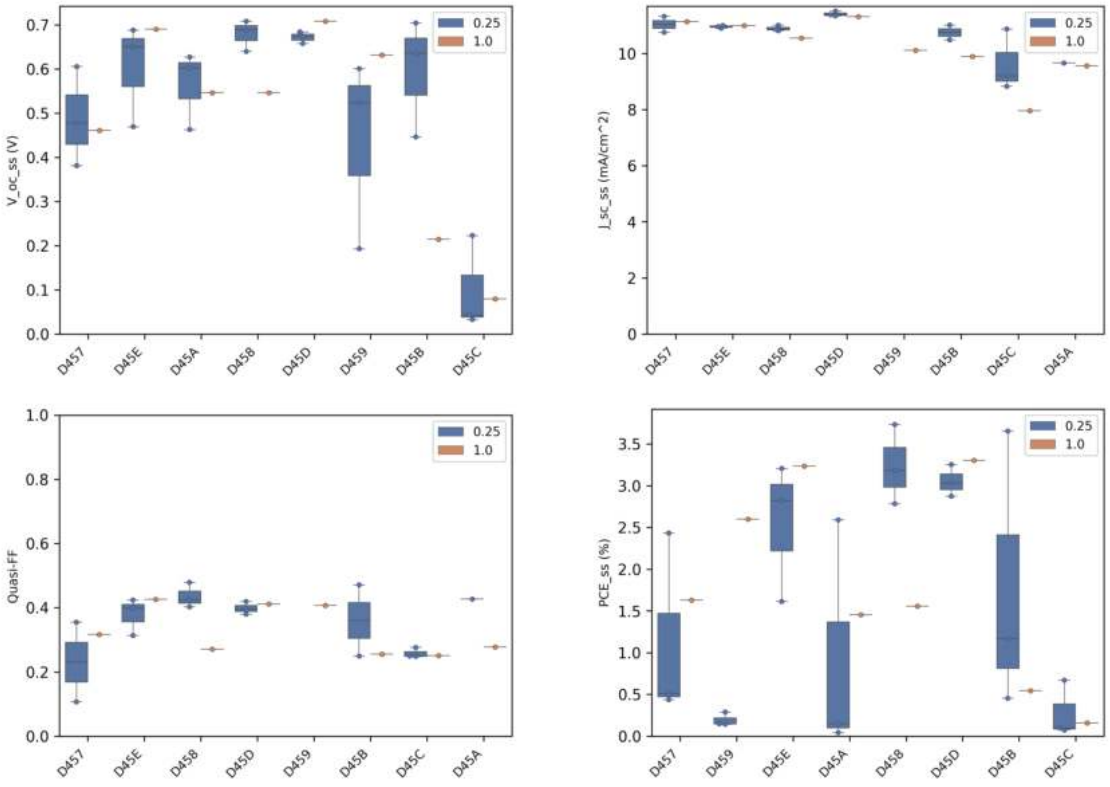


Figure 5.39: Statistical encapsulated device parameters of the active layer in $PTB7$: $PC_{70}BM$ (1:1.5) using the optimal co-solvents (2-MEA:Toluene) ratio after light ageing at 85° C for 172 hours in air, 525 hours post fabrication.

Table 5.6: Photovoltaic parameters of the $PTB7 : PC_{70}BM$ encapsulated devices with optimal co-solvent concentration of 2-MEA:Toulene (7:3) measured for a period of 697 hours.

Time (Hours)	J_{sc} (mA/cm^2)	V_{oc} (V)	FF (%)	R_{sh} $(\Omega \cdot cm^2)$	R_s $(\Omega \cdot cm^2)$	$PCE_{max}(Avg)$ (%)
0	12.66	0.78	58.4	2750	30.0	5.77 (5.68)
24	12.51	0.78	58.5	2012	32.1	5.69 (5.63)
96	12.45	0.78	59.4	1672	29.0	5.77 (5.48)
96 (Ageing for 22)	10.10	0.71	41.1	195.8	16.4	2.94 (2.66)
165 (Ageing for 25)	10.11	0.70	41.8	199.9	15.9	2.98 (2.95)
284 (Ageing for 72)	10.10	0.71	42.1	212.6	15.3	3.04 (2.99)
365 (Ageing for 88)	11.20	0.71	43.0	213.3	15.1	3.42 (3.35)
525 (Ageing for 172)	11.33	0.70	42.0	199.9	16.6	3.32 (3.25)

Table 5.7: Charge carrier mobilities for encapsulated devices with the active layer of $PTB7 : PC_{70}BM$ (1:1.5) in (2-MEA:Toulene) as the optimal concentration with a thickness of 136 nm measured over 697 hours.

Time (Hours)	μ ($\times 10^{-5}\ cm^2/V \cdot s$)
0	2.76
24	2.66
96	2.77
96 (Ageing for 22)	2.83
165 (Ageing for 25)	2.90
284 (Ageing for 72)	2.90
365 (Ageing for 88)	2.71
525 (Ageing for 172)	2.68

The investigation into the electrical characteristics of encapsulated devices reveals nuanced insights into the behaviour of these devices under varying conditions of ageing and storage. Initial findings, as showcased in Figure 5.30 (a), indicated a pronounced decline in PCE from 5.77% to 2.94% after the first 22-hour ageing period at a high temperature of 85° C in air. This reduction is attributed to the detrimental impacts of elevated temperatures on the solar cell components, particularly affecting the morphology and integrity of the active layer, which is crucial for efficient charge transport and separation [720]. The dark J-V curves in Figure 5.30 exhibit excellent diode quality with a very low leakage current density and high rectification ratio for the devices that have not gone the ageing process, whereas the devices that have gone under the ageing process produced higher leakage current density and lower rectification ratio.

The decrease in efficiency in the fabricated OSCs after the ageing process could be due to various factors. One significant reason for this decline is the degradation of the materials used in the solar cells over time, especially when exposed to environmental stressors like heat, humidity and UV radiation [721]. This degradation can lead to a

reduction in the performance of the solar cells, impacting their efficiency. Moreover, the impact of ageing on the morphology of OSCs is crucial. Ageing can cause changes in the structure and composition of the materials within the device, affecting their morphology. These changes can include phase segregation of the polymer and fullerene domains, which is influenced by factors like Ostwald ripening [722, 723]. Additionally, the vertical segregation profile towards the external electrodes plays a crucial role in device operation, affecting parameters such as leakage current, energy-level alignment, and interfacial recombination processes [724].

The essence of the efficiency stabilisation and slight recovery observed after successive ageing stages can be reasoned with a combination of material resilience and self-healing mechanisms inherent to the active layer materials used in these devices. Upon extended exposure to ageing conditions, it is conceivable that the materials undergo a form of structural reorganisation [725]. These effects has been observed by Ciammaruchi et al., 2016 when using the active layer $PTB7 : PCBM$ in encapsulated devices [726]. This reorganisation could mitigate the initial detrimental effects of high-temperature ageing, enabling a more stable charge transport pathway and, consequently, a gradual improvement in device performance.

Moreover, the storage periods, especially in controlled environments like a glove box, might play a crucial role in facilitating the relaxation of internal stresses within the device structure [727]. The glass transition temperature (T_g) of PTB7 and $PC_{70}BM$ provides insights into the stability of the frozen metastable BHJ state. PTB7 does not exhibit a T_g up to 200° C [722]. For a polymer:fullerene blend with PTB7, T_g is 200° C. This high Tg was achieved using a blend of unsubstituted C60 and C70 fullerenes with PTB7, is notable for maintaining stable photovoltaic performance even after annealing at temperatures up to 180° C, just below the onset of the glass transition [728]. This relaxation could help in reversing some of the degradation effects experienced during the high-temperature ageing process. The controlled environment could also protect the device from further oxidative or moisture-induced degradation, offering a conducive setting for the stabilisation of the device's electrical properties.

The statistical device parameters illustrated in Figures 5.32 through 5.39 further corroborate this trend, displaying a notable drop in device performance post the initial ageing phase, followed by a subtle yet consistent recovery after subsequent ageing cycles. This pattern suggests that while the initial ageing phase at elevated temperatures imposes a significant challenge to device stability, the materials' intrinsic properties, coupled with controlled storage conditions, contribute to a slow but steady recuperation of PCE as shown in Figure 5.40.

This detailed examination underscores the complexity of factors influencing the ageing and recovery of OSCs with $PTB7 : PC_{70}BM$ as an active layer. It highlights the interplay between temperature-induced degradation, material resilience, and environmental conditions in determining the long-term stability and performance of these devices. These findings, summarised in Table 5.6, provide a comprehensive view of the dynamic ageing behaviour of encapsulated devices using co-solvents and underline the potential for optimising device longevity and efficiency through understanding and mitigating ageing mechanisms.

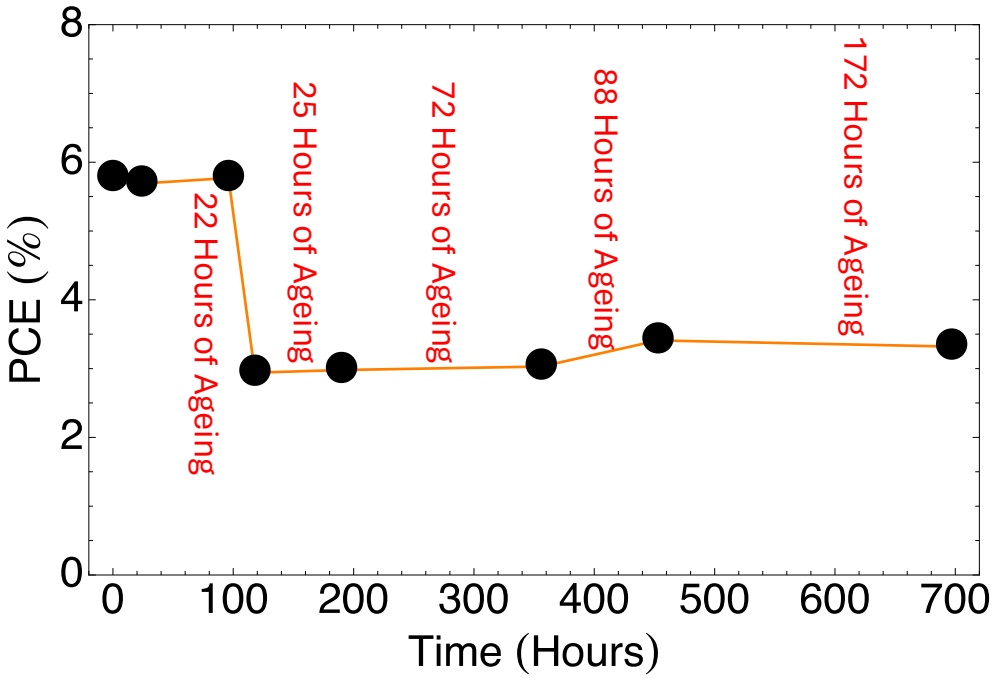


Figure 5.40: Evolution of PCE over 697 hours for the encapsulaled $PTB7 : PC_{70}BM$ devices.

NFA Based Organic Solar Cells: Green vs Chlorinated Solvents

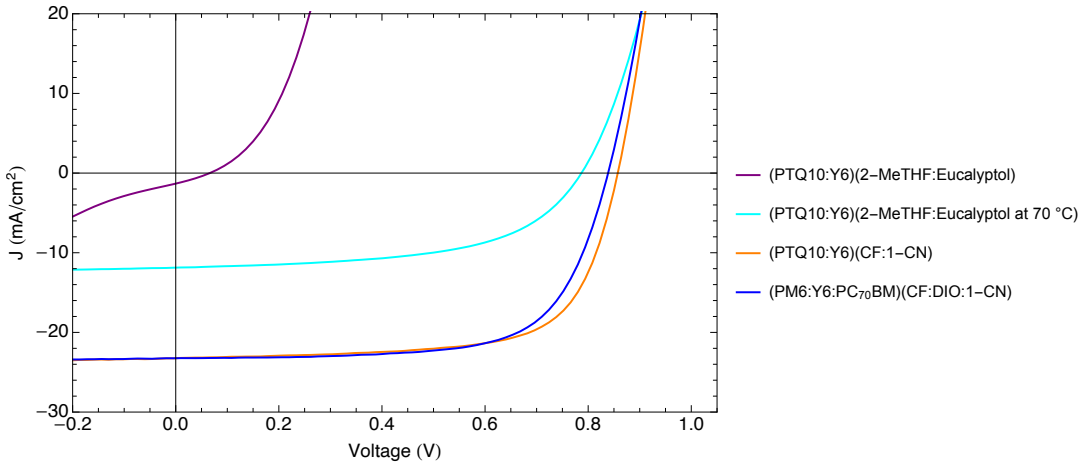
Non-fullerene acceptors (NFAs) have significantly advanced the field of OSCs in recent years, surpassing fullerene-based systems in both efficiency and stability. These materials have transformed the OSC landscape by offering improved absorption spectra, tunable energy levels, and better morphological stability, which are crucial for the long-term performance of OSCs [729, 730].

In the quest for more sustainable and environmentally friendly solar energy solutions, the development of OSCs using NFAs has emerged as a promising direction. A critical aspect of fabricating high-efficiency OSCs involves the selection of solvents for the solution-processing of active layers. Traditionally, chlorinated solvents have been the go-to choice due to their excellent solubility properties and ability to facilitate high-performance device fabrication. However, the environmental and health hazards associated with chlorinated solvents necessitate the exploration of greener, safer alternatives.

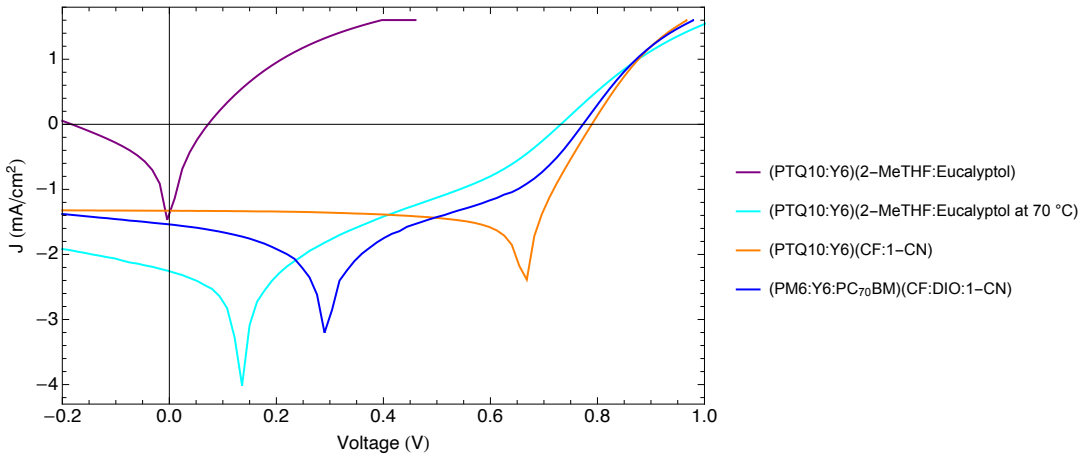
This section of the thesis presents a comprehensive analysis of the use of green solvents in the fabrication of NFA-based OSCs, emphasising the advantages of such a transition. The PTQ10 polymer serves as an efficient donor material, characterised by its solubility in a wide array of organic solvents and a high thermal decomposition threshold. This material exhibits robust optical absorption properties within the 400 - 600 nm spectrum, accompanied by a band gap of 1.9 eV [731]. Its compatibility with the NFA Y6 further broadens its absorption profile to reach up to 900 nm [732, 733]. This extended absorption range makes it an ideal candidate for bulk heterojunction applications in this study, as it significantly enhances the potential for photon harvesting across a large wavelength window.

In our study, we delve into an analysis comparing the impact of eco-friendly solvents

against conventional chlorinated solvents on the electrical properties of the active layers within NFA based OSCs. The selection of green co-solvents is informed by the computational data presented in Figure 5.2, alongside the parameters outlined in Table 5.1. These elements serve as pivotal factors in determining the manner in which each solvent engages with the donor/acceptor materials. The insights drawn from these calculations and parameters provide a foundational guideline for understanding the solvent-material interaction dynamics, emphasising the potential enhancements or drawbacks brought forth by the use of green solvents in the fabrication and performance optimisation of NFA-based OSCs. Through this exploration, we aim to shed light on the ecological and efficiency advantages of adopting green solvents in the production of OSCs, contributing to the development of more sustainable and high-performing solar energy solutions.



(a)



(b)

Figure 5.41: J-V curves of devices formed from Donor: NFA heterojunction with the photoactive layer being formed from the spin casting after dissolving in chlorinated and green co-solvents.

The observed variations in charge carrier mobilities in Figure 5.42 across NFA these devices, which incorporate different NFA materials and co-solvent systems, clearly illustrate the significant impact of solvent choice, concentration, and processing conditions on the morphology and performance of OPV devices. For instance, the very low mobility of

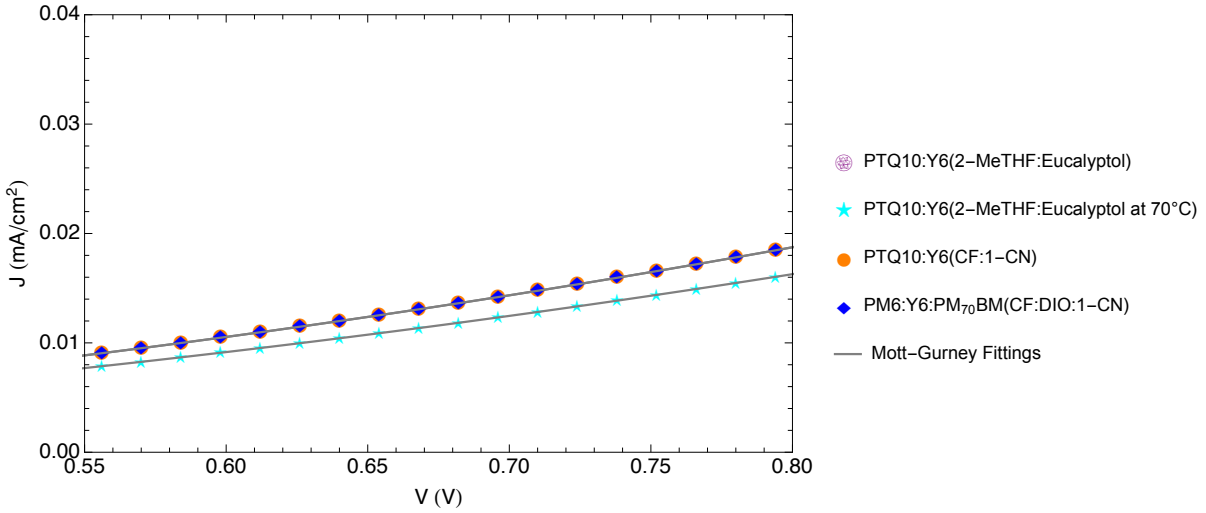


Figure 5.42: Fittings performed by Equation (5.3) over the dark J-V measurements (range of 0.55-0.8 V) for NFA based devices using various co-solvent systems.

1.90×10^{-5} $cm^2/V \cdot s$ in the PTQ10:Y6 system using a green co-solvent mixture of 2-MeTHF and Eucalyptol suggests inadequate dissolution or suboptimal phase separation, likely due to mismatched solubility parameters. However, when the same solvent mixture is heated to 70° C, the mobility increases significantly (2.49×10^{-5} $cm^2/V \cdot s$), indicating improved solubility and film morphology, possibly due to enhanced molecular ordering facilitated by increased temperature. In contrast, the use of a chlorinated co-solvent system (CF:1-CN) in the PTQ10:Y6 setup resulted in the highest mobility (8.87×10^{-5} $cm^2/V \cdot s$), suggesting that these solvents effectively dissolve both components and promote optimal molecular alignment and phase separation. Similarly, the ternary system involving $PM6 : Y6 : PC_{70}BM$ and CF:1-CN:DIO also shows high mobility (7.90×10^{-5} $cm^2/V \cdot s$), albeit slightly lower than the binary system, possibly due to the processing additive DIO altering the film's microstructure.
The J-V curves illustrated in Figure 5.43, reveals the impactful role of chlorinated co-solvents, augmented by the addition of 1-CN, in the performance of devices that feature PTQ10:Y6 as the active layer. The utilisation of chlorinated solvents stands out for its significant contribution to enhancing power PCE. Notably, the deployment of these solvents in the device fabrication process led to a peak PCE of 13.7% in one instance, with an average PCE of 12.34% across all devices. This performance metric starkly contrasts with the outcomes achieved using green solvents, thereby emphasising the superiority of chlorinated co-solvents in promoting higher PCE values, as corroborated by the analytical data presented in Figure 5.41.

Moreover, HSP analysis, detailed in Figure 5.2 and conducted under ambient conditions, underscores the complexity inherent in optimising the solubility of organic materials for PV applications. This complexity arises from the myriad of factors affecting solubility, including temperature, molecular weight distribution, and the polarity of solvents, which in turn influence the photovoltaic device's efficiency and stability [734].

The comparison between ternary and binary blends, particularly the $PM6 : Y6 : PC_{70}BM$ blend achieving a PCE of 13.3%, reveals another dimension of device optimisation. Although the ternary blend exhibits a slightly lower PCE compared to its binary

***PTQ10*:*Y6* (CF:0.5% 1-CN)**

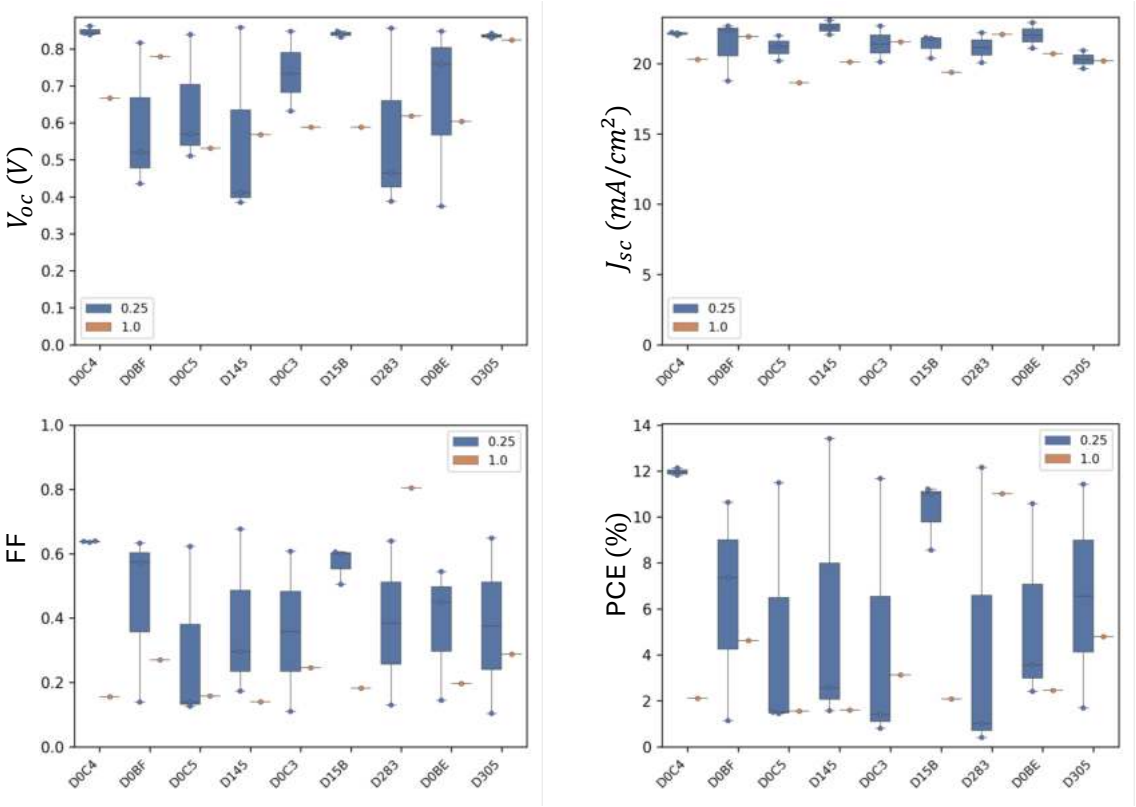


Figure 5.43: Statistical device parameters of the active layer of $PTQ10 : Y6$ (1:1.2) using Chloroform:1-Chloronapthalene(0.5%) as chlorinated co-solvents.

counterpart, the constancy of the short-circuit current J_{sc} at 23.2 mA/cm^2 for both device configurations underscores the nuanced balance between material composition and device performance. This observation suggests that while the inclusion of fullerene acceptor materials like $PC_{70}BM$ enhances electron mobility due to their superior electron-accepting capabilities [735], the strategic combination with non-fullerene acceptors like PM6:Y6, which offer adjustable optical and electronic properties [732, 736], is pivotal.

The synergy between fullerene and non-fullerene acceptors is further enriched by the use of additives like DIO and specific solvents such as chloroform. These additives and solvents play a critical role in refining the morphology of the active layer, thereby enhancing charge transport and reducing recombination, leading to improved PCE and device stability.

Figure 5.41 presents the J-V characteristics of organic solar cells whose photoactive layer formed from the PTQ10 and Y6 blend after dissolving in paired green and chlorinated solvents at ambient temperature. The results show that the blend film formed from the 2-MeTHF:Eucalyptol binary solvent does not yield optimal device performance parameters. The photovoltaic effect is rather weak despite the large absorption window and potential for large photon harvesting probability. This is indicative of a poor morphology in the bulk heterojunction that promotes germinate and bimordial recombination leading to the low J_{sc} and V_{oc} values. The poor device performance data corroborates with the

***PM6*:*Y6*:*$PC_{70}BM$* (CF:2.5% DIO:0.5%1-CN)**

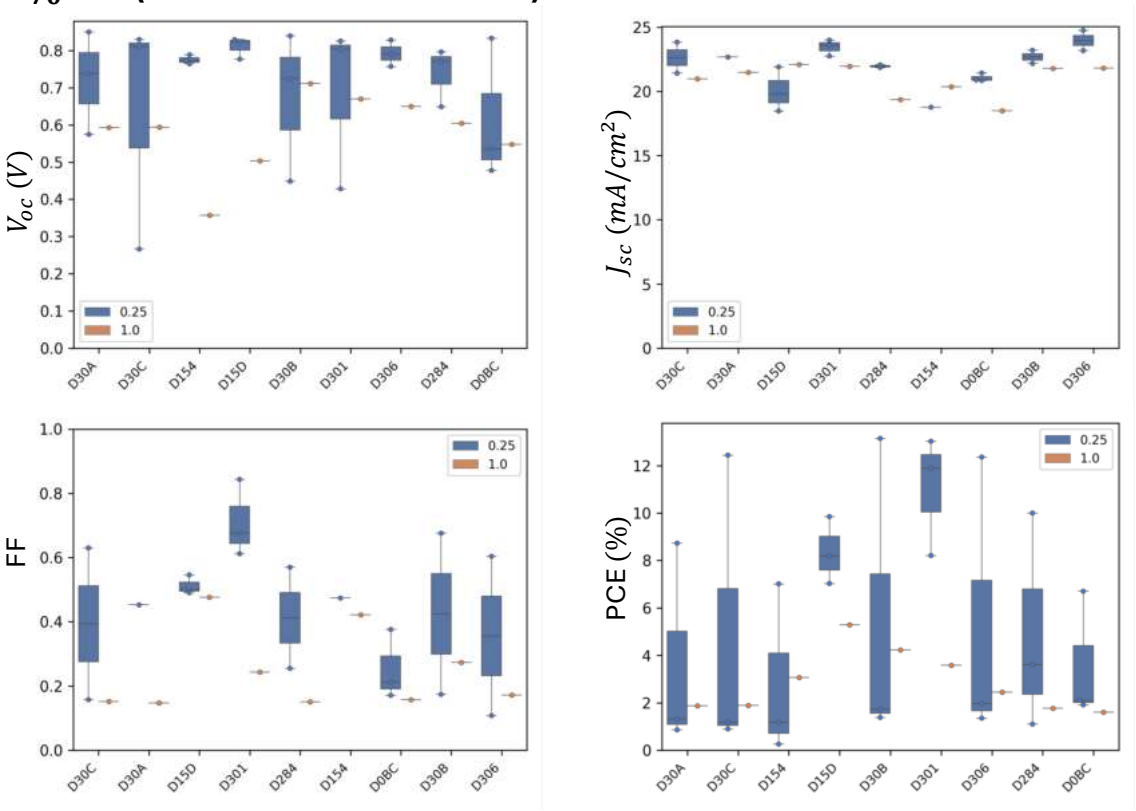


Figure 5.44: Statistical device parameters of the ternary active layer of $PM6 : Y6 : PC_{70}BM$ (1:1:0.2) using co-additives Chloroform:DIO(2.5%):1-CN(0.5%) as chlorinated co-solvents.

HSP values for the Donor and Acceptor materials. The investigation highlights that employing green co-solvents, specifically stirred overnight at ambient temperature, leads to diminished device PCE. To enhance the dissolution of the D and A, the blend solution was heated at 70° C and continuously stirred overnight. The results of the device spin case under this conditions of the blend film formation are presented in Figures 5.45 and 5.46 . It is evident that energetic or annealing favourably promotes the dissolution of the Donor from the high J_{sc} and V_{oc} values that have been measured.

A significant observation from Figures 5.45 and 5.46 is the disparity in the J_{sc} values, contingent upon the stirring temperature. The J_{sc} of devices stirred at room temperature markedly lags behind those stirred at 70° C, a variance implicating temperature as a crucial determinant in the solubility and, consequently, the material distribution quality.

The enhancement of device efficiency from a mere 0.043% to approximately 5% through the adjustment of stirring conditions, initially overnight stirring at room temperature followed by a 4-hour period at 70° C underscores the significance of phase separation and morphological optimisation in the PTQ10:Y6 active layer. This methodological shift not only ensures a thorough mixing but also enhances the distribution of the component materials, thus facilitating a morphological landscape that is conducive to efficient charge generation and transport.

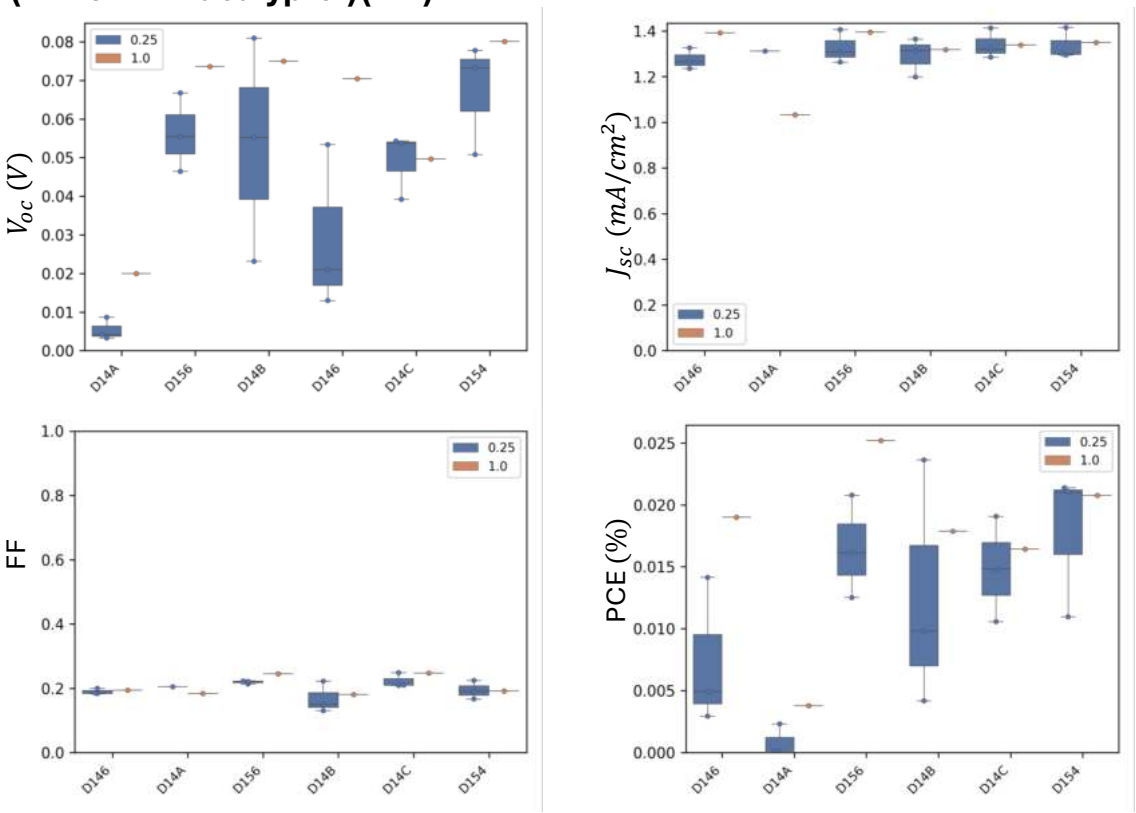


Figure 5.45: Statistical device parameters of the active layer of $PTQ10 : Y6$ (1:1.2) using 2-MeTHF:Eucalyptol as green co-solvents.

This improvement can be attributed to several factors. Firstly, the elevated temperature likely aids in the dissolution of stubborn, insoluble fractions of PTQ10 within the blend, which are otherwise resistant to dissolution at lower temperatures. This results in a more uniform active layer with reduced phase separation, improving the interface between the donor and acceptor materials, which is critical for effective charge separation and transport.

Secondly, the use of eco-friendly solvents such as 2-MeTHF and Eucalyptol, in a balanced 1:1 ratio, ideally the large V_{oc} is correlated to the low lying level of HOMO of PTQ10 (-5.50 eV), however there could be a red shift in the absorption which reduces the V_{oc} from 0.99 eV to $<$ 0.8 eV [737], thereby potentially reducing the incidence of phase separation and promoting a more homogeneous active layer morphology.

Moreover, the controlled stirring process, particularly at varied temperatures, is instrumental in achieving an optimised film morphology. This procedure likely facilitates the removal of any residual solvents, a critical step for ensuring a uniform film formation. Residual solvents can act as plasticisers, affecting the film's morphology and its electronic properties, thus their removal is essential for the stability and performance of OSCs.

In addition to the mechanical and thermal processing conditions, the intrinsic properties of the PTQ10:Y6 materials themselves, such as molecular weight, purity, and intrinsic solubility characteristics may also play a significant role in the observed outcomes. The

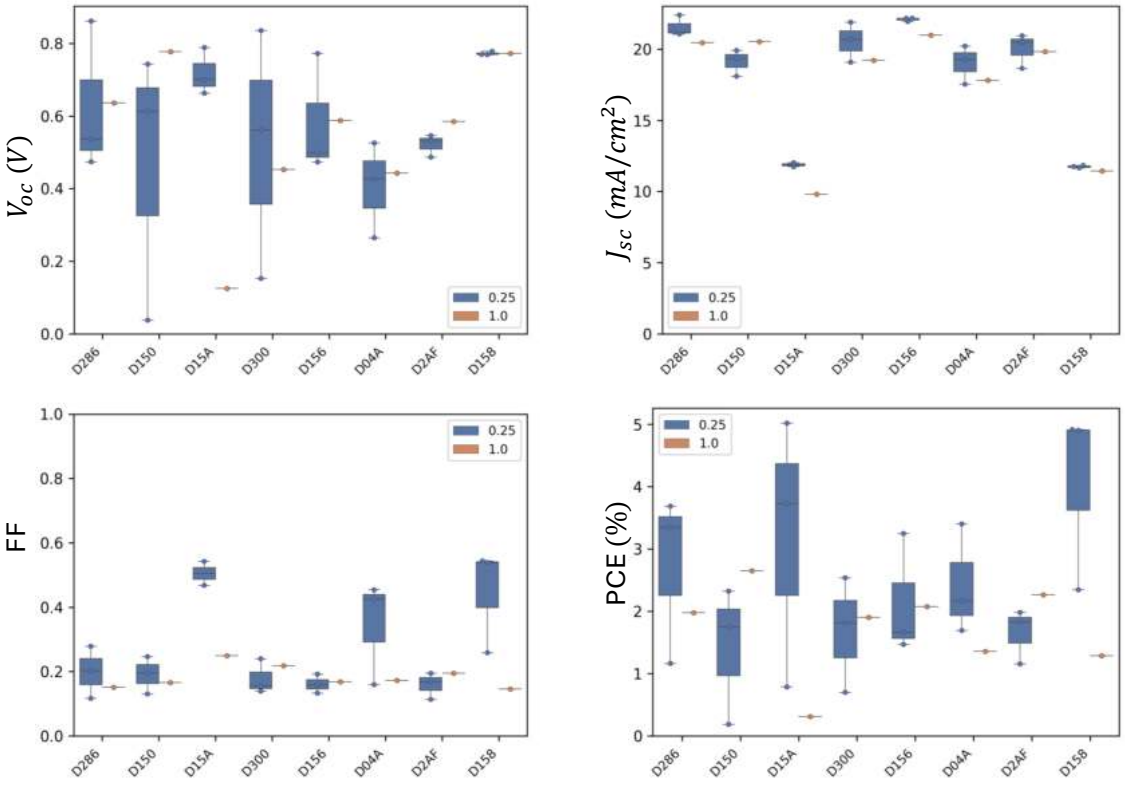


Figure 5.46: Statistical device parameters of the active layer of $PTQ10 : Y6$ (1:1.2) using 2-MeTHF:Eucalyptol as green co-solvents. The blend solution was stirred at temperature of 70° C.

interplay between these material properties and the solvent processing conditions could further influence the efficiency of the solar cells by affecting the crystallinity, molecular orientation, and overall morphology of the active layer [738, 739].

The comprehensive examination of the PTQ10:Y6 active layer through J-V measurements has elucidated the critical importance of solvent processing conditions, including solvent choice, temperature control, and stirring protocols, in enhancing the efficiency of OSCs. This study underscores the multifaceted nature of optimising device performance, where material solubility, processing conditions, and intrinsic material properties converge to dictate the overall efficiency of the PV cells.

The contrast in performance between devices employing chlorinated and green solvents is not merely a result of the solvent choice but is deeply rooted in the inherent properties of these solvents. Chlorinated solvents, owing to their unique solubility characteristics, facilitate a more efficient dissolution and blending of organic photovoltaic materials. This results in a more uniform and optimal morphological arrangement within the active layer, which is crucial for the effective separation of charge carriers and minimisation of recombination losses. On the other hand, while green solvents present an eco-friendly alternative, they require extensive optimisation efforts to achieve comparable PCEs, mainly due to their less favourable solubility properties for OPV materials.

Table 5.8: Photovoltaic parameters of the NFA active layer devices with chlorinated and green co-solvents.

Active Layer	Solvents	J_{sc} (mA/cm^2)	V_{oc} (V)	FF (%)	R_{sh} $(\Omega \cdot cm^2)$	R_s $(\Omega \cdot cm^2)$	$PCE_{max}(Avg)$ (%)
$PTQ10 : Y6$	2-MeTHF:Eu	1.42	0.095	31.9	109.4	41.0	0.043 (0.032)
$PTQ10 : Y6(70^\circ$ C)	2-MeTHF:Eu	11.89	0.79	56.1	2344	39.7	5.24 (3.63)
$PTQ10 : Y6$	CF:1-CN(0.5%)	23.2	0.86	68.9	14652	13.6	13.7 (11.9)
$PM6 : Y6 : PC_{70}BM$	CF:DIO(2.5%)1-CN(0.5%)	23.2	0.84	68.1	20481	16.0	13.3 (10.2)

5.3.6 External Quantum Efficiency Measurements

External Quantum Efficiency (EQE) measurements are a critical parameter in the characterisation of photovoltaic devices and other light-sensitive devices. EQE defines the efficiency with which a device converts photons into electrons, essentially measuring the number of electrons generated in the external circuit per incident photon on the device [90].

The EQE measurements were conducted using an experimental setup, consisting of a 75 W Xenon lamp, which served as the primary light source. This lamp was paired with both a chopper and a monochromator to precisely control and filter the light wavelengths reaching the pixel in the device. For ensuring the accuracy and reliability of the measurements, the system underwent calibration employing a Si photodiode, recognised for its stable and predictable response across a wide range of light wavelengths.

Upon conducting these measurements, the EQE response of the samples is compared to that obtained from a solar simulator, which is considered a standard reference in simulating sunlight. The comparison revealed a remarkable consistency, with the discrepancy in the EQE values being less than 5%. This minimal variance underscores the precision of our experimental setup in replicating real-world solar conditions and validates the effectiveness of the utilised calibration process with the Si photodiode. This alignment is crucial for affirming the reliability of our EQE data, providing a solid foundation for further analysis and interpretation of the photovoltaic properties of the materials under study.

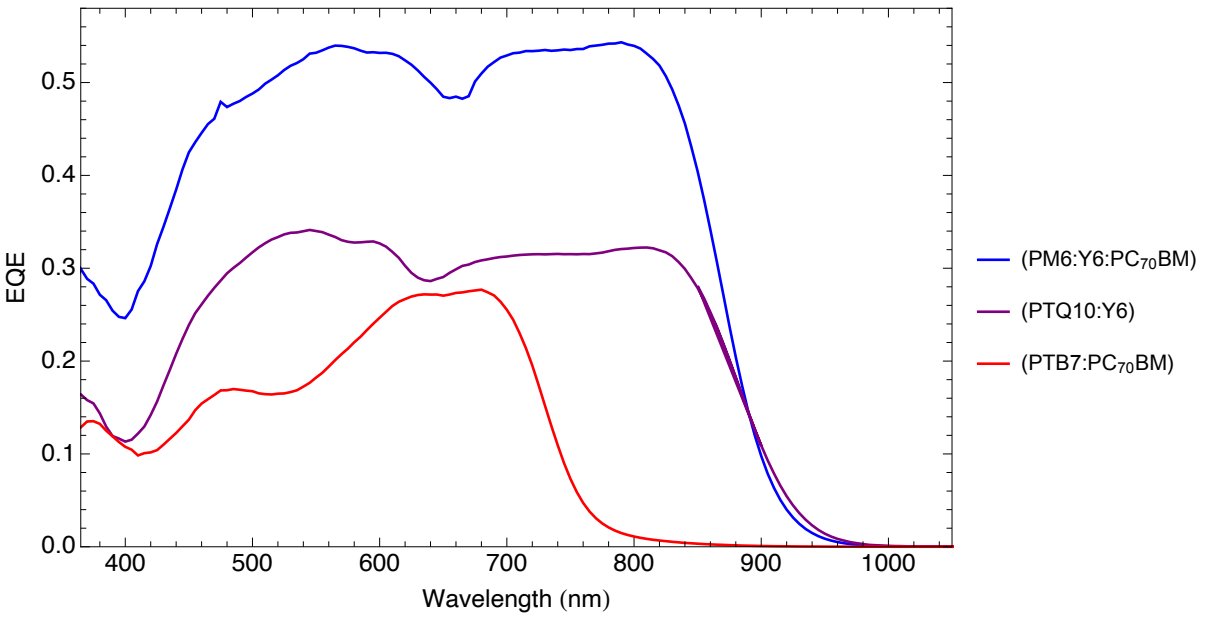


Figure 5.47: EQE spectra of the $PTB7 : PC_{70}BM$, PTQ10:Y6 and $PM6 : Y6 : PC_{70}BM$ OSCs. The devices had different thicknesses.

The broader photon response of PTQ10:Y6 based device in the region of 300-960 nm is attribute to the improved J_{sc} due to the expanded light absorption of the photoactive layer.

Figure 5.47 serves as a pivotal reference, illustrating that the PTQ10:Y6-based device manifests a comprehensive photon response spectrum extending from 300 nm to 960 nm. This expansive range slightly surpasses that of the ternary blend, which plays a significant role in the observed enhancement of PCE for the PTQ10:Y6 device. This phenomenon underscores the crucial impact of the spectral response on device performance, particularly how broader absorption capabilities can translate to improved energy conversion efficiencies.

Furthermore, the analysis reveals a noteworthy observation concerning the Jsc values. The PTQ10:Y6 and $PM6 : Y6 : PC_{70}BM$ based devices exhibit closely aligned J_{sc} figures, a result directly attributable to their photoactive layers augmented light absorption properties. This similarity in J_{sc} underscores the importance of the photoactive layer's composition and its capacity to capture a wide spectrum of light, thereby optimising the solar cells' overall performance.

Conversely, the device incorporating the fullerene-based active layer, $PTB7 : PC_{70}BM$, showcased distinct EQE values and demonstrated an absorption intensity that primarily spanned the 350 to 650 nm wavelength region. This narrower spectral response indicates a more limited photon absorption range, which is a critical factor in defining the device's efficiency parameters. The absorption characteristics of the $PTB7 : PC_{70}BM$ device elucidate the role of material selection in tailoring the spectral sensitivity and quantum efficiency of solar cells.

Through these EQE measurements, the study not only validates the J_{sc} values of the OSCs but also sheds light on the intricate interplay between the active layer composition, absorption spectrum, and the resultant efficiency of the devices. It highlights the nuanced understanding required to engineer materials and devices capable of maximising solar energy.

5.4 Conclusion

The work presented in this chapter highlights the significance of co-solvent additives in tuning the morphology of OSCs. Achieving an optimal nanoscale morphology within the photoactive layer of OSCs is paramount to improving their PCE and long-term stability. This study underscores the utility of HSPs as a predictive tool for selecting effective co-solvent systems, facilitating a comprehensive understanding of solvent-solute interactions crucial for morphology control.

Our investigation into the role of co-solvent additives reveals that careful selection based on HSPs can significantly enhance the solubility, miscibility, and crystallisation behaviour of donor-acceptor blends, ultimately leading to more favourable morphologies. Experimental results demonstrate that the use of optimised co-solvent systems, such as a mix of green and industrial solvents, not only improves the initial device performance but also ensures better stability under operational conditions.

Through a combination of theoretical computations and experimental validations, this chapter has achieved the following objectives: developed and validated a predictive model based on HSPs for selecting effective co-solvent systems, elucidated the fundamental

mechanisms by which co-solvent additives influence the morphology of OSCs, and experimentally demonstrated the enhancement in PCE and stability of OSCs through the application of optimised co-solvent additives.

The detailed morphological and optoelectronic characterisation using techniques such as GIWAXS and J-V measurements provided insights into the molecular ordering, phase separation, and charge transport dynamics influenced by different solvent environments. Specifically, the use of chlorinated solvents, despite their environmental concerns, has shown superior performance in terms of solubility and phase control. Conversely, green solvents, while presenting initial challenges, have proven to be effective under optimised processing conditions, showcasing the potential for sustainable and high-performing OSCs.

Overall, the findings emphasise the critical role of solvent engineering in OSC fabrication. By strategically selecting and combining solvents based on their HSP compatibility, it is possible to achieve a delicate balance between high efficiency, environmental sustainability, and long-term device stability. This research paves the way for further exploration into greener solvent alternatives and the continuous improvement of organic photovoltaic technologies.

Chapter 6

6 Conclusions and Recommendations

6.1 Conclusion

This thesis has embarked on an ambitious journey to explore the enhancement of photovoltaic (PV) device efficiency through innovative light management and morphological strategies, utilising both traditional and novel materials. The comparative study on the plasmonic effects and photovoltaic properties of silver Ag, Au, their SiO_2 core-shell counterparts, and magnetoplasmonic materials like Ni, Fe_3O_4, and their SiO_2 core-shell variants, has revealed significant insights into the optimisation of light absorption and charge carrier dynamics in Si PV devices.

One of the key findings of this research is the enhancement of PCE in Si-based solar cells through the use of superparamagnetic NPs exhibiting plasmonic behaviour. The meticulous calculation of Curie temperatures demonstrated that these NPs can effectively enhance light absorption and improve charge carrier dynamics due to plasmonic scattering and absorption effects. The introduction of a silica coating on magnetic NPs further amplified this enhancement, highlighting the synergy between light confinement and improved light scattering by larger Fe_3O_4/Au NPs. This work not only extends the knowledge of plasmonic effects in photovoltaic applications but also closes the gap in understanding the behaviour of magnetic NPs in enhancing solar cell efficiency.

Moreover, the study ventured into the realm of OSCs, examining the impact of solvent morphology on device performance. The employment of green and industrial solvents as co-solvents, particularly the pairing of toluene with 2-MEA, has showcased a path towards the replacement of chlorinated solvents, striking a balance between environmental sustainability and photovoltaic efficiency. This transition not only reduces the environmental footprint of PV device fabrication but also holds the potential to lower production costs, OPVs more accessible.

The findings of this thesis underscore the vast potential of integrating plasmonic NPs and optimising solvent morphology in enhancing the efficiency of photovoltaic devices. By bridging the gap between traditional plasmonic materials and magnetoplasmonic NPs, as well as championing the use of greener co-solvent systems, this work contributes to the advancement of solar technology towards higher efficiency and sustainability. As the field moves forward, the insights gained from this study will undoubtedly serve as a cornerstone for future research aimed at realising the full potential of photovoltaics in harnessing solar energy.

6.2 Future Work

6.2.1 Magetoplasmonic and Plasmonic Nanoparticles on Silicon Based Devices

The integration of magnetoplasmonic and plasmonic nanoparticles in silicon solar cells holds significant promise for enhancing photovoltaic performance. Future research should focus on refining the synthesis methods such as lithography for these nanoparticles to achieve greater uniformity and control over size and shape. Experimenting with different precursor concentrations, reaction temperatures, and synthesis times will be essential to produce nanoparticles with consistent and reproducible properties. To address concerns about uniformity, we will conduct more extensive characterisation using techniques such as high-resolution TEM, SEM, and DLS. These methods will provide detailed insights into the size distribution, shape, and uniformity of the core-shell nanoparticles, ensuring they meet the stringent requirements for photovoltaic applications.

Further research can investigate the optimal configurations and concentrations of nanoparticles within the silicon matrix to maximise light absorption and scattering. This includes studying the effects of different nanoparticle shapes (spheres, rods, cubes) and sizes on the optical properties of the solar cells. Additionally, future studies should focus on the long-term stability and durability of the integrated nanoparticles within the silicon solar cells. Testing the cells under various environmental conditions, such as temperature, humidity, and UV exposure, will be crucial to ensure sustained performance and reliability over time.

Exploring the use of hybrid nanostructures, such as combining different types of plasmonic and magnetoplasmonic nanoparticles, can lead to synergistic effects that further enhance the efficiency of silicon solar cells. Investigating the interaction between these hybrid structures and their collective impact on light management and charge carrier dynamics will be essential. Developing scalable fabrication techniques that can integrate these nanoparticles into silicon solar cells in a cost-effective manner is another critical area for future research. Methods such as spin coating, layer-by-layer assembly, and other deposition techniques need to be adapted for large-scale manufacturing.

Advanced computational simulations and modelling will play a pivotal role in predicting the behaviour of plasmonic and magnetoplasmonic nanoparticles in silicon solar cells. These models can help identify the most promising nanoparticle configurations and guide experimental efforts. Additionally, the application of these nanoparticles can be extended to tandem solar cells, where multiple layers of different photovoltaic materials are used to capture a broader spectrum of sunlight. Investigating the role of plasmonic and magnetoplasmonic nanoparticles in enhancing the efficiency of tandem cells could lead to significant advancements in solar technology.

By addressing these areas in future research, we can unlock the full potential of magnetoplasmonic and plasmonic nanoparticles in silicon solar cells, paving the way for more efficient and cost-effective solar energy solutions.

6.2.2 Co-Solvents on OSCs

Future work for this thesis will delve deeper into the expansive realm of solvents and their pairing as co-solvents to improve the morphology of OSCs, guided by Hansen solubility parameter (HSP) calculations. Our preliminary investigations, as illustrated in Figures 6.1 and 6.2, have begun to map out the landscape of organic materials with various green and industrial co-solvents, including chlorinated co-solvents. This initial exploration hints at the potential for enhancing the morphological features of solar cell active layers, which is crucial for the efficiency of these devices. High-resolution SEM images will be included to provide detailed insights into the film morphology of the polymer medium, enabling the observation of crystal growth and overall morphological characteristics.

RED Calculations for Industrial Solvents

Polymers	O-Xylene	P-Xylene	Limonene	Toulene	A-methylstyrene	NMP	THF
$PC_{70}BM$	RED= 1.856	RED= 1.856	RED= 1.810	RED= 1.8198	RED= 1.399	RED= 2.105	RED= 1.408
$PC_{61}BM$	RED= 0.9139	RED= 0.9139	RED= 0.8957	RED= 0.9002	RED= 0.9097	RED= 0.7340	RED= 0.7371
$PBDB-T$	RED= 1.036	RED= 1.036	RED= 0.9857	RED= 0.6234	RED= 0.5903	RED= 1.338	RED= 0.8118
$P3HT$	RED= 1.562	RED= 1.562	RED= 1.332	RED= 0.6124	RED= 1.281	RED= 2.343	RED= 1.736
$ITIC$	RED= 0.6358	RED= 0.6358	RED= 0.2893	RED= 0.9831	RED= 0.8114	RED= 1.341	RED= 0.7492
$PTB7$	RED= 0.8556	RED= 0.8556	RED= 0.8507	RED= 0.3743	RED= 0.7768	RED= 1.429	RED= 0.6388
$ITIC-Th$	RED= 1.137	RED= 1.137	RED= 1.089	RED= 1.187	RED= 0.9468	RED= 1.574	RED= 1.065
$ICBA$	RED= 1.007	RED= 1.007	RED= 1.215	RED= 0.9175	RED= 0.6948	RED= 2.078	RED= 1.702

Figure 6.1: HSP calculations on industrial and green solvents.

The insights gleaned from the HSP calculations outline possible device architectures, including sequential deposition techniques informed by HSP solubility calculations, providing a foundational knowledge base for future device fabrication strategies. Figures 6.1 and 6.2 show the HSP calculations for a few polymers using chlorinated and non-chlorinated solvents. These calculations were conducted using various solvents for the project, and they can be applied in multiple OSC architectures.

The use of industrial solvents in the fabrication of organic solar cells is poised to undergo significant changes. By transitioning to environmentally sustainable solvents like green solvents, halogen-free solvents, and non-halogenated aromatic solvents, the organic solar cell sector can enhance its environmental sustainability, reduce manufacturing costs, and improve the overall efficiency of solar cells. This shift towards eco-friendly solvents aligns with the industry's growing emphasis on greener practices and sustainable technologies. The adoption of industrial solvents in organic solar cell production is expected to drive innovation in material design, processing techniques, and device performance, ultimately

RED Calculations for D/A Materials in various Solvents

	CF	CB	o-DCB	DIO	Toulene	1,8 Oct	1-Chloro	1,2,4 Tri
$PC_{70}BM$	RED= 1.2998	RED= 0.9899	RED= 0.4168	RED= 1.1971	RED= 1.8198	RED= 1.3603	RED= 1.1312	RED= 2.01735
$PC_{61}BM$	RED= 0.8071	RED= 0.4221	RED= 0.2349	RED= 0.6585	RED= 0.9002	RED= 0.9317	RED= 0.2792	RED= 0.9954
$PBDB-T$	RED= 0.6346	RED= 0.2951	RED= 0.3081	RED= 0.4886	RED= 0.6234	RED= 0.8289	RED= 0.1382	RED= 0.1897
$P3HT$	RED= 0.8174	RED= 0.5697	RED= 1.0148	RED= 0.2858	RED= 0.6124	RED= 1.5974	RED= 1.230	RED= 1.2575
$ITIC$	RED= 0.2946	RED= 1.1626	RED= 0.9957	RED= 0.5211	RED= 0.9831	RED= 0.9868	RED= 1.49	RED= 1.3679
$PTB7$	RED= 0.5188	RED= 0.3080	RED= 0.2194	RED= 0.3635	RED= 0.3743	RED= 0.6427	RED= 0.5695	RED= 0.4658
$ITIC-Th$	RED= 0.6545	RED= 0.8950	RED= 0.8889	RED= 0.7786	RED= 1.2682	RED= 0.6266	RED= 1.2271	RED= 1.012
$ICBA$	RED= 0.8706	RED= 0.5999	RED= 0.9540	RED= 0.2727	RED= 0.5954	RED= 1.2925	RED= 1.3461	RED= 1.3107

Figure 6.2: HSP calculations on various chlorinated solvents.

leading to the development of more efficient and environmentally friendly photovoltaic technologies.

In situ studies utilising Grazing-Incidence Wide-Angle X-ray Scattering (GIWAXS) and Optical Spectroscopy play a crucial role in understanding the film formation and morphology evolution during the fabrication of organic solar cells. These techniques provide insights into the crystallisation steps that occur as solvents evaporate, thinning, and drying take place. By examining the crystalline intermediates and pathways, researchers can better comprehend the domain purification process involved in the production of organic solar cells. Specifically, the use of co-solvents like 1-CN has been shown to influence the drying process, promoting the aggregation of specific polymers and impacting the resulting morphology of the films. Through detailed analysis of these processes, researchers can optimise the fabrication of organic solar cells for enhanced efficiency and performance.

Moreover, small molecules and fullerene-based acceptors are known to promote $\pi - \pi$ stacking and improve crystallinity, which are critical for enhancing the efficiency of OSCs. Future work will also explore the mutual cooperation between these two types of acceptors, in addition to focusing on solvent systems. Understanding the synergistic effects between small molecules and fullerene-based acceptors will provide a more comprehensive approach to optimising the active layer morphology and device performance.

A significant avenue of future research will involve an exhaustive investigation into the thermodynamics of co-solvent systems to boost the power conversion efficiency of OSCs. Among the anticipated outcomes is the identification of an optimal co-solvent mixture that not only improves the solubility of active materials but also promotes superior film formation and blend morphology. Achieving these milestones is expected to elevate critical device performance metrics, including PCE, FF, and J_{sc}.

The pursuit of these research objectives is poised to advance the development of OSCs that are both more efficient and stable. The implications of such advancements are far-reaching, with potential applications in portable electronics, building-integrated photovoltaics, and solar farms. This is particularly relevant for devices leveraging cost-effective industrial solvents, where improvements in device architecture and efficiency can significantly enhance their viability and adoption in a variety of settings. As we venture into this uncharted territory, the combination of innovative solvent systems and meticulous morphological optimisation stands to herald a new era of photovoltaic device technology, underscoring the transformative potential of light management and material science in harnessing solar energy.

6.2.2.1 Future Research Directions

Continued research into advanced materials and device architectures is crucial for further improving the thermal stability and reliability of OSCs. Future research should focus on:

- Developing new NFAs and donor polymers with enhanced stability and performance.
- Exploring hybrid organic-inorganic materials to leverage the stability of inorganic components while maintaining the flexibility of organic materials.
- Advancing encapsulation techniques to protect OSCs from environmental degradation.
- Investigating the long-term stability of OSCs under real-world conditions, including temperature variations, humidity, and mechanical stress.
- Incorporating in situ morphology characterisation using GIWAXS during the mixing of solvents and spin coating. This time-dependent study of morphology will aid in decoupling the kinetics and energetics of morphology formation.

By addressing these challenges and leveraging recent advancements, OSCs have the potential to become a mainstream renewable energy technology, contributing significantly to the global energy transition and sustainability goals.

Appendix

The materials used for the calculations in the table in Figure 5.2 are:

- **$PC_{70}BM$:** $[6,6]$-Phenyl-C_{70}-butyric acid methyl ester
- **PTB7:** $\mathrm{Poly}[[4,8-bi[(2-ethylhexyl)oxy]benzo[1,2-b:4,5-b']dithiophene-2,6-diyl][3-fluoro-2-[(2-ethylhexyl)carbonyl]thieno[3,4-b]thiophenediyl]]$
- **PTQ10:** $\mathrm{Poly}[(5,6-difluoro-2,1,3-benzothiadiazol-4,7-diyl)-alt-(3,3'''-di(2-octyldodecyl)-2,2';5',2'';5'',2'''-quaterthiophen-5,5'''-diyl)]$
- **Y6:** $2,2'-((2Z,2'Z)-((12,13-bis(2-ethylhexyl)-3,9-diundecyl-12,13-dihydro-[1,2,5]thiadiazolo[3,4-e]thieno[2'',3'':4',5']thieno[2',3':4,5]pyrrolo[3,2-g]thieno[2',3':4,5]thieno[3,2-b]indole-2,10-diyl)bis(methanylylidene))bis(5,6-difluoro-3-oxo-1H-indene-2,1(3H)-diylidene))dimalononitrile$
- **PM6:** $\mathrm{Poly}[(2,6-(4,8-bis(5-(2-ethylhexyl)thiophen-2-yl)-benzo[1,2-b:4,5-b']dithiophene))-alt-(5,5-(1',3'-di-2-thienyl-5',7'-bis(2-ethylhexyl)benzo[1',2'-c:4',5'-c']dithiophene-4,8-dione))]$
- **ITIC-Th:** $3,9-bis(2-methylene-(3-(1,1-dicyanomethylene)-5,6-difluoro-4-oxo-2,3-dihydro-1H-indene-1-ylidene))-2,8-dithien-2-yl-5,6-dihydro-s-indaceno[1,2-b:5,6-b']dithiophene$

References

[1] S. Asumadu-Sarkodie and P. Owusu, "Carbon dioxide emissions, gdp, energy use, and population growth: a multivariate and causality analysis for ghana, 1971–2013," *Environmental Science and Pollution Research*, vol. 23, no. 13, pp. 13508–13520, 2016.

[2] S. Mathew, A. Yella, P. Gao, R. Humphry-Baker, B. Curchod, N. Ashari-Astani, I. Tavernelli, U. Rothlisberger, M. Nazeeruddin, and M. Grätzel, "Dye-sensitized solar cells with 13% efficiency achieved through the molecular engineering of porphyrin sensitizers," *Nature Chemistry*, vol. 6, no. 3, p. 242, 2014.

[3] F. Riva, A. Tognollo, F. Gardumi, and E. Colombo, "Long-term energy planning and demand forecast in remote areas of developing countries: Classification of case studies and insights from a modelling perspective," *Energy strategy reviews*, vol. 20, pp. 71–89, 2018.

[4] K. Kaygusuz, "Energy for sustainable development: A case of developing countries," *Renewable and sustainable energy reviews*, vol. 16, no. 2, pp. 1116–1126, 2012.

[5] R. Pinto, S. Henriques, P. Brockway, M. Heun, and T. Sousa, "The rise and stall of world electricity efficiency: 1900–2017, results and insights for the renewables transition," *Energy*, vol. 269, p. 126775, 2023.

[6] F. Santos, P. Ferreira, and J. Pedersen, "The climate change challenge: A review of the barriers and solutions to deliver a paris solution," *Climate*, vol. 10, no. 5, p. 75, 2022.

[7] H. Reid, M. Alam, R. Berger, T. Cannon, S. Huq, and A. Milligan, "Community-based adaptation to climate change: an overview," *Participatory learning and action*, vol. 60, no. 1, pp. 11–33, 2009.

[8] L. Lyu and L. Fang, "A study on ec translation of bp statistical review of world energy 2022 from the perspective of schema theory," *Journal of Linguistics and Communication Studies*, vol. 2, no. 1, pp. 10–14, 2023.

[9] A. Andrae, "Prediction studies of electricity use of global computing in 2030," *International Journal of Science and Engineering Investigations*, vol. 8, no. 86, pp. 27–33, 2019.

[10] T. Searchinger, R. Waite, C. Hanson, J. Ranganathan, P. Dumas, and E. Matthews, "Creating a sustainable food future: a menu of solutions to feed nearly 10 billion people by 2050-synthesis report," 2018.

[11] M. Flexas, A. Thompson, H. Torres, P. Klein, J. Farrar, H. Zhang, and D. Menemenlis, "Global estimates of the energy transfer from the wind to the ocean, with emphasis on near-inertial oscillations," *Journal of Geophysical Research: Oceans*, vol. 124, no. 8, pp. 5723–5746, 2019.

[12] N. Armaroli and V. Balzani, "The future of energy supply: challenges and opportunities," *Angewandte Chemie International Edition*, vol. 46, no. 1-2, pp. 52–66, 2007.

[13] I. Fridleifsson, "Status of geothermal energy amongst the world's energy sources," *Geothermics*, vol. 32, no. 4-6, pp. 379–388, 2003.

[14] P. Wilkinson, K. Smith, M. Joffe, and A. Haines, "A global perspective on energy: health effects and injustices," *The Lancet*, vol. 370, no. 9591, pp. 965–978, 2007.

[15] N. Lewis, G. Crabtree, A. Nozik, M. Wasielewski, P. Alivisatos, H. Kung, J. Tsao, E. Chandler, W. Walukiewicz, M. Spitler, *et al.*, "Basic research needs for solar energy utilization. report of the basic energy sciences workshop on solar energy utilization, april 18-21, 2005," tech. rep., DOESC (USDOE Office of Science (SC)), 2005.

[16] K. Tete, Y. Soro, S. Sidibé, and R. Jones, "Assessing energy security within the electricity sector in the west african economic and monetary union: Inter-country performances and trends analysis with policy implications," *Energy Policy*, vol. 173, p. 113336, 2023.

[17] K. Reddy, T. Deepak, G. Anjusree, S. Thomas, S. Vadukumpully, K. Subramanian, S. Nair, and A. Nair, "On global energy scenario, dye-sensitized solar cells and the promise of nanotechnology," *Physical Chemistry Chemical Physics*, vol. 16, no. 15, pp. 6838–6858, 2014.

[18] M. Green, E. Dunlop, J. Hohl-Ebinger, M. Yoshita, N. Kopidakis, and X. Hao, "Solar cell efficiency tables (version 57)," *Progress in photovoltaics: research and applications*, vol. 29, no. 1, pp. 3–15, 2021.

[19] A. Baiju and M. Yarema, "Status and challenges of multi-junction solar cell technology," *Frontiers in Energy Research*, vol. 10, p. 971918, 2022.

[20] M. Dada and P. Popoola, "Recent advances in solar photovoltaic materials and systems for energy storage applications: a review," *Beni-Suef University Journal of Basic and Applied Sciences*, vol. 12, no. 1, pp. 1–15, 2023.

[21] P. Pearce, J. Halme, J. Jiang, and N. Ekins-Daukes, "Efficiency limits and design principles for multi-junction coloured photovoltaics," *Energy & Environmental Science*, vol. 17, no. 3, pp. 1189–1201, 2024.

[22] M. Green, "Solar cells: operating principles, technology, and system applications," *Englewood Cliffs*, 1982.

[23] H. Meddeb, M. Götz-Köhler, N. Neugebohrn, U. Banik, N. Osterthun, O. Sergeev, D. Berends, C. Lattyak, K. Gehrke, and M. Vehse, "Tunable photovoltaics: adapting solar cell technologies to versatile applications," *Advanced Energy Materials*, vol. 12, no. 28, p. 2200713, 2022.

[24] T. Ishii, K. Otani, T. Takashima, and Y. Xue, "Solar spectral influence on the performance of photovoltaic (pv) modules under fine weather and cloudy weather conditions," *Progress in Photovoltaics: Research and Applications*, vol. 21, no. 4, pp. 481–489, 2013.

[25] E. Garnett, B. Ehrler, A. Polman, and E. Alarcon-Llado, "Photonics for photovoltaics: Advances and opportunities," *ACS photonics*, vol. 8, no. 1, pp. 61–70, 2020.

[26] Z. Kafafi, R. Martín-Palma, A. Nogueira, D. O'Carroll, J. Pietron, I. Samuel, F. So, N. Tansu, and L. Tsakalakos, "The role of photonics in energy," *Journal of photonics for energy*, vol. 5, no. 1, pp. 050997–050997, 2015.

[27] Y. Akimov and W. Koh, "Design of plasmonic nanoparticles for efficient subwavelength light trapping in thin-film solar cells," *Plasmonics*, vol. 6, pp. 155–161, 2011.

[28] E. Shaghouli, N. Granpayeh, and N. Manavizadeh, "Plasmonic enhanced ultrathin solar cell: A combined approach using fractal and nano-antenna structure to maximize absorption," *Results in Physics*, p. 106600, 2023.

[29] T. Rossi, P. Erhart, and M. Kuisma, "Hot-carrier generation in plasmonic nanoparticles: The importance of atomic structure," *ACS nano*, vol. 14, no. 8, pp. 9963–9971, 2020.

[30] H. Reddy and V. Shalaev, "Plasmonic hot-carriers and their applications: opinion," *Optical Materials Express*, vol. 11, no. 11, pp. 3827–3832, 2021.

[31] S. Kumar, A. Habib, and R. Sundararaman, "Plasmonic hot carriers scratch the surface," *Trends in Chemistry*, vol. 3, no. 11, pp. 902–910, 2021.

[32] J. Day, S. Senthilarasu, and T. Mallick, "Improving spectral modification for applications in solar cells: A review," *Renewable Energy*, vol. 132, pp. 186–205, 2019.

[33] A. Riverola, A. Vossier, and D. Chemisana, "Fundamentals of solar cells," in *Nanomaterials for Solar Cell Applications*, pp. 3–33, Elsevier, 2019.

[34] E. Arinze, B. Qiu, G. Nyirjesy, and S. Thon, "Plasmonic nanoparticle enhancement of solution-processed solar cells: practical limits and opportunities," *Acs Photonics*, vol. 3, no. 2, pp. 158–173, 2016.

[35] W. Erwin, H. Zarick, E. Talbert, and R. Bardhan, "Light trapping in mesoporous solar cells with plasmonic nanostructures," *Energy & Environmental Science*, vol. 9, no. 5, pp. 1577–1601, 2016.

[36] P. Yu, Y. Yao, J. Wu, X. Niu, A. Rogach, and Z. Wang, "Effects of plasmonic metal core-dielectric shell nanoparticles on the broadband light absorption enhancement in thin film solar cells," *Scientific reports*, vol. 7, no. 1, p. 7696, 2017.

[37] Y. Zhang, N. Stokes, B. Jia, S. Fan, and M. Gu, "Towards ultra-thin plasmonic silicon wafer solar cells with minimized efficiency loss," *Scientific reports*, vol. 4, no. 1, p. 4939, 2014.

[38] C. Rhodes, "Plasmonic nanoparticles and solar cells," *Science Progress*, vol. 99, no. 4, pp. 438–449, 2016.

[39] G. Jarosz, R. Marczyński, and R. Signerski, "Effect of band gap on power conversion efficiency of single-junction semiconductor photovoltaic cells under white light phosphor-based led illumination," *Materials Science in Semiconductor Processing*, vol. 107, p. 104812, 2020.

[40] B. Sutherland, "Solar materials find their band gap," *Joule*, vol. 4, no. 5, pp. 984–985, 2020.

[41] G. Huang, K. Wang, and C. Markides, "Efficiency limits of concentrating spectral-splitting hybrid photovoltaic-thermal (pv-t) solar collectors and systems," *Light: Science & Applications*, vol. 10, no. 1, p. 28, 2021.

[42] Y. Lei, Y. Li, and Z. Jin, "Photon energy loss and management in perovskite solar cells," *Energy Reviews*, p. 100003, 2022.

[43] R. Datt, S. Bishnoi, H. Lee, S. Arya, S. Gupta, V. Gupta, and W. Tsoi, "Down-conversion materials for organic solar cells: Progress, challenges, and perspectives: Photovoltaics: Special issue dedicated to professor yongfang li," *Aggregate*, vol. 3, no. 3, p. e185, 2022.

[44] P. Moraitis, R. Schropp, and W. Van Sark, "Nanoparticles for luminescent solar concentrators-a review," *Optical Materials*, vol. 84, pp. 636–645, 2018.

[45] V. Etacheri, C. Di Valentin, J. Schneider, D. Bahnemann, and S. Pillai, "Visible-light activation of tio2 photocatalysts: Advances in theory and experiments," *Journal of Photochemistry and Photobiology C: Photochemistry Reviews*, vol. 25, pp. 1–29, 2015.

[46] B. Ai, Z. Fan, and Z. Wong, "Plasmonic–perovskite solar cells, light emitters, and sensors," *Microsystems & Nanoengineering*, vol. 8, no. 1, p. 5, 2022.

[47] K. Chan, M. Wright, N. Elumalai, A. Uddin, and S. Pillai, "Plasmonics in organic and perovskite solar cells: optical and electrical effects," *Advanced Optical Materials*, vol. 5, no. 6, p. 1600698, 2017.

[48] Z. Abbas, S. Ryu, M. Haris, C. Song, H. Lee, S. Lee, W. Shin, T. Park, and J. Lee, "Optimized vertical phase separation via systematic y6 inner side-chain modulation for non-halogen solvent processed inverted organic solar cells," *Nano Energy*, vol. 101, p. 107574, 2022.

[49] G. Kini, S. Jeon, and D. Moon, "Latest progress on photoabsorbent materials for multifunctional semitransparent organic solar cells," *Advanced Functional Materials*, vol. 31, no. 15, p. 2007931, 2021.

[50] V. Sharma, A. Landep, S. Lee, S. Park, Y. Kim, and G. Kim, "Recent advances in polymeric and small molecule donor materials for y6 based organic solar cells," *Next Energy*, p. 100086, 2023.

[51] Y. Cui, Y. Xu, H. Yao, P. Bi, L. Hong, J. Zhang, Y. Zu, T. Zhang, J. Qin, J. Ren, *et al.*, "Single-junction organic photovoltaic cell with 19% efficiency," *Advanced Materials*, vol. 33, no. 41, p. 2102420, 2021.

[52] L. Zhu, M. Zhang, J. Xu, C. Li, J. Yan, G. Zhou, W. Zhong, T. Hao, J. Song, X. Xue, *et al.*, "Single-junction organic solar cells with over 19% efficiency enabled by a refined double-fibril network morphology," *Nature Materials*, vol. 21, no. 6, pp. 656–663, 2022.

[53] J. Wang, Y. Wang, P. Bi, Z. Chen, J. Qiao, J. Li, W. Wang, Z. Zheng, S. Zhang, X. Hao, *et al.*, "Binary organic solar cells with 19.2% efficiency enabled by solid additive," *Advanced Materials*, p. 2301583, 2023.

[54] N. Li, I. McCulloch, and C. Brabec, "Analyzing the efficiency, stability and cost potential for fullerene-free organic photovoltaics in one figure of merit," *Energy & Environmental Science*, vol. 11, no. 6, pp. 1355–1361, 2018.

[55] C. Zhang, T. Heumueller, S. Leon, W. Gruber, K. Burlafinger, X. Tang, J. Perea, I. Wabra, A. Hirsch, T. Unruh, *et al.*, "A top-down strategy identifying molecular phase stabilizers to overcome microstructure instabilities in organic solar cells," *Energy & Environmental Science*, vol. 12, no. 3, pp. 1078–1087, 2019.

[56] E. Speller, A. Clarke, J. Luke, H. Lee, J. Durrant, N. Li, T. Wang, H. Wong, J. Kim, W. Tsoi, *et al.*, "From fullerene acceptors to non-fullerene acceptors: prospects and challenges in the stability of organic solar cells," *Journal of Materials Chemistry A*, vol. 7, no. 41, pp. 23361–23377, 2019.

[57] Y. Zhang, Y. Xu, M. Ford, F. Li, J. Sun, X. Ling, Y. Wang, J. Gu, J. Yuan, and W. Ma, "Thermally stable all-polymer solar cells with high tolerance on blend ratios," *Advanced Energy Materials*, vol. 8, no. 18, p. 1800029, 2018.

[58] Y. He, T. Heumüller, W. Lai, G. Feng, A. Classen, X. Du, C. Liu, W. Li, N. Li, and C. Brabec, "Evidencing excellent thermal-and photostability for single-component organic solar cells with inherently built-in microstructure," *Advanced Energy Materials*, vol. 9, no. 21, p. 1900409, 2019.

[59] K. Hung, C. Tsai, S. Chang, Y. Lai, U. Jeng, F. Cao, C. Hsu, C. Su, and Y. Cheng, "Bispentafluorophenyl-containing additive: enhancing efficiency and morphological stability of polymer solar cells via hand-grabbing-like supramolecular pentafluorophenyl–fullerene interactions," *ACS applied materials & interfaces*, vol. 9, no. 50, pp. 43861–43870, 2017.

[60] M. Xiong, J. Wu, Q. Fan, Q. Liu, J. Lv, X. Ou, X. Guo, and M. Zhang, "Ternary organic solar cells with improved efficiency and stability enabled by compatible dual-acceptor strategy," *Organic Electronics*, vol. 96, p. 106227, 2021.

[61] T. Zhang, X. Zhao, D. Yang, Y. Tian, and X. Yang, "Ternary organic solar cells with¿ 11% efficiency incorporating thick photoactive layer and nonfullerene small molecule acceptor," *Advanced Energy Materials*, vol. 8, no. 4, p. 1701691, 2018.

[62] H. Hwang, D. Sin, C. Park, and K. Cho, "Ternary organic solar cells based on a wide-bandgap polymer with enhanced power conversion efficiencies," *Scientific reports*, vol. 9, no. 1, p. 12081, 2019.

[63] Z. Liu, L. Wang, H. Zhao, P. Chen, and X. Xie, "High-performance inverted ternary organic solar cells using solution-processed tin oxide as the electron transport layer," *Organic Electronics*, vol. 120, p. 106828, 2023.

[64] Q. An, F. Zhang, J. Zhang, W. Tang, Z. Deng, and B. Hu, "Versatile ternary organic solar cells: a critical review," *Energy & Environmental Science*, vol. 9, no. 2, pp. 281–322, 2016.

[65] R. Singh, T. Duan, Z. Kan, C. Chochos, G. Kini, M. Kumar, J. Park, J. Lee, and J. Lee, "Revealing the structural effects of non-fullerene acceptors on the performances of ternary organic photovoltaics under indoor light conditions," *Nano Energy*, vol. 75, p. 104934, 2020.

[66] H. Chen, S. Jeong, J. Tian, Y. Zhang, D. Naphade, M. Alsufyani, W. Zhang, S. Griggs, H. Hu, S. Barlow, *et al.*, "A 19% efficient and stable organic photovoltaic device enabled by a guest nonfullerene acceptor with fibril-like morphology," *Energy & Environmental Science*, vol. 16, no. 3, pp. 1062–1070, 2023.

[67] C. Brabec, M. Heeney, I. McCulloch, and J. Nelson, "Influence of blend microstructure on bulk heterojunction organic photovoltaic performance," *Chemical Society Reviews*, vol. 40, no. 3, pp. 1185–1199, 2011.

[68] I. Jacobs and A. Moulé, "Controlling molecular doping in organic semiconductors," *Advanced Materials*, vol. 29, no. 42, p. 1703063, 2017.

[69] H. Liao, C. Ho, C. Chang, M. Jao, S. Darling, and W. Su, "Additives for morphology control in high-efficiency organic solar cells," *Materials today*, vol. 16, no. 9, pp. 326–336, 2013.

[70] F. Liu, Y. Gu, J. Jung, W. Jo, and T. Russell, "On the morphology of polymer-based photovoltaics," *Journal of Polymer Science Part B: Polymer Physics*, vol. 50, no. 15, pp. 1018–1044, 2012.

[71] J. Helveston, G. He, and M. Davidson, "Quantifying the cost savings of global solar photovoltaic supply chains," *Nature*, pp. 1–5, 2022.

[72] J. Carlé and F. Krebs, "Technological status of organic photovoltaics (opv)," *Solar Energy Materials and Solar Cells*, vol. 119, pp. 309–310, 2013.

[73] M. Insel, H. Sadikoglu, and M. Melikoglu, "Assessment and determination of 2030 onshore wind and solar pv energy targets of türkiye considering several investment and cost scenarios," *Results in Engineering*, vol. 16, p. 100733, 2022.

[74] R. Fu, D. Feldman, and R. Margolis, "Us solar photovoltaic system cost benchmark: Q1 2018," tech. rep., National Renewable Energy Lab.(NREL), Golden, CO (United States), 2018.

[75] L. Saleh and T. Mezher, "Techno-economic analysis of sustainability and externality costs of water desalination production," *Renewable and Sustainable Energy Reviews*, vol. 150, p. 111465, 2021.

[76] E. Sadik-Zada, "Political economy of green hydrogen rollout: A global perspective," *Sustainability*, vol. 13, no. 23, p. 13464, 2021.

[77] D. K. Panda, *Nanostructured organic solar cells*. PhD thesis, University of Wollongong, 2011.

[78] A. Meletiou, M. Grace, M. Darbi, M. Pham, K. Locher-Krause, and H. Rueff, "Eu renewable energy policies, global biodiversity, and the un sdgs: a report of the eklipse project," tech. rep., 2019.

[79] D. PALACIOS-GOMEZ *et al.*, *Toward Efficient Organic Photovoltaics: From Formulation and Novel Materials to Device Architectures*. PhD thesis, Durham University, 2022.

[80] K. Jasim, "Dye sensitized solar cells-working principles, challenges and opportunities," *Solar Cells-Dye-Sensitized Devices*, vol. 8, p. 172Ā210, 2011.

[81] V. Fthenakis and P. Lynn, *Electricity from sunlight: photovoltaic-systems integration and sustainability*. John Wiley & Sons, 2018.

[82] A. Chodos, "April 25, 1954: Bell labs demonstrates the first practical silicon solar cell," *APS News-This month in Physics history*, 2009.

[83] C. Hempstead, *Semiconductors 1853-1919: an historical study of selenium and some related materials*. PhD thesis, Durham University, 1977.

[84] M. Ramrakhiani, "Recent advances in photovoltaics," Materials Research Forum LLC, 2017.

[85] D. Lincot, "The new paradigm of photovoltaics: From powering satellites to powering humanity," *Comptes Rendus Physique*, vol. 18, no. 7-8, pp. 381–390, 2017.

[86] D. Chapin, C. Fuller, and G. Pearson, "A new silicon p-n junction photocell for converting solar radiation into electrical power," *Journal of applied physics*, vol. 25, no. 5, pp. 676–677, 1954.

[87] A. Smets, K. Jäger, O. Isabella, R. Van Swaaij, and M. Zeman, *Solar Energy: The physics and engineering of photovoltaic conversion, technologies and systems*. Bloomsbury Publishing, 2016.

[88] M. Hayat, D. Ali, K. Monyake, L. Alagha, and N. Ahmed, "Solar energy—a look into power generation, challenges, and a solar-powered future," *International Journal of Energy Research*, vol. 43, no. 3, pp. 1049–1067, 2019.

[89] Z. Wu, J. Wang, Y. Liu, S. Hou, X. Liu, Q. Zhang, and F. Cao, "A review of spectral controlling for renewable energy harvesting and conserving," *Materials Today Physics*, vol. 18, p. 100388, 2021.

[90] M. Green and S. Bremner, "Energy conversion approaches and materials for high-efficiency photovoltaics," *Nature materials*, vol. 16, no. 1, pp. 23–34, 2017.

[91] N. Mariotti, M. Bonomo, L. Fagiolari, N. Barbero, C. Gerbaldi, F. Bella, and C. Barolo, "Recent advances in eco-friendly and cost-effective materials towards sustainable dye-sensitized solar cells," *Green chemistry*, vol. 22, no. 21, pp. 7168–7218, 2020.

[92] T. Razykov, C. Ferekides, D. Morel, E. Stefanakos, H. Ullal, and H. Upadhyaya, "Solar photovoltaic electricity: Current status and future prospects," *Solar Energy*, vol. 85, no. 8, pp. 1580–1608, 2011.

[93] K. Shanks, S. Senthilarasu, and T. Mallick, "Optics for concentrating photovoltaics: Trends, limits and opportunities for materials and design," *Renewable and Sustainable Energy Reviews*, vol. 60, pp. 394–407, 2016.

[94] F. Pelanchon and P. Mialhe, "Optimization of solar cell performance," *Solid-state electronics*, vol. 33, no. 1, pp. 47–51, 1990.

[95] M. Scarpulla, B. McCandless, A. Phillips, Y. Yan, M. Heben, C. Wolden, G. Xiong, W. Metzger, D. Mao, D. Krasikov, *et al.*, "Cdte-based thin film photovoltaics: Recent advances, current challenges and future prospects," *Solar Energy Materials and Solar Cells*, vol. 255, p. 112289, 2023.

[96] E. Pérez, S. Duenas, H. Castán, H. García, L. Bailón, D. Montero, R. García-Hernansanz, E. García-Hemme, J. Olea, and G. González-Díaz, "A detailed analysis of the energy levels configuration existing in the band gap of supersaturated silicon with titanium for photovoltaic applications," *Journal of Applied Physics*, vol. 118, no. 24, 2015.

[97] R. Saive, "Light trapping in thin silicon solar cells: A review on fundamentals and technologies," *Progress in Photovoltaics: Research and Applications*, vol. 29, no. 10, pp. 1125–1137, 2021.

[98] G. Conibeer, "Third-generation photovoltaics," *Materials today*, vol. 10, no. 11, pp. 42–50, 2007.

[99] S. Khalid, M. Sultan, E. Ahmed, and W. Ahmed, "Third-generation solar cells," in *Emerging Nanotechnologies for Renewable Energy*, pp. 3–35, Elsevier, 2021.

[100] M. Bui, S. Rost, M. Auge, J. Tu, L. Zhou, I. Aguilera, S. Blügel, M. Ghorbani-Asl, A. Krasheninnikov, A. Hashemi, *et al.*, "Low-energy se ion implantation in mos 2 monolayers," *npj 2D Materials and Applications*, vol. 6, no. 1, p. 42, 2022.

[101] L. Peter, "Towards sustainable photovoltaics: the search for new materials," *Philosophical Transactions of the Royal Society A: Mathematical, Physical and Engineering Sciences*, vol. 369, no. 1942, pp. 1840–1856, 2011.

[102] P. Kartikay, K. Mokurala, B. Sharma, R. Kali, N. Mukurala, D. Mishra, A. Kumar, S. Mallick, J. Song, and S. Jin, "Recent advances and challenges in solar photovoltaic and energy storage materials: future directions in indian perspective," *Journal of Physics: Energy*, vol. 3, no. 3, p. 034018, 2021.

[103] C. Schuster, I. Crupi, J. Halme, M. Koç, M. Mendes, I. Peters, and S. Yerci, "Empowering photovoltaics with smart light management technologies," in *Handbook of Climate Change Mitigation and Adaptation*, pp. 1165–1248, Springer, 2022.

[104] O. Almora, D. Baran, G. Bazan, C. Cabrera, S. Erten-Ela, K. Forberich, F. Guo, J. Hauch, A. Ho-Baillie, T. Jacobsson, *et al.*, "Device performance of emerging photovoltaic materials (version 3)," *Advanced energy materials*, vol. 13, no. 1, p. 2203313, 2023.

[105] H. Zhang, X. Ji, H. Yao, Q. Fan, B. Yu, and J. Li, "Review on efficiency improvement effort of perovskite solar cell," *Solar Energy*, vol. 233, pp. 421–434, 2022.

[106] N. Hartono, H. Köbler, P. Graniero, M. Khenkin, R. Schlatmann, C. Ulbrich, and A. Abate, "Stability follows efficiency based on the analysis of a large perovskite solar cells ageing dataset," *Nature Communications*, vol. 14, no. 1, p. 4869, 2023.

[107] C. Liu, Y. Yang, H. Chen, J. Xu, A. Liu, A. Bati, H. Zhu, L. Grater, S. Hadke, C. Huang, *et al.*, "Bimolecularly passivated interface enables efficient and stable inverted perovskite solar cells," *Science*, vol. 382, no. 6672, pp. 810–815, 2023.

[108] L. Zhan, S. Li, Y. Li, R. Sun, J. Min, Z. Bi, W. Ma, Z. Chen, G. Zhou, H. Zhu, *et al.*, "Desired open-circuit voltage increase enables efficiencies approaching 19% in symmetric-asymmetric molecule ternary organic photovoltaics," *Joule*, vol. 6, no. 3, pp. 662–675, 2022.

[109] Z. Wang, A. Tang, H. Wang, Q. Guo, Q. Guo, X. Sun, Z. Xiao, L. Ding, and E. Zhou, "Organic photovoltaic cells offer ultrahigh voc of 1.2 v under am 1.5 g light and a high efficiency of 21.2% under indoor light," *Chemical Engineering Journal*, vol. 451, p. 139080, 2023.

[110] F. Subhan, A. Khan, F. Hilal, A. Khan, S. Khan, R. Ullah, M. Imran, and M. Noman, "Efficient broadband light absorption in thin-film a-si solar cell based on double sided hybrid bi-metallic nanogratings," *RSC advances*, vol. 10, no. 20, pp. 11836–11842, 2020.

[111] Z. Khezripour, F. Mahani, and A. Mokhtari, "Performance improvement of thin-film silicon solar cells using transversal and longitudinal titanium nitride plasmonic nanogratings," *Optical Materials*, vol. 99, p. 109532, 2020.

[112] B. Wei, X. Mao, W. Liu, C. Ji, G. Yang, Y. Bao, X. Chen, F. Yang, and X. Wang, "Recent progress of surface plasmon–enhanced light trapping in gaas thin-film solar cells," *Plasmonics*, vol. 18, no. 6, pp. 2009–2029, 2023.

[113] Y. Gao, F. Jin, Z. Su, H. Zhao, Y. Luo, B. Chu, and W. Li, "Cooperative plasmon enhanced organic solar cells with thermal coevaporated au and ag nanoparticles," *Organic Electronics*, vol. 48, pp. 336–341, 2017.

[114] F. Qu, Diand Liu, J. Yu, W. Xie, Q. Xu, X. Li, and Y. Huang, "Plasmonic core-shell gold nanoparticle enhanced optical absorption in photovoltaic devices," *Applied Physics Letters*, vol. 98, no. 11, 2011.

[115] E. Kohlrausch, D. de Vasconcelos Freitas, C. da Silva Filho, L. Fernandes Loguercio, L. Santa-Cruz, L. Lins Maciel, M. Oliveira, C. dos Santos, and G. Machado, "Advances in carbon materials applied to carbon-based perovskite solar cells," *Energy Technology*, vol. 11, no. 4, p. 2200676, 2023.

[116] J. Shaikh, N. Shaikh, S. Mali, J. Patil, K. Pawar, P. Kanjanaboos, C. Hong, J. Kim, and P. Patil, "Nanoarchitectures in dye-sensitized solar cells: metal oxides, oxide perovskites and carbon-based materials," *Nanoscale*, vol. 10, no. 11, pp. 4987–5034, 2018.

[117] C. Chen, S. Zheng, and Song, "Photon management to reduce energy loss in perovskite solar cells," *Chemical Society Reviews*, vol. 50, no. 12, pp. 7250–7329, 2021.

[118] S. Carretero-Palacios, A. Jiménez-Solano, and H. Míguez, "Plasmonic nanoparticles as light-harvesting enhancers in perovskite solar cells: a user's guide," *ACS energy letters*, vol. 1, no. 1, pp. 323–331, 2016.

[119] R. Siavash Moakhar, S. Gholipour, S. Masudy-Panah, A. Seza, A. Mehdikhani, N. Riahi-Noori, S. Tafazoli, N. Timasi, Y. Lim, and M. Saliba, "Recent advances in plasmonic perovskite solar cells," *Advanced science*, vol. 7, no. 13, p. 1902448, 2020.

[120] R. Borah, R. Ninakanti, S. Bals, and S. Verbruggen, "Plasmon resonance of gold and silver nanoparticle arrays in the kretschmann (attenuated total reflectance) vs. direct incidence configuration," *Scientific Reports*, vol. 12, no. 1, p. 15738, 2022.

[121] S. Bremner, M. Levy, and C. Honsberg, "Analysis of tandem solar cell efficiencies under am1. 5g spectrum using a rapid flux calculation method," *Progress in photovoltaics: Research and Applications*, vol. 16, no. 3, pp. 225–233, 2008.

[122] H. Li and W. Zhang, "Perovskite tandem solar cells: from fundamentals to commercial deployment," *Chemical Reviews*, vol. 120, no. 18, pp. 9835–9950, 2020.

[123] Q. Wali, N. Elumalai, Y. Iqbal, A. Uddin, and R. Jose, "Tandem perovskite solar cells," *Renewable and Sustainable Energy Reviews*, vol. 84, pp. 89–110, 2018.

[124] J. Zhou, Q. Huang, Y. Ding, G. Hou, and Y. Zhao, "Passivating contacts for high-efficiency silicon-based solar cells: From single-junction to tandem architecture," *Nano Energy*, vol. 92, p. 106712, 2022.

[125] E. Raza and Z. Ahmad, "Review on two-terminal and four-terminal crystalline-silicon/perovskite tandem solar cells; progress, challenges, and future perspectives," *Energy Reports*, vol. 8, pp. 5820–5851, 2022.

[126] F. Martinho, "Challenges for the future of tandem photovoltaics on the path to terawatt levels: a technology review," *Energy & Environmental Science*, vol. 14, no. 7, pp. 3840–3871, 2021.

[127] M. Yamaguchi, K. Lee, K. Araki, and N. Kojima, "A review of recent progress in heterogeneous silicon tandem solar cells," *Journal of Physics D: Applied Physics*, vol. 51, no. 13, p. 133002, 2018.

[128] X. Wu, B. Li, Z. Zhu, C. Chueh, and A. Jen, "Designs from single junctions, heterojunctions to multijunctions for high-performance perovskite solar cells," *Chemical Society Reviews*, vol. 50, no. 23, pp. 13090–13128, 2021.

[129] A. Maalouf, T. Okoroafor, Z. Jehl, V. Babu, and S. Resalati, "A comprehensive review on life cycle assessment of commercial and emerging thin-film solar cell systems," *Renewable and Sustainable Energy Reviews*, vol. 186, p. 113652, 2023.

[130] S. Akhil, S. Akash, A. Pasha, B. Kulkarni, M. Jalalah, M. Alsaiari, F. Harraz, and R. Balakrishna, "Review on perovskite silicon tandem solar cells: Status and prospects 2t, 3t and 4t for real world conditions," *Materials & Design*, vol. 211, p. 110138, 2021.

[131] T. Leijtens, K. Bush, R. Prasanna, and M. McGehee, "Opportunities and challenges for tandem solar cells using metal halide perovskite semiconductors," *Nature Energy*, vol. 3, no. 10, pp. 828–838, 2018.

[132] P. Tockhorn, J. Sutter, A. Cruz, P. Wagner, K. Jäger, D. Yoo, F. Lang, M. Grischek, B. Li, J. Li, *et al.*, "Nano-optical designs for high-efficiency monolithic perovskite–silicon tandem solar cells," *Nature Nanotechnology*, vol. 17, no. 11, pp. 1214–1221, 2022.

[133] S. Palei, G. Murali, C. Kim, I. In, S. Lee, and S. Park, "A review on interface engineering of mxenes for perovskite solar cells," *Nano-Micro Letters*, vol. 15, no. 1, pp. 1–39, 2023.

[134] G. Wilson, M. Al-Jassim, W. Metzger, S. Glunz, P. Verlinden, G. Xiong, L. Mansfield, B. Stanbery, K. Zhu, Y. Yan, *et al.*, "The 2020 photovoltaic technologies roadmap," *Journal of Physics D: Applied Physics*, vol. 53, no. 49, p. 493001, 2020.

[135] M. Cenci, T. Scarazzato, D. Munchen, P. Dartora, H. Veit, A. Bernardes, and P. Dias, "Eco-friendly electronics—a comprehensive review," *Advanced Materials Technologies*, vol. 7, no. 2, p. 2001263, 2022.

[136] N. Rajput, U. Sharma, B. Kaur, P. Rani, K. Tongkachok, and V. Dornadula, "Current global green marketing standard: changing market and company branding," *International Journal of System Assurance Engineering and Management*, vol. 13, no. Suppl 1, pp. 727–735, 2022.

[137] I. Ilankoon, Y. Ghorbani, M. Chong, G. Herath, T. Moyo, and J. Petersen, "E-waste in the international context–a review of trade flows, regulations, hazards, waste management strategies and technologies for value recovery," *Waste management*, vol. 82, pp. 258–275, 2018.

[138] L. Xavier, M. Ottoni, and L. Abreu, "A comprehensive review of urban mining and the value recovery from e-waste materials," *Resources, Conservation and Recycling*, vol. 190, p. 106840, 2023.

[139] W. Mrozik, M. Rajaeifar, O. Heidrich, and P. Christensen, "Environmental impacts, pollution sources and pathways of spent lithium-ion batteries," *Energy & Environmental Science*, vol. 14, no. 12, pp. 6099–6121, 2021.

[140] V. Fthenakis, "Sustainability of photovoltaics: The case for thin-film solar cells," *Renewable and Sustainable Energy Reviews*, vol. 13, no. 9, pp. 2746–2750, 2009.

[141] E. Efaz, M. Rhaman, S. Al Imam, K. Bashar, F. Kabir, M. Mourtaza, S. Sakib, Mozahid, and FA, "A review of primary technologies of thin-film solar cells," *Engineering Research Express*, vol. 3, no. 3, p. 032001, 2021.

[142] A. Rajagopal, K. Yao, and A. Jen, "Toward perovskite solar cell commercialization: a perspective and research roadmap based on interfacial engineering," *Advanced Materials*, vol. 30, no. 32, p. 1800455, 2018.

[143] B. Akinoglu, B. Tuncel, and V. Badescu, "Beyond 3rd generation solar cells and the full spectrum project. recent advances and new emerging solar cells," *Sustainable Energy Technologies and Assessments*, vol. 46, p. 101287, 2021.

[144] E. Buitrago, A. Novello, and T. Meyer, "Third-generation solar cells: toxicity and risk of exposure," *Helvetica Chimica Acta*, vol. 103, no. 9, p. e2000074, 2020.

[145] L. Guilhot, "An analysis of china's energy policy from 1981 to 2020: Transitioning towards to a diversified and low-carbon energy system," *Energy Policy*, vol. 162, p. 112806, 2022.

[146] M. Rabaia, M. Abdelkareem, E. Sayed, K. Elsaid, K. Chae, T. Wilberforce, and A. Olabi, "Environmental impacts of solar energy systems: A review," *Science of The Total Environment*, vol. 754, p. 141989, 2021.

[147] M. Alaaeddin, . Sapuan, M. Zuhri, E. Zainudin, and F. Al-Oqla, "Photovoltaic applications: Status and manufacturing prospects," *Renewable and Sustainable Energy Reviews*, vol. 102, pp. 318–332, 2019.

[148] P. Subudhi and D. Punetha, "Progress, challenges, and perspectives on polymer substrates for emerging flexible solar cells: A holistic panoramic review," *Progress in Photovoltaics: Research and Applications*, vol. 31, no. 8, pp. 753–789, 2023.

[149] G. Han, S. Zhang, P. Boix, L. Wong, L. Sun, and S. Lien, "Towards high efficiency thin film solar cells," *Progress in Materials Science*, vol. 87, pp. 246–291, 2017.

[150] O. Abdulrazzaq, V. Saini, S. Bourdo, E. Dervishi, and A. Biris, "Organic solar cells: a review of materials, limitations, and possibilities for improvement," *Particulate science and technology*, vol. 31, no. 5, pp. 427–442, 2013.

[151] T. Lee and A. Ebong, "A review of thin film solar cell technologies and challenges," *Renewable and Sustainable Energy Reviews*, vol. 70, pp. 1286–1297, 2017.

[152] A. del Pilar Sánchez-Camargo, M. Bueno, F. Parada-Alfonso, A. Cifuentes, and E. Ibáñez, "Hansen solubility parameters for selection of green extraction solvents," *TrAC Trends in Analytical Chemistry*, vol. 118, pp. 227–237, 2019.

[153] Q. Zhang, J. Liu, X. Yu, and Y. Han, "Design optimized intermixed phase by tuning polymer-fullerene intercalation for free charge generation," *Chinese Chemical Letters*, vol. 30, no. 7, pp. 1405–1409, 2019.

[154] A. Osman, L. Chen, M. Yang, G. Msigwa, M. Farghali, S. Fawzy, D. Rooney, and P. Yap, "Cost, environmental impact, and resilience of renewable energy under a changing climate: a review," *Environmental Chemistry Letters*, vol. 21, no. 2, pp. 741–764, 2023.

[155] G. Jones and L. Bouamane, "" power from sunshine": A business history of solar energy," *Harvard Business School Working Paper Series*, 2012.

[156] A. El Hammoumi, S. Chtita, S. Motahhir, and A. El Ghzizal, "Solar pv energy: From material to use, and the most commonly used techniques to maximize the power output of pv systems: A focus on solar trackers and floating solar panels," *Energy Reports*, vol. 8, pp. 11992–12010, 2022.

[157] D. Vijayan, E. Koda, A. Sivasuriyan, J. Winkler, P. Devarajan, R. Kumar, A. Jakimiuk, P. Osinski, A. Podlasek, and M. Vaverková, "Advancements in solar panel technology in civil engineering for revolutionizing renewable energy solutions—a review," *Energies*, vol. 16, no. 18, p. 6579, 2023.

[158] P. Choudhary and R. Srivastava, "Sustainability perspectives-a review for solar photovoltaic trends and growth opportunities," *Journal of Cleaner Production*, vol. 227, pp. 589–612, 2019.

[159] M. Green, "Commercial progress and challenges for photovoltaics," *Nature Energy*, vol. 1, no. 1, pp. 1–4, 2016.

[160] S. Almosni, A. Delamarre, Z. Jehl, D. Suchet, L. Cojocaru, M. Giteau, B. Behaghel, A. Julian, C. Ibrahim, L. Tatry, *et al.*, "Material challenges for solar cells in the twenty-first century: directions in emerging technologies," *Science and Technology of advanced MaTerialS*, vol. 19, no. 1, pp. 336–369, 2018.

[161] A. Chilvery, S. Das, P. Guggilla, C. Brantley, and A. Sunda-Meya, "A perspective on the recent progress in solution-processed methods for highly efficient perovskite solar cells," *Science and Technology of advanced MaTerialS*, vol. 17, no. 1, pp. 650–658, 2016.

[162] R. Miles, G. Zoppi, and I. Forbes, "Inorganic photovoltaic cells," *Materials today*, vol. 10, no. 11, pp. 20–27, 2007.

[163] A. Machín and F. Márquez, "Advancements in photovoltaic cell materials: Silicon, organic, and perovskite solar cells," *Materials*, vol. 17, no. 5, p. 1165, 2024.

[164] M. Beard, J. Luther, and A. Nozik, "The promise and challenge of nanostructured solar cells," *Nature nanotechnology*, vol. 9, no. 12, pp. 951–954, 2014.

[165] W. Brooks, D. Lamb, and S. Irvine, "Ir reflectance imaging for crystalline si solar cell crack detection," *IEEE journal of photovoltaics*, vol. 5, no. 5, pp. 1271–1275, 2015.

[166] E. Solak and E. Irmak, "Advances in organic photovoltaic cells: a comprehensive review of materials, technologies, and performance," *RSC advances*, vol. 13, no. 18, pp. 12244–12269, 2023.

[167] D. Powell, M. Winkler, H. Choi, C. Simmons, D. Needleman, and T. Buonassisi, "Crystalline silicon photovoltaics: a cost analysis framework for determining technology pathways to reach baseload electricity costs," *Energy & Environmental Science*, vol. 5, no. 3, pp. 5874–5883, 2012.

[168] U. Haley and D. Schuler, "Government policy and firm strategy in the solar photovoltaic industry," *California Management Review*, vol. 54, no. 1, pp. 17–38, 2011.

[169] G. Bye and B. Ceccaroli, "Solar grade silicon: Technology status and industrial trends," *Solar Energy Materials and Solar Cells*, vol. 130, pp. 634–646, 2014.

[170] M. Green, "Photovoltaics: technology overview," *Energy policy*, vol. 28, no. 14, pp. 989–998, 2000.

[171] Z. Sun, X. Chen, Y. He, J. Li, J. Wang, H. Yan, and Y. Zhang, "Toward efficiency limits of crystalline silicon solar cells: recent progress in high-efficiency silicon heterojunction solar cells," *Advanced Energy Materials*, vol. 12, no. 23, p. 2200015, 2022.

[172] M. Green, "Self-consistent optical parameters of intrinsic silicon at 300 k including temperature coefficients," *Solar Energy Materials and Solar Cells*, vol. 92, no. 11, pp. 1305–1310, 2008.

[173] C. Ballif, F. Haug, M. Boccard, P. Verlinden, and G. Hahn, "Status and perspectives of crystalline silicon photovoltaics in research and industry," *Nature Reviews Materials*, vol. 7, no. 8, pp. 597–616, 2022.

[174] T. Ibn-Mohammed, S. Koh, I. Reaney, A. Acquaye, G. Schileo, K. Mustapha, and R. Greenough, "Perovskite solar cells: An integrated hybrid lifecycle assessment and review in comparison with other photovoltaic technologies," *Renewable and Sustainable Energy Reviews*, vol. 80, pp. 1321–1344, 2017.

[175] K. ElKhamisy, H. Abdelhamid, E. El-Rabaie, and N. Abdel-Salam, "A comprehensive survey of silicon thin-film solar cell: Challenges and novel trends," *Plasmonics*, pp. 1–20, 2023.

[176] P. Sharma, P. Goyal, *et al.*, "Evolution of pv technology from conventional to nanomaterials," *Materials Today: Proceedings*, vol. 28, pp. 1593–1597, 2020.

[177] A. Alami, *PV Technology and Manufacturing*. Springer Nature, 2023.

[178] K. Rakesh Tej Kumar, M. Ramakrishna, and G. Durga Sukumar, "A review on pv cells and nanocomposite-coated pv systems," *International Journal of Energy Research*, vol. 42, no. 7, pp. 2305–2319, 2018.

[179] S. Pouladi, *High-Efficiency Flexible Thin-Film Single-Crystal-Like GaAs Solar Cells Based on Cheap Metal Tape*. PhD thesis, University of Houston, 2020.

[180] J. Rath, "Low temperature polycrystalline silicon: a review on deposition, physical properties and solar cell applications," *Solar Energy Materials and Solar Cells*, vol. 76, no. 4, pp. 431–487, 2003.

[181] E. Gervais, S. Shammugam, L. Friedrich, and T. Schlegl, "Raw material needs for the large-scale deployment of photovoltaics–effects of innovation-driven roadmaps on material constraints until 2050," *Renewable and Sustainable Energy Reviews*, vol. 137, p. 110589, 2021.

[182] M. Dambhare, B. Butey, and S. Moharil, "Solar photovoltaic technology: A review of different types of solar cells and its future trends," in *Journal of Physics: Conference Series*, vol. 1913, p. 012053, IOP Publishing, 2021.

[183] A. Shah, "Thin-film silicon solar cells," in *Practical Handbook of Photovoltaics*, pp. 209–281, Elsevier, 2012.

[184] J. Roy and D. Bose, *Photovoltaic Science and Technology*. Cambridge University Press, 2018.

[185] E. Khorani, *Silicon-based ultrathin layers for hole-selective contacts in silicon solar cells*. PhD thesis, University of Southampton, 2020.

[186] Y. Salimi, "Optimization of emitter layer in n-type bifacial crystalline solar cell," Master's thesis, Middle East Technical University, 2022.

[187] Z. Eygi, *Production of amorphous silicon/p-type crystalline silicon heterojunction solar cells by sputtering and PECVD methods*. PhD thesis, Middle East Technical University, 2011.

[188] B. Demaurex, "Passivating contacts for homojunction solar cells using a-si: H/c-si hetero-interfaces," tech. rep., EPFL, 2014.

[189] M. Lu, *Silicon heterojunction solar cell and crystallization of amorphous silicon*. University of Delaware, 2008.

[190] S. Deb, "Recent advances and future opportunities for thin-film solar cells," *Thin-Film Solar Cells: Next Generation Photovoltaics and Its Applications*, pp. 15–42, 2004.

[191] M. Tucci, L. Serenelli, S. de Iuliis, D. Caputo, and G. de Cesare, "Light trapping in thin silicon solar cells," *Silicon Based Thin Film Solar Cells*, p. 395, 2013.

[192] V. Gowrishankar, S. Scully, M. McGehee, Q. Wang, and H. Branz, "Exciton splitting and carrier transport across the amorphous-silicon/polymer solar cell interface," *Applied Physics Letters*, vol. 89, no. 25, 2006.

[193] S. Prayogi, R. Asih, B. Priyanto, M. Baqiya, M. Naradipa, Y. Cahyono, Darminto, and A. Rusydi, "Observation of resonant exciton and correlated plasmon yielding correlated plexciton in amorphous silicon with various hydrogen content," *Scientific Reports*, vol. 12, no. 1, p. 21497, 2022.

[194] T. Bruton, *Photovoltaics from Milliwatts to Gigawatts: Understanding Market and Technology Drivers Toward Terawatts*. John Wiley & Sons, 2021.

[195] J. Kilner, S. Skinner, S. Irvine, and P. Edwards, *Functional materials for sustainable energy applications*. Elsevier, 2012.

[196] R. Birkmire and B. McCandless, "Cdte thin film technology: Leading thin film pv into the future," *Current Opinion in Solid State and Materials Science*, vol. 14, no. 6, pp. 139–142, 2010.

[197] A. Morales-Acevedo, "Thin film cds/cdte solar cells: research perspectives," *Solar Energy*, vol. 80, no. 6, pp. 675–681, 2006.

[198] M. Powalla, S. Paetel, E. Ahlswede, R. Wuerz, C. Wessendorf, and T. Magorian Friedlmeier, "Thin-film solar cells exceeding 22% solar cell efficiency: An overview on cdte-, cu (in, ga) se2-, and perovskite-based materials," *Applied Physics Reviews*, vol. 5, no. 4, 2018.

[199] R. Miles, K. Hynes, and I. Forbes, "Photovoltaic solar cells: An overview of state-of-the-art cell development and environmental issues," *Progress in crystal growth and characterization of materials*, vol. 51, no. 1-3, pp. 1–42, 2005.

[200] G. Schileo and G. Grancini, "Lead or no lead? availability, toxicity, sustainability and environmental impact of lead-free perovskite solar cells," *Journal of materials chemistry C*, vol. 9, no. 1, pp. 67–76, 2021.

[201] D. Bonnet and P. Meyers, "Cadmium-telluride—material for thin film solar cells," *Journal of Materials Research*, vol. 13, pp. 2740–2753, 1998.

[202] M. Tawalbeh, A. Al-Othman, F. Kafiah, E. Abdelsalam, F. Almomani, and M. Alkasrawi, "Environmental impacts of solar photovoltaic systems: A critical review of recent progress and future outlook," *Science of The Total Environment*, vol. 759, p. 143528, 2021.

[203] J. Major, R. Treharne, L. Phillips, and K. Durose, "A low-cost non-toxic post-growth activation step for cdte solar cells," *Nature*, vol. 511, no. 7509, pp. 334–337, 2014.

[204] E. Fan, L. Li, Z. Wang, J. Lin, Y. Huang, Y. Yao, R. Chen, and F. Wu, "Sustainable recycling technology for li-ion batteries and beyond: challenges and future prospects," *Chemical reviews*, vol. 120, no. 14, pp. 7020–7063, 2020.

[205] V. Fthenakis, C. Athias, A. Blumenthal, A. Kulur, J. Magliozzo, and D. Ng, "Sustainability evaluation of cdte pv: An update," *Renewable and Sustainable Energy Reviews*, vol. 123, p. 109776, 2020.

[206] H. Zhou, W. Hsu, H. Duan, B. Bob, W. Yang, T. Song, C. Hsu, and Y. Yang, "Czts nanocrystals: a promising approach for next generation thin film photovoltaics," *Energy & Environmental Science*, vol. 6, no. 10, pp. 2822–2838, 2013.

[207] S. Dwivedi, S. Tripathi, D. Tiwari, A. Chauhan, P. Dwivedi, and N. Prasad, "Low cost copper zinc tin sulphide (czts) solar cells fabricated by sulphurizing sol-gel deposited precursor using 1, 2-ethanedithiol (edt)," *Solar Energy*, vol. 224, pp. 210–217, 2021.

[208] T. Edler, Mand Rath, A. Schenk, A. Fischereder, W. Haas, M. Edler, B. Chernev, B. Kunert, F. Hofer, R. Resel, *et al.*, "Copper zinc tin sulfide layers prepared from solution processable metal dithiocarbamate precursors," *Materials chemistry and physics*, vol. 136, no. 2-3, pp. 582–588, 2012.

[209] T. Huang, X. Yin, G. Qi, and H. Gong, "Czts-based materials and interfaces and their effects on the performance of thin film solar cells," *physica status solidi (RRL)–Rapid Research Letters*, vol. 8, no. 09, pp. 735–762, 2014.

[210] E. Cochella Diaz, *Improving the Endurance of Small Unmanned Aerial Vehicles Utilizing Flexible Solar Cells*. PhD thesis, Monterey, CA; Naval Postgraduate School, 2022.

[211] A. Oliveira, J. Teixeira, D. Ramos, P. Fernandes, and P. Salomé, "Exploiting the optical limits of thin-film solar cells: A review on light management strategies in cu (in, ga) se2," *Advanced Photonics Research*, vol. 3, no. 6, p. 2100190, 2022.

[212] P. Jackson, R. Wuerz, D. Hariskos, E. Lotter, W. Witte, and M. Powalla, "Effects of heavy alkali elements in cu (in, ga) se2 solar cells with efficiencies up to 22.6%," *physica status solidi (RRL)–Rapid Research Letters*, vol. 10, no. 8, pp. 583–586, 2016.

[213] Y. Wang, S. Lv, and Z. Li, "Review on incorporation of alkali elements and their effects in cu (in, ga) se2 solar cells," *Journal of Materials Science & Technology*, vol. 96, pp. 179–189, 2022.

[214] C. Zhao, S. Yu, W. Tang, X. Yuan, H. Zhou, T. Qi, X. Zheng, D. Ning, M. Ma, J. Zhu, *et al.*, "Advances in cigs thin film solar cells with emphasis on the alkali element post-deposition treatment," *Materials Reports: Energy*, p. 100214, 2023.

[215] Z. Li, J. Li, J. Lei, S. Wei, and N. Wang, "Research progress of alkali doped cu (in, ga) se2 thin film solar cells," *Current Chinese Science*, vol. 1, no. 6, pp. 574–585, 2021.

[216] O. Nwakanma, S. Velumani, and A. Morales-Acevedo, "Review on the effects due to alkali metals on copper–indium–gallium–selenide solar cells," *Materials Today Energy*, vol. 20, p. 100617, 2021.

[217] T. Feurer, P. Reinhard, E. Avancini, B. Bissig, J. Löckinger, P. Fuchs, R. Carron, T. Weiss, J. Perrenoud, S. Stutterheim, *et al.*, "Progress in thin film cigs photovoltaics–research and development, manufacturing, and applications," *Progress in Photovoltaics: Research and Applications*, vol. 25, no. 7, pp. 645–667, 2017.

[218] T. Amrillah, A. Prasetio, A. Supandi, D. Sidiq, F. Putra, M. Nugroho, Z. Salsabilla, and R. Azmi, "Environment-friendly copper-based chalcogenide thin film solar cells: status and perspectives," *Materials Horizons*, vol. 10, no. 2, pp. 313–339, 2023.

[219] D. Stoltzfus, J. Donaghey, A. Armin, P. Shaw, PE an.d Burn, and P. Meredith, "Charge generation pathways in organic solar cells: assessing the contribution from the electron acceptor," *Chemical Reviews*, vol. 116, no. 21, pp. 12920–12955, 2016.

[220] S. Tiwari, T. Tiwari, S. Carter, J. Scott, and J. Yakhmi, "Advances in polymer-based photovoltaic cells: Review of pioneering materials, design, and device physics," *Handbook of Ecomaterials*, vol. 2, pp. 1055–1101, 2018.

[221] C. Deibel, T. Strobel, and V. Dyakonov, "Role of the charge transfer state in organic donor–acceptor solar cells," *Advanced materials*, vol. 22, no. 37, pp. 4097–4111, 2010.

[222] O. Ostroverkhova, "Organic optoelectronic materials: mechanisms and applications," *Chemical reviews*, vol. 116, no. 22, pp. 13279–13412, 2016.

[223] W. Cai, X. Gong, and Y. Cao, "Polymer solar cells: recent development and possible routes for improvement in the performance," *Solar energy materials and solar cells*, vol. 94, no. 2, pp. 114–127, 2010.

[224] J. Bombile, M. Janik, and S. Milner, "Energetics of exciton binding and dissociation in polythiophenes: a tight binding approach," *Physical Chemistry Chemical Physics*, vol. 21, no. 22, pp. 11999–12011, 2019.

[225] F. Etzold, I. Howard, R. Mauer, M. Meister, T. Kim, K. Lee, N. Baek, and F. Laquai, "Ultrafast exciton dissociation followed by nongeminate charge recombination in pcdtbt: Pcbm photovoltaic blends," *Journal of the American Chemical Society*, vol. 133, no. 24, pp. 9469–9479, 2011.

[226] G. Scholes, "Insights into excitons confined to nanoscale systems: electron–hole interaction, binding energy, and photodissociation," *ACS nano*, vol. 2, no. 3, pp. 523–537, 2008.

[227] A. Armin, W. Li, O. Sandberg, Z. Xiao, L. Ding, J. Nelson, D. Neher, K. Vandewal, S. Shoaee, T. Wang, *et al.*, "A history and perspective of non-fullerene electron acceptors for organic solar cells," *Advanced Energy Materials*, vol. 11, no. 15, p. 2003570, 2021.

[228] M. Wright and A. Uddin, "Organic—inorganic hybrid solar cells: A comparative review," *Solar energy materials and solar cells*, vol. 107, pp. 87–111, 2012.

[229] A. Najm, S. Alwash, N. Sulaiman, M. Chowdhury, and K. Techato, "N719 dye as a sensitizer for dye-sensitized solar cells (dsscs): A review of its functions and certain rudimentary principles," *Environmental Progress & Sustainable Energy*, vol. 42, no. 1, p. e13955, 2023.

[230] K. Prajapat, M. Dhonde, K. Sahu, P. Bhojane, V. Murty, and V. Shirage, "The evolution of organic materials for efficient dye-sensitized solar cells," *Journal of Photochemistry and Photobiology C: Photochemistry Reviews*, p. 100586, 2023.

[231] E. Muchuweni, B. Martincigh, and V. Nyamori, "Recent advances in graphene-based materials for dye-sensitized solar cell fabrication," *RSC advances*, vol. 10, no. 72, pp. 44453–44469, 2020.

[232] P. Shirage, "The evolution of organic materials for efficient dye-sensitized solar cells," 2023.

[233] M. Loi and J. Hummelen, "Hybrid solar cells: perovskites under the sun," *Nature materials*, vol. 12, no. 12, pp. 1087–1089, 2013.

[234] M. Nishat, M. Hossain, M. Hossain, S. Khanom, F. Ahmed, and M. Hossain, "Role of metal and anions in organo-metal halide perovskites ch 3 nh 3 mx 3 (m: Cu, zn, ga, ge, sn, pb; x: Cl, br, i) on structural and optoelectronic properties for photovoltaic applications," *RSC advances*, vol. 12, no. 21, pp. 13281–13294, 2022.

[235] S. Hoefler, G. Trimmel, and T. Rath, "Progress on lead-free metal halide perovskites for photovoltaic applications: a review," *Monatshefte für Chemie-Chemical Monthly*, vol. 148, pp. 795–826, 2017.

[236] P. Boix, S. Agarwala, T. Koh, N. Mathews, and S. Mhaisalkar, "Perovskite solar cells: beyond methylammonium lead iodide," *The journal of physical chemistry letters*, vol. 6, no. 5, pp. 898–907, 2015.

[237] A. Jena, A. Kulkarni, and T. Miyasaka, "Halide perovskite photovoltaics: background, status, and future prospects," *Chemical reviews*, vol. 119, no. 5, pp. 3036–3103, 2019.

[238] T. Nie, Z. Fang, X. Ren, Y. Duan, and S. Liu, "Recent advances in wide-bandgap organic–inorganic halide perovskite solar cells and tandem application," *Nano-Micro Letters*, vol. 15, no. 1, p. 70, 2023.

[239] M. Noman, M. Shahzaib, S. Jan, S. Shah, and A. Khan, "26.48% efficient and stable fapbi 3 perovskite solar cells employing srcu 2 o 2 as hole transport layer," *RSC advances*, vol. 13, no. 3, pp. 1892–1905, 2023.

[240] K. Wang, Z. Jin, L. Liang, H. Bian, D. Bai, H. Wang, J. Zhang, Q. Wang, and S. Liu, "All-inorganic cesium lead iodide perovskite solar cells with stabilized efficiency beyond 15%," *Nature communications*, vol. 9, no. 1, p. 4544, 2018.

[241] Y. Liu, B. Cai, H. Yang, G. Boschloo, and E. Johansson, "Solvent engineering of perovskite crystallization for high band gap fapbbr3 perovskite solar cells prepared in ambient condition," *ACS Applied Energy Materials*, vol. 6, no. 13, pp. 7102–7108, 2023.

[242] Z. Song, C. Chen, C. Li, R. Awni, D. Zhao, and Y. Yan, "Wide-bandgap, low-bandgap, and tandem perovskite solar cells," *Semiconductor Science and Technology*, vol. 34, no. 9, p. 093001, 2019.

[243] M. Ansari, A. Qurashi, and M. Nazeeruddin, "Frontiers, opportunities, and challenges in perovskite solar cells: A critical review," *Journal of Photochemistry and Photobiology C: Photochemistry Reviews*, vol. 35, pp. 1–24, 2018.

[244] T. Wu, Z. Qin, Y. Wang, Y. Wu, W. Chen, S. Zhang, M. Cai, S. Dai, J. Zhang, J. Liu, *et al.*, "The main progress of perovskite solar cells in 2020–2021," *Nano-Micro Letters*, vol. 13, pp. 1–18, 2021.

[245] F. Ma, Y. Zhao, Z. Qu, and J. You, "Developments of highly efficient perovskite solar cells," *Accounts of Materials Research*, vol. 4, no. 8, pp. 716–725, 2023.

[246] X. Jiang, Z. Zang, Y. Zhou, H. Li, Q. Wei, and Z. Ning, "Tin halide perovskite solar cells: an emerging thin-film photovoltaic technology," *Accounts of Materials Research*, vol. 2, no. 4, pp. 210–219, 2021.

[247] L. Qiu, L. Ono, and Y. Qi, "Advances and challenges to the commercialization of organic–inorganic halide perovskite solar cell technology," *Materials today energy*, vol. 7, pp. 169–189, 2018.

[248] P. Roy, N. Sinha, S. Tiwari, and A. Khare, "A review on perovskite solar cells: Evolution of architecture, fabrication techniques, commercialization issues and status," *Solar Energy*, vol. 198, pp. 665–688, 2020.

[249] G. Al-Dainy, S. Bourdo, V. Saini, B. Berry, and A. Biris, "Hybrid perovskite photovoltaic devices: properties, architecture, and fabrication methods," *Energy Technology*, vol. 5, no. 3, pp. 373–401, 2017.

[250] L. Chen and Z. Tseng, "Zno-based electron transporting layer for perovskite solar cells," *Nanostructured Solar Cells*, vol. 1, pp. 203–215, 2017.

[251] F. Zhang and K. Zhu, "Additive engineering for efficient and stable perovskite solar cells," *Advanced Energy Materials*, vol. 10, no. 13, p. 1902579, 2020.

[252] S. Liu, Y. Guan, Y. Sheng, Y. Hu, Y. Rong, A. Mei, and H. Han, "A review on additives for halide perovskite solar cells," *Advanced Energy Materials*, vol. 10, no. 13, p. 1902492, 2020.

[253] S. Abicho, B. Hailegnaw, G. Workneh, and T. Yohannes, "Role of additives and surface passivation on the performance of perovskite solar cells," *Materials for Renewable and Sustainable Energy*, vol. 11, no. 1, pp. 47–70, 2022.

[254] C. Pereyra, H. Xie, and M. Lira-Cantu, "Additive engineering for stable halide perovskite solar cells," *Journal of Energy Chemistry*, vol. 60, pp. 599–634, 2021.

[255] S. Habisreutinger, D. McMeekin, H. Snaith, and R. Nicholas, "Research update: Strategies for improving the stability of perovskite solar cells," *APL Materials*, vol. 4, no. 9, 2016.

[256] A. Mahapatra, S. Kumar, P. Kumar, and B. Pradhan, "Recent progress in perovskite solar cells: Challenges from efficiency to stability," *Materials Today Chemistry*, vol. 23, p. 100686, 2022.

[257] I. Hussain, H. Tran, J. Jaksik, J. Moore, N. Islam, and M. Uddin, "Functional materials, device architecture, and flexibility of perovskite solar cell," *Emergent Materials*, vol. 1, pp. 133–154, 2018.

[258] N. Sun, W. Gao, H. Dong, Y. Liu, X. Liu, Z. Wu, L. Song, C. Ran, and Y. Chen, "Architecture of pin sn-based perovskite solar cells: characteristics, advances, and perspectives," *ACS Energy Letters*, vol. 6, no. 8, pp. 2863–2875, 2021.

[259] S. Ma, G. Yuan, Y. Zhang, N. Yang, Y. Li, and Q. Chen, "Development of encapsulation strategies towards the commercialization of perovskite solar cells," *Energy & Environmental Science*, vol. 15, no. 1, pp. 13–55, 2022.

[260] J. Li, R. Xia, W. Qi, X. Zhou, J. Cheng, Y. Chen, G. Hou, Y. Ding, Y. Li, Y. Zhao, *et al.*, "Encapsulation of perovskite solar cells for enhanced stability: Structures, materials and characterization," *Journal of Power Sources*, vol. 485, p. 229313, 2021.

[261] L. Xiang, F. Gao, Y. Cao, D. Li, Q. Liu, H. Liu, and S. Li, "Progress on the stability and encapsulation techniques of perovskite solar cells," *Organic Electronics*, vol. 106, p. 106515, 2022.

[262] T. Chowdhury, M. Zafar, M. Islam, M. Shahinuzzaman, M. Islam, and M. Khandaker, "Stability of perovskite solar cells: issues and prospects," *RSC advances*, vol. 13, no. 3, pp. 1787–1810, 2023.

[263] L. Meng, J. You, and Y. Yang, "Addressing the stability issue of perovskite solar cells for commercial applications," *Nature communications*, vol. 9, no. 1, p. 5265, 2018.

[264] R. Azmi, S. Zhumagali, H. Bristow, S. Zhang, A. Yazmaciyan, A. Pininti, D. Utomo, A. Subbiah, and S. De Wolf, "Moisture-resilient perovskite solar cells for enhanced stability," *Advanced Materials*, p. 2211317, 2023.

[265] I. Holmes-Gentle, S. Tembhurne, C. Suter, and S. Haussener, "Kilowatt-scale solar hydrogen production system using a concentrated integrated photoelectrochemical device," *Nature Energy*, pp. 1–11, 2023.

[266] T. Dittrich, "Basic characteristics and characterization of solar cells," *Materials Concepts for Solar Cells*, pp. 3–43, 2018.

[267] J. Dhilipan, N. Vijayalakshmi, D. Shanmugam, R. J. Ganesh, S. Kodeeswaran, and S. Muralidharan, "Performance and efficiency of different types of solar cell material–a review," *Materials Today: Proceedings*, vol. 66, pp. 1295–1302, 2022.

[268] K. Hasan, S. Yousuf, M. Tushar, B. Das, P. Das, and M. Islam, "Effects of different environmental and operational factors on the pv performance: A comprehensive review," *Energy Science & Engineering*, vol. 10, no. 2, pp. 656–675, 2022.

[269] Z. Ling, Z. Zhang, G. Shi, X. Fang, L. Wang, X. Gao, Y. Fang, T. Xu, S. Wang, and X. Liu, "Review on thermal management systems using phase change materials for electronic components, li-ion batteries and photovoltaic modules," *Renewable and Sustainable Energy Reviews*, vol. 31, pp. 427–438, 2014.

[270] A. Allouhi, S. Rehman, M. Buker, and Z. Said, "Up-to-date literature review on solar pv systems: Technology progress, market status and r&d," *Journal of Cleaner Production*, vol. 362, p. 132339, 2022.

[271] A. Maka and J. Alabid, "Solar energy technology and its roles in sustainable development," *Clean Energy*, vol. 6, no. 3, pp. 476–483, 2022.

[272] L. Zhang, L. Mei, K. Wang, Y. Lv, S. Zhang, Y. Lian, X. Liu, Z. Ma, G. Xiao, Q. Liu, *et al.*, "Advances in the application of perovskite materials," *Nano-Micro Letters*, vol. 15, no. 1, p. 177, 2023.

[273] J. Liu, H. He, D. Xiao, S. Yin, W. Ji, S. Jiang, D. Luo, B. Wang, and Y. Liu, "Recent advances of plasmonic nanoparticles and their applications," *Materials*, vol. 11, no. 10, p. 1833, 2018.

[274] R. Singh and P. Sarswat, "From fundamentals to applications: The development of magnetoplasmonics for next-generation technologies," *Materials Today Electronics*, vol. 4, p. 100033, 2023.

[275] M. Himel, B. Sikder, T. Ahmed, and S. Choudhury, "Biomimicry in nanotechnology: a comprehensive review," *Nanoscale Advances*, 2023.

[276] M. Rahman, K. Islam, T. Dip, M. Chowdhury, S. Debnath, S. Hasan, M. Sakib, T. Saha, R. Padhye, and S. Houshyar, "A review on nanomaterial-based additive manufacturing: Dynamics in properties, prospects, and challenges," *Progress in Additive Manufacturing*, pp. 1–28, 2023.

[277] D. Furkan and M. Mehmet Emin, "Critical factors that affecting efficiency of solar cells," *smart grid and renewable energy*, vol. 2010, 2010.

[278] W. Ma, J. Tumbleston, L. Ye, C. Wang, J. Hou, and H. Ade, "Quantification of nano-and mesoscale phase separation and relation to donor and acceptor quantum efficiency, jsc, and ff in polymer: fullerene solar cells," *Advanced Materials*, vol. 26, no. 25, pp. 4234–4241, 2014.

[279] W. Tress, M. Yavari, K. Domanski, P. Yadav, B. Niesen, J. Baena, A. Hagfeldt, and M. Graetzel, "Interpretation and evolution of open-circuit voltage, recombination, ideality factor and subgap defect states during reversible light-soaking and irreversible degradation of perovskite solar cells," *Energy & Environmental Science*, vol. 11, no. 1, pp. 151–165, 2018.

[280] R. Hosen, S. Sikder, M. Uddin, M. Haque, H. Mamur, and M. Bhuiyan, "Effect of various layers on improving the photovoltaic efficiency of al/zno/cds/cdte/cu2o/ni solar cells," *Journal of Alloys and Metallurgical Systems*, vol. 4, p. 100041, 2023.

[281] Y. Cui, L. Hong, and J. Hou, "Organic photovoltaic cells for indoor applications: opportunities and challenges," *ACS applied materials & interfaces*, vol. 12, no. 35, pp. 38815–38828, 2020.

[282] G. Bernardo, T. Lopes, D. Lidzey, and A. Mendes, "Progress in upscaling organic photovoltaic devices," *Advanced Energy Materials*, vol. 11, no. 23, p. 2100342, 2021.

[283] Y. Wang, J. Luke, A. Privitera, N. Rolland, C. Labanti, G. Londi, V. Lemaur, D. Toolan, A. Sneyd, S. Jeong, *et al.*, "The critical role of the donor polymer in the stability of high-performance non-fullerene acceptor organic solar cells," *Joule*, vol. 7, no. 4, pp. 810–829, 2023.

[284] Q. Liao, Q. Kang, Y. Yang, Z. Zheng, J. Qin, B. Xu, and J. Hou, "Highly stable organic solar cells based on an ultraviolet-resistant cathode interfacial layer," *CCS Chemistry*, vol. 4, no. 3, pp. 938–948, 2022.

[285] H. Tang, Y. Bai, H. Zhao, X. Qin, Z. Hu, C. Zhou, F. Huang, and Y. Cao, "Interface engineering for highly efficient organic solar cells," *Advanced Materials*, p. 2212236, 2023.

[286] P. Cheng and Y. Yang, "Narrowing the band gap: The key to high-performance organic photovoltaics," *Accounts of chemical research*, vol. 53, no. 6, pp. 1218–1228, 2020.

[287] P. Murugan, T. Hu, X. Hu, and Y. Chen, "Advancements in organic small molecule hole-transporting materials for perovskite solar cells: past and future," *Journal of Materials Chemistry A*, vol. 10, no. 10, pp. 5044–5081, 2022.

[288] S. Arya and P. Mahajan, "Organic solar cells," in *Solar Cells: Types and Applications*, pp. 101–130, Springer, 2023.

[289] A. Armin, G. Juska, M. Ullah, M. Velusamy, P. Burn, P. Meredith, and A. Pivrikas, "Balanced carrier mobilities: not a necessary condition for high-efficiency thin organic solar cells as determined by mis-celiv," *Advanced Energy Materials*, vol. 4, no. 4, p. 1300954, 2014.

[290] S. Foster, F. Deledalle, A. Mitani, T. Kimura, K. Kim, T. Okachi, T. Kirchartz, J. Oguma, K. Miyake, J. Durrant, *et al.*, "Electron collection as a limit to polymer: Pcbm solar cell efficiency: Effect of blend microstructure on carrier mobility and device performance in ptb7: Pcbm," *Advanced energy materials*, vol. 4, no. 14, p. 1400311, 2014.

[291] C. Proctor, M. Kuik, and T. Nguyen, "Charge carrier recombination in organic solar cells," *Progress in Polymer Science*, vol. 38, no. 12, pp. 1941–1960, 2013.

[292] X. Kong, T. He, H. Qiu, L. Zhan, and S. Yin, "Progress in organic photovoltaics based on green solvents: from solubility enhancement to morphology optimization," *Chemical Communications*, vol. 59, no. 81, pp. 12051–12064, 2023.

[293] F. Zhao, C. Wang, and X. Zhan, "Morphology control in organic solar cells," *Advanced Energy Materials*, vol. 8, no. 28, p. 1703147, 2018.

[294] G. Cai, Z. Chen, X. Xia, Y. Li, J. Wang, H. Liu, P. Sun, C. Li, R. Ma, Y. Zhou, *et al.*, "Pushing the efficiency of high open-circuit voltage binary organic solar cells by vertical morphology tuning," *Advanced Science*, vol. 9, no. 14, p. 2200578, 2022.

[295] H. Cha and J. Wu, "Understanding what determines the organic solar cell stability," *Joule*, vol. 5, no. 6, pp. 1322–1325, 2021.

[296] Y. Sun, L. Nian, Y. Kan, Y. Ren, Z. Chen, L. Zhu, M. Zhang, H. Yin, H. Xu, J. Li, *et al.*, "Rational control of sequential morphology evolution and vertical distribution toward 17.18% efficiency all-small-molecule organic solar cells," *Joule*, vol. 6, no. 12, pp. 2835–2848, 2022.

[297] R. Noriega, J. Rivnay, K. Vandewal, F. Koch, N. Stingelin, P. Smith, M. Toney, and A. Salleo, "A general relationship between disorder, aggregation and charge transport in conjugated polymers," *Nature materials*, vol. 12, no. 11, pp. 1038–1044, 2013.

[298] A. Levitsky, S. Schneider, E. Rabkin, M. Toney, and G. Frey, "Bridging the thermodynamics and kinetics of temperature-induced morphology evolution in polymer/fullerene organic solar cell bulk heterojunction," *Materials Horizons*, vol. 8, no. 4, pp. 1272–1285, 2021.

[299] Z. Peng, N. Stingelin, H. Ade, and J. Michels, "A materials physics perspective on structure–processing–function relations in blends of organic semiconductors," *Nature Reviews Materials*, vol. 8, no. 7, pp. 439–455, 2023.

[300] S. Yoon, E. Shin, N. Cho, S. Park, H. Woo, and H. Son, "Progress in morphology control from fullerene to nonfullerene acceptors for scalable high-performance organic photovoltaics," *Journal of Materials Chemistry A*, vol. 9, no. 44, pp. 24729–24758, 2021.

[301] B. Li, X. Yang, S. Li, and J. Yuan, "Stable block copolymer single-material organic solar cells: progress and perspective," *Energy & Environmental Science*, 2023.

[302] K. Yao, Y. Xu, F. Li, X. Wang, and L. Zhou, "A simple and universal method to increase light absorption in ternary blend polymer solar cells based on ladder-type polymers," *Advanced Optical Materials*, vol. 3, no. 3, pp. 321–327, 2015.

[303] H. Lee, C. Park, D. Sin, J. Park, and K. Cho, "Recent advances in morphology optimization for organic photovoltaics," *Advanced Materials*, vol. 30, no. 34, p. 1800453, 2018.

[304] T. Wang, A. Pearson, A. Dunbar, P. Staniec, D. Watters, H. Yi, A. Ryan, R. Jones, A. Iraqi, and D. Lidzey, "Correlating structure with function in thermally annealed pcdtbt: Pc70bm photovoltaic blends," *Advanced Functional Materials*, vol. 22, no. 7, pp. 1399–1408, 2012.

[305] K. An, W. Zhong, L. Ying, P. Zhu, B. Fan, Z. Li, N. Li, F. Huang, and Y. Cao, "Optimization of processing solvent and film morphology to achieve efficient non-fullerene polymer solar cells processed in air," *Journal of Materials Chemistry C*, vol. 8, no. 1, pp. 270–275, 2020.

[306] G. Jo, S. Cho, H. Kim, H. Yoon, S. Han, and M. Chang, "Impacts of secondary solvents on morphology and charge transport of conjugated polymer thin films," *Organic Electronics*, vol. 81, p. 105688, 2020.

[307] Y. Gong, J. Zhang, B. Du, M. Wang, W. Lai, and W. Huang, "Design, synthesis, and postvapor treatment of neutral fulleropyrrolidine electron-collecting interlayers for high-efficiency inverted polymer solar cells," *ACS Applied Electronic Materials*, vol. 1, no. 6, pp. 854–861, 2019.

[308] X. Xu, Y. Li, and Q. Peng, "Ternary blend organic solar cells: understanding the morphology from recent progress," *Advanced Materials*, vol. 34, no. 46, p. 2107476, 2022.

[309] C. Tan and B. Wong, "Unraveling the mystery of ternary organic solar cells: a review on the influence of third component on structure–morphology–performance relationships," *Solar RRL*, vol. 5, no. 11, p. 2100503, 2021.

[310] L. Lu, M. Kelly, W. You, and L. Yu, "Status and prospects for ternary organic photovoltaics," *Nature Photonics*, vol. 9, no. 8, pp. 491–500, 2015.

[311] R. Yu, H. Yao, and J. Hou, "Recent progress in ternary organic solar cells based on nonfullerene acceptors," *Advanced Energy Materials*, vol. 8, no. 28, p. 1702814, 2018.

[312] T. Ameri, P. Khoram, J. Min, and C. Brabec, "Organic ternary solar cells: a review," *Advanced Materials*, vol. 25, no. 31, pp. 4245–4266, 2013.

[313] G. Zhang, K. Zhang, Q. Yin, X. Jiang, Z. Wang, J. Xin, W. Ma, H. Yan, F. Huang, and Y. Cao, "High-performance ternary organic solar cell enabled by a thick active layer containing a liquid crystalline small molecule donor," *Journal of the American Chemical Society*, vol. 139, no. 6, pp. 2387–2395, 2017.

[314] A. de Zerio and C. Müller, "Glass forming acceptor alloys for highly efficient and thermally stable ternary organic solar cells," *Advanced Energy Materials*, vol. 8, no. 28, p. 1702741, 2018.

[315] W. Zhao, S. Li, S. Zhang, X. Liu, and J. Hou, "Ternary polymer solar cells based on two acceptors and one donor for achieving 12.2% efficiency.," *Advanced Materials (Deerfield Beach, Fla.)*, vol. 29, no. 2, 2016.

[316] H. Benten, T. Nishida, D. Mori, H. Xu, H. Ohkita, and S. Ito, "High-performance ternary blend all-polymer solar cells with complementary absorption bands from visible to near-infrared wavelengths," *Energy & Environmental Science*, vol. 9, no. 1, pp. 135–140, 2016.

[317] T. Liu, Y. Guo, Y. Yi, L. Huo, X. Xue, X. Sun, H. Fu, W. Xiong, D. Meng, Z. Wang, *et al.*, "Ternary organic solar cells based on two compatible nonfullerene acceptors with power conversion efficiency > 10%," *Advanced Materials*, vol. 28, no. 45, pp. 10008–10015, 2016.

[318] Z. Xiao, X. Jia, L. Ding, *et al.*, "Ternary organic solar cells offer 14% power conversion efficiency," *Sci. Bull*, vol. 62, no. 23, pp. 1562–1564, 2017.

[319] Y. Su, S. Lan, and K. Wei, "Organic photovoltaics," *Materials Today*, vol. 15, no. 12, pp. 554–562, 2012.

[320] J. Zhang, W. Xu, P. Sheng, G. Zhao, and D. Zhu, "Organic donor–acceptor complexes as novel organic semiconductors," *Accounts of Chemical Research*, vol. 50, no. 7, pp. 1654–1662, 2017.

[321] M. Adnan, Z. Irshad, R. Hussain, W. Lee, M. Kim, and J. Lim, "Efficient ternary active layer materials for organic photovoltaics," *Solar Energy*, vol. 257, pp. 324–343, 2023.

[322] Y. Ma, Y. Zhang, and H. Zhang, "Solid additives in organic solar cells: progress and perspectives," *Journal of Materials Chemistry C*, vol. 10, no. 7, pp. 2364–2374, 2022.

[323] O. Alqahtani, J. Lv, T. Xu, V. Murcia, T. Ferron, T. McAfee, D. Grabner, T. Duan, and B. Collins, "High sensitivity of non-fullerene organic solar cells morphology and performance to a processing additive," *Small*, vol. 18, no. 23, p. 2202411, 2022.

[324] Q. Liang, W. Li, H. Lu, Z. Yu, X. Zhang, Q. Dong, C. Song, Z. Miao, and J. Liu, "Recent advances of solid additives used in organic solar cells: toward efficient and stable solar cells," *ACS Applied Energy Materials*, vol. 6, no. 1, pp. 31–50, 2022.

[325] Y. Jiang and Z. Li, "The effect of additives on the morphology of organic solar cells: A brief review," *Synthetic Metals*, p. 117480, 2023.

[326] A. Sharenko, D. Gehrig, F. Laquai, and T. Nguyen, "The effect of solvent additive on the charge generation and photovoltaic performance of a solution-processed small molecule: perylene diimide bulk heterojunction solar cell," *Chemistry of Materials*, vol. 26, no. 14, pp. 4109–4118, 2014.

[327] G. Mola, A. Ahmed, J. Ike, M. Liu, M. Hamed, and Y. Zhang, "Engineering nonfullerene acceptors as a mechanism to control film morphology and energy loss in organic solar cells," *Energy & Fuels*, vol. 36, no. 9, pp. 4691–4707, 2022.

[328] N. Gasparini, A. Salleo, I. McCulloch, and D. Baran, "The role of the third component in ternary organic solar cells," *Nature Reviews Materials*, vol. 4, no. 4, pp. 229–242, 2019.

[329] Y. Zhang and G. Li, "Functional third components in nonfullerene acceptor-based ternary organic solar cells," *Accounts of Materials Research*, vol. 1, no. 2, pp. 158–171, 2020.

[330] R. Hildner, A. Köhler, P. Müller-Buschbaum, F. Panzer, and M. Thelakkat, "π-conjugated donor polymers: Structure formation and morphology in solution, bulk and photovoltaic blends," *Advanced energy materials*, vol. 7, no. 16, p. 1700314, 2017.

[331] J. Peet, A. Heeger, and G. Bazan, ""plastic" solar cells: self-assembly of bulk heterojunction nanomaterials by spontaneous phase separation," *Accounts of Chemical Research*, vol. 42, no. 11, pp. 1700–1708, 2009.

[332] J. Slota, X. He, and W. Huck, "Controlling nanoscale morphology in polymer photovoltaic devices," *Nano Today*, vol. 5, no. 3, pp. 231–242, 2010.

[333] S. Collins, N. Ran, M. Heiber, and T. Nguyen, "Small is powerful: recent progress in solution-processed small molecule solar cells," *Advanced Energy Materials*, vol. 7, no. 10, p. 1602242, 2017.

[334] M. Ren, G. Zhang, Z. Chen, J. Xiao, X. Jiao, Y. Zou, H. Yip, and Y. Cao, "High-performance ternary organic solar cells with controllable morphology via sequential layer-by-layer deposition," *ACS applied materials & interfaces*, vol. 12, no. 11, pp. 13077–13086, 2020.

[335] L. Zhan, S. Li, H. Zhang, F. Gao, T. Lau, X. Lu, D. Sun, P. Wang, M. Shi, C. Li, *et al.*, "A near-infrared photoactive morphology modifier leads to significant current improvement and energy loss mitigation for ternary organic solar cells," *Advanced Science*, vol. 5, no. 8, p. 1800755, 2018.

[336] X. Ma, J. Wang, Q. An, J. Gao, Z. Hu, C. Xu, X. Zhang, Z. Liu, and F. Zhang, "Highly efficient quaternary organic photovoltaics by optimizing photogenerated exciton distribution and active layer morphology," *Nano Energy*, vol. 70, p. 104496, 2020.

[337] V. Moorthy and V. Srivastava, "Device modeling of organic photovoltaic cells with traditional and inverted cells using s-swcnt: C60 as active layer," *Nanomaterials*, vol. 12, no. 16, p. 2844, 2022.

[338] H. Zhang, Y. Li, X. Zhang, Y. Zhang, and H. Zhou, "Role of interface properties in organic solar cells: from substrate engineering to bulk-heterojunction interfacial morphology," *Materials Chemistry Frontiers*, vol. 4, no. 10, pp. 2863–2880, 2020.

[339] C. McDowell, M. Abdelsamie, M. Toney, and G. Bazan, "Solvent additives: key morphology-directing agents for solution-processed organic solar cells," *Advanced Materials*, vol. 30, no. 33, p. 1707114, 2018.

[340] M. Sajjad, A. Ruseckas, and I. Samuel, "Enhancing exciton diffusion length provides new opportunities for organic photovoltaics," *Matter*, vol. 3, no. 2, pp. 341–354, 2020.

[341] J. Gorenflot, A. Paulke, F. Piersimoni, J. Wolf, Z. Kan, F. Cruciani, A. Labban, D. Neher, P. Beaujuge, and F. Laquai, "From recombination dynamics to device performance: Quantifying the efficiency of exciton dissociation, charge separation, and extraction in bulk heterojunction solar cells with fluorine-substituted polymer donors," *Advanced Energy Materials*, vol. 8, no. 4, p. 1701678, 2018.

[342] X. Cao, L. Xie, X. Zhu, J. Lv, and H. Fan, "The principles of selecting green solvent additives for optimizing the phase separation structure of polymer solar cells based on ptb7: Pc71bm," *European Polymer Journal*, vol. 180, p. 111603, 2022.

[343] S. Kwon, H. Kang, J. Lee, J. Lee, S. Hong, H. Kim, and K. Lee, "Effect of processing additives on organic photovoltaics: recent progress and future prospects," *Advanced Energy Materials*, vol. 7, no. 10, p. 1601496, 2017.

[344] L. Liu, J. Chen, Y. Meng, C. Jin, F. Yi, C. Xu, and M. Xiao, "Two non-halogen additives significantly improve the efficiency of ptb7-th: Pc71bm-based polymer solar cells in non-halogen solvent," *Organic Electronics*, vol. 113, p. 106722, 2023.

[345] C. Sprau, J. Kattenbusch, Y. Li, E. Müller, D. Gerthsen, R. Berger, J. Michels, and A. Colsmann, "Revisiting solvent additives for the fabrication of polymer: fullerene solar cells: exploring a series of benzaldehydes," *Solar RRL*, vol. 5, no. 9, p. 2100238, 2021.

[346] L. Richter, D. DeLongchamp, and A. Amassian, "Morphology development in solution-processed functional organic blend films: an in situ viewpoint," *Chemical Reviews*, vol. 117, no. 9, pp. 6332–6366, 2017.

[347] D. Burke and D. Lipomi, "Green chemistry for organic solar cells," *Energy & Environmental Science*, vol. 6, no. 7, pp. 2053–2066, 2013.

[348] Y. Huang and C. Luscombe, "Towards green synthesis and processing of organic solar cells," *The Chemical Record*, vol. 19, no. 6, pp. 1039–1049, 2019.

[349] C. Clarke, W. Tu, O. Levers, A. Brohl, and J. Hallett, "Green and sustainable solvents in chemical processes," *Chemical reviews*, vol. 118, no. 2, pp. 747–800, 2018.

[350] Q. Bai, H. Sun, X. Guo, and L. Niu, "Advances in green-solvent-processable all-polymer solar cells," *Chinese Journal of Polymer Science*, vol. 40, no. 8, pp. 846–860, 2022.

[351] A. Sharma, S. Masoumi, D. Gedefaw, S. O'Shaughnessy, D. Baran, and A. Pakdel, "Flexible solar and thermal energy conversion devices: Organic photovoltaics (opvs), organic thermoelectric generators (otegs) and hybrid pv-teg systems," *Applied Materials Today*, vol. 29, p. 101614, 2022.

[352] Y. Zhang, Y. Lang, and G. Li, "Recent advances of non-fullerene organic solar cells: From materials and morphology to devices and applications," *Ecomat*, vol. 5, no. 1, p. e12281, 2023.

[353] K. Weng, L. Ye, L. Zhu, J. Xu, J. Zhou, X. Feng, G. Lu, S. Tan, F. Liu, and Y. Sun, "Optimized active layer morphology toward efficient and polymer batch insensitive organic solar cells," *Nature communications*, vol. 11, no. 1, p. 2855, 2020.

[354] G. Ding, T. Chen, M. Wang, X. Xia, C. He, X. Zheng, Y. Li, D. Zhou, X. Lu, L. Zuo, *et al.*, "Solid additive-assisted layer-by-layer processing for 19% efficiency binary organic solar cells," *Nano-Micro Letters*, vol. 15, no. 1, p. 92, 2023.

[355] K. Ueno, T. Oshikiri, Q. Sun, X. Shi, and H. Misawa, "Solid-state plasmonic solar cells," *Chemical reviews*, vol. 118, no. 6, pp. 2955–2993, 2017.

[356] P. Cheng, D. Wang, and P. Schaaf, "A review on photothermal conversion of solar energy with nanomaterials and nanostructures: From fundamentals to applications," *Advanced Sustainable Systems*, vol. 6, no. 9, p. 2200115, 2022.

[357] N. Zhou, V. López-Puente, Q. Wang, L. Polavarapu, I. Pastoriza-Santos, and Q. Xu, "Plasmon-enhanced light harvesting: applications in enhanced photocatalysis, photodynamic therapy and photovoltaics," *Rsc Advances*, vol. 5, no. 37, pp. 29076–29097, 2015.

[358] D. Shin, G. Kang, P. Gupta, S. Behera, H. Lee, A. Urbas, W. Park, and K. Kim, "Thermoplasmonic and photothermal metamaterials for solar energy applications," *Advanced Optical Materials*, vol. 6, no. 18, p. 1800317, 2018.

[359] I. Maksymov, "Magneto-plasmonic nanoantennas: Basics and applications," *Reviews in Physics*, vol. 1, pp. 36–51, 2016.

[360] Q. Gan, F. Bartoli, and Z. Kafifi, "Plasmonic nanostructures improve solar cell performance," *SPIE Newsroom*, vol. 29, 2013.

[361] H. Atwater and A. Polman, "Plasmonics for improved photovoltaic devices," *Nature Materials*, vol. 9, no. 3, pp. 205–213, 2010.

[362] B. Jia, X. Chen, J. Saha, Q. Qiao, Y. Wang, Z. Shi, and M. Gu, "Concept to devices: from plasmonic light trapping to upscaled plasmonic solar modules," *Photonics Research*, vol. 1, no. 1, pp. 22–27, 2013.

[363] T. Zhang, S. Iqbal, X. Zhang, W. Wu, D. Su, and H. Zhou, "Recent advances in highly efficient organic-silicon hybrid solar cells," *Solar Energy Materials and Solar Cells*, vol. 204, p. 110245, 2020.

[364] X. Cui, Q. Ruan, X. Zhuo, X. Xia, J. Hu, R. Fu, Y. Li, J. Wang, and H. Xu, "Photothermal nanomaterials: A powerful light-to-heat converter," *Chemical Reviews*, vol. 123, no. 11, pp. 6891–6952, 2023.

[365] V. Kravets, A. Kabashin, W. Barnes, and A. Grigorenko, "Plasmonic surface lattice resonances: a review of properties and applications," *Chemical reviews*, vol. 118, no. 12, pp. 5912–5951, 2018.

[366] A. Utyushev, V. Zakomirnyi, and I. Rasskazov, "Collective lattice resonances: Plasmonics and beyond," *Reviews in Physics*, vol. 6, p. 100051, 2021.

[367] I. Khan, K. Saeed, and I. Khan, "Nanoparticles: Properties, applications and toxicities," *Arabian journal of chemistry*, vol. 12, no. 7, pp. 908–931, 2019.

[368] A. Kesavan, A. Rao, and P. Ramamurthy, "Tailoring optoelectronic properties of ch3nh3pbi3 perovskite photovoltaics using al nanoparticle modified pc61bm layer," *Solar Energy*, vol. 201, pp. 621–627, 2020.

[369] S. Lv, Y. Du, F. Wu, Y. Cai, and T. Zhou, "Review on lspr assisted photocatalysis: effects of physical fields and opportunities in multifield decoupling," *Nanoscale Advances*, vol. 4, no. 12, pp. 2608–2631, 2022.

[370] N. Chander, A. Khan, E. Thouti, S. Sardana, P. Chandrasekhar, V. Dutta, and V. Komarala, "Size and concentration effects of gold nanoparticles on optical and electrical properties of plasmonic dye sensitized solar cells," *Solar Energy*, vol. 109, pp. 11–23, 2014.

[371] U. Mahajan, M. Dhonde, K. Sahu, P. Ghosh, and P. Shirage, "Titanium nitride (tin) as a promising alternative to plasmonic metals: a comprehensive review of synthesis and applications," *Materials Advances*, 2024.

[372] S. Gimondi, H. Ferreira, R. Reis, and N. Neves, "Microfluidic devices: a tool for nanoparticle synthesis and performance evaluation," *ACS nano*, vol. 17, no. 15, pp. 14205–14228, 2023.

[373] N. Maccaferri, "Coupling phenomena and collective effects in resonant meta-atoms supporting both plasmonic and (opto-) magnetic functionalities: an overview on properties and applications," *JOSA B*, vol. 36, no. 7, pp. E112–E131, 2019.

[374] Y. Jin, L. Zhou, J. Liang, and J. Zhu, "Electrochemically driven dynamic plasmonics," *Advanced Photonics*, vol. 3, no. 4, pp. 044002–044002, 2021.

[375] V. Juvé, M. Cardinal, A. Lombardi, A. Crut, P. Maioli, J. Pérez-Juste, L. Liz-Marzán, N. Del Fatti, and F. Vallée, "Size-dependent surface plasmon resonance broadening in nonspherical nanoparticles: single gold nanorods," *Nano letters*, vol. 13, no. 5, pp. 2234–2240, 2013.

[376] I. Krishchenko, É. Manoilov, S. Kravchenko, and B. Snopok, "Resonant optical phenomena in heterogeneous plasmon nanostructures of noble metals: a review," *Theoretical and Experimental Chemistry*, vol. 56, pp. 67–110, 2020.

[377] J. Boken, P. Khurana, S. Thatai, D. Kumar, and S. Prasad, "Plasmonic nanoparticles and their analytical applications: A review," *Applied Spectroscopy Reviews*, vol. 52, no. 9, pp. 774–820, 2017.

[378] N. Halas, S. Lal, W. Chang, S. Link, and P. Nordlander, "Plasmons in strongly coupled metallic nanostructures," *Chemical reviews*, vol. 111, no. 6, pp. 3913–3961, 2011.

[379] J. Jana, M. Ganguly, and T. Pal, "Enlightening surface plasmon resonance effect of metal nanoparticles for practical spectroscopic application," *RSC advances*, vol. 6, no. 89, pp. 86174–86211, 2016.

[380] V. Amendola, R. Pilot, M. Frasconi, O. Maragò, and M. Iatì, "Surface plasmon resonance in gold nanoparticles: a review," *Journal of Physics: Condensed Matter*, vol. 29, no. 20, p. 203002, 2017.

[381] S. Peng, J. McMahon, G. Schatz, S. Gray, and Y. Sun, "Reversing the size-dependence of surface plasmon resonances," *Proceedings of the National Academy of Sciences*, vol. 107, no. 33, pp. 14530–14534, 2010.

[382] J. Garcia-Peiro, J. Bonet-Aleta, C. Bueno-Alejo, and J. Hueso, "Recent advances in the design and photocatalytic enhanced performance of gold plasmonic nanostructures decorated with non-titania based semiconductor hetero-nanoarchitectures," *Catalysts*, vol. 10, no. 12, p. 1459, 2020.

[383] Y. Cai, Y. Choi, and C. Kagan, "Chemical and physical properties of photonic noble-metal nanomaterials," *Advanced Materials*, vol. 35, no. 34, p. 2108104, 2023.

[384] P. Khan, G. Brennan, J. Lillis, S. Tofail, N. Liu, and C. Silien, "Characterisation and manipulation of polarisation response in plasmonic and magneto-plasmonic nanostructures and metamaterials," *Symmetry*, vol. 12, no. 8, p. 1365, 2020.

[385] D. Gómez, K. Vernon, and T. Davis, "Symmetry effects on the optical coupling between plasmonic nanoparticles with applications to hierarchical structures," *Physical Review B*, vol. 81, no. 7, p. 075414, 2010.

[386] C. Downing and G. Weick, "Plasmonic modes in cylindrical nanoparticles and dimers," *Proceedings of the Royal Society A*, vol. 476, no. 2244, p. 20200530, 2020.

[387] M. Sonntag, J. Klingsporn, A. Zrimsek, B. Sharma, L. Ruvuna, and R. Van Duyne, "Molecular plasmonics for nanoscale spectroscopy," *Chemical Society Reviews*, vol. 43, no. 4, pp. 1230–1247, 2014.

[388] J. Pang, L. Tao, X. Lu, Q. Yang, V. Pachauri, Z. Wang, S. Ingebrandt, and X. Chen, "Photothermal effects induced by surface plasmon resonance at graphene/gold nanointerfaces: A multiscale modeling study," *Biosensors and Bioelectronics*, vol. 126, pp. 470–477, 2019.

[389] S. Gwo, H. Chen, M. Lin, L. Sun, and X. Li, "Nanomanipulation and controlled self-assembly of metal nanoparticles and nanocrystals for plasmonics," *Chemical Society Reviews*, vol. 45, no. 20, pp. 5672–5716, 2016.

[390] J. Zheng, X. Cheng, H. Zhang, X. Bai, R. Ai, L. Shao, and J. Wang, "Gold nanorods: the most versatile plasmonic nanoparticles," *Chemical Reviews*, vol. 121, no. 21, pp. 13342–13453, 2021.

[391] J. Edel, A. Kornyshev, A. Kucernak, and M. Urbakh, "Fundamentals and applications of self-assembled plasmonic nanoparticles at interfaces," *Chemical Society Reviews*, vol. 45, no. 6, pp. 1581–1596, 2016.

[392] M. Hossain, J. Park, D. Yoo, Y. Baek, Y. Kim, S. Kim, and D. Lee, "Surface plasmonic effects on dye-sensitized solar cells by sio2-encapsulated ag nanoparticles," *Current Applied Physics*, vol. 16, no. 3, pp. 397–403, 2016.

[393] P. Subramanyam, B. Meena, V. Biju, H. Misawa, and S. Challapalli, "Emerging materials for plasmon-assisted photoelectrochemical water splitting," *Journal of Photochemistry and Photobiology C: Photochemistry Reviews*, vol. 51, p. 100472, 2022.

[394] H. Duan, T. Wang, Z. Su, H. Pang, and C. Chen, "Recent progress and challenges in plasmonic nanomaterials," *Nanotechnology Reviews*, vol. 11, no. 1, pp. 846–873, 2022.

[395] G. Singh and S. Verma, "Plasmon enhanced light trapping in thin film gaas solar cells by al nanoparticle array," *Physics letters A*, vol. 383, no. 13, pp. 1526–1530, 2019.

[396] S. Morawiec, J. Holovskỳ, M. Mendes, M. Müller, K. Ganzerová, A. Vetushka, M. Ledinskỳ, F. Priolo, A. Fejfar, and I. Crupi, "Experimental quantification of useful and parasitic absorption of light in plasmon-enhanced thin silicon films for solar cells application," *Scientific reports*, vol. 6, no. 1, p. 22481, 2016.

[397] X. Yang, C. Chueh, C. Li, H. Yip, P. Yin, H. Chen, W. Chen, and A. Jen, "High-efficiency polymer solar cells achieved by doping plasmonic metallic nanoparticles into dual charge selecting interfacial layers to enhance light trapping," *Advanced Energy Materials*, vol. 3, no. 5, pp. 666–673, 2013.

[398] F. Xiu, H. Lin, M. Fang, G. Dong, S. Yip, and J. Ho, "Fabrication and enhanced light-trapping properties of three-dimensional silicon nanostructures for photovoltaic applications," *Pure and Applied Chemistry*, vol. 86, no. 5, pp. 557–573, 2014.

[399] D. Samajdar *et al.*, "Light-trapping strategy for pedot: Pss/c-si nanopyramid based hybrid solar cells embedded with metallic nanoparticles," *Solar Energy*, vol. 190, pp. 278–285, 2019.

[400] M. Olaimat, L. Yousefi, and O. Ramahi, "Using plasmonics and nanoparticles to enhance the efficiency of solar cells: review of latest technologies," *JOSA B*, vol. 38, no. 2, pp. 638–651, 2021.

[401] Z. Li, Y. Wenas, L. Fu, S. Mokkapati, H. Tan, and C. Jagadish, "Influence of electrical design on core–shell gaas nanowire array solar cells," *IEEE Journal of Photovoltaics*, vol. 5, no. 3, pp. 854–864, 2015.

[402] B. Yang, C. Li, Z. Wang, and Q. Dai, "Thermoplasmonics in solar energy conversion: materials, nanostructured designs, and applications," *Advanced Materials*, vol. 34, no. 26, p. 2107351, 2022.

[403] G. Luo, X. Ren, S. Zhang, H. Wu, W. Choy, Z. He, and Y. Cao, "Recent advances in organic photovoltaics: device structure and optical engineering optimization on the nanoscale," *Small*, vol. 12, no. 12, pp. 1547–1571, 2016.

[404] K. Gandhi, *Enhancement of light coupling to solar cells using plasmonic structures*. University of Surrey (United Kingdom), 2015.

[405] S. Balci, O. Balci, N. Kakenov, F. Atar, and C. Kocabas, "Dynamic tuning of plasmon resonance in the visible using graphene," *Optics letters*, vol. 41, no. 6, pp. 1241–1244, 2016.

[406] Y. Zhao, S. Gan, G. Zhang, and X. Dai, "High sensitivity refractive index sensor based on surface plasmon resonance with topological insulator," *Results in Physics*, vol. 14, p. 102477, 2019.

[407] H. Yu, Y. Peng, Y. Yang, and Z. Li, "Plasmon-enhanced light–matter interactions and applications," *npj Computational Materials*, vol. 5, no. 1, p. 45, 2019.

[408] X. Li, P. Li, Z. Wu, D. Luo, H. Yu, and Z. Lu, "Review and perspective of materials for flexible solar cells," *Materials Reports: Energy*, vol. 1, no. 1, p. 100001, 2021.

[409] M. Zhang, D. Xin, X. Zheng, Q. Chen, and W. Zhang, "Toward greener solution processing of perovskite solar cells," *ACS Sustainable Chemistry & Engineering*, vol. 8, no. 35, pp. 13126–13138, 2020.

[410] D. Zhao, M. Yu, L. Zheng, M. Li, S. Dai, D. Chen, T. Lee, and D. Yun, "Enhanced efficiency and stability of planar perovskite solar cells using a dual electron transport layer of gold nanoparticles embedded in anatase tio2 films," *ACS applied energy materials*, vol. 3, no. 10, pp. 9568–9575, 2020.

[411] F. Sayed, H. Elsayed, M. Al-Dossari, M. Eissa, A. Mehaney, and A. Aly, "Angular surface plasmon resonance-based sensor with a silver nanocomposite layer for effective water pollution detection," *Scientific Reports*, vol. 13, no. 1, p. 21793, 2023.

[412] R. Yeo, J. Yeo, S. Yu Tan, A. Sng, N. Tomczak, J. Muiruri, S. Wang, P. Wang, W. Thitsartarn, F. Wang, *et al.*, "Core-shell micro-and nano-structures for the modification of light-surface interactions," *Advanced Optical Materials*, vol. 12, no. 4, p. 2301955, 2024.

[413] C. Jones, L. Resina, F. Ferreira, P. Sanjuan-Alberte, and T. Esteves, "Conductive core–shell nanoparticles: Synthesis and applications," *The Journal of Physical Chemistry C*, 2024.

[414] J. Zhang and L. Zhang, "Nanostructures for surface plasmons," *Advances in Optics and Photonics*, vol. 4, no. 2, pp. 157–321, 2012.

[415] G. Hartland, "Optical studies of dynamics in noble metal nanostructures," *Chemical reviews*, vol. 111, no. 6, pp. 3858–3887, 2011.

[416] X. Dang, J. Qi, M. Klug, P. Chen, D. Yun, N. Fang, P. Hammond, and A. Belcher, "Tunable localized surface plasmon-enabled broadband light-harvesting enhancement for high-efficiency panchromatic dye-sensitized solar cells," *Nano letters*, vol. 13, no. 2, pp. 637–642, 2013.

[417] H. Zarick, O. Hurd, J. Webb, C. Hungerford, W. Erwin, and R. Bardhan, "Enhanced efficiency in dye-sensitized solar cells with shape-controlled plasmonic nanostructures," *Acs Photonics*, vol. 1, no. 9, pp. 806–811, 2014.

[418] M. Mohammadi, M. Eskandari, and D. Fathi, "Improving the efficiency of perovskite solar cells via embedding random plasmonic nanoparticles: Optical–electrical study on device architectures," *Solar Energy*, vol. 221, pp. 162–175, 2021.

[419] W. Wang and L. Qi, "Light management with patterned micro-and nanostructure arrays for photocatalysis, photovoltaics, and optoelectronic and optical devices," *Advanced Functional Materials*, vol. 29, no. 25, p. 1807275, 2019.

[420] M. Omrani and H. Fallah, "Improving light trapping of polymer solar cell via doping a new array of triple core-shell spherical nanoparticles utilizing realistic modeling," *Solar Energy*, vol. 163, pp. 600–609, 2018.

[421] C. Li and Y. Jin, "Shell-isolated plasmonic nanostructures for biosensing, catalysis, and advanced nanoelectronics," *Advanced Functional Materials*, vol. 31, no. 7, p. 2008031, 2021.

[422] X. Wan, J. Liu, and J. Zhang, "Construction of plasmonic metal@ semiconductor core–shell photocatalysts: From epitaxial to nonepitaxial strategies," *Small Structures*, vol. 3, no. 9, p. 2200045, 2022.

[423] L. Jiang, S. Zhou, J. Yang, H. Wang, H. Yu, H. Chen, Y. Zhao, X. Yuan, W. Chu, and H. Li, "Near-infrared light responsive tio2 for efficient solar energy utilization," *Advanced Functional Materials*, vol. 32, no. 12, p. 2108977, 2022.

[424] I. Ullah, M. Hossain, A. Armghan, M. Rana, and M. Al Asad, "The optoelectronic enhancement in perovskite solar cells using plasmonic metal-dielectric core-shell and nanorod nanoparticles," *Optical and Quantum Electronics*, vol. 55, no. 11, p. 1018, 2023.

[425] D. Smirnova and Y. Kivshar, "Multipolar nonlinear nanophotonics," *Optica*, vol. 3, no. 11, pp. 1241–1255, 2016.

[426] Á. Barreda, F. Vitale, A. Minovich, C. Ronning, and I. Staude, "Applications of hybrid metal-dielectric nanostructures: state of the art," *Advanced Photonics Research*, vol. 3, no. 4, p. 2100286, 2022.

[427] K. Nie, J. Li, X. Chen, Y. Xu, X. Tu, F. Ren, Q. Du, L. Fu, L. Kang, K. Tang, *et al.*, "Extreme absorption enhancement in znte: O/zno intermediate band core-shell nanowires by interplay of dielectric resonance and plasmonic bowtie nanoantennas," *Scientific Reports*, vol. 7, no. 1, p. 7503, 2017.

[428] Z. Yuan, P. Wu, and Y. Chen, "Optical resonator enhanced photovoltaics and photocatalysis: fundamental and recent progress," *Laser & Photonics Reviews*, vol. 16, no. 2, p. 2100202, 2022.

[429] V. Belotelov, I. Akimov, M. Pohl, V. Kotov, S. Kasture, A. Vengurlekar, A. Gopal, D. Yakovlev, A. Zvezdin, and M. Bayer, "Enhanced magneto-optical effects in magnetoplasmonic crystals," *Nature nanotechnology*, vol. 6, no. 6, pp. 370–376, 2011.

[430] M. Barsukova, A. Shorokhov, A. Musorin, D. Neshev, Y. Kivshar, and A. Fedyanin, "Magneto-optical response enhanced by mie resonances in nanoantennas," *Acs Photonics*, vol. 4, no. 10, pp. 2390–2395, 2017.

[431] J. Huang, X. Han, X. Zhao, and C. Meng, "Facile preparation of core-shell ag@ sio2 nanoparticles and their application in spectrally splitting pv/t systems," *Energy*, vol. 215, p. 119111, 2021.

[432] J. Kim, S. Yoo, D. Lee, J. Choi, S. Han, T. Ryu, H. Lee, M. Shin, and M. Song, "Highly efficient and stable solid-state fiber dye-sensitized solar cells with ag-decorated sio 2 nanoparticles," *Nano Research*, vol. 14, pp. 2728–2734, 2021.

[433] I. Mukha, O. Chepurna, N. Vityuk, A. Khodko, L. Storozhuk, V. Dzhagan, D. Zahn, V. Ntziachristos, A. Chmyrov, and T. Ohulchanskyy, "Multifunctional magnetoplasmonic fe3o4/au nanocomposites: Approaching magnetophoretically-enhanced photothermal therapy," *Nanomaterials*, vol. 11, no. 5, p. 1113, 2021.

[434] M. Hekmat, A. Shafiekhani, and M. Khabir, "Near field and far field plasmonic enhancements with bilayers of different dimensions agnps@ dlc for improved current density in silicon solar," *Scientific Reports*, vol. 12, no. 1, p. 19663, 2022.

[435] L. Jin, J. Zhai, L. Heng, T. Wei, L. Wen, L. Jiang, X. Zhao, and X. Zhang, "Bio-inspired multi-scale structures in dye-sensitized solar cell," *Journal of Photochemistry and Photobiology C: Photochemistry Reviews*, vol. 10, no. 4, pp. 149–158, 2009.

[436] M. Powalla, U. Lemmer, A. Colsmann, and G. Gomard, "Plant epidermal structures for enhanced sunlight harvesting in solar cells," *SPIE Newsroom*, vol. 10, no. 2.1201611, p. 006701, 2016.

[437] L. Luo, C. Xie, X. Wang, Y. Yu, C. Wu, H. Hu, K. Zhou, X. Zhang, and J. Jie, "Surface plasmon resonance enhanced highly efficient planar silicon solar cell," *Nano Energy*, vol. 9, pp. 112–120, 2014.

[438] Z. Liang, J. Sun, Y. Jiang, L. Jiang, and X. Chen, "Plasmonic enhanced optoelectronic devices," *Plasmonics*, vol. 9, pp. 859–866, 2014.

[439] A. Amirjani and S. Sadrnezhaad, "Computational electromagnetics in plasmonic nanostructures," *Journal of Materials Chemistry C*, vol. 9, no. 31, pp. 9791–9819, 2021.

[440] Y. Song and W. Zhang, *Inorganic and Organic Thin Films*. Wiley Online Library, 2021.

[441] Q. Zhuang, G. You, L. Wang, X. Lin, D. Zou, H. Zhen, and Q. Ling, "Enhanced performance and stability of tio2-nanoparticles-based perovskite solar cells employing a cheap polymeric surface modifier," *ChemSusChem*, vol. 12, no. 21, pp. 4824–4831, 2019.

[442] D. Ouyang, Z. Huang, and W. Choy, "Solution-processed metal oxide nanocrystals as carrier transport layers in organic and perovskite solar cells," *Advanced Functional Materials*, vol. 29, no. 1, p. 1804660, 2019.

[443] M. Alkhalayfeh, A. Aziz, and K. Pakhuruddin, M.Zand Katubi, "Recent advances of perovskite solar cells embedded with plasmonic nanoparticles," *physica status solidi (a)*, vol. 218, no. 17, p. 2100310, 2021.

[444] S. Shin, S. Lee, and S. Seok, "Metal oxide charge transport layers for efficient and stable perovskite solar cells," *Advanced Functional Materials*, vol. 29, no. 47, p. 1900455, 2019.

[445] C. Chueh, C. Li, and A. Jen, "Recent progress and perspective in solution-processed interfacial materials for efficient and stable polymer and organometal perovskite solar cells," *Energy & Environmental Science*, vol. 8, no. 4, pp. 1160–1189, 2015.

[446] J. Xiong, B. Yang, C. Cao, R. Wu, Y. Huang, J. Sun, J. Zhang, C. Liu, S. Tao, Y. Gao, *et al.*, "Interface degradation of perovskite solar cells and its modification using an annealing-free tio2 nps layer," *Organic Electronics*, vol. 30, pp. 30–35, 2016.

[447] T. Amollo, "Metallic nanoparticles and hybrids of metallic nanoparticles/graphene nanomaterials for enhanced photon harvesting and charge transport in polymer and dye sensitized solar cells," *Heliyon*, 2024.

[448] A. Barman, S. Mondal, S. Sahoo, and A. De, "Magnetization dynamics of nanoscale magnetic materials: A perspective," *Journal of Applied Physics*, vol. 128, no. 17, 2020.

[449] J. Ahsan and H. Singh, "Atomistic simulation study of feco alloy nanoparticles," *Applied Physics A*, vol. 128, no. 5, p. 443, 2022.

[450] P. Allia, G. Barrera, and P. Tiberto, "Hysteresis effects in magnetic nanoparticles: A simplified rate-equation approach," *Journal of Magnetism and Magnetic Materials*, vol. 496, p. 165927, 2020.

[451] H. Feng, F. Luo, R. Arenal, L. Henrard, F. García, G. Armelles, and A. Cebollada, "Active magnetoplasmonic split-ring/ring nanoantennas," *Nanoscale*, vol. 9, no. 1, pp. 37–44, 2017.

[452] C. Oubre and P. Nordlander, "Finite-difference time-domain studies of the optical properties of nanoshell dimers," *The Journal of Physical Chemistry B*, vol. 109, no. 20, pp. 10042–10051, 2005.

[453] M. Yuan, M. Harnett, T. Yan, E. Georgas, Y. Qin, H. Zhou, and Y. Wang, "Progress, opportunities, and challenges of magneto-plasmonic nanoparticles under remote magnetic and light stimulation for brain-tissue and cellular regeneration," *Nanomaterials*, vol. 12, no. 13, p. 2242, 2022.

[454] M. Talaikis, L. Mikoliunaite, A. Gkouzi, V. Petrikaitė, E. Stankevičius, A. Drabavičius, A. Selskis, R. Juškėnas, and G. Niaura, "Multiwavelength sers of magneto-plasmonic nanoparticles obtained by combined laser ablation and solvothermal methods," *ACS omega*, 2023.

[455] L. Han, Y. Zhang, Y. Zhang, Y. Shu, X. Chen, and J. Wang, "A magnetic polypyrrole/iron oxide core/gold shell nanocomposite for multimodal imaging and photothermal cancer therapy," *Talanta*, vol. 171, pp. 32–38, 2017.

[456] D. McCoy, A. Shneidman, A. Davis, and J. Aizenberg, "Finite-difference time-domain (fdtd) optical simulations: a primer for the life sciences and bio-inspired engineering," *Micron*, vol. 151, p. 103160, 2021.

[457] Y. Wu and P. Nordlander, "Finite-difference time-domain modeling of the optical properties of nanoparticles near dielectric substrates," *The Journal of Physical Chemistry C*, vol. 114, no. 16, pp. 7302–7307, 2010.

[458] M. Nguyen, I. Kherbouche, M. Braik, A. Belkhir, L. Boubekeur-Lecaque, J. Aubard, C. Mangeney, and N. Felidj, "Dynamic plasmonic platform to investigate the correlation between far-field optical response and sers signal of analytes," *ACS omega*, vol. 4, no. 1, pp. 1144–1150, 2019.

[459] K. Kelly, E. Coronado, L. Zhao, and G. Schatz, "The optical properties of metal nanoparticles: the influence of size, shape, and dielectric environment," *The Journal of physical chemistry*, vol. 107, no. 3, pp. 668–677, 2003.

[460] W. Vargas, J. Wang, and G. Niklasson, "Scattering and absorption cross sections of light diffusing materials retrieved from reflectance and transmittance spectra of collimated radiation," *Journal of Modern Optics*, vol. 67, no. 11, pp. 974–991, 2020.

[461] A. Yurkin, M.A and. Hoekstra, "The discrete dipole approximation: an overview and recent developments," *Journal of Quantitative Spectroscopy and Radiative Transfer*, vol. 106, no. 1-3, pp. 558–589, 2007.

[462] M. Yurkin, V. Maltsev, and A. Hoekstra, "Convergence of the discrete dipole approximation. i. theoretical analysis," *JOSA A*, vol. 23, no. 10, pp. 2578–2591, 2006.

[463] Z. Kuang, *Fundamental Limits of Nanophotonic Design*. PhD thesis, Yale University, 2023.

[464] P. Chaumet, "The discrete dipole approximation: A review," *Mathematics*, vol. 10, no. 17, p. 3049, 2022.

[465] F. Kahnert, "Numerical methods in electromagnetic scattering theory," *Journal of Quantitative Spectroscopy and Radiative Transfer*, vol. 79, pp. 775–824, 2003.

[466] M. Yurkin and A. Hoekstra, "The discrete-dipole-approximation code adda: Capabilities and known limitations," *Journal of Quantitative Spectroscopy and Radiative Transfer*, vol. 112, no. 13, pp. 2234–2247, 2011.

[467] J. Lakowicz, K. Ray, M. Chowdhury, H. Szmacinski, Y. Fu, J. Zhang, and K. Nowaczyk, "Plasmon-controlled fluorescence: a new paradigm in fluorescence spectroscopy," *Analyst*, vol. 133, no. 10, pp. 1308–1346, 2008.

[468] G. Perrakis, G. Kakavelakis, G. Kenanakis, C. Petridis, E. Stratakis, M. Kafesaki, and E. Kymakis, "Efficient and environmental-friendly perovskite solar cells via embedding plasmonic nanoparticles: an optical simulation study on realistic device architectures," *Optics express*, vol. 27, no. 22, pp. 31144–31163, 2019.

[469] V. Coviello, D. Forrer, and V. Amendola, "Recent developments in plasmonic alloy nanoparticles: synthesis, modelling, properties and applications," *ChemPhysChem*, vol. 23, no. 21, p. e202200136, 2022.

[470] N. Mousavi, K. Ramadi, Y. Song, and S. Kumar, "Plasmonics for neuroengineering," *Communications Materials*, vol. 4, no. 1, p. 101, 2023.

[471] C. Jin, Z. Wu, J. Molinski, J. Zhou, Y. Ren, and J. Zhang, "Plasmonic nanosensors for point-of-care biomarker detection," *Materials Today Bio*, vol. 14, p. 100263, 2022.

[472] A. Singh, M. Ansari, D. Rosenkranz, R. Maharjan, F. Kriegel, K. Gandhi, A. Kanase, R. Singh, P. Laux, and A. Luch, "Artificial intelligence and machine learning in computational nanotoxicology: unlocking and empowering nanomedicine," *Advanced Healthcare Materials*, vol. 9, no. 17, p. 1901862, 2020.

[473] N. Sizochenko, M. Syzochenko, A. Gajewicz, J. Leszczynski, and T. Puzyn, "Predicting physical properties of nanofluids by computational modeling," *The Journal of Physical Chemistry C*, vol. 121, no. 3, pp. 1910–1917, 2017.

[474] D. Fourches, D. Pu, C. Tassa, R. Weissleder, S. Shaw, R. Mumper, and A. Tropsha, "Quantitative nanostructure- activity relationship modeling," *ACS nano*, vol. 4, no. 10, pp. 5703–5712, 2010.

[475] C. Mehta, R. Narayan, and U. Nayak, "Computational modeling for formulation design," *Drug Discovery Today*, vol. 24, no. 3, pp. 781–788, 2019.

[476] A. Naseri, M. Jamei, I. Ahmadianfar, and M. Behbahani, "Nanofluids thermal conductivity prediction applying a novel hybrid data-driven model validated using monte carlo-based sensitivity analysis," *Engineering with Computers*, vol. 38, no. Suppl 1, pp. 815–839, 2022.

[477] R. Chen and J. Riviere, "Biological and environmental surface interactions of nanomaterials: characterization, modeling, and prediction," *Wiley Interdisciplinary Reviews: Nanomedicine and Nanobiotechnology*, vol. 9, no. 3, p. e1440, 2017.

[478] T. Andersen, E. Bundgaard, and M. Jørgensen, *Organic Based Solar Cells with Morphology Control*. PhD thesis, Technical University of Denmark, 2013.

[479] R. Zeng, L. Zhu, M. Zhang, W. Zhong, G. Zhou, J. Zhuang, T. Hao, Z. Zhou, L. Zhou, N. Hartmann, *et al.*, "All-polymer organic solar cells with nano-to-micron hierarchical morphology and large light receiving angle," *Nature Communications*, vol. 14, no. 1, p. 4148, 2023.

[480] Y. Wang, J. Lee, X. Hou, C. Labanti, J. Yan, E. Mazzolini, A. Parhar, J. Nelson, J. Kim, and Z. Li, "Recent progress and challenges toward highly stable nonfullerene acceptor-based organic solar cells," *Advanced Energy Materials*, vol. 11, no. 5, p. 2003002, 2021.

[481] Y. Xu, H. Yao, L. Ma, J. Wang, and J. Hou, "Efficient charge generation at low energy losses in organic solar cells: a key issues review," *Reports on Progress in Physics*, vol. 83, no. 8, p. 082601, 2020.

[482] S. Dimitrov and J. Durrant, "Materials design considerations for charge generation in organic solar cells," *Chemistry of Materials*, vol. 26, no. 1, pp. 616–630, 2014.

[483] L. Zhao, H. Wang, H. Ji, S. Li, X. Miao, C. Zhu, W. Wang, D. Huang, and X. Dong, "A review on smart strategies for active layer phase separation regulation of organic solar cells," *APL Materials*, vol. 11, no. 12, 2023.

[484] E. Manley, J. Strzalka, T. Fauvell, T. Marks, and L. Chen, "In situ analysis of solvent and additive effects on film morphology evolution in spin-cast small-molecule and polymer photovoltaic materials," *Advanced Energy Materials*, vol. 8, no. 23, p. 1800611, 2018.

[485] Z. Wang, K. Gao, Y. Kan, M. Zhang, C. Qiu, L. Zhu, Z. Zhao, X. Peng, W. Feng, Z. Qian, *et al.*, "The coupling and competition of crystallization and phase separation, correlating thermodynamics and kinetics in opv morphology and performances," *Nature communications*, vol. 12, no. 1, p. 332, 2021.

[486] F. Liu, S. Ferdous, E. Schaible, A. Hexemer, M. Church, X. Ding, C. Wang, and T. Russell, "Fast printing and in situ morphology observation of organic photovoltaics using slot-die coating," *Advanced materials*, vol. 27, no. 5, pp. 886–891, 2015.

[487] E. Verploegen, R. Mondal, C. Bettinger, S. Sok, M. Toney, and Z. Bao, "Effects of thermal annealing upon the morphology of polymer–fullerene blends," *Advanced Functional Materials*, vol. 20, no. 20, pp. 3519–3529, 2010.

[488] D. Luo, W. Jang, D. Babu, M. Kim, D. Wang, and A. Kyaw, "Recent progress in organic solar cells based on non-fullerene acceptors: materials to devices," *Journal of Materials Chemistry A*, vol. 10, no. 7, pp. 3255–3295, 2022.

[489] N. Shin, L. Richter, A. Herzing, R. Kline, and D. DeLongchamp, "Effect of processing additives on the solidification of blade-coated polymer/fullerene blend films via in-situ structure measurements," *Advanced Energy Materials*, vol. 3, no. 7, pp. 938–948, 2013.

[490] Q. Liang, J. Yao, Z. Hu, P. Wei, H. Lu, Y. Yin, K. Wang, and J. Liu, "Recent advances of film–forming kinetics in organic solar cells," *Energies*, vol. 14, no. 22, p. 7604, 2021.

[491] Y. Xiong, L. Ye, and C. Zhang, "Eco-friendly solution processing of all-polymer solar cells: Recent advances and future perspective," *Journal of Polymer Science*, vol. 60, no. 6, pp. 945–960, 2022.

[492] D. Corzo, D. Rosas-Villalva, G. Tostado-Blázquez, E. Alexandre, L. Hernandez, J. Han, H. Xu, M. Babics, S. De Wolf, and D. Baran, "High-performing organic electronics using terpene green solvents from renewable feedstocks," *Nature Energy*, vol. 8, no. 1, pp. 62–73, 2023.

[493] R. Gurney, D. Lidzey, and T. Wang, "A review of non-fullerene polymer solar cells: from device physics to morphology control," *Reports on Progress in Physics*, vol. 82, no. 3, p. 036601, 2019.

[494] L. Ye, B. Collins, X. Jiao, J. Zhao, H. Yan, and H. Ade, "Miscibility–function relations in organic solar cells: significance of optimal miscibility in relation to percolation," *Advanced Energy Materials*, vol. 8, no. 28, p. 1703058, 2018.

[495] J. Min, C. Cui, T. Heumueller, S. Fladischer, X. Cheng, E. Spiecker, Y. Li, and C. Brabec, "Side-chain engineering for enhancing the properties of small molecule solar cells: A trade-off beyond efficiency," *Advanced Energy Materials*, vol. 6, no. 14, p. 1600515, 2016.

[496] C. Zhang, A. Mumyatov, S. Langner, J. Perea, T. Kassar, J. Min, L. Ke, H. Chen, K. Gerasimov, D. Anokhin, *et al.*, "Overcoming the thermal instability of efficient polymer solar cells by employing novel fullerene-based acceptors," *Advanced Energy Materials*, vol. 7, no. 3, p. 1601204, 2017.

[497] Y. Hsieh, Y. Huang, W. Liu, Y. Su, C. Tsao, S. Rwei, and L. Wang, "Insights into the morphological instability of bulk heterojunction ptb7-th/pcbm solar cells upon high-temperature aging," *ACS Applied Materials & Interfaces*, vol. 9, no. 17, pp. 14808–14816, 2017.

[498] T. Heumueller, W. Mateker, A. Distler, U. Fritze, R. Cheacharoen, W. Nguyen, M. Biele, M. Salvador, M. von Delius, H. Egelhaaf, *et al.*, "Morphological and electrical control of fullerene dimerization determines organic photovoltaic stability," *Energy & Environmental Science*, vol. 9, no. 1, pp. 247–256, 2016.

[499] K. Sivula, C. Luscombe, B. Thompson, and J. Fréchet, "Enhancing the thermal stability of polythiophene: fullerene solar cells by decreasing effective polymer regioregularity," *Journal of the American chemical society*, vol. 128, no. 43, pp. 13988–13989, 2006.

[500] S. Bertho, B. Campo, F. Piersimoni, D. Spoltore, J. D'Haen, L. Lutsen, W. Maes, D. Vanderzande, and J. Manca, "Improved thermal stability of bulk heterojunctions based on side-chain functionalized poly (3-alkylthiophene) copolymers and pcbm," *Solar energy materials and solar cells*, vol. 110, pp. 69–76, 2013.

[501] Y. Zhang, H. Yip, O. Acton, S. Hau, F. Huang, and A. Jen, "A simple and effective way of achieving highly efficient and thermally stable bulk-heterojunction polymer solar cells using amorphous fullerene derivatives as electron acceptor," *Chemistry of Materials*, vol. 21, no. 13, pp. 2598–2600, 2009.

[502] P. Cheng, C. Yan, T. Lau, J. Mai, X. Lu, and X. Zhan, "Molecular lock: A versatile key to enhance efficiency and stability of organic solar cells," *Advanced materials*, vol. 28, no. 28, pp. 5822–5829, 2016.

[503] P. M. Fahey, P. Griffin, and J. Plummer, "Point defects and dopant diffusion in silicon," *Reviews of Modern Physics*, vol. 61, no. 2, p. 289, 1989.

[504] C. Chen, C. Huang, and S. Chuang, "Highly thermal stable and efficient organic photovoltaic cells with crosslinked networks appending open-cage fullerenes as additives," *Advanced Functional Materials*, vol. 25, no. 2, pp. 207–213, 2015.

[505] W. Feng, Z. Lin, J. Cui, W. Lv, W. Wang, and Q. Ling, "Photoactive layer crosslinking in all-polymer solar cells: Stabilized morphology and enhanced thermal-stability," *Solar Energy Materials and Solar Cells*, vol. 200, p. 109982, 2019.

[506] H. Hoppe, M. Niggemann, C. Winder, J. Kraut, R. Hiesgen, A. Hinsch, D. Meissner, and N. Sariciftci, "Nanoscale morphology of conjugated polymer/fullerene-based bulk-heterojunction solar cells," *Advanced Functional Materials*, vol. 14, no. 10, pp. 1005–1011, 2004.

[507] H. Hoppe and N. Sariciftci, "Morphology of polymer/fullerene bulk heterojunction solar cells," *Journal of Materials Chemistry*, vol. 16, no. 1, pp. 45–61, 2006.

[508] Y. Sun, T. Liu, Y. Kan, K. Gao, B. Tang, and Y. Li, "Flexible organic solar cells: progress and challenges," *Small Science*, vol. 1, no. 5, p. 2100001, 2021.

[509] W. Tarique and A. Uddin, "A review of progress and challenges in the research developments on organic solar cells," *Materials Science in Semiconductor Processing*, vol. 163, p. 107541, 2023.

[510] S. Li, Z. Li, X. Wan, and Y. Chen, "Recent progress in flexible organic solar cells," *eScience*, vol. 3, no. 1, p. 100085, 2023.

[511] B. Thompson and J. Fréchet, "Polymer–fullerene composite solar cells," *Angewandte chemie international edition*, vol. 47, no. 1, pp. 58–77, 2008.

[512] C. Cui and Y. Li, "Morphology optimization of photoactive layers in organic solar cells," *Aggregate*, vol. 2, no. 2, p. e31, 2021.

[513] S. Park, T. Kim, S. Yoon, C. Koh, H. Woo, and H. Son, "Progress in materials, solution processes, and long-term stability for large-area organic photovoltaics," *Advanced Materials*, vol. 32, no. 51, p. 2002217, 2020.

[514] A. Gertsen, M. Castro, R. Søndergaard, and J. Andreasen, "Scalable fabrication of organic solar cells based on non-fullerene acceptors," *Flexible and Printed Electronics*, vol. 5, no. 1, p. 014004, 2020.

[515] H. Ro, J. Downing, S. Engmann, A. Herzing, D. DeLongchamp, L. Richter, S. Mukherjee, H. Ade, M. Abdelsamie, L. Jagadamma, *et al.*, "Morphology changes upon scaling a high-efficiency, solution-processed solar cell," *Energy & Environmental Science*, vol. 9, no. 9, pp. 2835–2846, 2016.

[516] J. Jing, Y. Dou, S. Chen, K. Zhang, and F. Huang, "Solution sequential deposited organic photovoltaics: from morphology control to large-area modules," *eScience*, p. 100142, 2023.

[517] M. Li and F. He, "Organic solar cells developments: What's next?," *Next Energy*, vol. 2, p. 100085, 2024.

[518] M. Jee, H. Ryu, D. Lee, W. Lee, and H. Woo, "Recent advances in nonfullerene acceptor-based layer-by-layer organic solar cells using a solution process," *Advanced Science*, vol. 9, no. 25, p. 2201876, 2022.

[519] R. Po, A. Bernardi, A. Calabrese, C. Carbonera, G. Corso, and A. Pellegrino, "From lab to fab: how must the polymer solar cell materials design change?–an industrial perspective," *Energy & Environmental Science*, vol. 7, no. 3, pp. 925–943, 2014.

[520] M. Li, Q. Wang, J. Liu, Y. Geng, and L. Ye, "Sequential deposition enables high-performance nonfullerene organic solar cells," *Materials Chemistry Frontiers*, vol. 5, no. 13, pp. 4851–4873, 2021.

[521] M. Barr, S. Chambon, A. Fahy, T. Jones, M. Marcus, A. Kilcoyne, P. Dastoor, M. Griffith, and N. Holmes, "Nanomorphology of eco-friendly colloidal inks, relating non-fullerene acceptor surface energy to structure formation," *Materials Chemistry Frontiers*, vol. 5, no. 5, pp. 2218–2233, 2021.

[522] Y. Chang, X. Zhu, K. Lu, and Z. Wei, "Progress and prospects of thick-film organic solar cells," *Journal of Materials Chemistry A*, vol. 9, no. 6, pp. 3125–3150, 2021.

[523] C. Yi, Y. Yang, B. Liu, J. He, and Z. Nie, "Polymer-guided assembly of inorganic nanoparticles," *Chemical Society Reviews*, vol. 49, no. 2, pp. 465–508, 2020.

[524] W. Wang, M. Ramezani, A. Väkeväinen, P. Törmä, J. Rivas, and T. Odom, "The rich photonic world of plasmonic nanoparticle arrays," *Materials today*, vol. 21, no. 3, pp. 303–314, 2018.

[525] D. Su, N. Jin, Y. Yang, and T. Zhang, "Micro-and nano-scale optical focusing for carrier management in silicon solar cell," *Solar Energy*, vol. 264, p. 112026, 2023.

[526] A. Gabbani, C. Sangregorio, B. Tandon, A. Nag, M. Gurioli, and F. Pineider, "Magnetoplasmonics beyond metals: Ultrahigh sensing performance in transparent conductive oxide nanocrystals," *Nano Letters*, vol. 22, no. 22, pp. 9036–9044, 2022.

[527] K. Jeong, D. Lee, V. Tran, C. Wang, J. Lv, J. Park, Z. Tang, and J. Lee, "Helical magnetic field-induced real-time plasmonic chirality modulation," *ACS nano*, vol. 14, no. 6, pp. 7152–7160, 2020.

[528] W. Zhao, Y. Yan, X. Chen, and T. Wang, "Combining printing and nanoparticle assembly: Methodology and application of nanoparticle patterning," *The Innovation*, 2022.

[529] K. Chen, L. Shi, Y. Zhang, and Z. Liu, "Scalable chemical-vapour-deposition growth of three-dimensional graphene materials towards energy-related applications," *Chemical Society Reviews*, vol. 47, no. 9, pp. 3018–3036, 2018.

[530] A. Wibowo, M. Marsudi, M. Amal, M. Ananda, R. Stephanie, H. Ardy, and L. Diguna, "Zno nanostructured materials for emerging solar cell applications," *RSC advances*, vol. 10, no. 70, pp. 42838–42859, 2020.

[531] D. Di Girolamo, F. Di Giacomo, F. Matteocci, A. Marrani, D. Dini, and A. Abate, "Progress, highlights and perspectives on nio in perovskite photovoltaics," *Chemical Science*, vol. 11, no. 30, pp. 7746–7759, 2020.

[532] L. Tan, W. Fu, Q. Gao, and P. Wang, "Chiral plasmonic hybrid nanostructures: A gateway to advanced chiroptical materials," *Advanced Materials*, p. 2309033, 2023.

[533] S. Ulaeto, R. Rajan, J. Pancrecious, T. Rajan, and B. Pai, "Developments in smart anticorrosive coatings with multifunctional characteristics," *Progress in Organic Coatings*, vol. 111, pp. 294–314, 2017.

[534] S. Sinha, R. Kumar, J. Anand, R. Gupta, A. Gupta, K. Pant, S. Dohare, P. Tiwari, K. Kesari, S. Krishnan, *et al.*, "Nanotechnology-based solutions for antibiofouling applications: An overview," *ACS Applied Nano Materials*, vol. 6, no. 14, pp. 12828–12848, 2023.

[535] L. Pokrajac, A. Abbas, W. Chrzanowski, G. Dias, B. Eggleton, S. Maguire, E. Maine, T. Malloy, J. Nathwani, L. Nazar, *et al.*, "Nanotechnology for a sustainable future: Addressing global challenges with the international network4sustainable nanotechnology," 2021.

[536] N. Maccaferri, A. Gabbani, F. Pineider, T. Kaihara, T. Tapani, and P. Vavassori, "Magnetoplasmonics in confined geometries: Current challenges and future opportunities," *Applied Physics Letters*, vol. 122, no. 12, 2023.

[537] N. Maccaferri, I. Zubritskaya, I. Razdolski, I. Chioar, V. Belotelov, V. Kapaklis, P. Oppeneer, and A. Dmitriev, "Nanoscale magnetophotonics," *Journal of Applied Physics*, vol. 127, no. 8, 2020.

[538] D. Bossini, V. Belotelov, A. Zvezdin, A. Kalish, and A. Kimel, "Magnetoplasmonics and femtosecond optomagnetism at the nanoscale," *Acs Photonics*, vol. 3, no. 8, pp. 1385–1400, 2016.

[539] R. Chambers, *Electrons in metals and semiconductors*. Springer Science & Business Media, 2012.

[540] H. Fröhlich, "Electrons in lattice fields," *Advances in Physics*, vol. 3, no. 11, pp. 325–361, 1954.

[541] A. Indhu, L. Keerthana, and G. Dharmalingam, "Plasmonic nanotechnology for photothermal applications–an evaluation," *Beilstein Journal of Nanotechnology*, vol. 14, no. 1, pp. 380–419, 2023.

[542] M. Hartelt, P. Terekhin, T. Eul, A. Mahro, B. Frisch, E. Prinz, B. Rethfeld, B. Stadtmüller, and M. Aeschlimann, "Energy and momentum distribution of surface plasmon-induced hot carriers isolated via spatiotemporal separation," *ACS nano*, vol. 15, no. 12, pp. 19559–19569, 2021.

[543] S. Ghosh and T. Pal, "Interparticle coupling effect on the surface plasmon resonance of gold nanoparticles: from theory to applications," *Chemical reviews*, vol. 107, no. 11, pp. 4797–4862, 2007.

[544] A. Dorodnyy, Y. Salamin, P. Ma, J. Plestina, N. Lassaline, D. Mikulik, P. Romero-Gomez, A. i Morral, and J. Leuthold, "Plasmonic photodetectors," *IEEE Journal of Selected Topics in Quantum Electronics*, vol. 24, no. 6, pp. 1–13, 2018.

[545] G. Armelles, A. Cebollada, A. García-Martín, and M. González, "Magnetoplasmonics: combining magnetic and plasmonic functionalities," *Advanced Optical Materials*, vol. 1, no. 1, pp. 10–35, 2013.

[546] A. Gabbani, G. Petrucci, and F. Pineider, "Magneto-optical methods for magnetoplasmonics in noble metal nanostructures," *Journal of Applied Physics*, vol. 129, no. 21, 2021.

[547] T. Haider, "A review of magneto-optic effects and its application," *Int. J. Electromagn. Appl*, vol. 7, no. 1, pp. 17–24, 2017.

[548] A. Boardman and M. Xie, "Magneto-optics: a critical review," *Introduction to Complex Mediums for Optics and Electromagnetics*, vol. 123, p. 197, 2003.

[549] M. Elmahaishi, I. Ismail, F. Muhammad, *et al.*, "A review on electromagnetic microwave absorption properties: Their materials and performance," *Journal of Materials Research and Technology*, 2022.

[550] V. Markel, "Maxwell garnett approximation (advanced topics): tutorial," *JOSA A*, vol. 33, no. 11, pp. 2237–2255, 2016.

[551] V. Frilén, *A theoretical framework for interpretation and prediction of magneto-optical measurements*. PhD thesis, Uppsala University, July 2023.

[552] J. Jackson, "Classical electrodynamics," 1999.

[553] M. Haddad, F. Jonsson, R. Frey, and C. Flytzanis, "Nonlinear optical gyrotropy," *NONLINEAR OPTICS-READING-*, vol. 23, no. 3/4, pp. 251–268, 2000.

[554] J. del Toro Iniesta, *Introduction to spectropolarimetry*. Cambridge university press, 2003.

[555] A. Altland and B. Simons, *Condensed matter field theory*. Cambridge university press, 2010.

[556] K. Sato and T. Ishibashi, "Fundamentals of magneto-optical spectroscopy," *Frontiers in Physics*, vol. 10, p. 946515, 2022.

[557] R. Evans, "Atomistic modelling of nanogranular magnetic materials," 2008.

[558] R. Kodama and A. Berkowitz, "Atomic-scale magnetic modeling of oxide nanoparticles," *Physical Review B*, vol. 59, no. 9, p. 6321, 1999.

[559] C. Etz, L. Bergqvist, A. Bergman, A. Taroni, and O. Eriksson, "Atomistic spin dynamics and surface magnons," *Journal of Physics: Condensed Matter*, vol. 27, no. 24, p. 243202, 2015.

[560] J. Alzate-Cardona, D. Sabogal-Suárez, O. Arbeláez-Echeverri, and E. Restrepo-Parra, "Vegas: software package for the atomistic simulation of magnetic materials," *Revista mexicana de física*, vol. 64, no. 5, pp. 490–497, 2018.

[561] R. Evans, W. Fan, P. Chureemart, T. Ostler, M. Ellis, and R. Chantrell, "Atomistic spin model simulations of magnetic nanomaterials," *Journal of Physics: Condensed Matter*, vol. 26, no. 10, p. 103202, 2014.

[562] D. Hinzke and U. Nowak, "Monte carlo simulation of magnetization switching in a heisenberg model for small ferromagnetic particles," *Computer physics communications*, vol. 121, pp. 334–337, 1999.

[563] O. Eriksson, A. Bergman, L. Bergqvist, and J. Hellsvik, *Atomistic spin dynamics: foundations and applications*. Oxford university press, 2017.

[564] B. Skubic, J. Hellsvik, L. Nordström, and O. Eriksson, "A method for atomistic spin dynamics simulations: implementation and examples," *Journal of physics: condensed matter*, vol. 20, no. 31, p. 315203, 2008.

[565] J. Ramos-Guivar, C. Tamanaha-Vegas, F. Litterst, and E. Passamani, "Magnetic simulations of core–shell ferromagnetic bi-magnetic nanoparticles: The influence of antiferromagnetic interfacial exchange," *Nanomaterials*, vol. 11, no. 6, p. 1381, 2021.

[566] J. Ahsan and H. Singh, "Temperature dependent magnetization in co@ fe nanoparticles," *Physica B: Condensed Matter*, vol. 627, p. 413488, 2022.

[567] R. Evans, U. Atxitia, and R. Chantrell, "Quantitative simulation of temperature-dependent magnetization dynamics and equilibrium properties of elemental ferromagnets," *Physical Review B*, vol. 91, no. 14, p. 144425, 2015.

[568] J. Mo, H. Chen, R. Chen, M. Jin, M. Liu, and Y. Xia, "Nature of spin-glass behavior of cobalt-doped iron disulfide nanospheres using the monte carlo method," *The Journal of Physical Chemistry C*, vol. 127, no. 3, pp. 1475–1486, 2023.

[569] J. Byrne, V. Coker, S. Moise, P. Wincott, D. Vaughan, F. Tuna, E. Arenholz, G. Van Der Laan, R. Pattrick, J. Lloyd, *et al.*, "Controlled cobalt doping in biogenic magnetite nanoparticles," *Journal of The Royal Society Interface*, vol. 10, no. 83, p. 20130134, 2013.

[570] K. Brymora and F. Calvayrac, "Surface anisotropy of iron oxide nanoparticles and slabs from first principles: Influence of coatings and ligands as a test of the heisenberg model," *Journal of Magnetism and Magnetic Materials*, vol. 434, pp. 14–22, 2017.

[571] L. Ajroudi, N. Mliki, L. Bessais, V. Madigou, S. Villain, and C. Leroux, "Magnetic, electric and thermal properties of cobalt ferrite nanoparticles," *Materials Research Bulletin*, vol. 59, pp. 49–58, 2014.

[572] L. Cao, X. Dan, M. Guo, H. Park, and T. Fujita, "Size and shape effects on curie temperature of ferromagnetic nanoparticles," *Transactions of Nonferrous Metals Society of China*, vol. 17, no. 6, pp. 1451–1455, 2007.

[573] K. Binder, "A monte-carlo method for the calculation of the magnetization of the classical heisenberg model," *Physics Letters A*, vol. 30, no. 5, pp. 273–274, 1969.

[574] J. Mokkath, "Size and chemical order dependence of magnetic-ordering temperature and spin structure in fe@ ni and ni@ fe core–shell nanoparticles," *Physical Chemistry Chemical Physics*, vol. 22, no. 11, pp. 6275–6281, 2020.

[575] Q. Ong, *Structural and magnetic studies of core-shell and hollow nanoparticles*. PhD thesis, Purdue University, 2010.

[576] D. Tsamos, A. Krestou, M. Papagiannaki, and S. Maropoulos, "An overview of the production of magnetic core-shell nanoparticles and their biomedical applications," *Metals*, vol. 12, no. 4, p. 605, 2022.

[577] W. Liu, W. Zhong, and Y. Du, "Magnetic nanoparticles with core/shell structures," *Journal of Nanoscience and Nanotechnology*, vol. 8, no. 6, pp. 2781–2792, 2008.

[578] A. Boies, J. Roberts, S. Girshick, B. Zhang, T. Nakamura, and A. Mochizuki, "Sio2 coating of silver nanoparticles by photoinduced chemical vapor deposition," *Nanotechnology*, vol. 20, no. 29, p. 295604, 2009.

[579] A. Charlot, X. Deschanels, and G. Toquer, "Submicron coating of sio2 nanoparticles from electrophoretic deposition," *Thin Solid Films*, vol. 553, pp. 148–152, 2014.

[580] K. Dhanalekshmi, P. Magesan, K. Sangeetha, X. Zhang, K. Jayamoorthy, and N. Srinivasan, "Preparation and characterization of core-shell type ag@ sio2 nanoparticles for photodynamic cancer therapy," *Photodiagnosis and Photodynamic Therapy*, vol. 28, pp. 324–329, 2019.

[581] M. Lismont, C. Páez, and L. Dreesen, "A one-step short-time synthesis of ag@ sio2 core–shell nanoparticles," *Journal of colloid and interface science*, vol. 447, pp. 40–49, 2015.

[582] Y. Tang, F. Liu, W. Liu, S. Mo, X. Li, D. Yang, Y. Liu, and S. Bao, "Multifunctional carbon-armored ni electrocatalyst for hydrogen evolution under high current density in alkaline electrolyte solution," *Applied Catalysis B: Environmental*, vol. 321, p. 122081, 2023.

[583] C. Wang, X. Jie, Y. Qiu, Y. Zhao, H. Al-Megren, S. Alshihri, P. Edwards, and T. Xiao, "The importance of inner cavity space within ni@ sio2 nanocapsule catalysts for excellent coking resistance in the high-space-velocity dry reforming of methane," *Applied Catalysis B: Environmental*, vol. 259, p. 118019, 2019.

[584] K. Sentosun, M. Sanz Ortiz, K. Batenburg, L. Liz-Marzán, and S. Bals, "Combination of haadf-stem and adf-stem tomography for core–shell hybrid materials," *Particle & Particle Systems Characterization*, vol. 32, no. 12, pp. 1063–1067, 2015.

[585] A. Gatin, S. Sarvadii, N. Dokhlikova, V. Kharitonov, S. Ozerin, B. Shub, and M. Grishin, "Oxidation of supported nickel nanoparticles at low exposure to o2: Charging effects and selective surface activity," *Nanomaterials*, vol. 12, no. 7, p. 1038, 2022.

[586] S. Mourdikoudis, R. Pallares, and N. Thanh, "Characterization techniques for nanoparticles: comparison and complementarity upon studying nanoparticle properties," *Nanoscale*, vol. 10, no. 27, pp. 12871–12934, 2018.

[587] R. Tom, A. Nair, N. Singh, M. Aslam, C. Nagendra, R. Philip, K. Vijayamohanan, and T. Pradeep, "Freely dispersible au@ tio2, au@ zro2, ag@ tio2, and ag@ zro2 core- shell nanoparticles: one-step synthesis, characterization, spectroscopy, and optical limiting properties," *Langmuir*, vol. 19, no. 8, pp. 3439–3445, 2003.

[588] K. Dhanalekshmi, K. Meena, and I. Ramesh, "Synthesis and characterization of ag@ tio2 core-shell nanoparticles and study of its antibacterial activity," *Int J Nanotechnol*, vol. 3, no. 5, p. 9, 2013.

[589] H. He, Y. Zhong, X. Liang, W. Tan, J. Zhu, and C. Yan Wang, "Natural magnetite: an efficient catalyst for the degradation of organic contaminant," *Scientific Reports*, vol. 5, no. 1, p. 10139, 2015.

[590] M. Dar and S. Shivashankar, "Single crystalline magnetite, maghemite, and hematite nanoparticles with rich coercivity," *RSC Advances*, vol. 4, no. 8, pp. 4105–4113, 2014.

[591] H. Park, N. Myung, H. Jung, and H. Choi, "As (v) remediation using electrochemically synthesized maghemite nanoparticles," *Journal of Nanoparticle Research*, vol. 11, pp. 1981–1989, 2009.

[592] X. Zhang, M. Ezawa, and Y. Zhou, "Magnetic skyrmion logic gates: conversion, duplication and merging of skyrmions," *Scientific reports*, vol. 5, no. 1, pp. 1–8, 2015.

[593] B. Al-Swai, N. Osman, and B. Abdullah, "Catalytic performance of ni/mgo catalyst in methane dry reforming," in *AIP Conference Proceedings*, vol. 1891, AIP Publishing, 2017.

[594] T. Tran, B. Park, W. Yun, T. Duong, and H. Yoon, "Metal–organic framework–derived ni@ c and nio@ c as anode catalysts for urea fuel cells," *Scientific reports*, vol. 10, no. 1, p. 278, 2020.

[595] J. Li, P. Li, J. Li, Z. Tian, and F. Yu, "Highly-dispersed ni-nio nanoparticles anchored on an sio2 support for an enhanced co methanation performance," *Catalysts*, vol. 9, no. 6, p. 506, 2019.

[596] H. Yan, D. Zhang, J. Xu, Y. Lu, Y. Liu, K. Qiu, Y. Zhang, and Y. Luo, "Solution growth of nio nanosheets supported on ni foam as high-performance electrodes for supercapacitors," *Nanoscale research letters*, vol. 9, pp. 1–7, 2014.

[597] L. Gasparov, D. Tanner, D. Romero, H. Berger, G. Margaritondo, and L. Forro, "Infrared and raman studies of the verwey transition in magnetite," *Physical Review B*, vol. 62, no. 12, p. 7939, 2000.

[598] Y. Li, J. Church, and A. Woodhead, "Infrared and raman spectroscopic studies on iron oxide magnetic nano-particles and their surface modifications," *Journal of Magnetism and Magnetic Materials*, vol. 324, no. 8, pp. 1543–1550, 2012.

[599] L. Slavov, M. Abrashev, T. Merodiiska, C. Gelev, R. Vandenberghe, I. Markova-Deneva, and I. Nedkov, "Raman spectroscopy investigation of magnetite nanoparticles in ferrofluids," *Journal of Magnetism and Magnetic Materials*, vol. 322, no. 14, pp. 1904–1911, 2010.

[600] H. Si, C. Zhou, H. Wang, S. Lou, S. Li, Z. Du, and L. Li, "Controlled synthesis of different types iron oxides nanocrystals in paraffin oil," *Journal of colloid and interface science*, vol. 327, no. 2, pp. 466–471, 2008.

[601] M. Testa-Anta, M. Ramos-Docampo, M. Comesaña-Hermo, B. Rivas-Murias, and V. Salgueiriño, "Raman spectroscopy to unravel the magnetic properties of iron oxide nanocrystals for bio-related applications," *Nanoscale Advances*, vol. 1, no. 6, pp. 2086–2103, 2019.

[602] C. Gellini, F. Deepak, M. Muniz-Miranda, S. Caporali, F. Muniz-Miranda, A. Pedone, C. Innocenti, and C. Sangregorio, "Magneto-plasmonic colloidal nanoparticles obtained by laser ablation of nickel and silver targets in water," *The Journal of Physical Chemistry C*, vol. 121, no. 6, pp. 3597–3606, 2017.

[603] R. Yuvakkumar, S. Lee, G. Lee, and S. Hong, "An environment benign biomimetic synthesis of mesoporous nio concentric stacked doughnuts architecture," *Microporous and Mesoporous Materials*, vol. 207, pp. 185–194, 2015.

[604] M. Tadic, M. Panjan, D. Markovic, B. Stanojevic, D. Jovanovic, I. Milosevic, and V. Spasojevic, "Nio core–shell nanostructure with ferromagnetic-like behavior at room temperature," *Journal of alloys and compounds*, vol. 586, pp. S322–S325, 2014.

[605] D. Leontyeva, I. Leontyev, M. Avramenko, Y. Yuzyuk, Y. Kukushkina, and N. Smirnova, "Electrochemical dispergation as a simple and effective technique toward preparation of nio based nanocomposite for supercapacitor application," *Electrochimica Acta*, vol. 114, pp. 356–362, 2013.

[606] M. Vidales-Hurtado and A. Mendoza-Galván, "Electrochromism in nickel oxide-based thin films obtained by chemical bath deposition," *Solid State Ionics*, vol. 179, no. 35-36, pp. 2065–2068, 2008.

[607] N. Dharmaraj, P. Prabu, S. Nagarajan, C. Kim, J. Park, and H. Kim, "Synthesis of nickel oxide nanoparticles using nickel acetate and poly (vinyl acetate) precursor," *Materials Science and Engineering: B*, vol. 128, no. 1-3, pp. 111–114, 2006.

[608] W. Brown Jr, "Theory of the approach to magnetic saturation," *Physical Review*, vol. 58, no. 8, p. 736, 1940.

[609] P. Dutta, A. Manivannan, M. Seehra, N. Shah, and G. Huffman, "Magnetic properties of nearly defect-free maghemite nanocrystals," *Physical Review B*, vol. 70, no. 17, p. 174428, 2004.

[610] C. Bean and J. Livingston, "Superparamagnetism," *Journal of Applied Physics*, vol. 30, no. 4, pp. S120–S129, 1959.

[611] P. Curie, *Propriétés magnétiques des corps a diverses températures.* No. 4, Gauthier-Villars et fils, 1895.

[612] M. Khan, W. Khan, M. Ahamed, and A. Alhazaa, "Investigation on the structure and physical properties of fe3o4/rgo nanocomposites and their photocatalytic application," *Materials Science in Semiconductor Processing*, vol. 99, pp. 44–53, 2019.

[613] R. Liang, F. Jing, L. Shen, N. Qin, and L. Wu, "M@ mil-100 (fe)(m= au, pd, pt) nanocomposites fabricated by a facile photodeposition process: Efficient visible-light photocatalysts for redox reactions in water," *Nano Research*, vol. 8, pp. 3237–3249, 2015.

[614] E. Polydorou, A. Zeniou, D. Tsikritzis, A. Soultati, I. Sakellis, S. Gardelis, T. Papadopoulos, J. Briscoe, L. Palilis, S. Kennou, *et al.*, "Surface passivation effect by fluorine plasma treatment on zno for efficiency and lifetime improvement of inverted polymer solar cells," *Journal of materials chemistry A*, vol. 4, no. 30, pp. 11844–11858, 2016.

[615] J. Zou, W. Deng, J. Jiang, X. He, N. Li, J. Fang, J. Hsu, *et al.*, "Built-in electric field-assisted step-scheme heterojunction of carbon nitride-copper oxide for highly selective electrochemical detection of p-nonylphenol," *Electrochimica Acta*, vol. 354, p. 136658, 2020.

[616] K. Wang, C. Yi, C. Liu, X. Hu, S. Chuang, and X. Gong, "Effects of magnetic nanoparticles and external magnetostatic field on the bulk heterojunction polymer solar cells," *Scientific Reports*, vol. 5, no. 1, p. 9265, 2015.

[617] A. Philip and A. Kumar, "The performance enhancement of surface plasmon resonance optical sensors using nanomaterials: A review," *Coordination Chemistry Reviews*, vol. 458, p. 214424, 2022.

[618] E. Dauzon, X. Sallenave, C. Plesse, F. Goubard, A. Amassian, and T. Anthopoulos, "Pushing the limits of flexibility and stretchability of solar cells: A review," *Advanced Materials*, vol. 33, no. 36, p. 2101469, 2021.

[619] S. George, A. Soosaimanickam, and S. Sundaram, "Third-generation photovoltaics: Introduction, overview, innovation, and potential markets," in *Photovoltaics Beyond Silicon*, pp. 75–110, Elsevier, 2024.

[620] R. Sorrentino, E. Kozma, S. Luzzati, and R. Po, "Interlayers for non-fullerene based polymer solar cells: distinctive features and challenges," *Energy & Environmental Science*, vol. 14, no. 1, pp. 180–223, 2021.

[621] J. Yi, G. Zhang, H. Yu, and H. Yan, "Advantages, challenges and molecular design of different material types used in organic solar cells," *Nature Reviews Materials*, vol. 9, no. 1, pp. 46–62, 2024.

[622] M. Wu, B. Ma, S. Li, J. Han, and W. Zhao, "Powering the future: A critical review of research progress in enhancing stability of high-efficiency organic solar cells," *Advanced Functional Materials*, vol. 33, no. 50, p. 2305445, 2023.

[623] Y. Liu, Q. Fan, H. Liu, I. Jalan, Y. Jin, J. Stam, E. Moons, E. Wang, X. Lu, O. Inganas, *et al.*, "In situ optical spectroscopy demonstrates the effect of solvent additive in the formation of all-polymer solar cells," *The journal of physical chemistry letters*, vol. 13, no. 50, pp. 11696–11702, 2022.

[624] N. Gasparini, S. Kahmann, M. Salvador, J. Perea, A. Sperlich, A. Baumann, N. Li, S. Rechberger, E. Spiecker, V. Dyakonov, *et al.*, "Favorable mixing thermodynamics in ternary polymer blends for realizing high efficiency plastic solar cells," *Advanced Energy Materials*, vol. 9, no. 19, p. 1803394, 2019.

[625] P. Cheng, C. Yan, Y. Wu, J. Wang, M. Qin, Q. An, J. Cao, L. Huo, F. Zhang, L. Ding, *et al.*, "Alloy acceptor: superior alternative to pcbm toward efficient and stable organic solar cells," *Advanced Materials*, vol. 28, no. 36, pp. 8021–8028, 2016.

[626] G. Vebber, P. Pranke, and C. Pereira, "Calculating hansen solubility parameters of polymers with genetic algorithms," *Journal of Applied Polymer Science*, vol. 131, no. 1, 2014.

[627] J. Lv, H. Tang, J. Huang, C. Yan, K. Liu, Q. Yang, D. Hu, R. Singh, J. Lee, S. Lu, *et al.*, "Additive-induced miscibility regulation and hierarchical morphology enable 17.5% binary organic solar cells," *Energy & Environmental Science*, vol. 14, no. 5, pp. 3044–3052, 2021.

[628] A. Karki, A. Gillett, R. Friend, and T. Nguyen, "The path to 20% power conversion efficiencies in nonfullerene acceptor organic solar cells," *Advanced Energy Materials*, vol. 11, no. 15, p. 2003441, 2021.

[629] H. Feng, N. Qiu, X. Wang, Y. Wang, B. Kan, X. Wan, M. Zhang, A. Xia, C. Li, F. Liu, *et al.*, "An ada type small-molecule electron acceptor with end-extended conjugation for high performance organic solar cells," *Chemistry of Materials*, vol. 29, no. 18, pp. 7908–7917, 2017.

[630] G. Wang, M. Adil, J. Zhang, and Z. Wei, "Large-area organic solar cells: material requirements, modular designs, and printing methods," *Advanced Materials*, vol. 31, no. 45, p. 1805089, 2019.

[631] M. Sawatzki-Park, S. Wang, H. Kleemann, and K. Leo, "Highly ordered small molecule organic semiconductor thin-films enabling complex, high-performance multi-junction devices," *Chemical Reviews*, vol. 123, no. 13, pp. 8232–8250, 2023.

[632] J. Lee, S. Yoshikawa, and T. Sagawa, "Fabrication of efficient organic and hybrid solar cells by fine channel mist spray coating," *Solar energy materials and solar cells*, vol. 127, pp. 111–121, 2014.

[633] F. Huang, M. Li, P. Siffalovic, G. Cao, and J. Tian, "From scalable solution fabrication of perovskite films towards commercialization of solar cells," *Energy & Environmental Science*, vol. 12, no. 2, pp. 518–549, 2019.

[634] Z. Li, T. Klein, D. Kim, M. Yang, J. Berry, M. Van Hest, and K. Zhu, "Scalable fabrication of perovskite solar cells," *Nature Reviews Materials*, vol. 3, no. 4, pp. 1–20, 2018.

[635] X. Sun, W. Zha, T. Lin, J. Wei, I. Ismail, Z. Wang, J. Lin, Q. Luo, C. Ding, L. Zhang, *et al.*, "Water-assisted formation of highly conductive silver nanowire electrode for all solution-processed semi-transparent perovskite and organic solar cells," *Journal of Materials Science*, vol. 55, pp. 14893–14906, 2020.

[636] C. Liu, C. Xiao, C. Xie, and W. Li, "Flexible organic solar cells: Materials, large-area fabrication techniques and potential applications," *Nano Energy*, vol. 89, p. 106399, 2021.

[637] P. V. Sampaio, M. González, P. de Oliveira Ferreira, P. da Cunha Jacome Vidal, J. Pereira, H. Ferreira, and P. Oprime, "Overview of printing and coating techniques in the production of organic photovoltaic cells," *International Journal of Energy Research*, vol. 44, no. 13, pp. 9912–9931, 2020.

[638] Y. Li, G. Xu, C. Cui, and Y. Li, "Flexible and semitransparent organic solar cells," *Advanced Energy Materials*, vol. 8, no. 7, p. 1701791, 2018.

[639] S. Karunakaran, G. Arumugam, W. Yang, S. Ge, S. Khan, X. Lin, and G. Yang, "Recent progress in inkjet-printed solar cells," *Journal of Materials Chemistry A*, vol. 7, no. 23, pp. 13873–13902, 2019.

[640] F. Brunetti, A. Operamolla, S. Castro-Hermosa, G. Lucarelli, V. Manca, G. Farinola, and T. Brown, "Printed solar cells and energy storage devices on paper substrates," *Advanced Functional Materials*, vol. 29, no. 21, p. 1806798, 2019.

[641] P. Xue, P. Cheng, R. Han, and X. Zhan, "Printing fabrication of large-area non-fullerene organic solar cells," *Materials Horizons*, vol. 9, no. 1, pp. 194–219, 2022.

[642] S. Razza, S. Castro-Hermosa, A. Di Carlo, and T. Brown, "Research update: Large-area deposition, coating, printing, and processing techniques for the upscaling of perovskite solar cell technology," *Apl Materials*, vol. 4, no. 9, 2016.

[643] A. Reale, L. La Notte, L. Salamandra, G. Polino, G. Susanna, T. Brown, F. Brunetti, and A. Di Carlo, "Spray coating for polymer solar cells: An up-to-date overview," *Energy Technology*, vol. 3, no. 4, pp. 385–406, 2015.

[644] F. Krebs, M. Jørgensen, K. Norrman, O. Hagemann, J. Alstrup, T. Nielsen, J. Fyenbo, K. Larsen, and J. Kristensen, "A complete process for production of flexible large area polymer solar cells entirely using screen printing—first public demonstration," *Solar Energy Materials and Solar Cells*, vol. 93, no. 4, pp. 422–441, 2009.

[645] M. Pagliaro, R. Ciriminna, and G. Palmisano, "Flexible solar cells," *ChemSusChem: Chemistry & Sustainability Energy & Materials*, vol. 1, no. 11, pp. 880–891, 2008.

[646] D. Yang, R. Yang, S. Priya, and S. Liu, "Recent advances in flexible perovskite solar cells: fabrication and applications," *Angewandte Chemie International Edition*, vol. 58, no. 14, pp. 4466–4483, 2019.

[647] N. Noel, B. Wenger, S. Habisreutinger, and H. Snaith, "Utilizing nonpolar organic solvents for the deposition of metal-halide perovskite films and the realization of organic semiconductor/perovskite composite photovoltaics," *ACS Energy Letters*, vol. 7, no. 4, pp. 1246–1254, 2022.

[648] C. Wang and C. Hua, "Solubility of c60 and pcbm in organic solvents," *The Journal of Physical Chemistry B*, vol. 119, no. 45, pp. 14496–14504, 2015.

[649] D. Qiu, M. Adil, K. Lu, and Z. Wei, "The crystallinity control of polymer donor materials for high-performance organic solar cells," *Frontiers in Chemistry*, vol. 8, p. 603134, 2020.

[650] Y. Lin and X. Zhan, "Non-fullerene acceptors for organic photovoltaics: an emerging horizon," *Materials Horizons*, vol. 1, no. 5, pp. 470–488, 2014.

[651] Y. Li, X. Huang, K. Ding, H. Sheriff Jr, L. Ye, H. Liu, C. Li, H. Ade, and S. Forrest, "Non-fullerene acceptor organic photovoltaics with intrinsic operational lifetimes over 30 years," *Nature communications*, vol. 12, no. 1, p. 5419, 2021.

[652] C. Nielsen, S. Holliday, H. Chen, S. Cryer, and I. McCulloch, "Non-fullerene electron acceptors for use in organic solar cells," *Accounts of chemical research*, vol. 48, no. 11, pp. 2803–2812, 2015.

[653] J. Oh, H. Park, J. Kim, S. Chen, S. Lee, J. Kim, X. Song, H. Kang, S. Jang, S. Kwon, *et al.*, "A series of selenium-containing non-fullerene acceptors with side chain engineering for organic solar cells," *Dyes and Pigments*, vol. 207, p. 110646, 2022.

[654] A. Boman and J. Wahlberg, *Organic solvents*. Springer, 2000.

[655] D. Lide, *Properties of organic solvents*. CRC Press, 1996.

[656] A. Covington, *Physical chemistry of organic solvent systems*. Springer Science & Business Media, 2012.

[657] H. Ukai, S. Inui, S. Takada, J. Dendo, J. Ogawa, K. Isobe, T. Ashida, M. Tamura, K. Tabuki, and M. Ikeda, "Types of organic solvents used in small-to medium-scale industries in japan; a nationwide field survey," *International archives of occupational and environmental health*, vol. 70, pp. 385–392, 1997.

[658] F. Byrne, S. Jin, G. Paggiola, T. Petchey, J. Clark, T. Farmer, A. Hunt, C. Robert McElroy, and J. Sherwood, "Tools and techniques for solvent selection: green solvent selection guides," *Sustainable Chemical Processes*, vol. 4, pp. 1–24, 2016.

[659] Y. Jiang, X. Wang, and A. Pan, "Properties of excitons and photogenerated charge carriers in metal halide perovskites," *Advanced Materials*, vol. 31, no. 47, p. 1806671, 2019.

[660] M. Szymański, B. Łuszczyńska, and J. Ulański, "Inkjet printing of super yellow: ink formulation, film optimization, oleds fabrication, and transient electroluminescence," *Scientific reports*, vol. 9, no. 1, p. 8493, 2019.

[661] B. Jewłoszewicz, K. Bogdanowicz, W. Przybył, K. Dysz, A. Dylong, A. Gonciarz, R. Pich, W. Mech, K. Korona, M. Kamińska, *et al.*, "A comprehensive optical and electrical study of unsymmetrical imine with four thiophene rings and their binary and ternary compositions with ptb7 and pc 70 bm towards organic photovoltaics," *RSC advances*, vol. 10, no. 73, pp. 44958–44972, 2020.

[662] R. Steyrleuthner, M. Schubert, I. Howard, B. Klaumünzer, K. Schilling, Z. Chen, P. Saalfrank, F. Laquai, A. Facchetti, and D. Neher, "Aggregation in a high-mobility n-type low-bandgap copolymer with implications on semicrystalline morphology," *Journal of the American Chemical Society*, vol. 134, no. 44, pp. 18303–18317, 2012.

[663] S. Lee, D. Jeong, C. Kim, C. Lee, H. Kang, H. Woo, and B. Kim, "Eco-friendly polymer solar cells: Advances in green-solvent processing and material design," *Acs Nano*, vol. 14, no. 11, pp. 14493–14527, 2020.

[664] S. McAfee, J. Topple, I. Hill, and G. Welch, "Key components to the recent performance increases of solution processed non-fullerene small molecule acceptors," *Journal of Materials Chemistry A*, vol. 3, no. 32, pp. 16393–16408, 2015.

[665] P. Bi, S. Zhang, J. Wang, J. Ren, and J. Hou, "Progress in organic solar cells: materials, physics and device engineering," *Chinese Journal of Chemistry*, vol. 39, no. 9, pp. 2607–2625, 2021.

[666] S. Podapangi, F. Jafarzadeh, S. Mattiello, T. Korukonda, A. Singh, L. Beverina, and T. Brown, "Green solvents, materials, and lead-free semiconductors for sustainable fabrication of perovskite solar cells," *RSC advances*, vol. 13, no. 27, pp. 18165–18206, 2023.

[667] D. Corzo, *Ink Formulation, Green Processing, And Integration Strategies For Printable Organic Photovoltaics*. PhD thesis, King Abdullah University of Science and Technology, 2022.

[668] A. Arias, J. MacKenzie, R. Stevenson, J. Halls, M. Inbasekaran, E. Woo, D. Richards, and R. Friend, "Photovoltaic performance and morphology of polyfluorene blends: a combined microscopic and photovoltaic investigation," *Macromolecules*, vol. 34, no. 17, pp. 6005–6013, 2001.

[669] M. Hasegawa and K. Horie, "Photophysics, photochemistry, and optical properties of polyimides," *Progress in Polymer Science*, vol. 26, no. 2, pp. 259–335, 2001.

[670] H. Tong, Y. Dong, Y. Hong, M. Häussler, J. Lam, H. Sung, X. Yu, J. Sun, I. Williams, H. Kwok, *et al.*, "Aggregation-induced emission: effects of molecular structure, solid-state conformation, and morphological packing arrangement on light-emitting behaviors of diphenyldibenzofulvene derivatives," *The Journal of Physical Chemistry C*, vol. 111, no. 5, pp. 2287–2294, 2007.

[671] L. Huang, T. Li, B. Liu, L. Zhang, Z. Bai, X. Li, X. Huang, and D. Lu, "A transformation process and mechanism between the α-conformation and β-conformation of conjugated polymer pfo in precursor solution," *Soft Matter*, vol. 11, no. 13, pp. 2627–2638, 2015.

[672] J. Langer, D. Jimenez de Aberasturi, J. Aizpurua, R. Alvarez-Puebla, B. Auguié, J. Baumberg, G. Bazan, S. Bell, A. Boisen, A. Brolo, *et al.*, "Present and future of surface-enhanced raman scattering," *ACS nano*, vol. 14, no. 1, pp. 28–117, 2019.

[673] L. Arunagiri, Z. Peng, X. Zou, H. Yu, G. Zhang, Z. Wang, J. Lai, J. Zhang, Y. Zheng, C. Cui, *et al.*, "Selective hole and electron transport in efficient quaternary blend organic solar cells," *Joule*, vol. 4, no. 8, pp. 1790–1805, 2020.

[674] T. Sharma, P. Mahajan, M. Adil Afroz, A. Singh, Yukta, N. Kumar Tailor, S. Purohit, S. Verma, B. Padha, V. Gupta, *et al.*, "Recent progress in advanced organic photovoltaics: emerging techniques and materials," *ChemSusChem*, vol. 15, no. 5, p. e202101067, 2022.

[675] Y. Chang, *Device Fabrication and Material Design for High Performance Organic Photovoltaics Based on Non-Fullerene Acceptors with Bulky Flanking Side-Chains*. Hong Kong University of Science and Technology (Hong Kong), 2022.

[676] C. Chen, G. Wen, Z. Xiao, J. Peng, R. Hu, Z. Chen, C. Zhang, and W. Zhang, "Charge photogeneration and recombination dynamics in ptq10: Y6 solar cells," in *Photonics*, vol. 9, p. 892, MDPI, 2022.

[677] M. Zhang, X. Chen, L. Wang, X. Deng, and S. Tan, "Simultaneously enhancing the photovoltaic parameters of ternary organic solar cells by incorporating a fused ring electron acceptor," *RSC advances*, vol. 13, no. 25, pp. 17354–17361, 2023.

[678] H. Lu, M. Li, Z. Bi, X. Gong, G. Li, S. Feng, X. Xu, W. Ma, and Z. Bo, "Using ternary blend as a strategy to improve the driving force for charge transfer and facilitate electron transport in polymer solar cells," *Organic Electronics*, vol. 65, pp. 419–425, 2019.

[679] R. Ma, H. Li, T. Dela Peña, X. Xie, P. Fong, Q. Wei, C. Yan, J. Wu, P. Cheng, M. Li, *et al.*, "Tunable donor aggregation dominance in a ternary matrix of all-polymer blends with improved efficiency and stability," *Advanced Materials*, p. 2304632, 2023.

[680] Y. Ma, R. Sun, Z. Chen, S. Zhang, D. Cai, S. Wan, W. Lin, S. Zhang, Q. Tu, W. Ma, *et al.*, "17% efficiency for linear-shaped ada-type nonfullerene acceptors enabled by 3d reticulated molecular packing," *Nano Energy*, vol. 107, p. 108116, 2023.

[681] B. Fan, X. Du, F. Liu, W. Zhong, L. Ying, R. Xie, X. Tang, K. An, J. Xin, N. Li, *et al.*, "Fine-tuning of the chemical structure of photoactive materials for highly efficient organic photovoltaics," *Nature Energy*, vol. 3, no. 12, pp. 1051–1058, 2018.

[682] D. Khim, A. Luzio, G. Bonacchini, G. Pace, M. Lee, Y. Noh, and M. Caironi, "Uniaxial alignment of conjugated polymer films for high-performance organic field-effect transistors," *Advanced Materials*, vol. 30, no. 20, p. 1705463, 2018.

[683] F. Zhao, H. Zhang, R. Zhang, J. Yuan, D. He, Y. Zou, and F. Gao, "Emerging approaches in enhancing the efficiency and stability in non-fullerene organic solar cells," *Advanced Energy Materials*, vol. 10, no. 47, p. 2002746, 2020.

[684] G. Zhang, J. Zhao, P. Chow, K. Jiang, J. Zhang, Z. Zhu, J. Zhang, F. Huang, and H. Yan, "Nonfullerene acceptor molecules for bulk heterojunction organic solar cells," *Chemical reviews*, vol. 118, no. 7, pp. 3447–3507, 2018.

[685] J. Chen, Y. Chen, L. Feng, C. Gu, G. Li, N. Su, G. Wang, S. Swick, W. Huang, X. Guo, *et al.*, "Hole (donor) and electron (acceptor) transporting organic semiconductors for bulk-heterojunction solar cells," *EnergyChem*, vol. 2, no. 5, p. 100042, 2020.

[686] R. Ma, X. Jiang, J. Fu, T. Zhu, C. Yan, K. Wu, P. Müller-Buschbaum, and G. Li, "Revealing the underlying solvent effect on film morphology in high-efficiency organic solar cells through combined ex situ and in situ observations," *Energy & Environmental Science*, vol. 16, no. 5, pp. 2316–2326, 2023.

[687] Z. Shen, J. Yu, G. Lu, K. Wu, Q. Wang, L. Bu, X. Liu, Y. Zhu, and G. Lu, "Surface crystallinity enhancement in organic solar cells induced by spinodal demixing of acceptors and additives," *Energy & Environmental Science*, vol. 16, no. 7, pp. 2945–2956, 2023.

[688] C. Li, X. Gu, Z. Chen, X. Han, N. Yu, Y. Wei, J. Gao, H. Chen, M. Zhang, A. Wang, *et al.*, "Achieving record-efficiency organic solar cells upon tuning the conformation of solid additives," *Journal of the American Chemical Society*, vol. 144, no. 32, pp. 14731–14739, 2022.

[689] Z. Zheng, J. Wang, P. Bi, J. Ren, Y. Wang, Y. Yang, X. Liu, S. Zhang, and J. Hou, "Tandem organic solar cell with 20.2% efficiency," *Joule*, vol. 6, no. 1, pp. 171–184, 2022.

[690] A. Jiménez, L. Sánchez-González, S. Desobry, A. Chiralt, and E. Tehrany, "Influence of nanoliposomes incorporation on properties of film forming dispersions and films based on corn starch and sodium caseinate," *Food Hydrocolloids*, vol. 35, pp. 159–169, 2014.

[691] C. Jones and J. Steed, "Gels with sense: supramolecular materials that respond to heat, light and sound," *Chemical Society Reviews*, vol. 45, no. 23, pp. 6546–6596, 2016.

[692] Y. Wu, S. Schneider, C. Walter, A. Chowdhury, B. Bahrami, H. Wu, Q. Qiao, M. Toney, and Z. Bao, "Fine-tuning semiconducting polymer self-aggregation and crystallinity enables optimal morphology and high-performance printed all-polymer solar cells," *Journal of the American Chemical Society*, vol. 142, no. 1, pp. 392–406, 2019.

[693] J. Liu, J. Han, Q. Liang, J. Xin, Y. Tang, W. Ma, X. Yu, and Y. Han, "Balancing crystal size in small-molecule nonfullerene solar cells through fine-tuning the film-forming kinetics to fabricate interpenetrating network," *ACS omega*, vol. 3, no. 7, pp. 7603–7612, 2018.

[694] S. Li, W. Zhao, J. Zhang, X. Liu, Z. Zheng, C. He, B. Xu, Z. Wei, and J. Hou, "Influence of covalent and noncovalent backbone rigidification strategies on the aggregation structures of a wide-band-gap polymer for photovoltaic cells," *Chemistry of Materials*, vol. 32, no. 5, pp. 1993–2003, 2020.

[695] Q. Li, Z. Yao, J. Wang, and J. Pei, "Multi-level aggregation of conjugated small molecules and polymers: from morphology control to physical insights," *Reports on Progress in Physics*, vol. 84, no. 7, p. 076601, 2021.

[696] Y. Huang, E. Kramer, A. Heeger, and G. Bazan, "Bulk heterojunction solar cells: morphology and performance relationships," *Chemical reviews*, vol. 114, no. 14, pp. 7006–7043, 2014.

[697] D. Egbe, S. Türk, S. Rathgeber, F. Kuhnlenz, R. Jadhav, A. Wild, E. Birckner, G. Adam, A. Pivrikas, V. Cimrova, *et al.*, "Anthracene based conjugated polymers: Correlation between π- π-stacking ability, photophysical properties, charge carrier mobility, and photovoltaic performance," *Macromolecules*, vol. 43, no. 3, pp. 1261–1269, 2010.

[698] M. Qiu, D. Zhu, L. Yan, N. Wang, L. Han, X. Bao, Z. Du, Y. Niu, and R. Yang, "Strategy to manipulate molecular orientation and charge mobility in d–a type conjugated polymer through rational fluorination for improvements of photovoltaic performances," *The Journal of Physical Chemistry C*, vol. 120, no. 40, pp. 22757–22765, 2016.

[699] J. Li, Z. Liang, Y. Wang, H. Li, J. Tong, X. Bao, and Y. Xia, "Enhanced efficiency of polymer solar cells through synergistic optimization of mobility and tuning donor alloys by adding high-mobility conjugated polymers," *Journal of Materials Chemistry C*, vol. 6, no. 41, pp. 11015–11022, 2018.

[700] Y. Tamai, H. Ohkita, H. Benten, and S. Ito, "Exciton diffusion in conjugated polymers: from fundamental understanding to improvement in photovoltaic conversion efficiency," *The journal of physical chemistry letters*, vol. 6, no. 17, pp. 3417–3428, 2015.

[701] T. Liu, Z. Luo, Q. Fan, G. Zhang, L. Zhang, W. Gao, X. Guo, W. Ma, M. Zhang, C. Yang, *et al.*, "Use of two structurally similar small molecular acceptors enabling ternary organic solar cells with high efficiencies and fill factors," *Energy & Environmental Science*, vol. 11, no. 11, pp. 3275–3282, 2018.

[702] J. Huang, Z. Yin, and Q. Zheng, "Applications of zno in organic and hybrid solar cells," *Energy & Environmental Science*, vol. 4, no. 10, pp. 3861–3877, 2011.

[703] S. Shoaee, M. Stolterfoht, and D. Neher, "The role of mobility on charge generation, recombination, and extraction in polymer-based solar cells," *Advanced Energy Materials*, vol. 8, no. 28, p. 1703355, 2018.

[704] N. Ran, J. Love, M. Heiber, X. Jiao, M. Hughes, A. Karki, M. Wang, V. Brus, H. Wang, D. Neher, *et al.*, "Charge generation and recombination in an organic solar cell with low energetic offsets," *Advanced Energy Materials*, vol. 8, no. 5, p. 1701073, 2018.

[705] M. Ghorab, A. Fattah, and M. Joodaki, "Fundamentals of organic solar cells: A review on mobility issues and measurement methods," *Optik*, vol. 267, p. 169730, 2022.

[706] L. Pauling, "Electronic processes in ionic crystals. by nf mott and rw gurney.," *The Journal of Physical Chemistry*, vol. 45, no. 7, pp. 1142–1142, 1941.

[707] A. Kokil, K. Yang, and J. Kumar, "Techniques for characterization of charge carrier mobility in organic semiconductors," *Journal of polymer science part b: polymer physics*, vol. 50, no. 15, pp. 1130–1144, 2012.

[708] F. Araujo, D. Amorim, B. Torres, D. Coutinho, and R. Faria, "Electrical performance of ptb7-th: Pc71bm solar cell when in contact with the environment," *Solar Energy*, vol. 208, pp. 583–590, 2020.

[709] X. Guo, C. Cui, M. Zhang, L. Huo, Y. Huang, J. Hou, and Y. Li, "High efficiency polymer solar cells based on poly (3-hexylthiophene)/indene-c 70 bisadduct with solvent additive," *Energy & Environmental Science*, vol. 5, no. 7, pp. 7943–7949, 2012.

[710] Q. Zhang, Z. Chen, W. Ma, Z. Xie, and Y. Han, "Optimizing domain size and phase purity in all-polymer solar cells by solution ordered aggregation and confinement effect of the acceptor," *Journal of Materials Chemistry C*, vol. 7, no. 40, pp. 12560–12571, 2019.

[711] B. Kim, X. Ma, C. Chen, Y. Ie, E. Coir, H. Hashemi, Y. Aso, P. Green, J. Kieffer, and J. Kim, "Energy level modulation of homo, lumo, and band-gap in conjugated polymers for organic photovoltaic applications," *Advanced Functional Materials*, vol. 23, no. 4, pp. 439–445, 2013.

[712] L. Ye, K. Weng, J. Xu, X. Du, S. Chandrabose, K. Chen, J. Zhou, G. Han, S. Tan, Z. Xie, *et al.*, "Unraveling the influence of non-fullerene acceptor molecular packing on photovoltaic performance of organic solar cells," *Nature communications*, vol. 11, no. 1, p. 6005, 2020.

[713] V. Pranculis, A. Ruseckas, D. Vithanage, G. Hedley, I. Samuel, and V. Gulbinas, "Influence of blend ratio and processing additive on free carrier yield and mobility in ptb7: Pc71bm photovoltaic solar cells," *The Journal of Physical Chemistry C*, vol. 120, no. 18, pp. 9588–9594, 2016.

[714] F. Zhang, K. Jespersen, C. Björström, M. Svensson, M. Andersson, V. Sundström, K. Magnusson, E. Moons, A. Yartsev, and O. Inganäs, "Influence of solvent mixing on the morphology and performance of solar cells based on polyfluorene copolymer/fullerene blends," *Advanced Functional Materials*, vol. 16, no. 5, pp. 667–674, 2006.

[715] Y. Diao, L. Shaw, Z. Bao, and S. Mannsfeld, "Morphology control strategies for solution-processed organic semiconductor thin films," *Energy & Environmental Science*, vol. 7, no. 7, pp. 2145–2159, 2014.

[716] R. Roesch, T. Faber, E. Von Hauff, T. Brown, M. Lira-Cantu, and H. Hoppe, "Procedures and practices for evaluating thin-film solar cell stability," *Advanced Energy Materials*, vol. 5, no. 20, p. 1501407, 2015.

[717] Y. Cui, L. Hong, T. Zhang, H. Meng, H. Yan, F. Gao, and J. Hou, "Accurate photovoltaic measurement of organic cells for indoor applications," *Joule*, vol. 5, no. 5, pp. 1016–1023, 2021.

[718] J. Fu, P. Fong, H. Liu, C. Huang, X. Lu, S. Lu, M. Abdelsamie, T. Kodalle, C. Sutter-Fella, Y. Yang, *et al.*, "19.31% binary organic solar cell and low non-radiative recombination enabled by non-monotonic intermediate state transition," *Nature communications*, vol. 14, no. 1, p. 1760, 2023.

[719] A. Gavrik, A. Mannanov, S. Tsarev, V. Bruevich, V. Trukhanov, Y. Chernikov, P. Savchenko, J. Gvozdkova, A. Solodukhin, P. Troshin, *et al.*, "Spectral technique for accurate efficiency measurements of emerging solar cells," *Solar Energy*, vol. 206, pp. 770–777, 2020.

[720] W. Mateker and M. McGehee, "Progress in understanding degradation mechanisms and improving stability in organic photovoltaics," *Advanced materials*, vol. 29, no. 10, p. 1603940, 2017.

[721] T. Rahman, A. Mansur, M. Hossain Lipu, M. Rahman, R. Ashique, M. Houran, R. Elavarasan, and E. Hossain, "Investigation of degradation of solar photovoltaics: A review of aging factors, impacts, and future directions toward sustainable energy management," *Energies*, vol. 16, no. 9, p. 3706, 2023.

[722] S. Dkhil, M. Pfannmöller, M. Saba, M. Gaceur, H. Heidari, C. Videlot-Ackermann, O. Margeat, A. Guerrero, J. Bisquert, G. Garcia-Belmonte, *et al.*, "Toward high-temperature stability of ptb7-based bulk heterojunction solar cells: impact of fullerene size and solvent additive," *Advanced Energy Materials*, vol. 7, no. 4, p. 1601486, 2017.

[723] L. Xue, J. Zhang, and Y. Han, "Phase separation induced ordered patterns in thin polymer blend films," *Progress in polymer science*, vol. 37, no. 4, pp. 564–594, 2012.

[724] F. Zhang, X. Xu, W. Tang, J. Zhang, Z. Zhuo, J. Wang, J. Wang, Z. Xu, and Y. Wang, "Recent development of the inverted configuration organic solar cells," *Solar Energy Materials and Solar Cells*, vol. 95, no. 7, pp. 1785–1799, 2011.

[725] S. Neuser and V. Michaud, "Effect of aging on the performance of solvent-based self-healing materials," *Polymer Chemistry*, vol. 4, no. 18, pp. 4993–4999, 2013.

[726] L. Ciammaruchi, F. Brunetti, and I. Visoly-Fisher, "Solvent effects on the morphology and stability of ptb7: Pcbm based solar cells," *Solar Energy*, vol. 137, pp. 490–499, 2016.

[727] J. Dagar and T. Brown, "Biological/metal oxide composite transport layers cast from green solvents for boosting light harvesting response of organic photovoltaic cells indoors," *Nanotechnology*, vol. 33, no. 40, p. 405404, 2022.

[728] A. de Zerio Mendaza, A. Melianas, F. Nugroho, O. Bäcke, E. Olsson, C. Langhammer, O. Inganäs, and C. Müller, "A fullerene alloy based photovoltaic blend with a glass transition temperature above 200 c," *Journal of materials chemistry A*, vol. 5, no. 8, pp. 4156–4162, 2017.

[729] M. Günther, N. Kazerouni, D. Blätte, J. Perea, B. Thompson, and T. Ameri, "Models and mechanisms of ternary organic solar cells," *Nature Reviews Materials*, vol. 8, no. 7, pp. 456–471, 2023.

[730] H. Fu, Z. Wang, and Y. Sun, "Polymer donors for high-performance non-fullerene organic solar cells," *Angewandte Chemie International Edition*, vol. 58, no. 14, pp. 4442–4453, 2019.

[731] C. Sun, F. Pan, H. Bin, J. Zhang, L. Xue, B. Qiu, Z. Wei, Z. Zhang, and Y. Li, "A low cost and high performance polymer donor material for polymer solar cells," *Nature communications*, vol. 9, no. 1, p. 743, 2018.

[732] L. Chang, M. Sheng, L. Duan, and A. Uddin, "Ternary organic solar cells based on non-fullerene acceptors: A review," *Organic Electronics*, vol. 90, p. 106063, 2021.

[733] M. Keshtov, A. Khokhlov, D. Shikin, V. Alekseev, G. Chayal, H. Dahiya, M. Singh, F. Chen, and G. Sharma, "Medium bandgap nonfullerene acceptor for efficient ternary polymer solar cells with high open-circuit voltage," *ACS omega*, vol. 8, no. 2, pp. 1989–2000, 2023.

[734] M. Irimia-Vladu, ""green" electronics: biodegradable and biocompatible materials and devices for sustainable future," *Chemical Society Reviews*, vol. 43, no. 2, pp. 588–610, 2014.

[735] R. Ganesamoorthy, G. Sathiyan, and P. Sakthivel, "Fullerene based acceptors for efficient bulk heterojunction organic solar cell applications," *Solar Energy Materials and Solar Cells*, vol. 161, pp. 102–148, 2017.

[736] L. Zhu, M. Zhang, W. Zhong, S. Leng, G. Zhou, Y. Zou, X. Su, H. Ding, P. Gu, F. Liu, *et al.*, "Progress and prospects of the morphology of non-fullerene acceptor based high-efficiency organic solar cells," *Energy & Environmental Science*, vol. 14, no. 8, pp. 4341–4357, 2021.

[737] T. Liu, R. Ma, Z. Luo, Y. Guo, G. Zhang, Y. Xiao, T. Yang, Y. Chen, G. Li, Y. Yi, *et al.*, "Concurrent improvement in j sc and v oc in high-efficiency ternary organic solar cells enabled by a red-absorbing small-molecule acceptor with a high lumo level," *Energy & Environmental Science*, vol. 13, no. 7, pp. 2115–2123, 2020.

[738] J. Rech, J. Neu, Y. Qin, S. Samson, J. Shanahan, R. Josey III, H. Ade, and W. You, "Designing simple conjugated polymers for scalable and efficient organic solar cells," *ChemSusChem*, vol. 14, no. 17, pp. 3561–3568, 2021.

[739] J. Panidi, E. Mazzolini, F. Eisner, Y. Fu, F. Furlan, Z. Qiao, M. Rimmele, Z. Li, X. Lu, J. Nelson, *et al.*, "Biorenewable solvents for high-performance organic solar cells," *ACS Energy Letters*, vol. 8, no. 7, pp. 3038–3047, 2023.